



NATIONAL TECHNICAL UNIVERSITY OF ATHENS
SCHOOL OF APPLIED MATHEMATICAL AND PHYSICAL
SCIENCES

**Cross-section studies of deuteron reactions and application in light
element ion beam analysis techniques**

DOCTORAL DISSERTATION

NTEMOU ELENI

Diploma, School of Applied Mathematical and Physical Sciences, N.T.U.A.

M.Sc., Physics and Technological Applications, N.T.U.A.

Supervisor: Kokkoris Michael, Professor N.T.U.A

Athens, February 2020



Ευρωπαϊκή Ένωση
European Social Fund

Operational Programme
**Human Resources Development,
Education and Lifelong Learning**

Co-financed by Greece and the European Union





NATIONAL TECHNICAL UNIVERSITY OF ATHENS
SCHOOL OF APPLIED MATHEMATICAL AND PHYSICAL
SCIENCES

**Cross-section studies of deuteron reactions and application in light
element ion beam analysis techniques**

DOCTORAL DISSERTATION

NTEMOU ELENI

ADVISORY COMMITTEE

1. M. Kokkoris, Professor N.T.U.A
2. A. Lagoyannis, Researcher,
N.C.S.R. “Demokritos”
3. R. Vlastou-Zanni, Professor
N.T.U.A.

EXAMINATION COMMITTEE

1. M. Kokkoris, Professor N.T.U.A.
2. A. Lagoyannis, Researcher,
N.C.S.R. “Demokritos”
3. R. Vlastou-Zanni, Professor
N.T.U.A.
4. A. F. Gurbich, Professor IPPE
Obninsk
5. N. Patronis, Associate Professor,
UoI
6. I. Bogdanovic-Radovic, RBI
7. M. Mayer, Researcher, IPP,
Garching



Ευρωπαϊκή Ένωση
European Social Fund

Operational Programme
Human Resources Development,
Education and Lifelong Learning

Co-financed by Greece and the European Union





ΕΘΝΙΚΟ ΜΕΤΣΟΒΙΟ ΠΟΛΥΤΕΧΝΕΙΟ
ΣΧΟΛΗ ΕΦΑΡΜΟΣΜΕΝΩΝ ΜΑΘΗΜΑΤΙΚΩΝ ΚΑΙ
ΦΥΣΙΚΩΝ ΕΠΙΣΤΗΜΩΝ

**Μελέτη ενεργών διατομών αντιδράσεων δευτερίων και εφαρμογή σε
ιοντικές τεχνικές ανάλυσης ελαφρών στοιχείων**

ΔΙΔΑΚΤΟΡΙΚΗ ΔΙΑΤΡΙΒΗ

ΝΤΕΜΟΥ ΕΛΕΝΗ

Διπλωματούχος Σχολής Εφαρμοσμένων Μαθηματικών και Φυσικών Επιστημών,
Ε.Μ.Π.

Μεταπτυχιακό Δίπλωμα Ειδίκευσης, Φυσική και Τεχνολογικές Εφαρμογές, Ε.Μ.Π

Επιβλέπων: Κόκκορης Μιχαήλ, Καθηγητής ΕΜΠ

Αθήνα, Φεβρουάριος 2020



Επιχειρησιακό Πρόγραμμα
Ανάπτυξη Ανθρώπινου Δυναμικού,
Εκπαίδευση και Διά Βίου Μάθηση

Με τη συγχρηματοδότηση της Ελλάδας και της Ευρωπαϊκής Ένωσης





ΕΘΝΙΚΟ ΜΕΤΣΟΒΙΟ ΠΟΛΥΤΕΧΝΕΙΟ
ΣΧΟΛΗ ΕΦΑΡΜΟΣΜΕΝΩΝ ΜΑΘΗΜΑΤΙΚΩΝ ΚΑΙ
ΦΥΣΙΚΩΝ ΕΠΙΣΤΗΜΩΝ

**Μελέτη ενεργών διατομών αντιδράσεων δευτερίων και εφαρμογή σε
ιοντικές τεχνικές ανάλυσης ελαφρών στοιχείων**

ΔΙΔΑΚΤΟΡΙΚΗ ΔΙΑΤΡΙΒΗ
ΝΤΕΜΟΥ ΕΛΕΝΗ

**ΤΡΙΜΕΛΗΣ ΣΥΜΒΟΥΛΕΥΤΙΚΗ
ΕΠΙΤΡΟΠΗ**

1. Μ. Κόκκορης, Καθηγητής Ε.Μ.Μ.
2. Α. Λαγογιάννης, Ερευνητής,
Ε.Κ.Ε.Φ.Ε. «Δημόκριτος»
3. Ρ. Ζάννη- Βλαστού, Καθηγήτρια
Ε.Μ.Π.

**ΕΠΤΑΜΕΛΗΣ ΕΞΕΤΑΣΤΙΚΗ
ΕΠΙΤΡΟΠΗ**

1. Μ. Κόκκορης, Καθηγητής
Ε.Μ.Μ.
2. Α. Λαγογιάννης, Ερευνητής,
Ε.Κ.Ε.Φ.Ε. «Δημόκριτος»
3. Ρ. Ζάννη- Βλαστού,
Καθηγήτρια Ε.Μ.Π.
4. Α. F. Gurbich, Καθηγητής IPPE
Obninsk
5. Ν. Πατρώνης, Αναπληρωτής
Καθηγητής, Παν. Ιωαννίνων
6. I. Bogdanovic-Radovic, RBI
7. M. Mayer, Researcher, IPP,
Garching



Ευρωπαϊκή Ένωση
Ευρωπαϊκό Κοινωνικό Ταμείο

Επιχειρησιακό Πρόγραμμα
Ανάπτυξη Ανθρώπινου Δυναμικού,
Εκπαίδευση και Διά Βίου Μάθηση

Με τη συγχρηματοδότηση της Ελλάδας και της Ευρωπαϊκής Ένωσης



«Το έργο συγχρηματοδοτείται από την Ελλάδα και την Ευρωπαϊκή Ένωση (Ευρωπαϊκό Κοινωνικό Ταμείο) μέσω του Επιχειρησιακού Προγράμματος «Ανάπτυξη Ανθρώπινου Δυναμικού, Εκπαίδευση και Διά Βίου Μάθηση», στο πλαίσιο της Πράξης «Ενίσχυση του ανθρώπινου ερευνητικού δυναμικού μέσω της υλοποίησης διδακτορικής έρευνας» (MIS-5000432), που υλοποιεί το Ίδρυμα Κρατικών Υποτροφιών (ΙΚΥ)»



Ευρωπαϊκή Ένωση
Ευρωπαϊκό Κοινωνικό Ταμείο

Επιχειρησιακό Πρόγραμμα
Ανάπτυξη Ανθρώπινου Δυναμικού,
Εκπαίδευση και Διά Βίου Μάθηση

Με τη συγχρηματοδότηση της Ελλάδας και της Ευρωπαϊκής Ένωσης



«This research is co-financed by Greece and the European Union (European Social Fund-ESF) through the Operational Programme «Human Resources Development, Education and Lifelong Learning» in the context of the project “Strengthening Human Resources Research Potential via Doctorate Research” (MIS-5000432), implemented by the State Scholarships Foundation (IKY)»



Ευρωπαϊκή Ένωση
European Social Fund

Operational Programme
Human Resources Development,
Education and Lifelong Learning

Co-financed by Greece and the European Union



Acknowledgments

I would like to express my sincere appreciation to Dr. Michael Kokkoris, professor of N.T.U.A. and to Dr. Anastasios Lagoyannis, Researcher at the N.C.S.R. “Demokritos”, for their constant support and precious mentoring throughout all of these years. It was an ideal collaboration. Moreover, I am grateful for plenty fruitful discussions and the opportunity to interact with such an esteemed advisor as Dr. Roza Vlastou-Zanni, Professor of N.T.U.A. I would also like to acknowledge the contribution of the examination committee through their constructive comments and valuable feedback. Especially, Dr. A.F. Gurbich, Professor at the IPPE of Obninsk, in Russian Federation, for his hospitality, truly valuable guidance and time dedicated during our collaboration at Obninsk.

I would also like to thank all of the staff members of the Tandem Accelerator Laboratory of NCSR "Demokritos" for their significant assistance during all the experiments conducted in the context of the present thesis, as well as for the friendly environment which helped me immensely throughout the past four years. I would like to specifically thank Michail Axiotis, Researcher at the N.C.S.R “Demokritos” for his willingness and ability to assist in any situation that occurred.

I could never forget the team of the N.T.U.A. (from 2014 to present) for offering their lavish help during my undergraduate, master’s and doctoral studies while creating the ideal balance between academic research and social interaction.

I would like to thank my close friends for making my life delightful with their continuous love, patience and support. Last but not least, I deeply thank my parents, Victoria and Serafeim, and my sister, Vasileia, for their infinite support in every way, encouragement and sincere love all of these years.

This research is co-financed by Greece and the European Union (European Social Fund- ESF) through the Operational Programme «Human Resources Development, Education and Lifelong Learning» in the context of the project “Strengthening Human Resources Research Potential via Doctorate Research” (MIS-5000432), implemented by the State Scholarships Foundation (IKY).

Table of Contents

Περίληψη	10
Θεωρητικό πλαίσιο	12
Μετρήσεις διαφορικών ενεργών διατομών	19
Μελέτη της ελαστικής σκέδασης $^{16}\text{O}(d,d_0)^{16}\text{O}$	52
Προοπτικές	63
Introduction	65
Chapter 1 Deuteron Physics & Basic Principles of Theory	67
1.1 Theory of Elastic Scattering.....	68
1.2 Optical Model for Elastic Scattering.....	73
1.3 Reaction mechanisms.....	76
1.4 R-Matrix theory	82
1.4.1 Introduction	82
1.4.2 Basic principles	83
1.4.3 Elastic scattering of a spinless particle by a central potential	84
1.4.4 The single channel multi-level R-matrix	87
Chapter 2 Motivation and IBA techniques	88
2.1 Light Elements.....	88
2.2 Ion Beam Analysis Techniques.....	90
2.2.1 Rutherford Backscattering Spectrometry	90
2.2.2 Elastic Recoil Detection Analysis	91
2.2.3 Elastic (non-Rutherford) Backscattering Spectroscopy	92
2.2.4 Nuclear Reaction Analysis	92
2.2.5 Parameters for choosing the most suitable IBA technique for each case	92
2.3 Deuteron Nuclear Reaction Analysis Technique	93
2.4 Deuteron Elastic Backscattering spectroscopy	94
2.5 Content and goals of the present work.....	95
Chapter 3 Experimental Setup	97
3.1 5.5 MV Tandem Accelerator	97
3.2 Scattering chamber.....	99
3.3 Detection System	100
3.4 Electronics.....	101
3.5 Target Preparation.....	102
3.5.1 Targets manufactured using the evaporation procedure for cross section measurements	
103	

3.5.2	<i>Purchased targets for cross section measurements</i>	106
3.5.3	<i>Targets for the benchmarking experiments</i>	106

Chapter 4 Methodology, Data Analysis, Results and Discussion

108

4.1	Differential cross section determination – Methodology	108
4.1.1	<i>Spectrum analysis</i>	110
4.1.1.1	Peak Identification – Calibration ADC	111
4.1.1.2	Peak integration	114
4.1.2	<i>Target thickness calculation</i>	115
4.1.3	<i>Differential cross section calculation for the heavy element</i>	116
4.1.4	<i>Energy determination</i>	117
4.1.4.1	Accelerator calibration	117
4.1.4.2	Energy loss - Mean Energy Approximation	119
4.2	Validation procedure – Benchmarking methodology	120
4.3	Cross section measurements for the ${}^6\text{Li}(d,d_0){}^6\text{Li}$ elastic scattering	122
4.3.1	<i>Target characterization</i>	125
4.3.2	<i>Uncertainties</i>	129
4.3.3	<i>Results and Discussion</i>	130
4.4	Cross section measurements for the ${}^7\text{Li}(d,d_0){}^7\text{Li}$ elastic scattering	136
4.4.1	<i>Target characterization</i>	140
4.4.2	<i>Uncertainties</i>	142
4.4.3	<i>Results and Discussion</i>	143
4.5	Cross section measurements for the ${}^9\text{Be}(d,d_0){}^9\text{Be}$ elastic scattering	150
4.5.1	<i>Target characterization</i>	153
4.5.2	<i>Uncertainties</i>	155
4.5.3	<i>Results and Discussion</i>	156
4.6	Cross section measurements for the ${}^{\text{nat}}\text{N}(d,d_0){}^{\text{nat}}\text{N}$ elastic scattering	161
4.6.1	<i>Target characterization</i>	164
4.6.2	<i>Uncertainties</i>	165
4.6.3	<i>Results and Discussion</i>	165
4.7	Cross section measurements for the ${}^{23}\text{Na}(d,d_0){}^{23}\text{Na}$ elastic scattering	174
4.7.1	<i>Target characterization</i>	176
4.7.2	<i>Uncertainties</i>	177
4.7.3	<i>Results and Discussion</i>	178
4.8	Cross section measurements for the ${}^{\text{nat}}\text{Si}(d,d_0){}^{\text{nat}}\text{Si}$ elastic scattering	188
4.8.1	<i>Target characterization</i>	190
4.8.2	<i>Uncertainties</i>	190
4.8.3	<i>Results and Discussion</i>	191
4.8.4	<i>Benchmarking of the obtained ${}^{\text{nat}}\text{Si}(d,d_0){}^{\text{nat}}\text{Si}$ differential cross section values</i>	201

Chapter 5	The study of the $^{nat}\text{O}(d,d_0)^{nat}\text{O}$ elastic scattering	206
5.1	Cross section measurements for the $^{nat}\text{O}(d,d_0)^{nat}\text{O}$ elastic scattering	206
5.1.1	<i>Target characterization</i>	210
5.1.2	<i>Uncertainties</i>	211
5.1.3	<i>Results and Discussion</i>	211
5.2	Benchmarking procedure of the $^{nat}\text{O}(d,d_0)^{nat}\text{O}$ elastic scattering	219
5.3	Theoretical Investigation of the $^{16}\text{O}(d,d_0)^{16}\text{O}$ elastic scattering	222
5.3.1	<i>The Code</i>	222
5.3.2	<i>The $^{16}\text{O}+d$ channel</i>	225
5.3.3	<i>Parameters and calculations</i>	227
5.3.3.1	Optical model calculations	227
5.3.3.2	Resonances	229
5.3.4	<i>Results</i>	232
	Conclusions and future perspectives	237

Περίληψη

Οι αναλυτικές τεχνικές με δέσμες ιόντων (Ion Beam Analysis (IBA) techniques) χρησιμοποιούνται ευρέως για την ανάλυση στοιχείων ή/και ισοτόπων στα επιφανειακά στρώματα στερεών. Η ευρεία χρήση τέτοιων μεθόδων έγκειται στο γεγονός ότι είναι -σχεδόν- μη καταστροφικές για τα υπό ανάλυση δείγματα. Η εφαρμογή τους περιλαμβάνει την ανίχνευση των σωματιδίων ή της ακτινοβολίας που προκύπτει μετά την αλληλεπίδραση των σωματιδίων της δέσμης με τα άτομα ή τους πυρήνες των επιφανειακών στρωμάτων του στόχου και καταλήγει στον ποσοτικό προσδιορισμό και στην κατά βάθος ανάλυση στοιχείων σε ένα δείγμα. Για να εφαρμοσθούν ιοντικές τεχνικές ανάλυσης και να εξαχθούν τα αντίστοιχα συμπεράσματα είναι απαραίτητη η εκ των προτέρων γνώση των αντίστοιχων τιμών της διαφορικής ενεργού διατομής. Ωστόσο, ο αναλυτικός υπολογισμός τέτοιων τιμών, στην ενεργειακή περιοχή των MeV, είναι αδύνατος εφόσον η φυσική που περιλαμβάνεται στην αλληλεπίδραση δέσμης-στόχου είναι μόνο μερικώς γνωστή. Επομένως, η εφαρμογή αυτών των αναλυτικών τεχνικών βασίζεται στην ύπαρξη των αντίστοιχων πειραματικών δεδομένων στην βιβλιογραφία.

Τα ελαφρά στοιχεία χρησιμοποιούνται ευρέως στην βιομηχανία. Είναι καίριας σημασίας στον τομέα της ανάλυσης υλικών λόγω της ύπαρξης τους στα κεραμικά, στα γυαλιά και στα πολυμερή ενώ συχνά προστίθενται σε μεταλλικά κράματα με σκοπό να βελτιώσουν συγκεκριμένες ιδιότητες όπως είναι η σκληρότητα και η δυσκαμψία υλικών αλλά και η αντοχή τους στην φθορά και η θερμική αντίσταση. Συνεπώς, ο ακριβής ποσοτικός προσδιορισμός της κατά βάθος κατανομής των ελαφρών στοιχείων, τα οποία βρίσκονται σε μια πληθώρα διαφορετικών μητρών, έχει τεράστια σημασία για την σύγχρονη έρευνα και τεχνολογία. Τέτοια αποτελέσματα μπορούν να εξαχθούν με την εφαρμογή πυρηνικών αναλυτικών τεχνικών και πιο συγκεκριμένα μέσω της μεθόδου ανίχνευσης του ελαστικά ανακρουόμενου πυρήνα (ERDA - Elastic Recoil Detection Analysis) για λεπτά επιφανειακά στρώματα και μέσω της μεθόδου πυρηνικών αντιδράσεων (NRA - Nuclear Reaction Analysis) λόγω της παραγωγής απομονωμένων κορυφών (περιλαμβάνονται υψηλές τιμές Q) με αμελητέο υπόβαθρο. Παράλληλα, η χρήση της δέσμης δευτερίων παρουσιάζει το πολύ μεγάλο πλεονέκτημα της καλύτερης διακριτικής ικανότητας βάθους σε σύγκριση με μια δέσμη πρωτονίων και παράλληλα της ταυτόχρονης διέγερσης σχεδόν όλων των ελαφρών στοιχείων/ισοτόπων που συνυπάρχουν σε ένα δείγμα. Η εφαρμογή της τεχνικής d-NRA θα μπορούσε να ενισχυθεί με την ανάλυση των ελαστικών κορυφών που παράγονται ταυτόχρονα στο φάσματα με χρήση της ίδια πειραματικής διάταξης και συνθηκών. Η γενικευμένη εφαρμογή της τεχνικής EBS περιορίζεται κυρίως από τη μεγάλη βιβλιογραφική έλλειψη αξιόπιστων και ολοκληρωμένων δεδομένων ενεργών διατομών σε διάφορες γωνίες και ενέργειες κατάλληλες για την εφαρμογή ιοντικών τεχνικών ανάλυσης.

Η συμβολή της παρούσας διατριβής στο πεδίο των ιοντικών τεχνικών ανάλυσης αποτελείται από δύο μέρη. Το πρώτο μέρος είναι μια συνολική μέτρηση των τιμών της διαφορικής ενεργού διατομής της ελαστικής σκέδασης δευτερίων σε πολλά σημαντικά σταθερά ελαφρά ισότοπα και στοιχεία, όπως είναι ${}^6\text{Li}$, ${}^7\text{Li}$, ${}^9\text{Be}$, ${}^{14}\text{N}$, ${}^{\text{nat}}\text{O}$, ${}^{23}\text{Na}$ και ${}^{\text{nat}}\text{Si}$, σε ενέργειες και γωνίες κατάλληλες για αναλυτικούς σκοπούς. Σε συγκεκριμένες περιπτώσεις (${}^{\text{nat}}\text{O}$, ${}^{23}\text{Na}$, ${}^{\text{nat}}\text{Si}$) ελέγχθηκε και η αξιοπιστία των εξαγόμενων πειραματικών δεδομένων (benchmarking) με χρήση παχέων στόχων γνωστής και ακριβής στοιχειομετρίας. Όλες οι μετρήσεις πραγματοποιήθηκαν στο εργαστήριο του Ινστιτούτου Πυρηνικής και Σωματιδιακής Φυσικής του Ε.Κ.Ε.Φ.Ε. «Δημόκριτος» χρησιμοποιώντας τον επιταχυντή 5.5 MV Tandem. Τα περισσότερα δεδομένα έχουν ήδη παραχωρηθεί στην IBANDL (Ion Beam Analysis Nuclear Data Library) υπό την αιγίδα της Διεθνούς Επιτροπής Ατομικής Ενέργειας, ώστε να αξιοποιηθούν από τη διεθνή επιστημονική κοινότητα τόσο σε προβλήματα βασικής έρευνας όσο και σε τεχνολογικές εφαρμογές ανάλυσης υλικών.

Το δεύτερο μέρος της παρούσας διατριβής έγκειται στην συμπλήρωση των πειραματικών δεδομένων της ελαστικής σκέδασης δευτερίων σε φυσικό οξυγόνο με θεωρητικούς υπολογισμούς με σκοπό την επέκταση της υπάρχουσας φαινομενολογικής μελέτης (evaluation) σε υψηλότερες ενέργειες δευτερίων. Το οξυγόνο επιλέχθηκε καθώς αποτελεί το πιο σημαντικό στοιχείο, μεταξύ των μελετώμενων, από άποψη εφαρμογών. Η θεωρητική μελέτη πραγματοποιήθηκε στα πλαίσια της θεωρίας R-matrix, η οποία αποτελεί την καταλληλότερη θεωρητική προσέγγιση για τον υπολογισμό διαφορικών ενεργών διατομών ελαστικών σκεδάσεων συντονισμού. Η θεωρία R-matrix λαμβάνει υπόψη την αλληλεπίδραση του προσπίπτοντος ιόντος με τον πυρήνα συνολικά και οι παράμετροι του συγκεκριμένου θεωρητικού μοντέλου προσδιορίζονται με βάση τις πειραματικά προσδιορισμένες τιμές της διαφορικής ενεργού διατομής.

Η παρούσα εργασία είναι δομημένη σε 2 αντίστοιχες ενότητες και συμπληρώνεται από το απαραίτητο θεωρητικό πλαίσιο και τις προοπτικές αυτής της μελέτης.

Θεωρητικό πλαίσιο

Η θεωρία που πλαισιώνει την παρούσα εργασία είναι η θεωρία ελαστικής σκέδασης, το οπτικό μοντέλο ελαστικής σκέδασης, οι μηχανισμοί αντίδρασης και η θεωρία R-matrix.

Θεωρία ελαστικής σκέδασης

Όταν μια δέσμη φορτισμένων ιόντων αλληλεπιδρά με ένα πυρήνα-στόχο δρουν η πυρηνική δύναμη και η δύναμη Coulomb. Η αλληλεπίδραση αυτών των δυνάμεων εξαρτάται από την ενέργεια της δέσμης, τη γωνία σκέδασης και τον πυρήνα-στόχο. Οι διαφορετικές αποστάσεις στις οποίες αυτές οι δυο δυνάμεις δρουν οδηγούν σε περιοχές που κυριαρχεί η δύναμη Coulomb και περιοχές που κυριαρχεί η πυρηνική δύναμη, καθώς η τελευταία είναι 100 φορές ισχυρότερη από την δύναμη Coulomb σε μικρές αποστάσεις, περίπου 1 fm. Στο σημείο αυτό για να περιγράψουμε την ενεργό διατομή για καθεμιά από τις αλληλεπιδράσεις (Coulomb και πυρηνική) θα εξετάσουμε την σκέδαση Coulomb και την πυρηνική σκέδαση ξεχωριστά.

Σκέδαση Coulomb

Στην περίπτωση που οι μόνες δυνάμεις που δρουν όταν ένα βλήμα πλησιάζει ένα στόχο είναι οι ηλεκτρικές (δύναμη Coulomb) τότε η τιμή της διαφορικής ενεργού διατομής μπορεί να εξαχθεί από την διατήρηση της ενέργειας και της ορμής μαζί με την παράμετρο κρούσης (b). Η παράμετρος κρούσης ορίζεται ως η κάθετη απόσταση μεταξύ του βλήματος και του στόχου από την οποία το βλήμα θα διέρχονταν αν δεν υπήρχε καμία αλληλεπίδραση. Η εξαγόμενη σχέση της σκέδασης Rutherford περιγράφει την πιθανότητα ενός σωματιδίου με μάζα M_1 , φορτίο z and ενέργεια E να σκεδαστεί σε γωνία θ από έναν πυρήνα-στόχο με μάζα M_2 , Z και η διαφορική ενεργός διατομή υπολογίζεται από την σχέση (στο σύστημα αναφοράς του εργαστηρίου):

$$\left(\frac{d\sigma_R}{d\Omega}\right)_{E,\theta} = \left(\frac{zZe^2}{4E}\right)^2 \frac{2[(M_2^2 - M_1^2 \sin^2 \theta)^{1/2} + M_2 \cos \theta]^2}{M_2 \sin^4 \theta (M_2^2 - M_1^2 \sin^2 \theta)^{1/2}} \quad (i)$$

Καθώς η ενέργεια του βλήματος αυξάνεται, θα υπάρξει ένα σημείο στο οποίο η απόσταση εγγύτατης προσέγγισης θα είναι ίση με την ακτίνα του πυρήνα (που δίνεται από την σχέση: $r = r_0 \cdot A^{1/3}$ fm, όπου A είναι ο μαζικός αριθμός και $r_0 \approx 1.2$ fm ή $r_0 = (1.1-1.5)$ fm[1]) και η πυρηνική δύναμη θα αρχίσει να γίνεται αισθητή. Στο σημείο αυτό, η παραπάνω σχέση της σκέδασης Rutherford παύει να ισχύει καθώς εξάχθηκε με την υπόθεση ότι μόνο ηλεκτρικές δυνάμεις λαμβάνουν χώρα. Πυρηνικοί όροι πρέπει να συμπεριληφθούν στην σχέση (i) λόγω της αλληλεπίδρασης μεταξύ της σκέδασης Coulomb και της πυρηνικής σκέδασης. Ωστόσο, σε τόσο

μικρές αποστάσεις που δρα η πυρηνική δύναμη, η ταυτόχρονη γνώση της ορμής και της θέσης (άρα και της παραμέτρου κρούσης) του σκεδαζόμενου σωματιδίου είναι αδύνατη σύμφωνα με την αρχή αβεβαιότητας του Heisenberg. Συνεπώς, οι πυρηνικές δυνάμεις δεν μπορούν να εισαχθούν σε καμία θεωρία που προϋποθέτει ότι η πορεία του σωματιδίου είναι γνωστή. Επομένως, η κβαντομηχανική φυσική πρέπει να χρησιμοποιηθεί έναντι της κλασικής φυσικής [1], [2].

Πυρηνική σκέδαση

Αρχικά θα εξεταστεί η πυρηνική σκέδαση ενός βλήματος χωρίς φορτίο. Η εισερχόμενη δέσμη στον άξονα z μπορεί να παρασταθεί από ένα επίπεδο κύμα e^{ikz} με ορμή $p=\hbar k$, όπου k είναι το διάνυσμα διάδοσης $k = \frac{p}{\hbar} = \frac{1}{\lambda}$. Αυτό το κύμα μπορεί να αναπαρασταθεί ως μια επαλληλία σφαιρικών κυμάτων (αφού τα εξερχόμενα σωματίδια αναπαρίστανται από σφαιρικά κύματα) σύμφωνα με την σχέση:

$$\Psi_{inc} = Ae^{ikz} = A \sum_{\ell=0}^{\infty} i^{\ell} (2\ell + 1) j_{\ell}(kr) P_{\ell}(\cos\theta) \quad (ii)$$

όπου A είναι η παράμετρος κανονικοποίησης. Τα $j_{\ell}(kr)$ αποτελούν τις σφαιρικές συναρτήσεις Bessel και είναι οι λύσεις για το σφαιρικό μέρος της εξίσωσης Schrödinger, σε περιοχές μακριά από τον στόχο, όπου το πυρηνικό δυναμικό εξαφανίζεται. Οι γωνιακές συναρτήσεις $P_{\ell}(\cos\theta)$ είναι τα πολυώνυμα του Legendre ($P_0(\cos\theta) = 1$, $P_1(\cos\theta) = \cos\theta$, $P_3(\cos\theta) = \frac{1}{2}(3\cos^2\theta - 1)$).

Η σχέση (ii) αποτελεί την ανάπτυξη σε μερικά κύματα όπου το κάθε μερικό κύμα έχει συγκεκριμένη τροχιακή στροφορμή ℓ . Αυτή η ανάπτυξη σε μερικά κύματα ισχύει μόνο όταν το πυρηνικό δυναμικό θεωρηθεί κεντρικό.

Σε μακρινές αποστάσεις από τον πυρήνα, όπου το πυρηνικό δυναμικό δεν γίνεται αισθητό ($kr \ll \ell$) η σχέση (ii) παίρνει την μορφή:

$$\Psi_{inc} = \frac{A}{2kr} \sum_{\ell=0}^{\infty} i^{\ell+1} (2\ell + 1) \left[e^{-i(kr - \frac{\ell\pi}{2})} - e^{+i(kr - \frac{\ell\pi}{2})} \right] P_{\ell} \cos\theta \quad (iii)$$

Η σκέδαση επηρεάζει το εισερχόμενο κύμα με δύο τρόπους: είτε αλλάζει το μήκος κύματος (διαφορά φάσης) είτε αλλάζει το πλάτος. Η αλλαγή στη φάση δηλώνει ελαστική σκέδαση ενώ η αλλαγή στο πλάτος δηλώνει ανελαστική σκέδαση (ή κάποιου είδους πυρηνική αντίδραση) και η ενέργεια (ή ακόμα και η ταυτότητα) του εξερχόμενου σωματιδίου μπορεί να αλλάξει. Για να εκφραστούν αυτές οι αλλαγές εισάγεται ένας μιγαδικός συντελεστής S_{ℓ} στο εξερχόμενο κύμα και τότε το συνολικό κύμα μπορεί να αναπαρασταθεί μέσω της σχέσης:

$$\Psi = \frac{A}{2kr} \sum_{\ell=0}^{\infty} i^{\ell+1} (2\ell + 1) \left[e^{-i(kr - \frac{\ell\pi}{2})} - S_{\ell} e^{+i(kr - \frac{\ell\pi}{2})} \right] P_{\ell} \cos\theta \quad (iv)$$

Ο μιγαδικός συντελεστής S_{ℓ} περιλαμβάνει την αλλαγή στο πλάτος μέσω του πραγματικού μέρους και την αλλαγή στη φάση μέσω του φανταστικού μέρους. Η σχέση (iv) είναι η υπέρθεση του εισερχόμενου και του σκεδαζόμενου κύματος. Το σκεδαζόμενο κύμα μπορεί να βρεθεί αφαιρώντας την σχέση (iii) από την σχέση (iv) ($\Psi_{scat} = \Psi - \Psi_{inc}$):

$$\Psi_{scat} = \frac{A}{2k} \frac{e^{ikr}}{r} \sum_{\ell=0}^{\infty} i (2\ell + 1) (1 - S_{\ell}) P_{\ell} \cos\theta \quad (v)$$

Η παραπάνω σχέση αναφέρεται μόνο σε κύματα με κυματάρθμο k ίδιο με αυτόν του εισερχόμενου κύματος και επομένως αναφέρεται μόνο στην ελαστική σκέδαση.

Με χρήση των σχέσεων για τις πυκνότητες πιθανότητας η διαφορική ενεργός διατομή για οποιαδήποτε αντίδραση (ελαστική ή ανελαστική) υπολογίζεται ως:

$$\frac{d\sigma}{d\Omega} = \frac{1}{4k^2} \left| \sum_{\ell=0}^{\infty} (2\ell + 1) i (1 - S_{\ell}) P_{\ell} \cos\theta \right|^2 \quad (vi)$$

Οι πιο σημαντικοί όροι στην παραπάνω εξίσωση είναι οι k και S_{ℓ} , εφόσον το δυναμικό που χρησιμοποιείται για την λύση της εξίσωσης Schrödinger εξαρτάται από αυτούς τους όρους. Ολοκληρώνοντας την σχέση (vi) και χρησιμοποιώντας τις ιδιότητες των πολυωνύμων Legendre μπορεί να υπολογιστεί η τιμή της ενεργού διατομής μέσω της σχέσης:

$$\sigma_{scat} = \sum_{\ell=0}^{\infty} \pi \lambda^2 (2\ell + 1) |1 - S_{\ell}|^2 \quad (vii)$$

Στην περίπτωση που λαμβάνει χώρα μόνο η ελαστική σκέδαση, τότε $|S_{\ell}| = 1$ και $S_{\ell} = e^{2i\delta_{\ell}}$, όπου δ_{ℓ} είναι η διαφορά φάσης του ℓ μερικού κύματος. Στην περίπτωση αυτή $|1 - S_{\ell}|^2 = |1 - e^{2i\delta_{\ell}}|^2 = |1 - (\cos(2\delta_{\ell}) + i\sin(2\delta_{\ell}))|^2 = (1 - \cos(2\delta_{\ell}))^2 + (\sin(2\delta_{\ell}))^2 = 4 \sin^2 \delta_{\ell}$ και η ολική ενεργός διατομή σκέδασης δίνεται από την σχέση:

$$\sigma_{scat} = \sum_{\ell=0}^{\infty} 4\pi \lambda^2 (2\ell + 1) \sin^2 \delta_{\ell} \quad (viii)$$

Στην περίπτωση που συμβαίνουν και άλλες αντιδράσεις μαζί με την ελαστική τότε η παραπάνω σχέση δεν ισχύει καθώς $|S_{\ell}| < 1$. Η ενεργός διατομή για όλες τις άλλες αντιδράσεις ονομάζεται «ενεργός διατομή αντίδρασης», σ_{react} , και για τον υπολογισμό της χρησιμοποιούνται οι πυκνότητες πιθανότητας. Η τελική σχέση που εξάγεται είναι:

$$\sigma_{react} = \sum_{\ell=0}^{\infty} \pi \lambda^2 (2\ell + 1) (1 - |S_{\ell}|^2) \quad (ix)$$

Συνεπώς η ολική ενεργός διατομή μπορεί να υπολογισθεί μέσω της σχέσης:

$$\sigma_{total} = \sigma_{scat} + \sigma_{react} = \sum_{\ell=0}^{\infty} 2\pi \lambda^2 (2\ell + 1) (1 - \text{Re } S_{\ell}) \quad (x)$$

Στην περίπτωση που συμβαίνει μόνο ελαστική σκέδαση ισχύει ότι $|S_{\ell}| = 1$, και η εξίσωση (ix) εξαφανίζεται. Επίσης, παρατηρείται ότι είναι αδύνατο να συμβούν αντιδράσεις χωρίς να συμβεί ελαστική σκέδαση, εφόσον για κάθε τιμή των S_{ℓ} για την οποία ισχύει ότι $\sigma_{react} \neq 0$ για κάποιο μερικό κύμα, αυτόματα, μέσω της σχέσης (vii), ισχύει ότι $\sigma_{scat} \neq 0$ για το συγκεκριμένο μερικό κύμα.

Στην περίπτωση που το εισερχόμενο σωματίδιο είναι φορτισμένο, αλληλεπιδρά με τον συνδυασμό του πυρηνικού δυναμικού και του δυναμικού Coulomb του πυρήνα. Η σχέση για την ενεργό διατομή σκέδασης, η οποία προκύπτει από την εξίσωση (x) και την εξίσωση (i), ώστε να ληφθεί υπόψιν η σκέδαση Coulomb, είναι:

$$\frac{d\sigma}{d\Omega} = \left| f_c(\theta) + \frac{1}{2ki} \sum_{\ell=0}^{\infty} (2\ell + 1) (S_{\ell} - 1) e^{2i\sigma_{\ell}} P_{\ell}(\cos\theta) \right|^2 \quad (\text{xi})$$

όπου $f_c(\theta)$ και σ_{ℓ} είναι το πλάτος σκέδασης και η διαφορά φάσης του δυναμικού Coulomb, αντίστοιχα [1], [2].

Για να λυθεί η εξίσωση Schrödinger και να υπολογισθούν τα S_{ℓ} , με αποτέλεσμα τον υπολογισμό της ελαστικής ενεργού διατομής, μια μορφή του πυρηνικού δυναμικού πρέπει να υποτεθεί.

Οπτικό δυναμικό ελαστικής σκέδασης

Η αλληλεπίδραση ενός προσπίπτοντος σωματιδίου με ένα πυρήνα μπορεί να περιγραφεί ως το άθροισμα όλων των αλληλεπιδράσεων μεταξύ του προσπίπτοντος σωματιδίου και καθενός από τα νουκλεόνια του πυρήνα. Ωστόσο, το δυναμικό της σκέδασης δυο νουκλεονίων δεν είναι γνωστό. Επιπρόσθετα, το άθροισμα αυτών των αλληλεπιδράσεων δεν θα οδηγούσε στον υπολογισμό της ακριβούς αλληλεπίδρασης αφού αποτελεί ένα άλυτο πρόβλημα πολλών σωμάτων. Για να αποφευχθούν αυτές οι δυσκολίες αλλά να λυθεί με κάποιο τρόπο αυτή η περίπλοκη αλληλεπίδραση, χρησιμοποιούνται εμπειρικά οπτικά δυναμικά. Ο όρος οπτικά δυναμικά πηγάζει από το γεγονός ότι ο πυρήνας είναι ένα ισχυρά απορροφητικό μέσο, ως προς τα προσπίπτοντα νουκλεόνια, το οποίο συμπεριφέρεται όπως μια αδιαφανής γυάλινη σφαίρα ως προς τα εισερχόμενα κύματα φωτός, προκαλώντας ανάκλαση και απορρόφηση.

Σε αυτήν την ενότητα θα περιγραφεί το οπτικό μοντέλο. Στα πλαίσια αυτού του μοντέλου ο πυρήνας αντιπροσωπεύεται από ένα δυναμικό $U(r)$ και επομένως μπορεί να υποτεθεί ότι το προσπίπτον σωματίδιο αλληλεπιδρά με τον πυρήνα σαν ολότητα. Αυτό το δυναμικό παρουσιάζει χαρακτηριστικά τα οποία προκύπτουν από την αλληλεπίδραση μεταξύ νουκλεονίων. Αρχικά, πρέπει να συμβαδίζει με την κατανομή της πυρηνικής ύλης, η οποία μειώνεται καθώς πλησιάζουμε την πυρηνική επιφάνεια. Είναι αναμενόμενο αυτή η μείωση να συμβαίνει εκθετικά, όπως η αλληλεπίδραση μεταξύ δυο νουκλεονίων. Ακόμη, το δυναμικό $U(r)$ πρέπει να περιλαμβάνει έναν πραγματικό όρο, ώστε να υπολογίζεται η ελαστική σκέδαση, καθώς και έναν φανταστικό ώστε να υπολογίζονται οι μη ελαστικές διαδικασίες. Όλα αυτά τα χαρακτηριστικά συγκεντρώνονται στην τελική εξίσωση για το μοντέλο του οπτικού δυναμικού, η οποία μπορεί να γραφεί στην μορφή:

$$U(r) = U_R(r) + U_I(r) + U_D(r) + U_S(r) + U_C(r) \quad (\text{xii})$$

Η παραπάνω εξίσωση περιέχει παραμέτρους των οποίων οι τιμές ποικίλουν με την ενέργεια και την μάζα και επιλέγονται με βάση τα διαθέσιμα πειραματικά δεδομένα. Ωστόσο, για να έχει νόημα το οπτικό δυναμικό δεν πρέπει να παρουσιάζει σημαντικές μεταβολές για γειτονικές μάζες και κοντινές ενέργειες.

Ο πρώτος όρος της εξίσωσης (xii),

$$U_R(r) = -V f(r, R, a) \quad (\text{xiii})$$

είναι πραγματικό όρος που αντιπροσωπεύει ένα πυρηνικό πηγάδι με βάθος V το οποίο συνήθως πολλαπλασιάζεται με έναν όρο Woods-Saxon, ο οποίος έχει την μορφή:

$$f(r, R, a) = \{1 + \exp[(r - R)/a]\}^{-1} \quad (\text{xiv})$$

όπου R είναι η ακτίνα του πυρήνα, a είναι η διάχυση (diffuseness) του δυναμικού. Οι παράμετροι V , R και a , αποτελούν παραμέτρους προσαρμογής του οπτικού μοντέλου.

Οι επόμενοι δύο όροι $U_I(r)$ και $U_D(r)$ της σχέσης (xii) υπολογίζουν για τις μη ελαστικές διαδικασίες δηλαδή τα φαινόμενα απορρόφησης και άρα είναι φανταστικοί. $U_I(r)$ περιλαμβάνει την απορρόφηση σε όλο τον όγκο του πυρήνα ενώ ο όρος περιλαμβάνει την απορρόφηση στην περιοχή κοντά στην επιφάνεια του πυρήνα.

Ο τέταρτος όρος της εξίσωσης (xii) είναι όρος αλληλεπίδρασης spin-orbit, δανεισμένος από την ατομική φυσική. Ο όρος αυτός περιέχει παραμέτρους που προσαρμόζονται σε πειραματικά δεδομένα και είναι απαραίτητος καθώς τα νουκλεόνια έχουν spin $\frac{1}{2}$ και ακόμα και αν η προσπίπτουσα δέσμη δεν είναι πολωμένη, η σκεδαζόμενη δέσμη θα είναι πολωμένη στην κάθετη διεύθυνση ως προς το επίπεδο σκέδασης. Επομένως, ο όρος αυτός αντιπροσωπεύει την πόλωση της δέσμης.

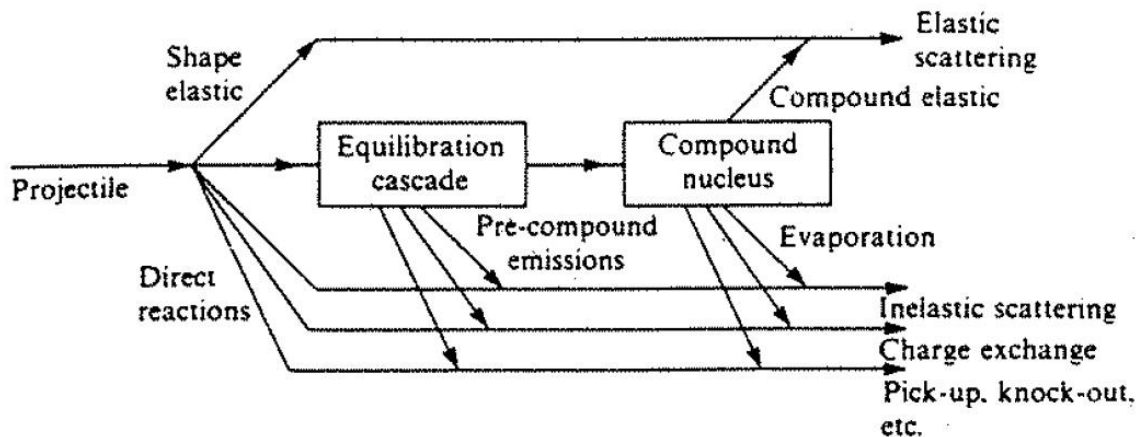
Ο τελευταίος όρος της εξίσωσης (xii) , $U_C(r)$, αντιστοιχεί στην σκέδαση Coulomb, στην περίπτωση που φορτισμένα σωματίδια συμμετέχουν στην αλληλεπίδραση. Έχει την μορφή:

$$U_C(r) = \begin{cases} \frac{Z_1 Z_2 e^2}{2R_C} \left(3 - \frac{r^2}{R_C^2} \right) & r \leq R_C \\ \frac{Z_1 Z_2 e^2}{r} & r > R_C \end{cases} \quad (\text{xv})$$

όπου ο πυρήνας θεωρείται μια ομοιόμορφα φορτισμένη σφαίρα με ακτίνα ίση με το φράγμα δυναμικού Coulomb (R_C) [1], [3], [4].

Μηχανισμοί αντίδρασης

Οι πυρηνικές αλληλεπιδράσεις χαρακτηρίζονται από διαφορετικούς μηχανισμούς αντίδρασης. Ο μηχανισμός που διέπει κάθε αλληλεπίδραση εξαρτάται από την ενέργεια και την γωνία του προσπίπτοντος σωματιδίου και από το είδος των σωματιδίων που συμμετέχουν στην αλληλεπίδραση. Όλοι οι πιθανοί μηχανισμοί περιλαμβάνονται στο Σχήμα (i) και οι πιο σημαντικοί εξ αυτών, στις περιπτώσεις που τα δευτέρια αποτελούν τα εισερχόμενα σωματίδια, αναλύονται παρακάτω.



Σχήμα ι Σχεδιάγραμμα των πιθανών αλληλεπιδράσεων που προκύπτουν από την αλληλεπίδραση νουκλεονίου-πυρήνα [3].

Στην περίπτωση των **αντιδράσεων σύνθετου πυρήνα** (compound nucleus) υπάρχουν δυο διακριτά βήματα. Στο πρώτο βήμα απορροφάται το βλήμα, σχηματίζοντας προσωρινά έναν σύνθετο πυρήνα και στο δεύτερο βήμα ο σύνθετος πυρήνας αποδιεγείρεται. Η κινητική ενέργεια του βλήματος μοιράζεται σε όλα τα νουκλεόνια του συστήματος (βλήμα και στόχος) και επομένως ο σύνθετος πυρήνας βρίσκεται σε κατάσταση θερμοδυναμικής ισορροπίας. Ο χρόνος που χρειάζεται για να πραγματοποιηθεί μια αντίδραση σύνθετου πυρήνα είναι 10^{-16} - 10^{-18} s. Κατά την αλληλεπίδραση, τα νουκλεόνια ανακατατάσσονται και χάνουν κάθε μνήμη σχετικά με την προέλευσή τους (αρχή ανεξαρτησίας του Bohr). Επομένως, η αποδιέγερση του σύνθετου πυρήνα εξαρτάται μόνο από την διαθέσιμη ενέργεια. Ακόμη, αξίζει να αναφερθεί σε αυτό το σημείο ότι είναι πιθανό για κάποιο νουκλεόνιο, το οποίο έχει περισσότερη κινητική ενέργεια από τα υπόλοιπα, να διαφύγει πριν την επίτευξη θερμοδυναμικής ισορροπίας. Οι αντίδραση αυτή ονομάζεται **αντίδραση προΐσορροπίας** (pre-equilibrium reaction).

Υφίσταται και η περίπτωση των **άμεσων αντιδράσεων** κατά τις οποίες συμμετέχει μόνο ένας μικρός αριθμός νουκλεονίων ή το βλήμα αλληλεπιδρά μόνο με το δυναμικό, Coulomb (διαφορική ενεργός διατομή που δίνεται από την σχέση Rutherford (i)) ή πυρηνικό, του πυρήνα-στόχου. Αυτές οι διαδικασίες ολοκληρώνονται σε σχετικά μικρούς χρόνους της τάξης των 10^{-22} s.

Υπάρχει και η περίπτωση κατά την οποία διεγείρεται ο σύνθετος πυρήνας σε ενέργειες που υπάρχουν διακριτές στάθμες (όπως δηλαδή στις άμεσες αντιδράσεις) αλλά βρισκόμαστε στην συντονιστική ενεργειακή περιοχή του σύνθετου πυρήνα (όπως στις αντιδράσεις σύνθετου πυρήνα). Αυτές οι στάθμες παρουσιάζουν μεγάλες τιμές της ενεργού διατομής, δηλαδή υψηλές πιθανότητες δημιουργίας, ενώ έχουν μικρά εύρη, δηλαδή σχετικά μεγάλους χρόνους ζωής. Η αποδιέγερση αυτών των σταθμών πραγματοποιείται είτε με αποδιέγερση ακτινοβολίας γ (ανελαστική σκέδαση) είτε επανεκπέμποντας το εισερχόμενο σωματίδιο (ελαστική σκέδαση).

Όλοι οι παραπάνω μηχανισμοί πραγματοποιούνται ταυτόχρονα και επομένως για τον υπολογισμό της τελικής τιμής της ενεργού διατομής συμβάλλουν. Η συμβολή μεταξύ της σκέδασης συντονισμού (resonant scattering) και της σκέδασης από το δυναμικό (potential scattering) μπορεί να οδηγήσει σε χαμηλότερες ή υψηλότερες τιμές της ενεργού διατομής συγκριτικά με το να συνέβαινε κάθε διαδικασία μόνη της.

Θεωρία R-matrix

Η R-matrix (1947, [5]) αποτελεί μια θεωρητική προσέγγιση για τον υπολογισμό των διαφορικών ενεργών διατομών όταν η δομή τους παρουσιάζει ελάχιστα και μέγιστα τα οποία αντιστοιχούν σε διακριτές καταστάσεις του σύνθετου πυρήνα που σχηματίζεται. Θεωρεί ότι η αλληλεπίδραση πραγματοποιείται μεταξύ του εισερχομένου σωματιδίου και του πυρήνα σαν ένα μαύρο κουτί με άγνωστη εσωτερική δομή. Οι ιδιότητες αυτής της δομής, που αντιστοιχούν σε στοιχεία του R-matrix, χρησιμοποιούνται ως παράμετροι των θεωρητικών υπολογισμών οι οποίοι προσαρμόζονται στα διαθέσιμα πειραματικά δεδομένα [5].

Η προσέγγιση R-matrix βασίζεται στην αλληλεπίδραση του βλήματος με τον στόχο μέσω του μηχανισμού σύνθετου πυρήνα καθώς και από το γεγονός ότι η δομή της ενεργού διατομής κυριαρχείται από την συμβολή του resonant scattering και του potential scattering. Στην περίπτωση των δευτερίων με μέγιστη ενέργεια τα 2.5 MeV τα οποία προσπίπτουν σε στόχους με χαμηλό και μεσαίο ατομικό αριθμό Z , ο κυρίαρχος μηχανισμός αλληλεπίδρασης είναι ο μηχανισμός σύνθετου πυρήνα. Για τον λόγο αυτό, η θεωρία R-matrix είναι η πλέον κατάλληλη για την ανάλυση τέτοιων περιπτώσεων ελαστικής σκέδασης.

Η βασική ιδέα της θεωρίας R-matrix είναι ο διαχωρισμός του χώρου του προβλήματος σε δύο περιοχές, την εσωτερική περιοχή και την εξωτερική περιοχή. Η εσωτερική περιοχή αντιστοιχεί στον σύνθετο πυρήνα ενώ η εξωτερική περιοχή αντιστοιχεί σε όλες τις πιθανές αντιδράσεις ή κανάλια, τα οποία μπορεί να προκύψουν από τον σύνθετο πυρήνα ή να φτάσουν σε αυτόν.

Στην παρούσα εργασία πραγματοποιήθηκε η θεωρητική αναπαραγωγή των διαφορικών ενεργών διατομών της ελαστικής σκέδασης $d+^{16}\text{O}$ στην ενεργειακή περιοχή 1.98-2.5 MeV με την χρήση της θεωρίας R-matrix για την περίπτωση του ενός καναλιού πολλών στάθμων (single channel multi-level). Ο λόγος που μελετήθηκε στην συγκεκριμένη ενεργειακή περιοχή είναι ότι το παρών evaluation σταματά στην ενέργεια 1.98 MeV.

Μετρήσεις διαφορικών ενεργών διατομών

Στα πλαίσια της παρούσας διατριβής μελετήθηκε η ελαστική σκέδαση δευτερίων σε συγκεκριμένα ελαφρά στοιχεία/ισότοπα τα οποία παρουσιάζουν μεγάλο τεχνολογικό ενδιαφέρον. Οι πειραματικές μετρήσεις διαφορικών ενεργών διατομών περιλαμβάνουν τις εξής σκεδάσεις: ${}^6\text{Li}(d,d_0){}^6\text{Li}$, ${}^7\text{Li}(d,d_0){}^7\text{Li}$, ${}^9\text{Be}(d,d_0){}^9\text{Be}$, ${}^{14}\text{N}(d,d_0){}^{14}\text{N}$, ${}^{23}\text{Na}(d,d_0){}^{23}\text{Na}$ and ${}^{\text{nat}}\text{Si}(d,d_0){}^{\text{nat}}\text{Si}$ στην ενεργειακή περιοχή των 0.9–2.2 MeV, με ποικίλα ενεργειακά βήματα, ανάλογα με την περίπτωση, και για γωνίες ανίχνευσης μεταξύ 120° και 170° με βήματα των 10° (στις περισσότερες περιπτώσεις). Για να εξεταστεί η αξιοπιστία των δεδομένων πραγματοποιήθηκαν πειράματα ελέγχου αξιοπιστίας στις περιπτώσεις της ελαστικής σκέδασης δευτερίων σε ${}^{16}\text{O}$, ${}^{23}\text{Na}$ και ${}^{\text{nat}}\text{Si}$. Τέτοια αποτελέσματα θα είναι χρήσιμα για την IBA κοινότητα στην εφαρμογή της τεχνικής EBS.

Τα πειράματα αυτά πραγματοποιήθηκαν στο εργαστήριο του Ινστιτούτου Πυρηνικής και Σωματιδιακής Φυσικής του Ε.Κ.Ε.Φ.Ε. «Δημόκριτος» χρησιμοποιώντας τον επιταχυντή 5.5 MV Tandem. Η δέσμη δευτερίων, μετά την παραγωγή της από μια πηγή duoplasmatron, οδηγείται σε έναν αναλυτικό μαγνήτη 90° όπου επιλέγεται η επιθυμητή τιμή της ενέργειας διαλέγοντας τον κατάλληλο λόγο φορτίου προς μάζα (Nuclear Magnetic Resonance) και καταλήγει σε ένα θάλαμο σκέδασης (ακτίνα 40 cm). Στο κέντρο είναι τοποθετημένοι οι στόχοι ενώ οι ανιχνευτές στις κατάλληλες γωνίες, μέσω των δύο γωνιομετρικών τραπεζών υψηλής ακρίβειας που υπάρχουν μέσα στο θάλαμο σκέδασης. Το ανιχνευτικό σύστημα αποτελούταν από πέντε τέσσερις, πέντε ή έξι ανιχνευτές επιφανειακού φραγμού πυριτίου (Silicon Surface barrier - SSB) (παραχωρήθηκαν από τον Δρ. Ν. Πατρώνη, ιδιοκτησία του τμήματος Φυσικής στο Πανεπιστήμιο Ιωαννίνων) με πάχος 500 μm . Μπροστά από τους ανιχνευτές ήταν τοποθετημένες ορθογώνιες σχισμές, ώστε να περιορίζεται το σφάλμα της γωνίας μέτρησης στη 1° καθώς και σωλήνες από αλουμίνιο με μήκος 30 - 70 mm, και διάμετρο 10 mm ώστε να εμποδίζουν τα σωματίδια που σκεδάζονται από τον θάλαμο σκέδασης να εισέρχονται στους ανιχνευτές και να καταγράφονται στα φάσματα συνεισφέροντας στο υπόβαθρο των μετρήσεων. Η πλειοψηφία των στόχων που χρησιμοποιήθηκαν κατασκευάστηκαν στο εργαστήριο του επιταχυντή με την χρήση του εξαχνωτήρα και τα υλικά που χρησιμοποιήθηκαν φαίνονται στον Πίνακα I. Οι στόχοι που αγοράστηκαν αφορούσαν τις μετρήσεις των διαφορικών ενεργών διατομών του βηρυλλίου, του πυριτίου και του αζώτου και ήταν μια υπέρλεπτη μεμβράνη Si_3N_4 με ένα στρώμα βηρυλλίου εναποτιθέμενο από πάνω για την περίπτωση του βηρυλλίου και μια υπέρλεπτη μεμβράνη Si_3N_4 με ένα στρώμα χρυσού εξαχνωμένο από πάνω για τις περιπτώσεις του πυριτίου και του αζώτου. Όπως παρατηρείται, το στρώμα του χρυσού υπάρχει σε όλους τους στόχους, εκτός από του βηρυλλίου, και ο σκοπός του είναι η χημική σταθερότητα του στόχου καθώς και η κανονικοποίηση. Οι στόχοι που χρησιμοποιήθηκαν στις περιπτώσεις που πραγματοποιήθηκαν πειράματα ελέγχου αξιοπιστίας

ήταν ένας παχύς στόχος NaCl με ένα λεπτό στρώμα χρυσού εξαχνωμένο από πάνω για την περίπτωση του νατρίου, ένα παχύ στρώμα πυριτίου με ένα λεπτό στρώμα χρυσού εξαχνωμένο από πάνω για την περίπτωση του πυριτίου και ένας παχύς στόχος ZnO για την περίπτωση του οξυγόνου.

Cross section measurement	Substrate	Powder evaporated on top of the substrate	Powder melting point (°C)	Top layer	Suitable Boats
${}^6\text{Li}(d,d_0){}^6\text{Li}$	C	${}^6\text{LiF}$ enriched 97%	841	Au	Ni, Ta, Mo, W
${}^7\text{Li}(d,d_0){}^7\text{Li}$	C	${}^{\text{nat}}\text{LiF}$	841	Au	Ni, Ta, Mo, W
${}^{\text{nat}}\text{O}(d,d_0){}^{\text{nat}}\text{O}$	C	Na_2HPO_4	250	Au	
${}^{23}\text{Na}(d,d_0){}^{23}\text{Na}$	C	Na_2O	1132	Au	

Πίνακας 1 Υλικά που χρησιμοποιήθηκαν για την κατασκευή των στόχων.

Μεθοδολογία μετρήσεων διαφορικών ενεργών διατομών

Οι τιμές των διαφορικών ενεργών διατομών υπολογίστηκαν χρησιμοποιώντας την σχετική μέθοδο μέσω της εξίσωσης:

$$\left(\frac{d\sigma}{d\Omega}\right)_{E,\theta}^{\text{light isot}} = \left(\frac{d\sigma}{d\Omega}\right)_{E,\theta}^{\text{heavy elem}} \cdot \frac{Y_{\text{light isot}}}{Y_{\text{heavy elem}}} \cdot \frac{N_t^{\text{heavy elem}}}{N_t^{\text{light isot}}} \quad (\text{xvi})$$

όπου $Y_{\text{light isot}}$ και $Y_{\text{heavy elem}}$ αντιστοιχούν στον αριθμό των ανιχνευόμενων σωματιδίων τα οποία σκεδάστηκαν από το υπό μελέτη ελαφρύ ισότοπο/στοιχείο και από το βαρύ στοιχείο, αντίστοιχα, $\left(\frac{d\sigma}{d\Omega}\right)_{E,\theta}^{\text{heavy elem}}$ και $\left(\frac{d\sigma}{d\Omega}\right)_{E,\theta}^{\text{light isot}}$ είναι οι τιμές της διαφορικής ενεργού διατομής για το ελαφρύ ισότοπο/στοιχείο και για το βαρύ στοιχείο για τις αντίστοιχες τιμές ενέργειας και γωνίας, αντίστοιχα, και $N_t^{\text{light isot}}$ και $N_t^{\text{heavy elem}}$ είναι τα πάχος του ελαφριού ισότοπου και του βαριού στοιχείου σε atoms/cm². Τα τελικά αποτελέσματα των τιμών της διαφορικής ενεργού διατομής είναι mb/sr. Η παράμετρος E αντιπροσωπεύει την ενέργεια στην μέση του πάχους του στόχου ενώ η παράμετρος E' είναι η ενέργεια στην επιφάνεια του παχέος στοιχείου. Σε όλες τις περιπτώσεις που υπήρχε χρυσός στο υπό-μελέτη δείγμα το βαρύ στοιχείο ήταν ο χρυσός και το ελαφρύ ισότοπο ήταν το υπό-μελέτη στοιχείο.

Στην περίπτωση του βηρυλλίου, όπου ο στόχος δεν περιείχε χρυσό, για τον προσδιορισμό των διαφορικών ενεργών διατομών χρησιμοποιήθηκε η εξίσωση:

$$\left(\frac{d\sigma}{d\Omega}\right)_{E,\theta}^{9\text{Be}} = \left(\frac{d\sigma}{d\Omega}\right)_{1000,\theta}^{\text{Si,Ruth}} \cdot \frac{Y_{9\text{Be}}}{Y_{\text{natSi}}} \cdot \frac{Q_{\text{Ruth}}^{1000}}{Q_{9\text{Be}}} \cdot \frac{N_t^{\text{Si}}}{N_t^{9\text{Be}}} \quad (\text{xvii})$$

Για τον υπολογισμό της διαφορικής ενεργού διατομής του πυριτίου στα 1000 keV χρησιμοποιήθηκε ο τύπος της σκέδασης Rutherford καθώς, όπως είναι αποδεδειγμένο στο παρελθόν [6], η διαφορική ενεργός διατομή της ${}^{\text{nat}}\text{Si}(d,d_0){}^{\text{nat}}\text{Si}$ ακολουθεί τη σκέδαση Rutherford

στα 1000 keV. Ο υπολογισμός των όρων σε καθμία από τις δυο παραπάνω εξισώσεις πραγματοποιήθηκε χωριστά. Για τον υπολογισμό του αριθμού των ανιχνευόμενων σωματιδίων σε κάθε περίπτωση πραγματοποιήθηκε ολοκλήρωση ή προσαρμογή, στις περιπτώσεις που υπήρχε μερική επικάλυψη μεταξύ κοντινών κορυφών, των γεγονότων στην αντίστοιχη κορυφή μέσω των προγραμμάτων SpectrW [7] και Tv [8]. Οι τιμές της διαφορικής ενεργού διατομής του χρυσού και του πυριτίου στα 1000 keV υπολογίστηκαν αναλυτικά μέσω της σχέσης της σκέδασης Rutherford (i) ενώ ο λόγος των παχών υπολογίστηκε ανεξάρτητα χρησιμοποιώντας διαφορετική τεχνική με φορτισμένες δέσμες και το πρόγραμμα SIMNRA [9]. Συγκεκριμένα χρησιμοποιήθηκε η τεχνική p-EBS. Η ενέργεια E' προσδιορίστηκε μέσω της διαδικασίας της ενεργειακής βαθμονόμησης του επιταχυντή με χρήση του λεπτού συντονισμού της αντίδρασης $^{27}\text{Al}(p,\gamma)^{28}\text{Si}$ ή της αντίδρασης $^{13}\text{C}(p,\gamma)^{14}\text{N}$, ανάλογα την περίπτωση. Για τον υπολογισμό της ενέργειας E, στην μέση του πάχους του στόχου, χρησιμοποιήθηκε η περιγραφή του στόχου μέσω της τεχνικής p-EBS και ο υπολογισμός της απώλειας ενέργειας στα επιφανειακά στρώματα του στόχου μέχρι να φτάσει η δέσμη στη μέση του πάχους του στόχου.

Μεθοδολογία ελέγχου αξιοπιστίας (benchmarking)

Για να ελέγξουμε την ακρίβεια των αποτελεσμάτων της διαφορικής ενεργού διατομής χρησιμοποιούνται τα πειράματα ελέγχου αξιοπιστίας (benchmarking). Στα πλαίσια της παρούσας διατριβής πειράματα benchmarking πραγματοποιήθηκαν στις περιπτώσεις ^{16}O , ^{23}Na και ^{nat}Si . Η διαδικασία αξιολόγησης των αποτελεσμάτων περιλαμβάνει την ακτινοβόληση παχέων στόχων γνωστής στοιχειομετρίας χρησιμοποιώντας την ίδια δέσμη με αυτήν που προσδιορίστηκε η ενεργός διατομή και στη συνέχεια την λεπτομερή προσομοίωση των αποκτηθέντων φασμάτων σε κατάλληλο πρόγραμμα με χρήση της μετρημένης διαφορική ενεργού διατομής.

Τα σημεία κλειδιά αυτών των πειραμάτων είναι η επιλογή του στόχου και το παράθυρο ολοκλήρωσης. Ο στόχος ιδανικά πρέπει να είναι στιλπνός και να περιλαμβάνει ένα στοιχείο με μεσαίο ατομικό αριθμό κατάλληλο για την κανονικοποίηση του φορτίου αλλά όχι πολύ βαρύ, ώστε να μην εισάγει μεγάλο αριθμό γεγονότων στα φάσματα. Το παράθυρο ολοκλήρωσης είναι η περιοχή του φάσματος κοντά στην επιφάνεια στην οποία πραγματοποιείται η σύγκριση μεταξύ του προσομοιωμένου και του πειραματικού αριθμού γεγονότων. Συνήθως επιλέγεται να είναι ~150-200 keV ώστε η συμβολή του διασκεδασμού της δέσμης και της πολλαπλής σκέδασης (στα βαριά στοιχεία) να μην είναι σημαντική.

Ωστόσο, τα πειράματα benchmarking περιλαμβάνουν κάποιες αβεβαιότητες. Αυτές οφείλονται στις συστηματικές αβεβαιότητες της ισχύς ανάσχεσης (stopping power), η στατιστική των γεγονότων και ο σωστός προσδιορισμός της παραμέτρου $Q\cdot\Omega$ [10]. Η επιλογή διαφορετικών σετ των stopping powers οδηγεί σε διαφορές μικρότερες του 1% οπότε δεν εισάγονται συστηματικές αβεβαιότητες, ωστόσο η ακρίβεια των σετ των stopping powers παραμένει ένα ανοιχτό ζήτημα και δεν μπορεί με κάποιο τρόπο να συνυπολογιστεί στην εκτίμηση της ολικής αβεβαιότητας. Η αβεβαιότητα αυτής της παραμέτρου εξαρτάται από την υπό-μελέτη περίπτωση και αναφέρεται σε κάθε περίπτωση χωριστά, όπως και η στατιστική των γεγονότων και ο προσδιορισμός του όρου $Q\cdot\Omega$.

Το μεγαλύτερο πρόβλημα στο benchmarking των φασμάτων d-EBS, το οποίο εισάγει μεγαλύτερες αβεβαιότητες και μπορεί ακόμα και να εξαιρέσει φάσματα από της διαδικασία, είναι η συμβολή των καναλιών d-NRA κάτω από τα ελαστικά κανάλια. Ειδικότερα σε υψηλότερες ενέργειες (πάνω από 2 MeV) (d,p_x) και (d,α_x) κανάλια διεγείρονται και μπορούν να συμβάλλουν σημαντικά κάτω από τις ελαστικές σκεδάσεις. Για να επιλυθεί το πρόβλημα αυτό είναι απαραίτητη η χρήση μαγνητικού φασματομέτρου για τον διαχωρισμό των πρωτονίων, των δευτερίων και των σωματιδίων άλφα. Στα πλαίσια της παρούσας εργασίας, λόγω απουσίας μαγνητικού φασματομέτρου, δεν εξήχθησαν αποτελέσματα στις περιπτώσεις όπου η συμβολή των (d,p_x) καναλιών ήταν σημαντική.

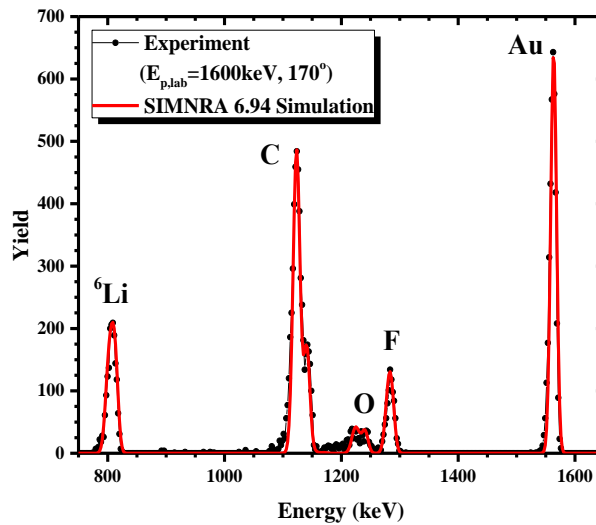
Υπολογισμός διαφορικής ενεργού διατομής της ελαστικής σκέδασης ${}^6\text{Li}(d,d_0){}^6\text{Li}$

Η διαφορική ενεργός διατομή της ελαστικής σκέδασης δευτερίων σε ${}^6\text{Li}$ μελετήθηκε στην ενεργειακή περιοχή μεταξύ 940-2000 keV με ενεργειακό βήμα ~20-30 keV και για τις γωνίες σκέδασης 125°, 140°, 150°, 160°, 170°. Καθώς η δομή της υπό-μελέτη ενεργού διατομής δεν είναι γνωστή, αφού δεν έχει μετρηθεί στο παρελθόν σε αυτό το ενεργειακό εύρος, η θεωρητική μελέτη των στάθμεων του σύνθετου πυρήνα που δημιουργείται είναι υψίστης σημασίας. Από την ύπαρξη και τα χαρακτηριστικά αυτών των στάθμεων εξαρτάται το ενεργειακό βήμα των μετρήσεων και το πάχος του στόχου. Στην συγκεκριμένη περίπτωση ο σύνθετος πυρήνας που δημιουργείται, ${}^8\text{Be}$, περιλαμβάνει την στάθμη με ενέργεια $E_x^* = 22980$ keV και εύρος $\Gamma = 230$ keV. Επιπρόσθετα, οι στάθμες με ενέργεια $E_x^* = 22240$ keV, $E_x^* = 23980$ keV και εύρος $\Gamma = 800$ keV, $\Gamma \approx 7\text{MeV}$ αντίστοιχα, παρόλο που βρίσκονται εκτός της περιοχής μελέτης, μπορούν να επηρεάσουν την δομή της διαφορικής ενεργού διατομής λόγω του μεγάλου εύρους τους.

Ο λόγος των παχών υπολογίστηκε με σύγκριση του εμπλουτισμένου και ενός φυσικού στόχου ${}^{\text{nat}}\text{LiF}$, μέσω της σχέσης $\frac{N_{t,Au}}{N_{t,6Li}} = \frac{N_{t,Au}}{f_{enr} \cdot N_{t,natLi}}$, όπου f_{enr} είναι ο παράγοντας εμπλουτισμού του

στόχου. Η αριθμητική τιμή του λόγου $\frac{N_{t,Au}}{N_{t,natLi}}$ υπολογίστηκε βασιζόμενοι στην υπόθεση ότι το LiF

διατηρεί την στοιχειομετρία του και χρησιμοποιώντας τα φάσματα των δευτερίων σε χαμηλές ενέργειες όπου η διαφορική ενεργός διατομή του φθορίου ακολουθεί την σκέδαση Rutherford [11]. Η τιμή αυτού του λόγου ήταν ίση με 0.091 ± 0.004 . Η τιμή του παράγοντα εμπλουτισμού υπολογίστηκε με χρήση της τεχνικής p-EBS ως 97% και βρίσκεται σε εξαιρετική συμφωνία με την τιμή του κατασκευαστή (97%). Το αποτέλεσμα αυτής της διαδικασίας φαίνεται στο Σχήμα 2.

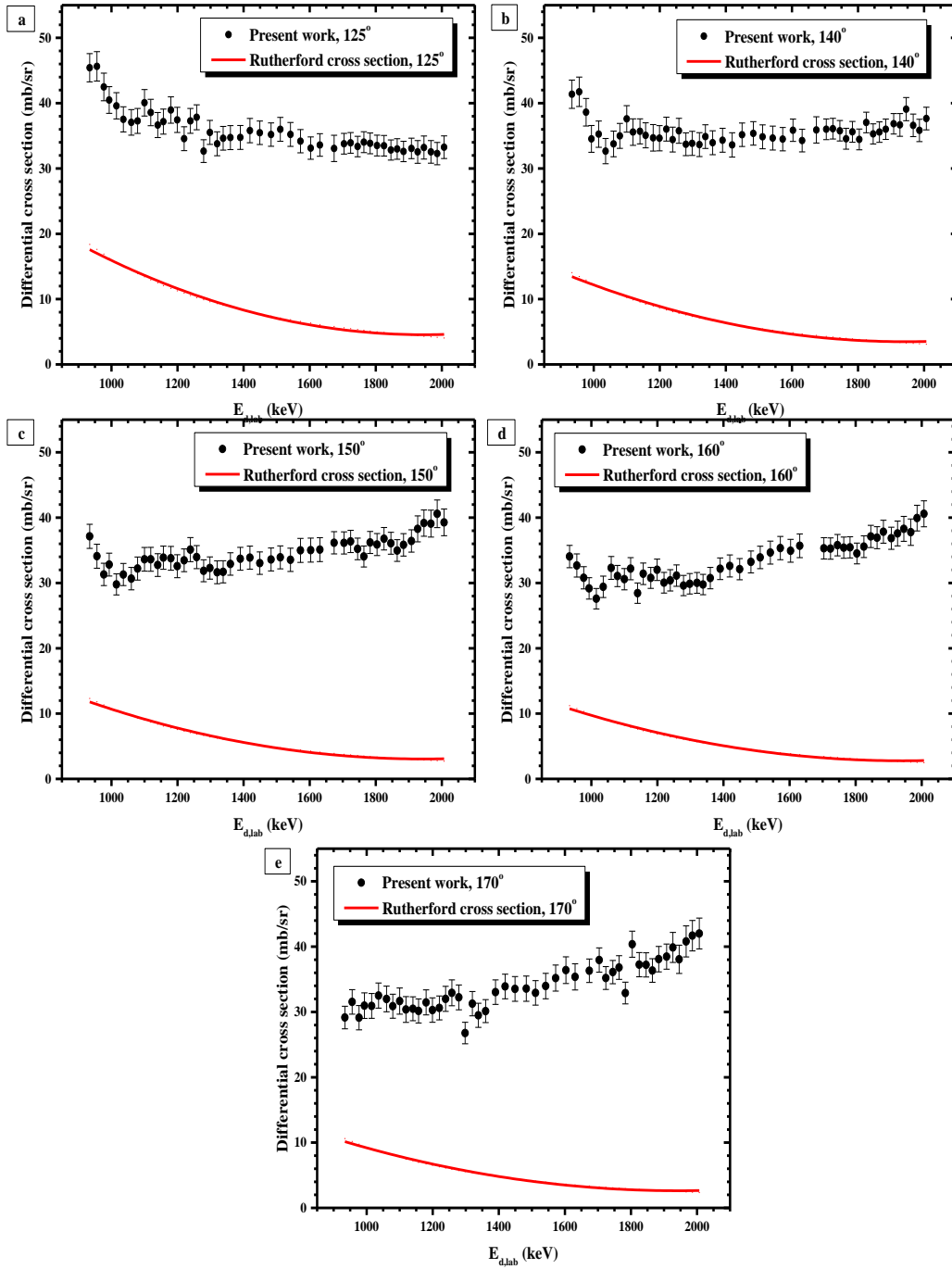


Σχήμα ii Πειραματικό και θεωρητικό φάσμα πρωτονίων σε ενέργεια $E_{p,lab} = 1600$ keV και γωνία 170° , μαζί με την αναγνώριση των αντίστοιχων κορυφών, χρησιμοποιώντας τα δεδομένα του Fasoli et al. [12] για τις τιμές της διαφορικής ενεργού διατομής της ελαστικής σκέδασης πρωτονίων από ${}^6\text{Li}$.

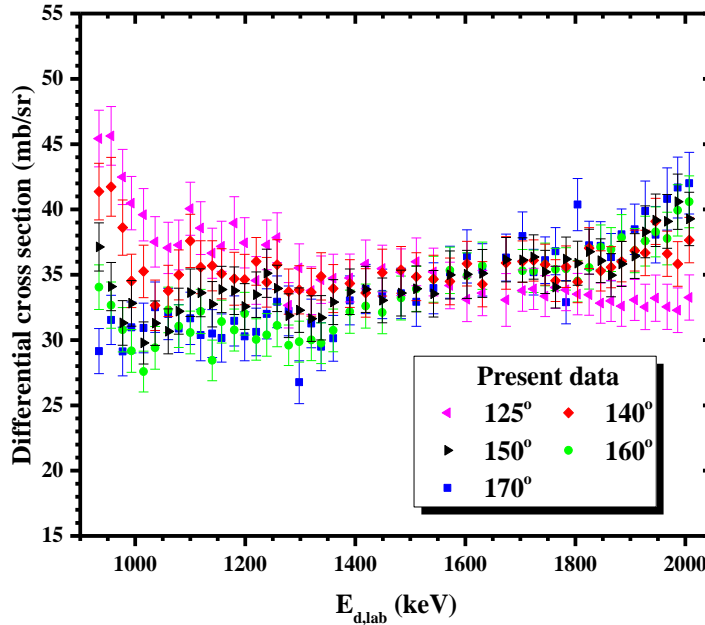
Οι τιμές της διαφορικής ενεργού διατομής της ελαστικής σκέδασης των δευτερίων σε ${}^6\text{Li}$, στο ενεργειακό εύρος 940 – 2000 keV και για γωνίες οπισθοσκέδασης 125° , 140° , 150° , 160° and 170° παρουσιάζονται σε γραφική μορφή στο Σχήμα (iii), μαζί με τις αντίστοιχες αβεβαιότητες. Αυτές οι αβεβαιότητες είναι μόνο οι στατιστικές, σύμφωνα με την κοινή σύμβαση. Ταυτόχρονα, στον οριζόντιο άξονα οι αβεβαιότητες στην ενέργεια δεν είναι ορατές λόγω της επιλεγμένη κλίμακας.

Οι τελικές τιμές της διαφορικής ενεργού διατομής είναι σημαντικά υψηλότερες από τις αντίστοιχες τιμές Rutherford. Όλη η δομή έχει επηρεαστεί από τις επικαλυπτόμενες στάθμες του σύνθετου πυρήνα ${}^8\text{Be}$ με ενέργειες $E_x^* = 22240$ keV, 22980 keV και εύρη $\Gamma = 800$ keV, 230 keV και 7000 keV, αντίστοιχα. Πιο συγκεκριμένα, στο χαμηλοενεργειακό εύρος ενεργειών (930-980 keV) η δομή προσομοιάζει την ούρα ενός συντονισμού σε χαμηλότερη ενέργεια όπου θα μπορούσε να οφείλεται στην στάθμη με ενέργεια $E_x^* = 22240$ keV και εύρος $\Gamma = 800$ keV. Αυτές οι επικαλυπτόμενες στάθμες μπορεί να δημιούργησαν τις μικρές μεταβολές της ενεργού διατομής σε όλο το ενεργειακό εύρος ~ 1.1 MeV.

Σχετικά με την γωνιακή εξάρτηση των διαφορικών ενεργών διατομών της ελαστικής σκέδασης δευτερίων σε ${}^6\text{Li}$, όπως φαίνεται στο Σχήμα (iv), υφίσταται μια ενεργειακή περιοχή (~ 1400 - 1800 keV) όπου οι αλλαγές στην γωνία καθώς και στην ενέργεια είναι ελάχιστες. Αυτό το χαρακτηριστικό θα μπορούσε να χρησιμοποιηθεί σε αναλυτικές εφαρμογές σχετικά με τον προσδιορισμό της κατανομής βάθους του ${}^6\text{Li}$ όπου η ενέργεια και/ή γωνίας σκέδασης δεν είναι γνωστές με μεγάλη ακρίβεια.



Σχήμα iii Τιμές της διαφορικής ενεργού διατομής (mb/sr) της ελαστικής σκέδασης ${}^6\text{Li}(d,d_0){}^6\text{Li}$, η οποία μετρήθηκε στο ενεργειακό εύρος $E_{d,lab} = 940\text{--}2000$ keV και για γωνίες σκέδασης 125° , 140° , 150° , 160° , 170° , με ενεργειακά βήματα $\sim 20\text{--}30$ keV. Η ολική στατιστική αβεβαιότητα των τιμών περιλαμβάνεται στα γραφήματα.



Σχήμα iv Τιμές της διαφορικής ενεργού διατομής (mb/sr) για την ελαστική σκέδαση ${}^6\text{Li}(d,d_0){}^6\text{Li}$ elastic scattering σε διαφορετικές γωνίες, για ενέργειες μεταξύ $E_{d,\text{lab}}=940\text{--}2000$ keV και για όλες τις γωνίες σκέδασης που μετρήθηκαν στα πλαίσια της παρούσας εργασίας.

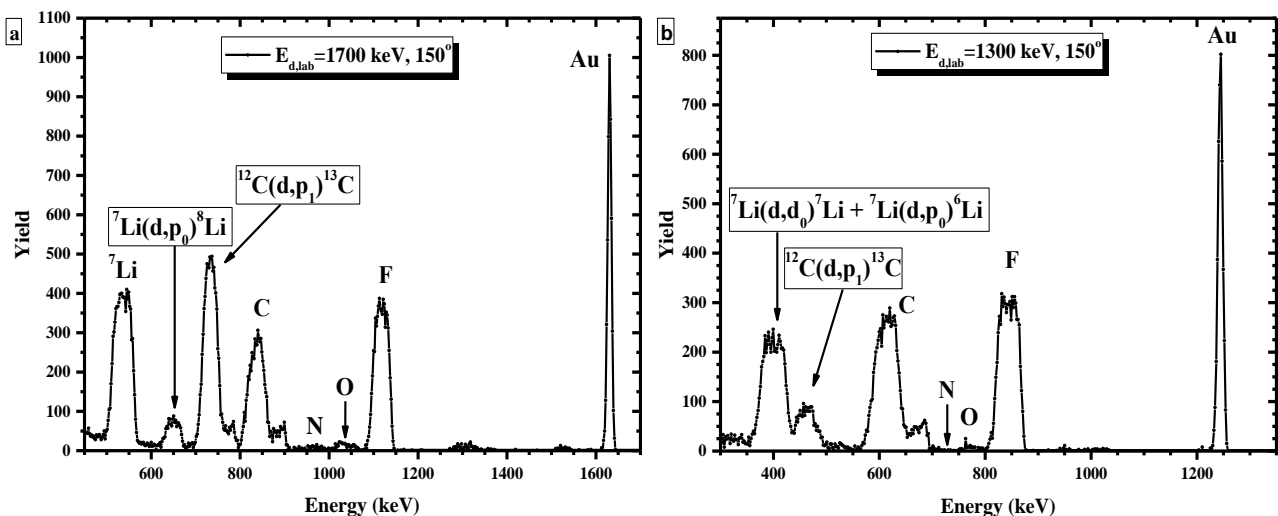
Υπολογισμός διαφορικής ενεργού διατομής της ελαστικής σκέδασης ${}^7\text{Li}(d,d_0){}^7\text{Li}$

Οι τιμές της διαφορικής ενεργού διατομής της ελαστικής σκέδασης ${}^7\text{Li}(d,d_0){}^7\text{Li}$ μετρήθηκαν στο ενεργειακό εύρος 940-2000 keV με διαφορετικό ενεργειακό βήμα (5-50 keV) για τις γωνίες οπισθοσκέδασης 125° , 140° , 150° , 160° και 170° . Ο σύνθετος πυρήνας που σχηματίζεται, ${}^9\text{Be}$, περιέχει, στην ενεργειακή περιοχή που μελετάμε, τις στάθμες με ενέργεια $E_x^*=17495$ keV και εύρος $\Gamma=47$ keV και ενέργεια $E_x^*=18020$ keV με άγνωστο εύρος. Επίσης, υπάρχουν δυο ακόμα στάθμες, οι οποίες μπορεί να επηρεάσουν την ενεργό διατομή λόγω του μεγάλου εύρους τους ($E_x^*=17300$ keV με $\Gamma=95$ keV και $E_x^*=18580$ keV με άγνωστο εύρος).

Ένα πειραματικό φάσμα από τον λεπτό στόχο LiF εξαχνωμένο πάνω σε ένα λεπτό φύλλο C με ένα λεπτό φύλλο χρυσού από πάνω φαίνεται στο Σχήμα ν (a) για την ενέργεια 1700 keV και για την γωνία σκέδασης των 150° . Ωστόσο, για μερικούς συνδυασμούς ενέργειας και γωνίας, υπάρχει μερική ή ολική επικάλυψη μεταξύ της ελαστικής σκέδασης στο ${}^7\text{Li}$ και των αντιδράσεων ${}^7\text{Li}(d,p_0){}^6\text{Li}$ ($Q_v = -191.95$ keV) και ${}^{12}\text{C}(d,p_1){}^{13}\text{C}$, όπως φαίνεται στο Σχήμα ν (b). Στις περιπτώσεις όπου δεν μπορούσε να πραγματοποιηθεί η διαδικασία της προσαρμογής, εξαιτίας της επικάλυψης κορυφών, η συνολική κορυφή που περιέχει τις συνεισφορές των ${}^7\text{Li}(d,d_0){}^7\text{Li}$, ${}^7\text{Li}(d,p_0){}^6\text{Li}$ και ${}^{12}\text{C}(d,p_1){}^{13}\text{C}$ ολοκληρώθηκε. Έπειτα, υπολογίστηκε η συνεισφορά της αντίδρασης ${}^{12}\text{C}(d,p_1){}^{13}\text{C}$ στην συνολική κορυφή μέσω του υπολογισμού της ποσότητας άνθρακα μέσα στον στόχο χρησιμοποιώντας τα πειραματικά φάσματα και τον κώδικα SIMNRA. Πιο συγκεκριμένα, η ποσότητα του άνθρακα υπολογίστηκε μέσω των φασμάτων δευτερίων με χρήση των

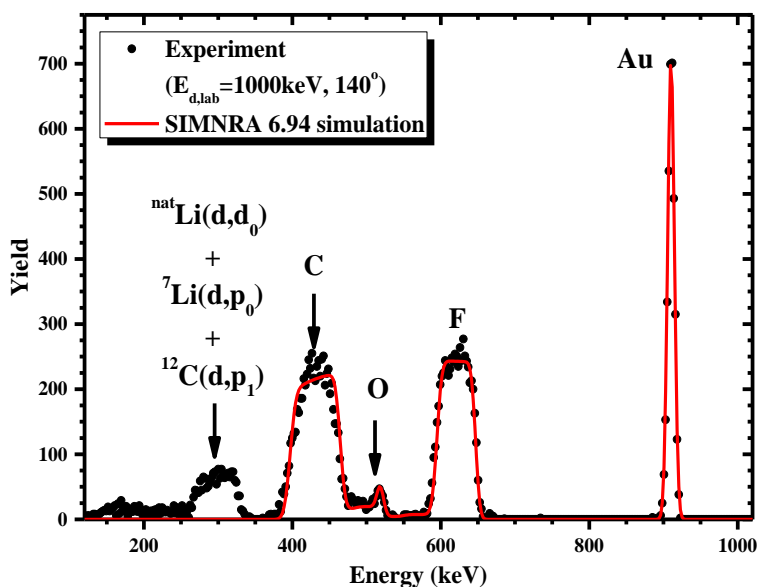
αξιολογημένων (evaluated) τιμών της ενεργού διατομής της ελαστικής σκέδασης $^{12}\text{C}(\text{d},\text{d}_0)^{12}\text{C}$ μέσω του προγράμματος SIMNRA καθώς και μέσω των φασμάτων πρωτονίων με χρήση των αξιολογημένων δεδομένων για την ελαστική σκέδαση $^{12}\text{C}(\text{p},\text{p}_0)^{12}\text{C}$. Στη συνέχεια, η επιβεβαίωση της ποσότητας του άνθρακα κρίθηκε απαραίτητη και πραγματοποιήθηκε μέσω των ενεργειών χωρίς επικάλυψη κορυφών όπου η κορυφή της αντίδρασης $^{12}\text{C}(\text{d},\text{p}_1)^{13}\text{C}$ μπορούσε να ολοκληρωθεί και ο αριθμός αυτός συγκρίθηκε με τον προσομοιωμένο αριθμό γεγονότων, ο οποίος υπολογίστηκε με χρήση των δεδομένων του Kokkoris et al. [13] για την αντίδραση $^{12}\text{C}(\text{d},\text{p}_1)^{13}\text{C}$. Μέσω της διαδικασίας αυτής επιβεβαιώθηκε η ποσότητα του άνθρακα στον στόχο και επομένως υπολογίστηκε και αφαιρέθηκε ο αριθμός των σωματιδίων της αντίδρασης $^{12}\text{C}(\text{d},\text{p}_1)^{13}\text{C}$, για τις ενέργειες που υπάρχει επικάλυψη, από τον αριθμό των σωματιδίων της συνολικής κορυφής. Η διαδικασία αυτή δεν πραγματοποιήθηκε για την γωνία σκέδασης των 125° επειδή τα δεδομένα της αντίδρασης $^{12}\text{C}(\text{d},\text{p}_1)^{13}\text{C}$ που χρησιμοποιήθηκαν δεν ήταν μετρημένα για αυτή τη γωνία οπότε τα τελικά αποτελέσματα για τις 125° ξεκινάνε από τα 1420 keV. Στην περίπτωση των 140° , καθώς δεν υπάρχουν μετρήσεις για αυτή την γωνία, χρησιμοποιήθηκαν οι μετρήσεις για τις 145° καθώς η γωνιακή κατανομή της αντίδρασης $^{12}\text{C}(\text{d},\text{p}_1)^{13}\text{C}$ παρουσιάζει μικρές διακυμάνσεις σε διάστημα 10° για χαμηλές ενέργειες δευτερίων.

Η ίδια διαδικασία, δυστυχώς, δεν μπορούσε να πραγματοποιηθεί για την αντίδραση $^7\text{Li}(\text{d},\text{p}_0)^6\text{Li}$ καθώς υπάρχει παντελής έλλειψη πειραματικών δεδομένων στην βιβλιογραφία. Επομένως, τα τελικά δεδομένα διαφορικών ενεργών διατομών αναφέρονται στον συνδυασμό των $^7\text{Li}(\text{d},\text{d}_0)^7\text{Li}$ και $^7\text{Li}(\text{d},\text{p}_0)^6\text{Li}$ για συγκεκριμένες ενέργειες όπου η επικάλυψη συνέβη. Ωστόσο, αυτή η κατάσταση δεν καθιστά τα τελικά δεδομένα αχρείαστα καθώς σε μετρήσεις με παχύς στόχους, απουσία μαγνητικού φασματομέτρου ή συστήματος μέτρησης χρόνου πτήσης (time of flight - ToF) όπου θα διαχώριζε τα πρωτόνια από τα δευτερία, αυτή η επικάλυψη θα υπάρχει στα πειραματικά φάσματα.



Σχήμα ν (α) Πειραματικό φάσμα του στόχου LiF εξαχνωμένο πάνω σε ένα λεπτό φύλλο C με ένα λεπτό φύλλο χρυσού από πάνω σε ενέργεια 1700 keV και γωνία 150° μαζί με την αναγνώριση των αντίστοιχων κορυφών (β) Πειραματικό φάσμα του ίδιου στόχου σε ενέργεια δευτερίων 1300 keV και γωνία σκέδασης 150° μαζί με την αναγνώριση των αντίστοιχων κορυφών.

Για τον υπολογισμό του λόγου των παχών $N_{t,Au} : N_{t, {}^7\text{Li}}$ χρησιμοποιήθηκε η υπόθεση ότι το LiF διατηρεί την στοιχειομετρία του, όπως στην περίπτωση του ${}^6\text{Li}$, και επομένως χρησιμοποιήθηκε η εξίσωση $\frac{N_{t,Au}}{N_{t, {}^7\text{Li}}} = \frac{N_{t,Au}}{0.9241 \cdot N_{t, \text{natLi}}} = \frac{N_{t,Au}}{0.9241 \cdot N_{t,F}}$. Σε αυτήν την περίπτωση ο παράγοντας εμπλουτισμού δεν ήταν άγνωστη ποσότητα αλλά η περιεκτικότητα του φυσικού λιθίου σε ${}^7\text{Li}$, δηλαδή 0.9241. Για τον υπολογισμό του λόγου των παχών χρησιμοποιήθηκαν τα φάσματα δευτερίων σε χαμηλές ενέργειες (<~1200 keV) και για γωνίες 140° και 150° όπου το φθόριο ακολουθεί την σκέδαση Rutherford εντός 2% [11]. Η τιμή του λόγου των παχών υπολογίστηκε ίση με 0.0084 ± 0.0004 . Ένα τυπικό φάσμα παρουσιάζεται στο Σχήμα νι για ενέργεια δευτερίων 1000 keV κα γωνία σκέδασης 140°. Για την προσομοίωση των φασμάτων δευτερίων χρησιμοποιήθηκαν τιμές Rutherford για τις ενεργές διατομές του φθορίου και του χρυσού, ενώ για τον άνθρακα [14] και το οξυγόνο [14] χρησιμοποιήθηκαν οι αξιολογημένες τιμές, οι οποίες υπολογίστηκαν μέσω του SigmaCalc 2.0, όπως αυτό έχει εισαχθεί στο SIMNRA 6.94.

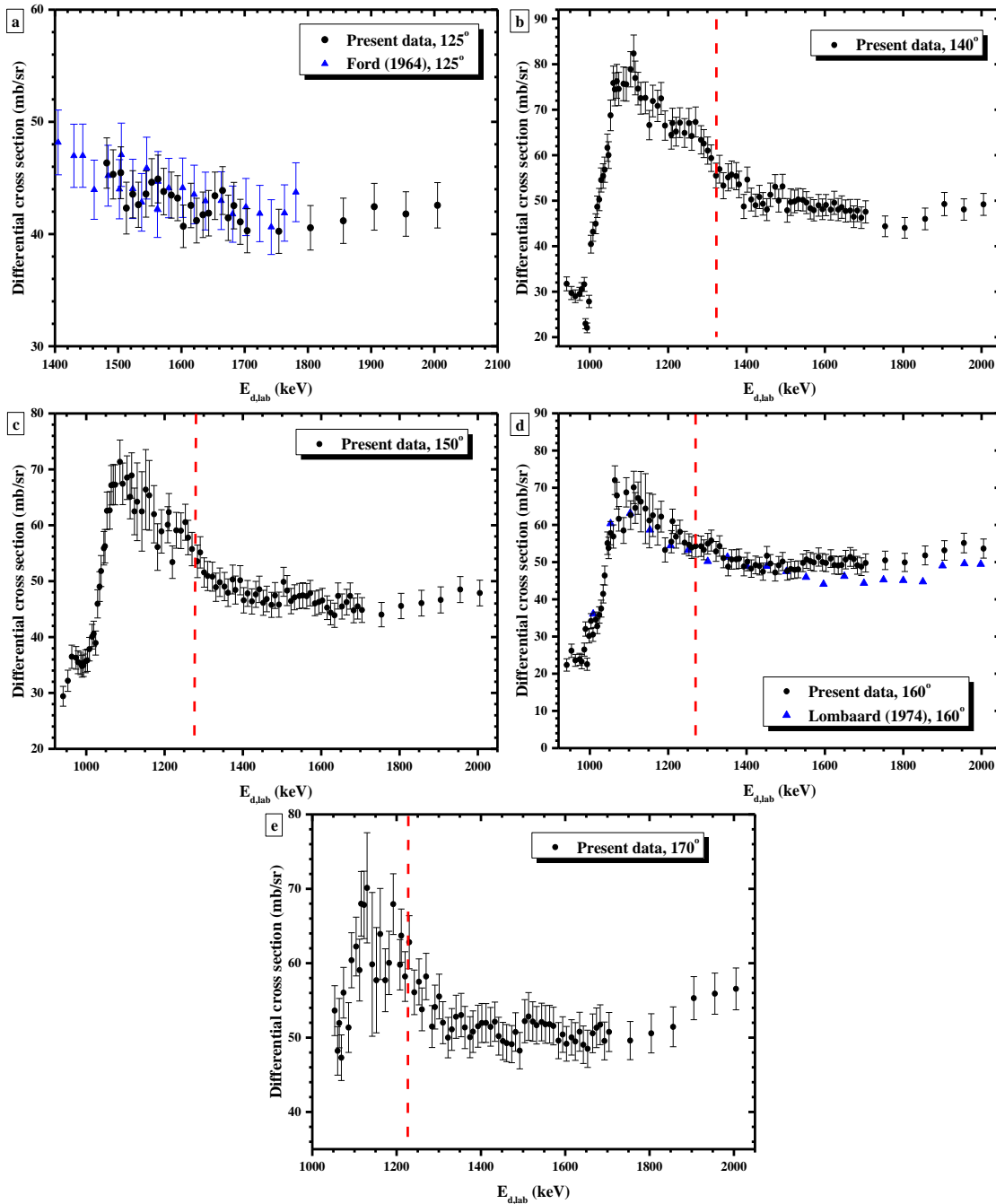


Σχήμα νι Πειραματικό και προσομοιωμένο φάσμα για την ενέργεια δευτερίων $E_{d,lab} = 1000 \text{ keV}$ για την γωνία σκέδασης 140° μαζί με την αναγνώριση των αντίστοιχων κορυφών.

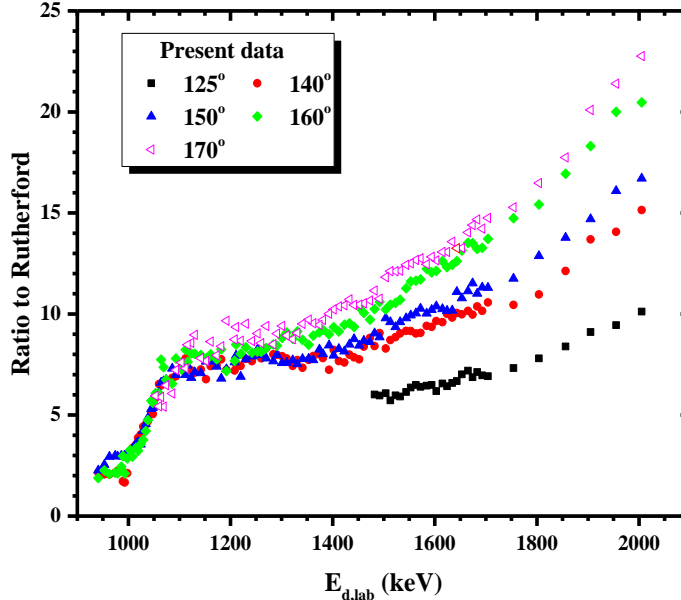
Οι τελικές τιμές της διαφορικής ενεργού διατομής της ελαστικής σκέδασης ${}^7\text{Li}(d,d_0){}^7\text{Li}$ για υψηλές ενέργειες και οι τελικές τιμές της διαφορικής ενεργού διατομής του αθροίσματος των

αντιδράσεων ${}^7\text{Li}(d,d_0){}^7\text{Li}$ και ${}^7\text{Li}(d,p_0){}^6\text{Li}$ για χαμηλές ενέργειες παρουσιάζονται σε γραφική μορφή στο Σχήμα vii a-e. Η κάθετη κόκκινη γραμμή στα Σχήματα vii b-e χωρίζει τα γραφήματα σε δυο περιοχές αποτελεσμάτων. Όπως συζητήθηκε παραπάνω, για τις 125° (Σχήμα vii a) δεν υπάρχουν δεδομένα για την αντίδραση ${}^{12}\text{C}(d,p_1){}^{13}\text{C}$ στην βιβλιογραφία και επομένως δεν εξήχθησαν αποτελέσματα για την χαμηλή περιοχή ενεργειών. Για τις υψηλές ενέργειες δευτερίων, στο Σχήμα vii a η διαφορική ενεργός διατομή που προσδιορίστηκε συγκρίνεται με την υπάρχουσα στην βιβλιογραφία από τον Ford [15] υποδεικνύοντας καλή συμφωνία εντός σφαλμάτων, έως και 5%. Στα σχήματα vii b-e ένας συντονισμός αναδεικνύεται στην ενεργειακή περιοχή των 1000 keV ο οποίος θα μπορούσε να αποδοθεί στο άθροισμα των δύο αντιδράσεων ${}^7\text{Li}(d,d_0){}^7\text{Li}$ και ${}^7\text{Li}(d,p_0){}^6\text{Li}$ εξαιτίας της στάθμης με ενέργεια $E_x^* = 17495$ keV και εύρος $\Gamma = 47$ keV του σύνθετου πυρήνα ${}^9\text{Be}$. Η στάθμη αυτή αντιστοιχεί σε δευτέρια ενέργειας 1027 keV (στο σύστημα αναφοράς του εργαστηρίου). Στο Σχήμα vii d περιλαμβάνονται και τα υπάρχοντα δεδομένα από τους Lombaard et al. [16], τα οποία αντιστοιχούν μόνο στην ελαστική σκέδαση ${}^7\text{Li}(d,d_0){}^7\text{Li}$ σε όλο το ενεργειακό εύρος. Σε αυτά τα δεδομένα η επικάλυψη μεταξύ των κορυφών που αντιστοιχούν στις αντιδράσεις ${}^7\text{Li}(d,d_0){}^7\text{Li}$, ${}^7\text{Li}(d,p_0){}^6\text{Li}$ και ${}^{12}\text{C}(d,p_1){}^{13}\text{C}$ ήταν παρούσα στα φάσματα, εφόσον δεν υπήρχε κάποιο σύστημα ικανό να διαχωρίζει μάζες σωματιδίων. Η συμβολή της αντίδρασης ${}^{12}\text{C}(d,p_1){}^{13}\text{C}$ υπολογίστηκε μέσω του αριθμού των ελαστικά σκεδαζόμενων δευτερίων από την επιμόλυνση του άνθρακα, όπως στην παρούσα εργασία ενώ για την αντίδραση ${}^7\text{Li}(d,p_0){}^6\text{Li}$, καθώς η κορυφή πρωτονίων κινούταν μέσα από την ελαστική σκέδαση υπό-μελέτη, η συνεισφορά της υπολογίστηκε παίρνοντας τον μέσο όρο του αριθμού πρωτονίων στις δυο πλευρές της περιοχής επικάλυψης. Σε όλη την περιοχή μελέτης η συμφωνία είναι ικανοποιητική εντός σφαλμάτων.

Αξίζει να επισημανθεί ότι οι τιμές της διαφορικής ενεργού διατομής που προσδιορίστηκαν είναι εξαιρετικά υψηλότερες από τις αντίστοιχες τιμές Rutherford. Ειδικά για υψηλές ενέργειες και γωνίες έντονης οπισθοσκέδασης οι τιμές που προσδιορίστηκαν είναι έως και 23 φορές υψηλότερες από τις αντίστοιχες Rutherford, όπως φαίνεται στο Σχήμα viii. Σχετικά με την γωνιακή κατανομή της διαφορικής ενεργού διατομής της ελαστικής σκέδασης δευτερίων σε ${}^7\text{Li}$, δεν είναι εξαιρετικά έντονη, όπως φαίνεται στο Σχήμα viii καθώς σε διάστημα 10° δεν εμφανίζονται σημαντικές αλλαγές ανάμεσα στις τιμές των διαφορικών ενεργών διατομών.



Σχήμα vii a) Διαφορική ενεργός διατομή της ελαστικής σκέδασης ${}^7\text{Li}(d,d_0){}^7\text{Li}$ σε γωνία σκέδασης 125° που προσδιορίστηκε στα πλαίσια της παρούσας εργασίας και συγκρίνεται με τα δεδομένα του Ford, b,c) Διαφορική ενεργός διατομή για τις γωνίες 140° και 150° αντίστοιχα της της ελαστικής σκέδασης ${}^7\text{Li}(d,d_0){}^7\text{Li}$ για ενέργειες δευτερίων υψηλότερες από $E_{d,lab} = \sim 1300$ keV (κόκκινη κάθετη γραμμή) και για το άθροισμα των αντιδράσεων ${}^7\text{Li}(d,d_0){}^7\text{Li}$ and ${}^7\text{Li}(d,p_0){}^6\text{Li}$ σε χαμηλότερες ενέργειες, d) Διαφορική ενεργός διατομή για την γωνία 160° της ελαστικής σκέδασης ${}^7\text{Li}(d,d_0){}^7\text{Li}$ για ενέργειες δευτερίων υψηλότερες από $E_{d,lab} = 1270$ keV (κόκκινη κάθετη γραμμή) και για το άθροισμα των αντιδράσεων ${}^7\text{Li}(d,d_0){}^7\text{Li}$ and ${}^7\text{Li}(d,p_0){}^6\text{Li}$ για χαμηλότερες ενέργειες δευτερίων μαζί με τα δεδομένα από τους Lombard et al. (που αντιστοιχούν μόνο στην ελαστική σκέδαση ${}^7\text{Li}(d,d_0){}^7\text{Li}$ σε όλο το ενεργειακό εύρος e) Διαφορική ενεργός διατομή για την γωνία 170° της ελαστικής σκέδασης ${}^7\text{Li}(d,d_0){}^7\text{Li}$ για ενέργειες δευτερίων υψηλότερες από $E_{d,lab} = 1220$ keV (κόκκινη κάθετη γραμμή) και για το άθροισμα των αντιδράσεων ${}^7\text{Li}(d,d_0){}^7\text{Li}$ and ${}^7\text{Li}(d,p_0){}^6\text{Li}$ για χαμηλότερες ενέργειες δευτερίων.



Σχήμα viii Λόγος ως προς την Rutherford της ελαστικής σκέδασης ${}^7\text{Li}(d,d_0){}^7\text{Li}$ για το ενεργειακό εύρος 940-2000 keV για όλες τις γωνίες οπισθοσκέδασης που μετρήθηκαν.

Υπολογισμός διαφορικής ενεργού διατομής της ελαστικής σκέδασης ${}^9\text{Be}(d,d_0){}^9\text{Be}$

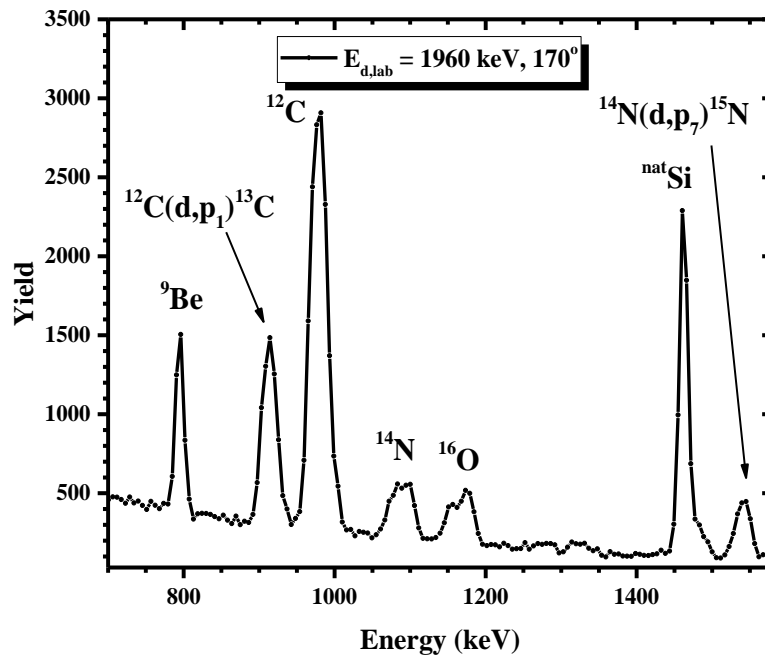
Η διαφορική ενεργός διατομή της ελαστικής σκέδασης δευτερίων σε ${}^9\text{Be}$ προσδιορίστηκε για το ενεργειακό εύρος 1600 – 2200 keV, με βήμα 20 keV και για τις γωνίες σκέδασης 120° , 140° , 150° , 160° , 170° was studied. Στην περιοχή μελέτης του σύνθετου πυρήνα ${}^{11}\text{B}$ υπάρχουν δυο στάθμες με ενέργειες $E_x^* = 17310$ keV και $E_x^* = 17500$ keV με εύρη $\Gamma \approx 1$ MeV and $\Gamma = 116$ keV, αντίστοιχα. Η στάθμη με ενέργεια $E_x^* = 18000$ keV και εύρος $\Gamma = 870$ keV μπορεί επίσης να επηρεάσει την υπό μελέτη ενεργό διατομή λόγω του μεγάλου εύρους της.

Ο στόχος που ακτινοβολήθηκε ήταν ένα φύλλο Si_3N_4 με ένα λεπτό στρώμα βηρυλλίου εναποτιθέμενο από πάνω και ένα τυπικό φάσμα φαίνεται στο Σχήμα ix για την ενέργεια δευτερίων 1960 keV και για την γωνία σκέδασης των 170° . Όπως φαίνεται τα φάσματα περιέχουν τις παρασιτικές συνεισφορές από άνθρακα και οξυγόνο οι οποίες οφείλεται στην τεχνική εναπόθεσης του βηρυλλίου στον στόχο. Φάσματα πάρθηκαν επίσης και για χαμηλότερες ενέργειες δευτερίων (~1000-1600 keV), ωστόσο το πρόβλημα των επικαλυπτόμενων κορυφών μεταξύ της ελαστικής σκέδασης σε ${}^9\text{Be}$ και της αντίδρασης ${}^{12}\text{C}(d,p_1){}^{13}\text{C}$ εμφανίστηκε και σε αυτήν την περίπτωση. Η αφαίρεση της συνεισφοράς της αντίδρασης ${}^{12}\text{C}(d,p_1){}^{13}\text{C}$, με τον ίδιο τρόπο που πραγματώθηκε στην περίπτωση της ελαστικής σκέδασης σε ${}^7\text{Li}$, ήταν αδύνατη σε αυτήν την περίπτωση καθώς η συνεισφορά της αντίδρασης ${}^{12}\text{C}(d,p_1){}^{13}\text{C}$ ήταν μεγαλύτερη από αυτή της ελαστικής σκέδασης ${}^9\text{Be}(d,d_0){}^9\text{Be}$, το οποίο θα οδηγούσε σε μη αξιόπιστα αποτελέσματα. was again present. Επομένως, δεδομένα εξήχθησαν μόνο για τις υψηλότερες ενέργειες (1600 – 2200 keV) όπου αυτή η επικάλυψη δεν υπήρχε.

Οι τελικές τιμές της ενεργού διατομής της ελαστικής σκέδασης του βηρυλλίου υπολογίστηκαν μέσω της σχέσης (xvii).

Ο όρος $\left(\frac{d\sigma}{d\Omega}\right)_{1000,\theta}^{Si,Ruth}$ υπολογίστηκε χρησιμοποιώντας την σχέση της σκέδασης Rutherford, με έναν διορθωτικό παράγοντα για το φαινόμενο της θωράκισης (screening effect), καθώς η διαφορική ενεργός διατομή της $^{nat}Si(d,d_0)^{nat}Si$ δεν παρουσιάζει αποκλίσεις από τη σκέδαση Rutherford για ενέργεια δευτερίων 1000 keV [6]. Η ενέργεια των δευτερίων η οποία χρησιμοποιήθηκε για τον υπολογισμό της ενεργού διατομής του πυριτίου αντιστοιχούσε στην ενέργεια στη μέση του πάχους του Si_3N_4 στόχου, συμπεριλαμβάνοντας την απώλεια ενέργειας στο στρώμα βηρυλλίου.

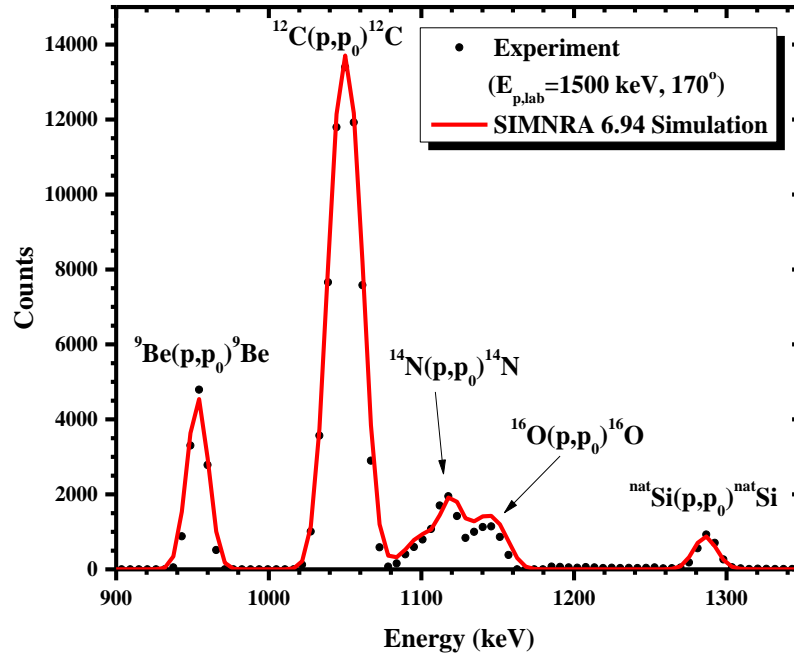
Οι όροι Q_{Ruth}^{1000} και Q_{Be} προσδιορίστηκαν χρησιμοποιώντας τον ολοκληρωτή φορτίου (current integrator) ο οποίος χρησιμοποιούταν κατά τη διάρκεια των μετρήσεων. Το συστηματικό σφάλμα του current integrator αναμένεται να διαγραφεί καθώς η σχετική μέθοδος που χρησιμοποιήθηκε περιλαμβάνει λόγους και όχι απόλυτες τιμές.



Σχήμα ix Τυπικό πειραματικό φάσμα της μεμβράνης Si_3N_4 με το λεπτό στρώμα βηρυλλίου από πάνω για την ενέργεια δευτερίων $E_{d,lab}=1960$ keV και για την γωνία σκέδασης των 170° μαζί με την αναγνώριση των αντίστοιχων κορυφών.

Για να υπολογίσουμε τον όρο $\frac{N_t^{Si}}{N_t^{Be}}$ χρησιμοποιήθηκε η τεχνική p-EBS. Φάσματα πρωτονίων αποκτήθηκαν στις ενέργειες 1200 keV και 1500 keV και στις γωνίες σκέδασης 150° , 160° και 170° όπου η ενεργός διατομή δεν παρουσιάζει μεγάλες διακυμάνσεις και λεπτούς συντονισμούς. Για την προσομοίωση της κορυφής της ελαστικής σκέδασης $^9Be(p,p_0)^9Be$, απουσία αξιολογημένων

δεδομένων ή benchmarked δεδομένων, χρησιμοποιήθηκαν δεδομένα από την βιβλιογραφία. Συγκεκριμένα χρησιμοποιήθηκαν τα δεδομένων των Liu et al. [17] στις 170° , τα οποία συμφωνούσαν εντός 4%, με τα δεδομένα των Krat et al. [18] στις 165° . Ένα πειραματικό φάσμα μαζί με το προσομοιωμένο παρουσιάζεται στο Σχήμα x για την ενέργεια πρωτονίων 1500 keV και για την γωνία σκέδασης 170° . Η τεχνική p-EBS οδήγησε σε τιμή του λόγου των παχών $N_t^{Si} : N_t^{Be}$ ίση με 0.200 ± 0.010 , έχοντας ένα σχετικό στατιστικό σφάλμα 5%.

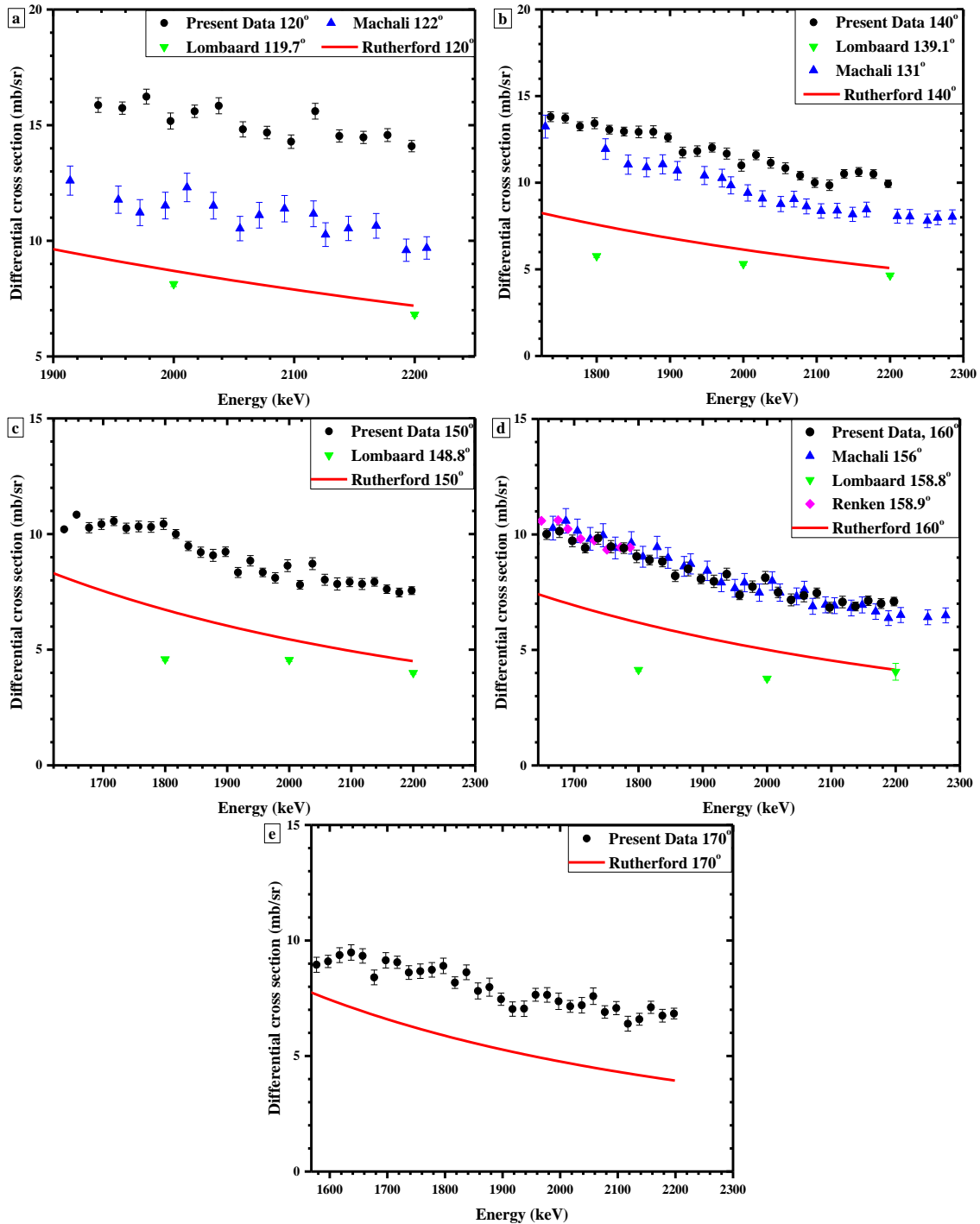


Σχήμα x Πειραματικό και προσομοιωμένο φάσμα πρωτονίων που αποκτήθηκε στην ενέργεια $E_{p,lab}=1500$ keV και στη γωνία 170° μαζί με την αναγνώριση των αντίστοιχων κορυφών.

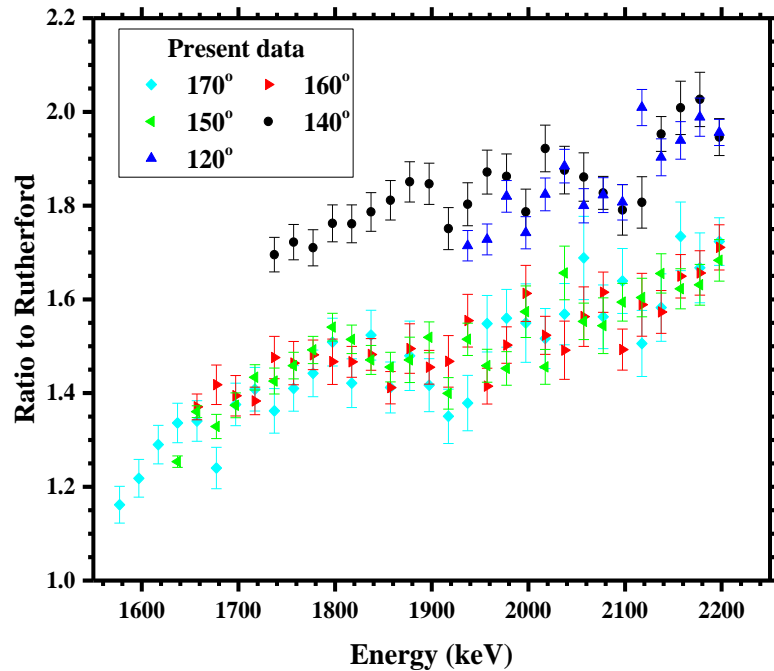
Οι τελικές τιμές για τη διαφορική ενεργό διατομή της ελαστικής σκέδασης ${}^9\text{Be}(d,d_0){}^9\text{Be}$ στο ενεργειακό εύρος $E_{d,lab}=1600\text{--}2200$ keV, με βήμα, και για τις γωνίες σκέδασης 120° , 140° , 150° , 160° και 170° παρουσιάζονται σε γραφική μορφή στα Σχήματα xi a-e, μαζί με τα δεδομένα που υπάρχουν στη βιβλιογραφία. Τα συνολικά σχετικά στατιστικά σφάλματα δεν υπερβαίνουν το 5% σε κάθε ενέργεια για όλες τις γωνίες. Όσον αφορά τα συστηματικά σφάλματα που αφορούν τις διαφορές μεταξύ θεωρητικών και πειραματικών δεδομένων για την ισχύ ανασχεσης είναι ~4% για το πυρίτιο και ~3.4% για το βηρύλλιο, όπως αναφέρεται στη σελίδα του SRIM (<http://www.srim.org/>). Οι αβεβαιότητες όσον αφορά την ενέργεια της δέσμης ήταν ~3 keV από την βαθμονόμηση του επιταχυντή και ~2.2 keV από τον διασκεδασμό της δέσμης μέσα στον στόχο που προσδιορίστηκε.

Η δομή των μετρημένων δεδομένων μπορεί να οφείλεται στις στάθμες του συνθέτου πυρήνα οι οποίες αναφέρθηκαν παραπάνω. Στα σχήματα χι a-d παρουσιάζονται μεγάλες αποκλίσεις με τα δεδομένα των Lombaard et al. [19] σε όλο το ενεργειακό εύρος και για όλες τις γωνίες σκέδασης, χωρίς ωστόσο να υπάρχει σαφής λόγος. Μια πιθανή εξήγηση είναι ότι η απόκλιση αυτή σχετίζεται με τον τρόπο που έγινε η αφαίρεση της συνεισφοράς της αντίδρασης $^{12}\text{C}(d,p_1)^{13}\text{C}$ από την κορυφή της $^9\text{Be}(d,d_0)^9\text{Be}$ από τους Lombaard et al. Συγκρίνοντας τα δεδομένα της παρούσας εργασίας με τα αντίστοιχα των Machali et al. [20], για την γωνία σκέδασης των 160° παρατηρείται καλή σύγκριση ενώ για τις γωνίες σκέδασης 120° και 140° παρατηρούνται διαφορές με τα δεδομένα των Machali et al. να είναι συστηματικά πιο χαμηλά. Οι διαφορές στις γωνίες των 120° και 140° μπορεί να οφείλονται στον νεκρό χρόνο των πολυκαναλικών αναλυτών, όπου, όπως αναφέρεται στο [20], ήταν η κύρια πηγή αβεβαιότητας στις πιο μπροστινές γωνίες και μπορεί να εξηγήσει την τάση που υπάρχει. Τα δεδομένα στο σχήμα χι b των Machali et al. μετρήθηκαν στις 131° και συγκρίνονται με τα παρόντα δεδομένα στις 140° καθώς ήταν η πιο κοντινή γωνία που πραγματοποιήθηκαν μετρήσεις. Για την μόνη κοινή γωνία με τα δεδομένα του Renken [21] στις 160° , παρατηρείται καλή συμφωνία εντός των ορίων αβεβαιότητας παρόλο που τα δεδομένα του Renken μετρήθηκαν στις 158.9° .

Αποκλίσεις των μετρημένων τιμών παρατηρούνται από τις αντίστοιχες Rutherford τιμές, με τις μετρημένες τιμές να είναι σε κάποιες περιπτώσεις διπλάσιες, όπως φαίνεται στο Σχήμα xii. Μια ισχυρή γωνιακή κατανομή εμφανίζεται στο Σχήμα xii με τις δυο πιο μπροστινές γωνίες (120° and 140°) να εμφανίζουν μεγάλες διαφορές από τις πιο πίσω γωνίες. Αυτή η συμπεριφορά θα μπορούσε να οφείλεται στην γωνιακή εξάρτηση των στάθμων του σύνθετου πυρήνα στην ενεργειακή περιοχή που μελετάται.



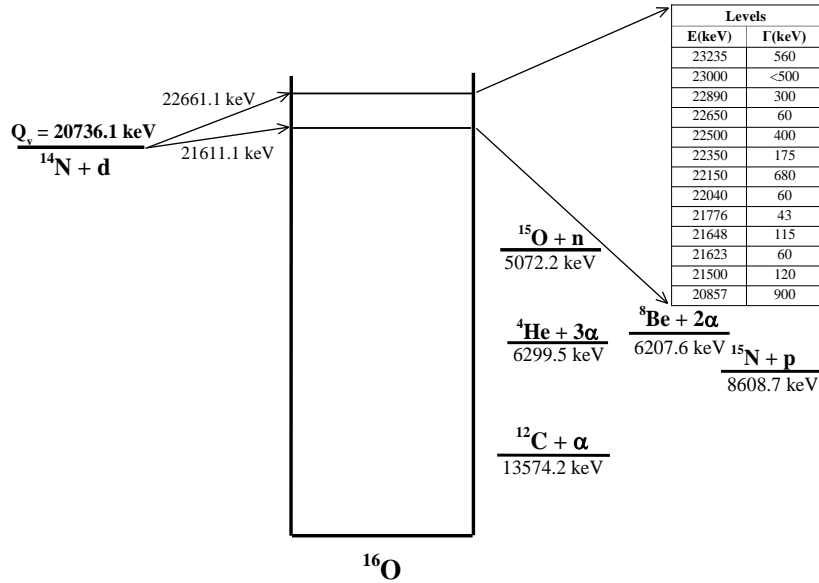
Σχήμα xi a-e Τιμές της διαφορικής ενεργού διατομής (mb/sr) της ελαστικής σκέδασης ${}^9\text{Be}(d,d_0){}^9\text{Be}$ η οποία μετρήθηκε στο ενεργειακό εύρος $E_{d,lab} \sim 1600 - 2200$ keV και για γωνίες σκέδασης 120° , 140° , 150° , 160° και 170° , με ενεργειακά βήματα ~ 20 keV, μαζί με τα υπάρχοντα δεδομένα στην βιβλιογραφία.



Σχήμα xii Λόγος της μετρημένης διαφορικής ενεργού διατομής ως προς τις αντίστοιχες Rutherford τιμές της ελαστικής σκέδασης ${}^9\text{Be}(d,d_0){}^9\text{Be}$ για το ενεργειακό εύρος δευτερίων 1600-2200 keV για όλες τις γωνίες σκέδασης που μετρήθηκαν.

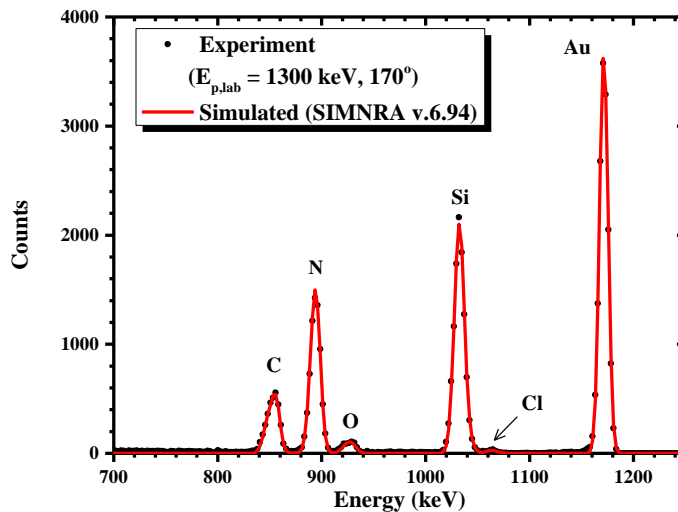
Υπολογισμός διαφορικής ενεργού διατομής της ελαστικής σκέδασης ${}^{\text{nat}}\text{N}(d,d_0){}^{\text{nat}}\text{N}$

Η διαφορική ενεργός διατομή της ελαστικής σκέδασης δευτερίων σε ${}^{\text{nat}}\text{N}$ μετρήθηκε στο ενεργειακό εύρος 1000 – 2200 keV με βήματα ~ 10 keV και για τις γωνίες σκέδασης 120° , 130° , 140° , 150° , 160° και 170° . Το ενεργειακό εύρος του σύνθετου πυρήνα ${}^{16}\text{O}$ που μελετήθηκε περιλαμβάνει πολλές και επικαλυπτόμενες στάθμες, οι οποίες φαίνονται στο ενεργειακό διάγραμμα του Σχήματος xiii.



Σχήμα xiii Ενεργειακό διάγραμμα του συστήματος $d+^{14}\text{N}$ στο σύστημα αναφοράς μαζών

Ο προσδιορισμός του λόγου παχών $N_{\text{Au}}/N_{\text{N}}^{\text{nat}}$ προσδιορίστηκε με χρήση της τεχνικής p-EBS για τις ενέργειες πρωτονίων 980, 1200 και 1300 keV. Η χρήση της συγκεκριμένης τεχνικής προτιμήθηκε εφόσον οι τιμές της διαφορικής ενεργού διατομής της ελαστικής σκέδασης των πρωτονίων από άζωτο έχει αξιολογημένα και benchmarked δεδομένα [22]. Η τελική τιμή του λόγου $N_{\text{Au}}:N_{\text{nat}_N}$ ήταν 0.0423 ± 0.0011 , δηλαδή είχε σχετικό στατιστικό σφάλμα 2.6%.

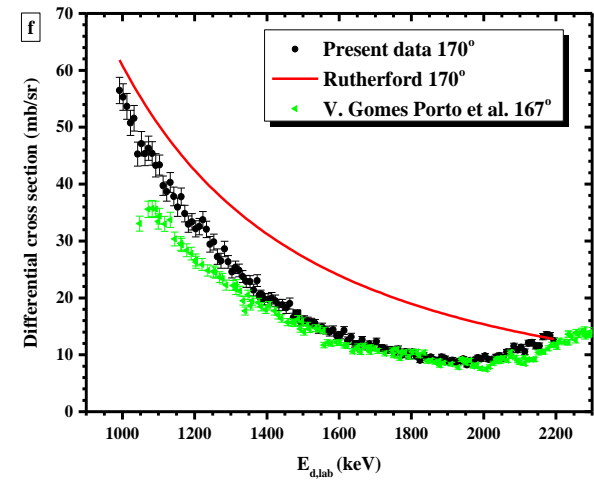
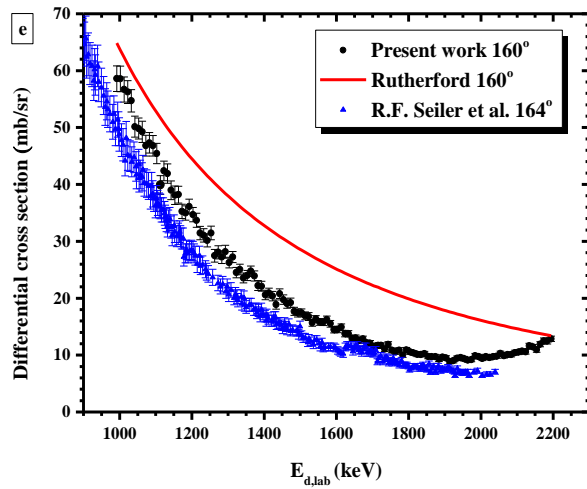
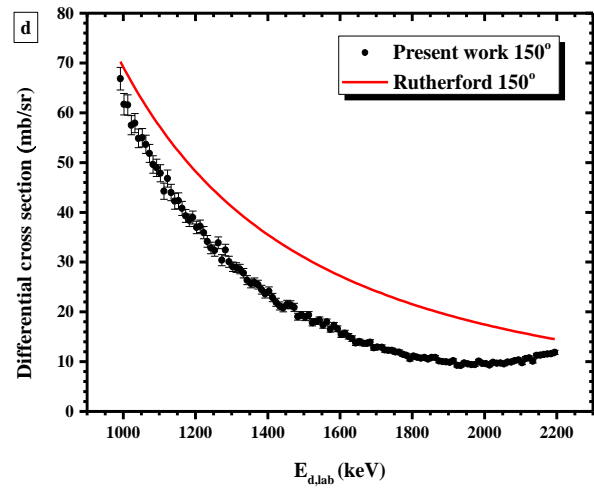
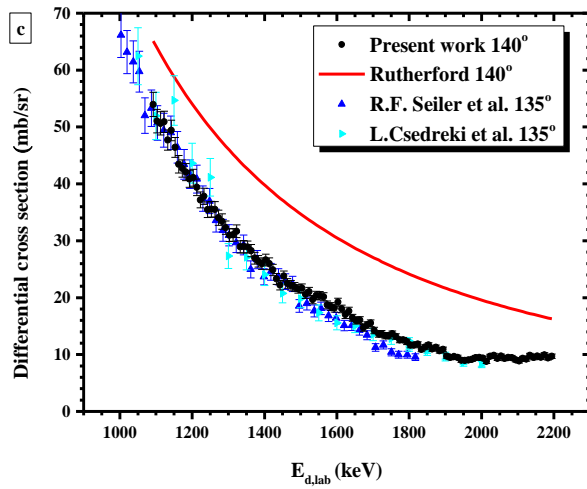
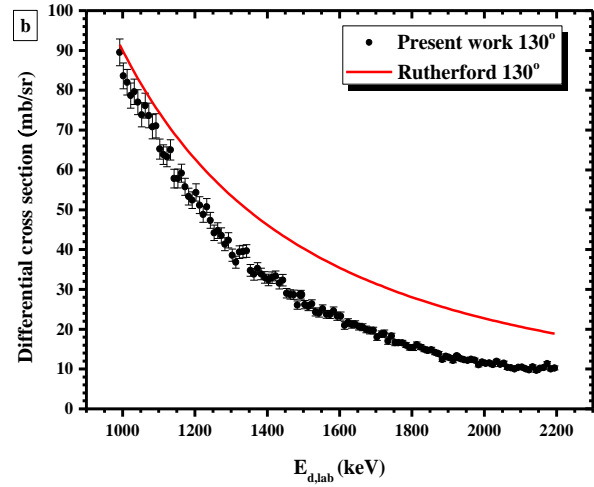
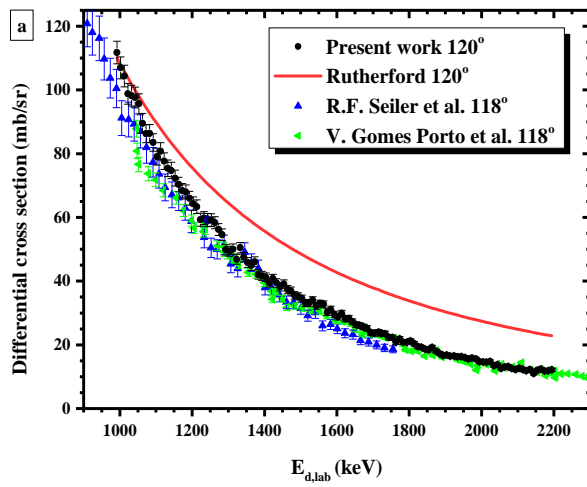


Σχήμα xiv Πειραματικό και προσομοιωμένο φάσμα πρωτονίων ενέργειας 1300 keV για την γωνία σκέδασης των 170° ώστε να χαρακτηριστεί ο στόχος και να προσδιοριστούν οι τιμές της διαφορικής ενεργού διατομής της ελαστικής σκέδασης $^{nat}\text{N}(d,d_0)^{nat}\text{N}$.

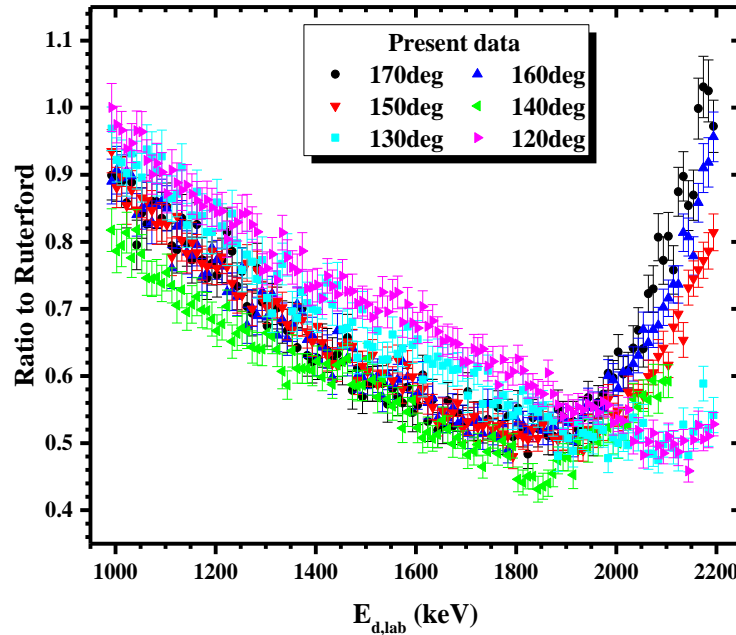
Οι τελικές τιμές της διαφορικής ενεργού διατομής της ελαστικής σκέδασης δευτερίων από ^{nat}N παρουσιάζονται στο Σχήμα xv a-f για το ενεργειακό εύρος 1000 – 2200 keV με βήματα ~ 10 keV και για τις γωνίες σκέδασης 120° , 130° , 140° , 150° , 160° και 170° . Οι συνολικές σχετικές στατιστικές αβεβαιότητες δεν ξεπερνούν το 5.3% για όλες τις περιπτώσεις. Οι συστηματικές αβεβαιότητες σχετικά με τις διαφορές των θεωρητικών και των πειραματικών δεδομένων για την ισχύ ανάσχεσης σε πυρίτιο ήταν 4% ενώ για την περίπτωση του αζώτου ήταν $\sim 2.9\%$, όπως αναφέρεται στην ιστοσελίδα του SRIM. Οι αβεβαιότητες σχετικά με την ενέργεια της δέσμης ήταν 3 keV από την ενεργειακή βαθμονόμηση του επιταχυντή και 2.3-2.4 keV από τον διασκεδασμό της δέσμης μέσα στον στόχο που υπολογίστηκε.

Στο Σχήμα xv a τα μετρημένα αποτελέσματα βρίσκονται σε καλή συμφωνία για τις περισσότερες τιμές της ενέργειας, κυρίως στις υψηλές τιμές της ενέργειας με τα δεδομένα των Seiler et al. [23] και των Gomes Porto et al. [24], τα οποία είναι μετρημένα στις 118° , ενώ για τις χαμηλές ενέργειες τα προϋπάρχοντα δεδομένα παρουσιάζουν χαμηλότερες τιμές. Η ίδια κατάσταση παρουσιάζεται και στο Σχήμα xv f, δηλαδή πολύ καλή συμφωνία εντός σφαλμάτων με τα δεδομένα των Gomes Porto et al. στις 167° για τις υψηλές ενέργειες (υψηλότερες από 1500 keV), ενώ για τις χαμηλότερες ενέργειες οι αποκλίσεις αυξάνονται. Στο σχήμα xv b, η κατάσταση είναι αντίστροφη δηλαδή υπάρχει συμφωνία εντός σφαλμάτων με τα δεδομένα Seiler et al. για τις χαμηλές ενέργειες ενώ για τις υψηλές ενέργειες τα δεδομένα των Seiler et al. παρουσιάζουν τιμές συστηματικά χαμηλότερες. Για την γωνία σκέδασης των 160° , τα δεδομένα των Seiler et al., μετρημένα στις 164° , είναι συστηματικά πιο χαμηλά σε όλο το υπό μελέτη ενεργειακό εύρος. Στην γωνία των 140° , η συμφωνία με τα δεδομένα των Csedreki et al. [25] είναι εντός σφαλμάτων, όπως φαίνεται στο Σχήμα xv c. Σε περιπτώσεις όπου χρησιμοποιούνται αέριοι στόχοι και η απόλυτη μέθοδος για τον προσδιορισμό της ενεργού διατομής, όπως συνέβη στις περιπτώσεις [23] και [24], οι αβεβαιότητες που προκύπτουν είναι μεγαλύτερες. Αντίθετα, στην παρούσα εργασία, όπου χρησιμοποιήθηκε στερεός στόχος και η σχετική μέθοδος μέτρησης, προσδιορίστηκαν συστηματικά δεδομένα για τον υπολογισμό των οποίων είχε εξαλειφθεί η αβεβαιότητα της παραμέτρου $Q \times \Omega$ και είχαν περιοριστεί οι συστηματικές αβεβαιότητες που προκύπτουν από το προσδιορισμό του πάχους του στόχου.

Η επίδραση του σύνθετου μηχανισμού αντίδρασης μελετάται μέσω του Σχήματος xvi όπου εξετάζονται οι λόγοι των διαφορικών ενεργών διατομών της ελαστικής σκέδασης δευτερίων σε άζωτο ως προς τις αντίστοιχες Rutherford τιμές. Παρατηρείται ότι οι μετρημένες τιμές των διαφορικών ενεργών διατομών είναι χαμηλότερα από τις αντίστοιχες Rutherford τιμές σε όλο το ενεργειακό εύρος υπό μελέτη, αν και υπάρχει μια αυξητική τάση στις υψηλές ενέργειες και για τις πιο πίσω γωνίες σκέδασης. Αυτή η συμπεριφορά θα μπορούσε να αποδοθεί στις πολλές επικαλυπτόμενες στάθμες του σύνθετου πυρήνα στην περιοχή μελέτης αλλά και στις ενεργειακά κοντινές περιοχές, οποίες φαίνονται στο Σχήμα xiii. Η επίδραση αυτών των επικαλυπτόμενων στάθμων θα μπορούσε να οδηγήσει σε απουσία έντονων ελαχίστων και μέγιστων στη συμπεριφορά της ενεργού διατομής με ισχυρή εξάρτηση από την γωνία, όπως φαίνεται στο Σχήμα xvi, για υψηλές ενέργειες και πίσω γωνίες σκέδασης.



Σχήμα xv a-f Τιμές της διαφορικής ενεργού διατομής (mb/sr) της ελαστικής σκέδασης $^{14}\text{N}(d,d_0)^{14}\text{N}$, οι οποίες μετρήθηκαν στο ενεργειακό εύρος $E_{d,\text{lab}} \sim 1000\text{--}2200$ keV και για τις γωνίες σκέδασης 120° , 130° , 140° , 150° , 160° and 170° , με ενεργειακά βήματα ~ 20 keV, μαζί με τα δεδομένα που υπάρχουν στην βιβλιογραφία.



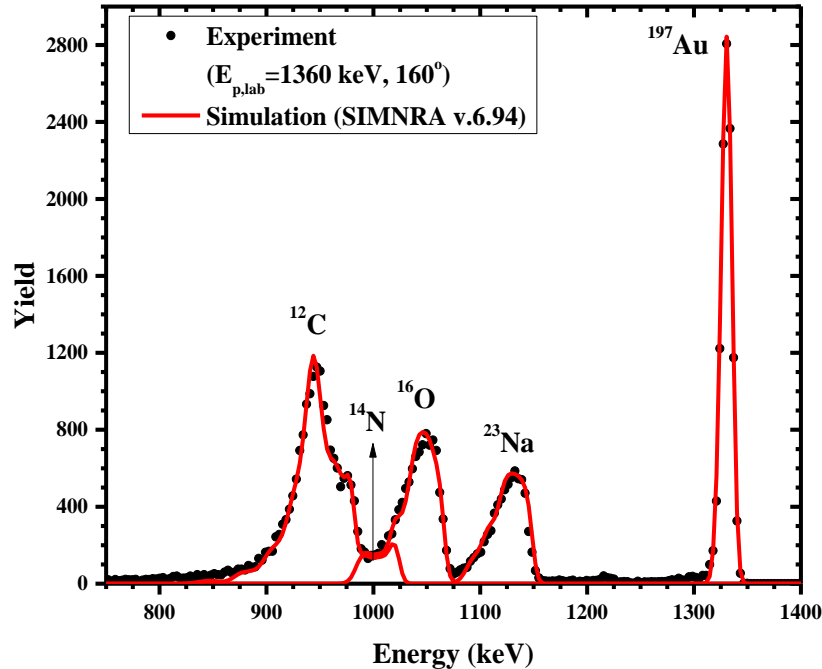
Σχήμα xvi Λόγος των διαφορικών ενεργών διατομών που μετρήθηκαν για την ελαστική σκέδαση $^{14}\text{N}(d,d_0)^{14}\text{N}$ ως προς τις αντίστοιχες τιμές Rutherford στο ενεργειακό εύρος δευτερίων 1000-2200 keV για όλες τις γωνίες σκέδασης που μετρήθηκαν.

Υπολογισμός διαφορικής ενεργού διατομής της ελαστικής σκέδασης $^{23}\text{Na}(d,d_0)^{23}\text{Na}$

Η διαφορική ενεργός διατομή της ελαστικής σκέδασης δευτερίων από ^{23}Na μελετήθηκε στο ενεργειακό εύρος $E_{d,\text{lab}} = 1060\text{--}2400$ keV με βήματα $\sim 20\text{--}30$ keV και για τις γωνίες σκέδασης 140° , 150° , 160° and 170° . Στο ενεργειακό εύρος που μελετήθηκε δεν υπάρχουν γνωστές στάθμες στον σύνθετο πυρήνα που δημιουργείται ^{25}Mg .

Ο λόγος παχών $^{197}\text{Au}:^{23}\text{Na}$ προσδιορίστηκε μέσω της τεχνικής p-EBS όπου φάσματα πρωτονίων πάρθηκαν στις ενέργειες $E_{p,\text{lab}} = 1200, 1360, 1430$ keV και για τις γωνίες σκέδασης 170° , 160° and 150° , ώστε να αποφευχθούν αβεβαιότητες εξαιτίας του διασκεδασμού της δέσμης μέσα στον στόχο. Η τιμή του λόγου $N_{t,\text{Au}}/N_{t,\text{Na}}$ υπολογίστηκε ίση με 0.038 ± 0.001 , δηλαδή παρουσιάζει σχετικό στατιστικό σφάλμα 2.6%. Αξίζει να σημειωθεί εδώ ότι το φάσμα σε ενέργεια 1200 keV και για γωνία σκέδασης 150° δεν συμπεριλήφθηκε στον υπολογισμό του λόγου παχών του στόχου εφόσον παρουσιάστηκε μια μερική επικάλυψη μεταξύ των ελαστικών κορυφών του νατρίου και

του οξυγόνου. Τα αποτελέσματα αυτής της διαδικασίας φαίνονται στο Σχήμα xvii για την ενέργεια πρωτονίων 1360 keV και για την γωνία σκέδασης των 160°.

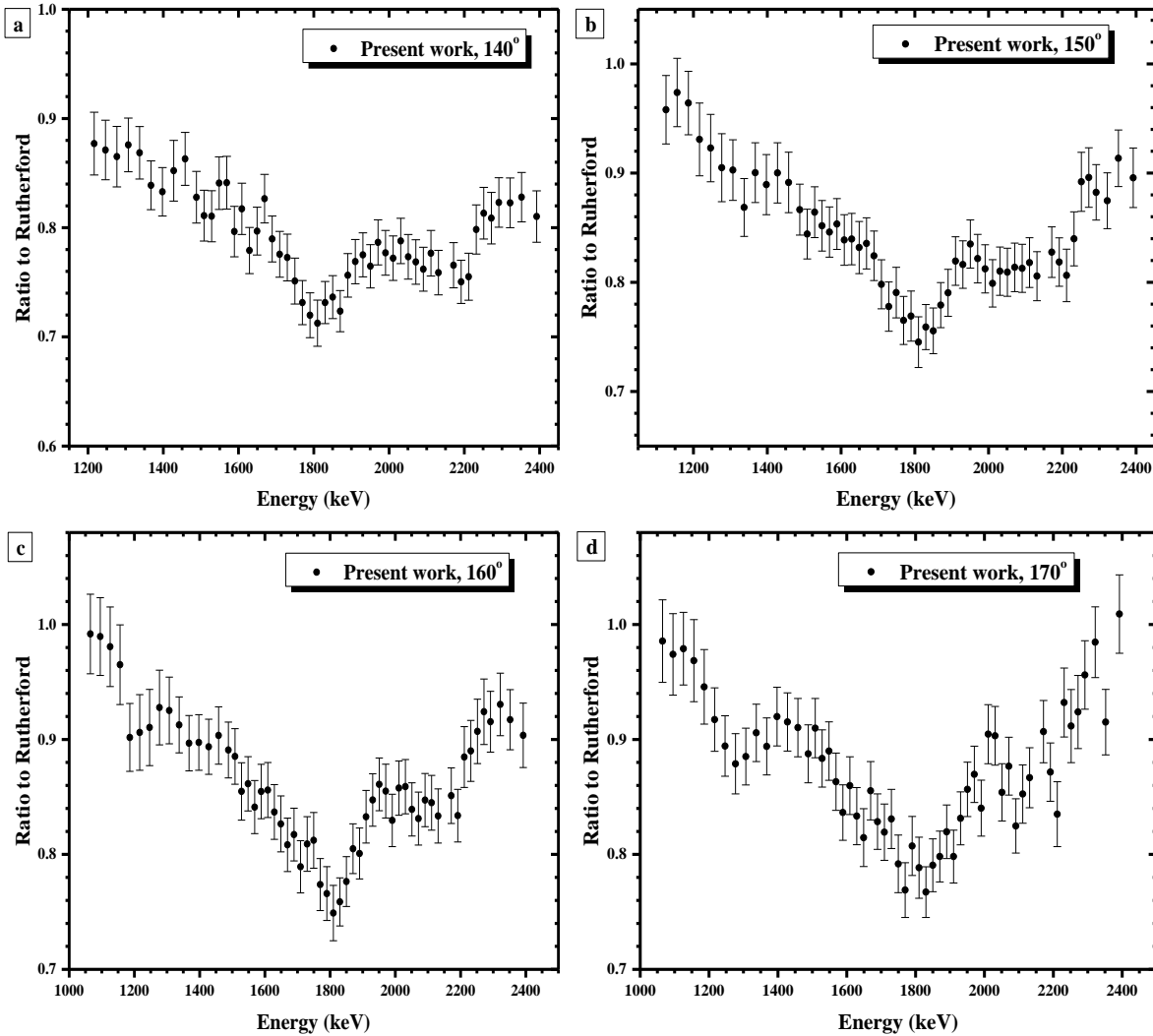


Σχήμα xvii Πειραματικό και προσομοιωμένο φάσμα πρωτονίων, το οποίο αποκτήθηκε για τον προσδιορισμό του λόγου των παχών, σε ενέργεια 1360 keV και γωνία σκέδασης 160° μαζί με την αναγνώριση των αντίστοιχων κορυφών.

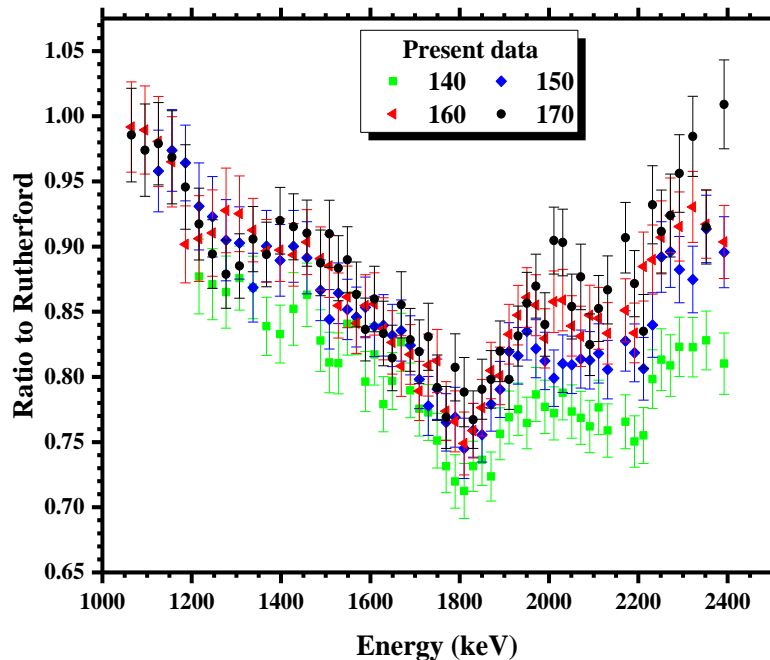
Ο λόγος των διαφορικών ενεργών διατομών της ελαστικής σκέδασης δευτερίων σε ^{23}Na ως προς τις αντίστοιχες τιμές Rutherford στο ενεργειακό εύρος 1060–2400 keV με βήμα $\sim 20\text{--}30$ keV για τις τέσσερις μετρημένες γωνίες 140°, 150°, 160° and 170° παρουσιάζεται σε γραφική μορφή στα Σχήματα xviii a-d. Τα συνολικά σχετικά στατιστικά σφάλματα δεν ξεπέρασαν το $\sim 4\%$ σε όλες τις περιπτώσεις. Οι συστηματικές αβεβαιότητες που οφείλονται στις διαφορές μεταξύ των πειραματικών και των θεωρητικών τιμών της ισχύς ανάσχεσης ήταν 3.6% για την περίπτωση του χρυσού ενώ για την περίπτωση του νατρίου είναι άγνωστες. Εξετάζοντας τους γειτονικούς πυρήνες, δηλαδή το νέον και το αλουμίνιο διαφορές μέχρι 2.8% παρουσιάζονται. Οι αβεβαιότητες στην ενέργεια της δέσμης προσδιορίστηκαν ως ~ 3 keV από την βαθμονόμηση του επιταχυντή και 5.1 keV από τον ενεργειακό διασκεδασμό της δέσμης στον προσδιορισμένο στόχο.

Ισχυρές αποκλίσεις παρατηρούνται στα Σχήματα xviii a-d σε σχέση με τις αντίστοιχες Rutherford τιμές, ειδικά σε υψηλές ενέργειες δευτερίων όπου οι μετρούμενες τιμές σε κάποιες περιπτώσεις φτάνουν μέχρι και 35% χαμηλότερα από την Rutherford. Παρόμοια συμπεριφορά είχε παρατηρηθεί και στην περίπτωση της ελαστικής σκέδασης $^{nat}\text{N}(d,d_0)^{nat}\text{N}$, όπου οι μετρημένες τιμές ήταν χαμηλότερα από τις αντίστοιχες Rutherford τιμές σε όλη την ενεργειακή περιοχή

μελέτης. Στα σχήματα xviii a-d παρατηρείται επίσης ένα ελάχιστο σε ενέργεια ~ 1800 keV. Εξαιτίας της απουσίας ενεργειακών στάθμων στον σύνθετο πυρήνα ^{25}Mg , η παρουσία αυτού του ελάχιστου δεν μπορεί ξεκάθαρα να συσχετιστεί με συντονισμό κάποια στάθμης του σύνθετου πυρήνα. Από το Σχήμα xix, όπου έχουν παρασταθεί γραφικά όλες οι γωνίες σκέδασης, παρατηρείται ότι η γωνιακή κατανομή είναι ομαλή.



Σχήμα xviii Λόγος των διαφορικών ενεργών διατομών της ελαστικής σκέδασης $^{23}\text{Na}(d,d_0)^{23}\text{Na}$ ως προς τις αντίστοιχες τιμές Rutherford στο ενεργειακό εύρος 1060-2400 keV με βήμα ~ 20 -30 keV και για τις τέσσερις μετρημένες γωνίες 140° , 150° , 160° and 170° . Οι τιμές της συνολικής στατιστικής αβεβαιότητας περιλαμβάνονται στα γραφήματα.

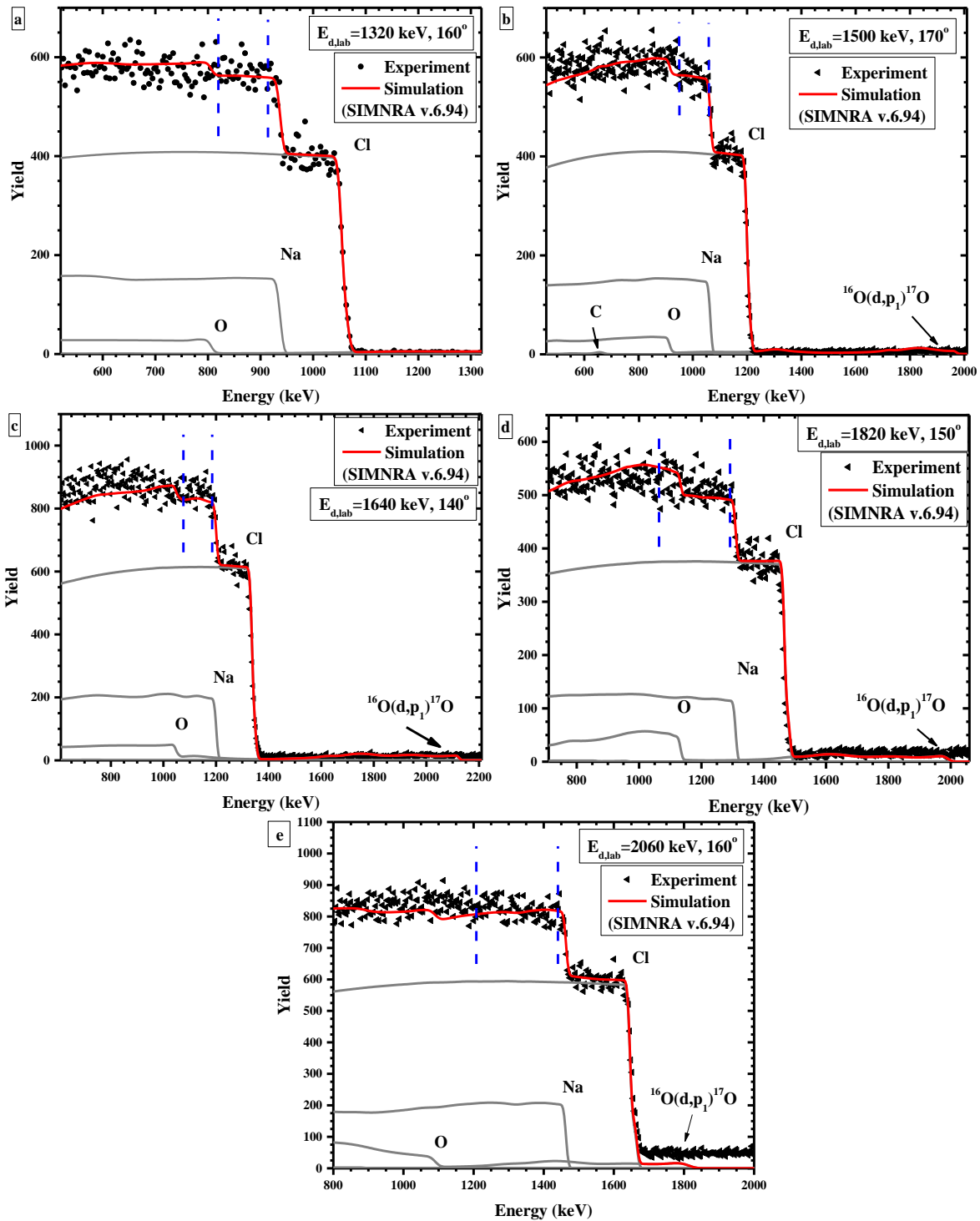


Σχήμα xix Λόγος των διαφορικών ενεργών διατομών της ελαστικής σκέδασης $^{23}\text{Na}(d,d_0)^{23}\text{Na}$ ως προς τις αντίστοιχες τιμές Rutherford στο ενεργειακό εύρος δευτερίων 1060-2400 keV και για όλες τις γωνίες σκέδασης που μετρήθηκαν.

Έλεγχος αξιοπιστίας για την ελαστική σκέδαση $^{\text{nat}}\text{Si}(d,d_0)^{\text{nat}}\text{Si}$

Ο έλεγχος αξιοπιστίας (benchmarking) των διαφορικών ενεργών διατομών που προσδιορίστηκαν για την ελαστική σκέδαση δευτερίων από ^{23}Na πραγματοποιήθηκε ακτινοβολώντας έναν παχύ στόχο NaCl με δευτέρια ενεργειών $E_{d,\text{lab}}=1110, 1320, 1500, 1640, 1820, 2060$ και 2300 keV για όλες τις γωνίες σκέδασης που μετρήθηκαν, δηλαδή $140^\circ, 150^\circ, 160^\circ$ and 170° . Για την προσομοίωση των φασμάτων παχέος στόχου χρησιμοποιήθηκαν Rutherford τιμές της διαφορικής ενεργού διατομής για τα ισότοπα του χλωρίου (^{35}Cl και ^{37}Cl) μαζί με την διόρθωση για το φαινόμενο του screening στο πρόγραμμα SIMNRA. Για την παρασιτική συνεισφορά του οξυγόνου και του άνθρακα χρησιμοποιήθηκαν αξιολογημένα δεδομένα από το SigmaCalc 2.0, για τις ελαστικές σκεδάσεις, $^{12}\text{C}(d,d_0)^{12}\text{C}$ και $^{16}\text{O}(d,d_0)^{16}\text{O}$ αλλά και για τις αντιδράσεις $^{16}\text{O}(d,p_1)^{17}\text{O}$ και $^{16}\text{O}(d,a_0)^{14}\text{N}$. Οι παρασιτικές αυτές συνεισφορές του άνθρακα και ειδικά του οξυγόνου είναι αναπόφευκτες εξαιτίας της υδροσκοπικής φύσης της σκόνης NaCl. Ωστόσο, η επιλογή αυτής της σκόνης αποτελεί μια συνετή επιλογή καθώς αν επιλέγοντας ένας στόχος που περιέχει κάποιο στοιχείο με μεγάλο ατομικό αριθμό π.χ. NaBr ή NaI – ή ενώσεις με οξυγόνο στον χημικό τους τύπο π.χ. Na_2O ή NaOH, τότε το στοιχείο με τον μεγάλο ατομικό αριθμό θα δημιουργούσε σημαντικό υπόβαθρο κάτω από την συνεισφορά του Na, οδηγώντας σε υψηλότερη στατιστική αβεβαιότητα. Το ίδιο ισχύει και για την συνεισφορά των καναλιών αντίδρασης στην περίπτωση του οξυγόνου.

Η διαδικασία benchmarking ξεκίνησε με τον προσδιορισμό της σύστασης του στόχου. Αυτό πραγματοποιήθηκε χρησιμοποιώντας το πειραματικό φάσμα που αντιστοιχεί στην ενέργεια 1110 keV και στην γωνία σκέδασης 170° καθώς το νάτριο ακολουθεί την σκέδαση Rutherford εντός 2-3%. Έπειτα προσομοιώθηκαν όλα τα πειραματικά φάσματα και ο παράγοντας $Q \times \Omega$ προσδιορίστηκε χρησιμοποιώντας την συνεισφορά του χλωρίου, για κάθε συνδυασμό ενέργειας δέσμης/γωνία σκέδασης. Μερικά παραδείγματα φαίνονται στα Σχήματα xx a-e για διαφορετικούς συνδυασμούς ενέργεια δέσμης/γωνία σκέδασης. Όπως γίνεται φανερό στα σχήματα, η παρουσία του οξυγόνου μέσω της αντίδρασης $^{16}\text{O}(d,p_1)^{17}\text{O}$ προκαλεί σημαντικό υπόβαθρο, ιδιαίτερα για υψηλότερες ενέργειες δέσμης, ενώ η αντίδραση $^{16}\text{O}(d,p_1)^{17}\text{O}$ παρουσιάζει συντονισμούς σε όλο το εύρος μελέτης. Επομένως, αποκλείονται από την διαδικασία του benchmarking οι ενέργειες 1640 keV and 2060 keV όπου η συνεισφορά της αντίδρασης $^{16}\text{O}(d,p_1)^{17}\text{O}$ είναι ιδιαίτερα σημαντική κάτω από το σκαλοπάτι του νατρίου, καθώς και όλες οι ενέργειες πάνω από τα 2000 keV όπου η συνεισφορά της αντίδρασης $^{16}\text{O}(d,p_1)^{17}\text{O}$ είναι αρκετά μικρή και δεν μπορεί να αναπαράξει ικανοποιητικά το πειραματικό φάσμα. Αυτό υποδεικνύει πιθανή συνεισφορά από τα κανάλια αντίδρασης $^{23}\text{Na}(d,p_x)^{24}\text{Na}$. Το παράθυρο ολοκλήρωσης, στο οποίο πραγματοποιείται σύγκριση ανάμεσα στον προσομοιωμένο και τον πειραματικό αριθμό σωματιδίων τα οποία έχουν σκεδαστεί από νάτριο (τα σωματίδια που έχουν σκεδαστεί από οξυγόνο και χλώριο αφαιρέθηκαν), είναι μαρκαρισμένο στα Σχήματα xx a-e με μπλε διακεκομμένη γραμμή και περιλαμβάνει ~180 keV (~60 κανάλια) από την άκρη του σκαλοπατιού του νατρίου. Τα αποτελέσματα της διαδικασίας benchmarking μέσα στο παράθυρο ολοκλήρωσης παρουσιάζονται στον Πίνακα II. Η μεγαλύτερη διαφορά ήταν 13.6% για την ενέργεια 1320 keV και την γωνία σκέδασης 170° . Ωστόσο, αυτοί οι αριθμοί υποδεικνύουν μια ικανοποιητική συμφωνία καθώς πρέπει να ληφθεί υπόψιν ότι αυτοί οι αριθμοί συμπεριλαμβάνουν τυχόν αβεβαιότητες της αντίδρασης $^{16}\text{O}(d,p_1)^{17}\text{O}$, η οποία έστω και μερικώς, συμπεριλαμβάνεται στο παράθυρο ολοκλήρωσης. Οι αριθμοί του Πίνακα II δεν δείχνουν κάποια συστηματικότητα και επομένως δεν πραγματοποιήθηκε κανονικοποίηση των τελικών τιμών της διαφορικής ενεργού διατομής.



Σχήμα xx a-e Τυπικά πειραματικά και προσομοιωμένα φάσματα παχέος στόχου (NaCl) για διαφορετικούς συνδυασμούς ενέργεια δέσμης/γωνία σκέδασης μαζί με την αναγνώριση των αντίστοιχων συνεισφορών. Οι μπλε διακεκομμένες γραμμές παριστάνουν τα παράθυρα ολοκλήρωσης τα οποία περιλαμβάνουν ~180 keV (~60 κανάλια).

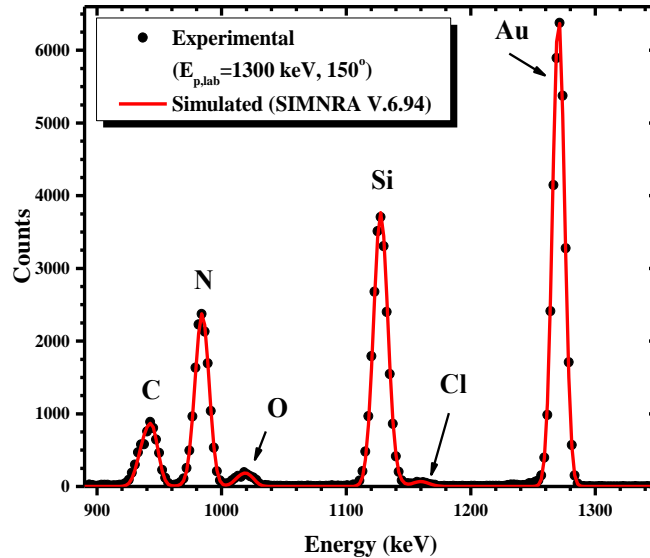
Energy (keV)	140°	150°	160°	170°
1110	-	-	+6.7	-
1320	-13.1	-12.9	+1.2	-13.6
1500	-11.4	-9.9	-7.6	-3.0
1820	-12.6	-12.0	+6.5	-10.4

Πίνακας II Διαφορές (επί %) μεταξύ του προσομοιωμένου και του πειραματικού αριθμού σωματιδίων εντός του παράθυρου ολοκλήρωσης για κάθε συνδυασμό ενέργεια δέσμης/γωνία σκέδασης. Οι αρνητικές τιμές αντιστοιχούν σε χαμηλότερη τιμή του ολοκληρώματος του πειραματικού αριθμού σωματιδίων ενώ οι θετικές τιμές αντιστοιχούν σε μεγαλύτερη τιμή του πειραματικού αριθμού σωματιδίων μέσα στο παράθυρο ολοκλήρωσης.

Υπολογισμός διαφορικής ενεργού διατομής της ελαστικής σκέδασης $^{23}\text{Na}(d,d_0)^{23}\text{Na}$

Η διαφορική ενεργός διατομή της ελαστικής σκέδασης δευτερίων σε ^{nat}Si μελετήθηκε στο ενεργειακό εύρος $E_{d,lab} = 1000 - 2200$ keV σε βήματα 10 keV και για τις γωνίες σκέδασης 120°, 130°, 140°, 150°, 160° και 170°.

Ο λόγος παχών $N_{t,Au}:N_{t,Si}$ υπολογίστηκε χρησιμοποιώντας την τεχνική p-EBS, μέσω φασμάτων πρωτονίων σε ενέργειες 1200 και 1300 keV και σε έξι γωνίες οπισθοσκέδασης (120°, 130°, 140°, 150°, 160°, 170°). Για την ανάλυση των φασμάτων πρωτονίων χρησιμοποιήθηκαν διαφορικές ενεργές διατομές Rutherford για την ελαστική σκέδαση του ^{197}Au ενώ για την ελαστική σκέδαση δευτερίων σε ^{12}C , ^{nat}N [26], ^{16}O και ^{nat}Si [27], χρησιμοποιήθηκαν αξιολογημένες τιμές της διαφορικής ενεργού διατομής οι οποίες αποκτήθηκαν από το SigmaCalc 2.0. Η μέση τιμή του λόγου $N_{t,Au}:N_{t,Si}$ προσδιορίστηκε ίση με 0.0431 ± 0.0005 δηλαδή με σχετικό στατιστικό σφάλμα 1.1%. Η προσομοίωση του πειραματικού φάσματος φαίνεται στο Σχήμα xxι για την ενέργεια πρωτονίων 1300 keV και για την γωνία σκέδασης 150°.

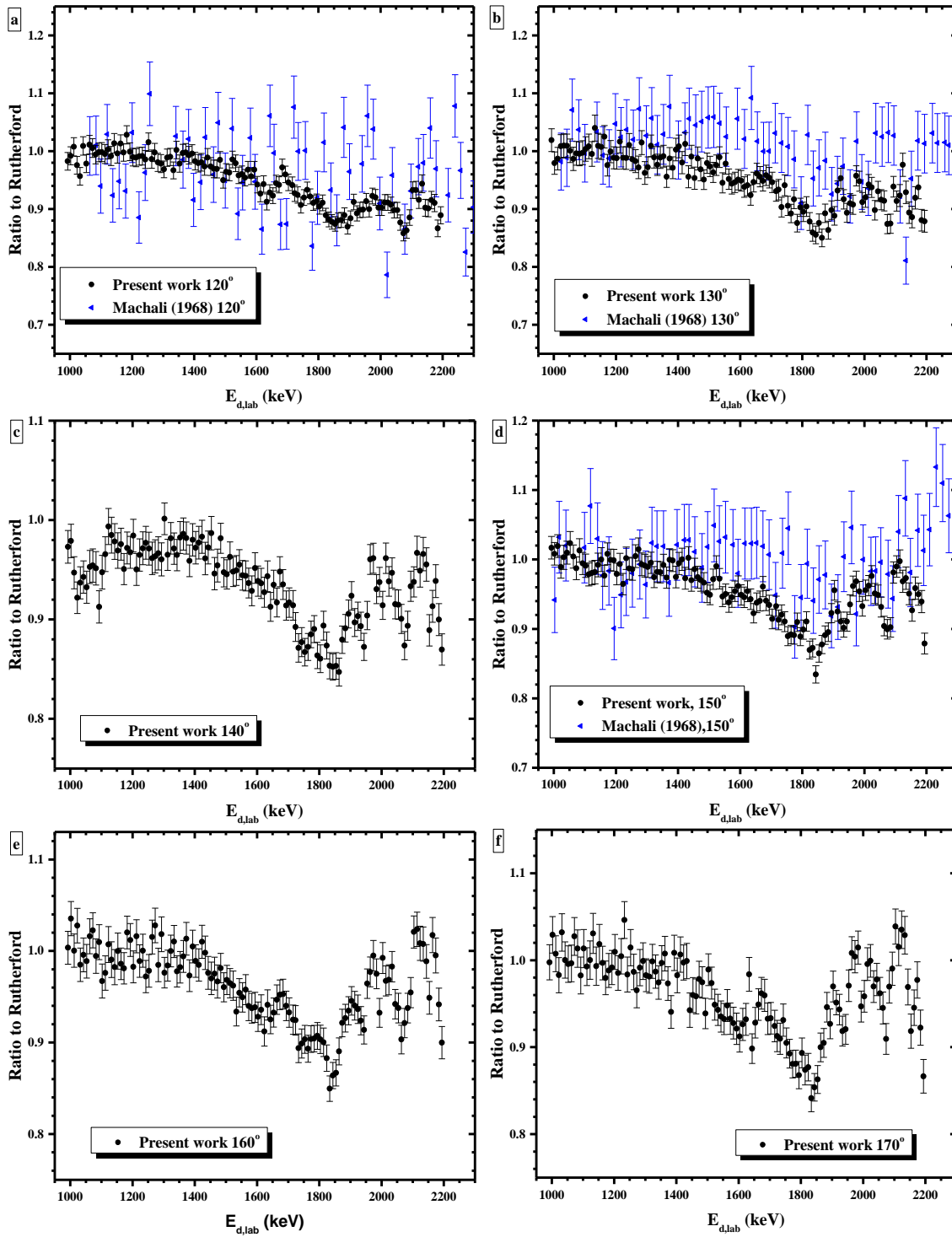


Σχήμα χxi Πειραματικό και προσομοιωμένο φάσμα πρωτονίων σε ενέργεια 1300 keV και για την γωνία σκέδασης 150° μαζί με την αναγνώριση των αντίστοιχων κορυφών.

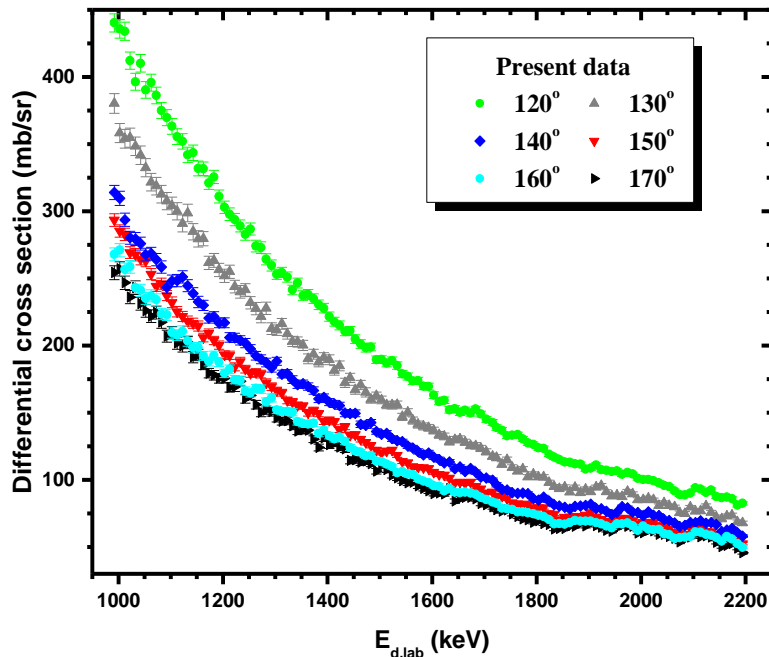
Ο λόγος των τιμών της διαφορικής ενεργού διατομής της ελαστικής σκέδασης δευτερίων από ^{nat}Si ως προς τις αντίστοιχες τιμές Rutherford παριστάνεται γραφικά στα Σχήματα χxii a-f στο ενεργειακό εύρος 1000-2200 keV με βήματα 10 keV και για τις γωνίες σκέδασης 120°, 130°, 140°, 150°, 160° και 170° are presented. Στα Σχήματα χxii a-f συμπεριλαμβάνονται επίσης τα προϋπάρχοντα δεδομένα της βιβλιογραφίας ώστε να συγκριθούν με τα παρόντα αποτελέσματα και τα συνολικά στατιστικά σφάλματα των αποτελεσμάτων. Τα συνολικά σχετικά στατιστικά σφάλματα των αποτελεσμάτων δεν ξεπερνούν το 2.3% σε όλες τις περιπτώσεις. Τα συστηματικά σφάλματα που οφείλονται στις διαφορές μεταξύ θεωρητικών και πειραματικών τιμών της ισχύος ανάσχεσης είναι ~4% για πρωτόνια που προσπίπτουν σε πυρίτιο και 3.6% για πρωτόνια που προσπίπτουν σε χρυσό, όπως αναφέρεται στην ιστοσελίδα του SRIM. Οι αβεβαιότητες στην ενέργεια της δέσμης που προκύπτουν από την διαδικασία της βαθμονόμησης του επιταχυντή ήταν ~3 keV και η αβεβαιότητα λόγω του ενεργειακού διασκεδασμού της δέσμης μέσα στο στόχο που προσδιορίστηκε με την τεχνική p-EBS ήταν ~2.4 keV. Αυτές οι δύο τιμές προστίθενται τετραγωνικά και έχουν ως αποτέλεσμα συνολική αβεβαιότητα στο x-άξονα ίση με 4 keV σε όλες τις περιπτώσεις.

Για τις κοινές γωνίες (120°, 130°, 150°) με τα δεδομένα των Machali et al. [20] παρατηρείται καλή συμφωνία στην περιοχή χαμηλών ενεργειών (μέχρι 1400 keV), ενώ για τις υψηλότερες ενέργειες παρατηρούνται αποκλίσεις με τα δεδομένα των Machali et al. να εμφανίζουν συστηματικά υψηλότερες τιμές. Η αιτία αυτών των αποκλίσεων δεν είναι ξεκάθαρη, ωστόσο μπορεί να σχετίζεται με ζητήματα σχετικά με τον στόχο. Οι αποκλίσεις των παρόντων αποτελεσμάτων από τις αντίστοιχες τιμές Rutherford είναι μικρές στην περιοχή χαμηλών ενεργειών (μέχρι ~1600 keV) ενώ για υψηλότερες ενέργειες οι αποκλίσεις μεγαλώνουν με τα παρόντα αποτελέσματα να

εμφανίζουν χαμηλότερες τιμές. Εξαιτίας του γεγονότος ότι δεν υπάρχει καμία πληροφορία για τις ενεργειακές στάθμες του σύνθετου πυρήνα στην περιοχή μελέτης δεν μπορούμε να συσχετίσουμε την συμπεριφορά της διαφορικής ενεργού διατομής με το μηχανισμό σύνθετου πυρήνα. Εξετάζοντας την γωνιακή εξάρτηση μέσω του Σχήματος xxiii, για ενέργειες μεγαλύτερες των ~1800 keV, εκδηλώνεται μια ξεκάθαρη γωνιακή συσχέτιση όπου η γωνία 170° παρουσιάζει τις υψηλότερες τιμές της ενεργού διατομής ενώ η γωνία 120° παρουσιάζει τις χαμηλότερες τιμές και όλες οι ενδιάμεσες γωνίες παρουσιάζουν τιμές που περιλαμβάνονται στις ακραίες τιμές που ορίζουν οι γωνίες 170° και 120° .



Σχήμα xii a-f Λόγος ως προς τις αντίστοιχες τιμές Rutherford της διαφορικής ενεργού διατομής της ελαστικής σκέδασης δευτερίων από ^{nat}Si στο ενεργειακό εύρος 1000-2200 keV σε βήματα 10 keV για τις γωνίες σκέδασης 120° , 130° , 140° , 150° , 160° , 170° μαζί με τα προϋπάρχοντα δεδομένα στην βιβλιογραφία..

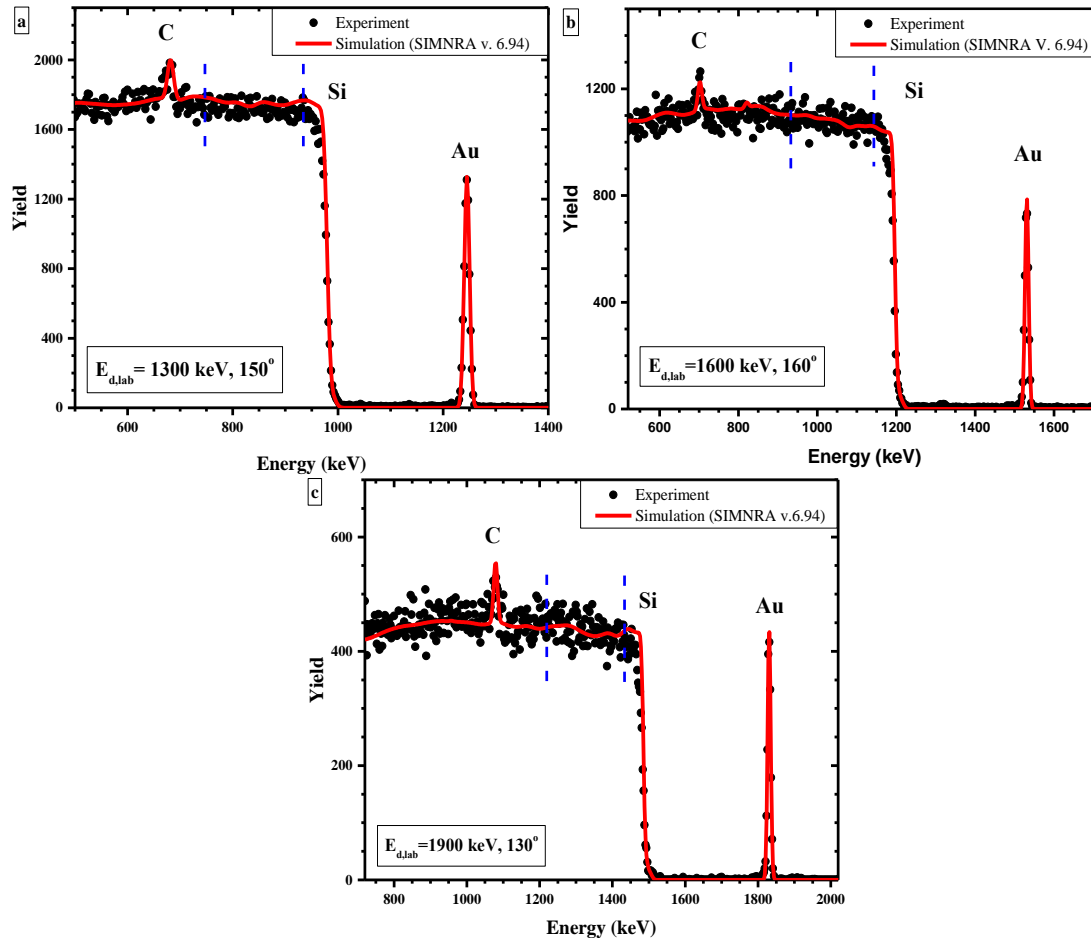


Σχήμα xxiii Τιμές της διαφορικής ενεργού διατομής (mb/sr) της ελαστικής σκέδασης $^{nat}\text{Si}(d,d_0)^{nat}\text{Si}$ στο ενεργειακό εύρος 1060-2200 keV για όλες τις γωνίες σκέδασης που μετρήθηκαν.

Έλεγχος αξιοπιστίας για την ελαστική σκέδαση $^{23}\text{Na}(d,d_0)^{23}\text{Na}$

Για τον έλεγχο αξιοπιστίας των τιμών της διαφορικής ενεργού διατομής της ελαστικής σκέδασης δευτερίων ^{nat}Si , ακτινοβολήθηκε ένας παχύς στιλπνός κρυσταλλικός στόχος Si [111] με ένα λεπτό στρώμα χρυσού από πάνω σε τέσσερις ενέργειες (1300, 1600, 1900, 2200 keV) και για τέσσερις γωνίες (130°, 140°, 150° and 160°). Το πρώτο βήμα της διαδικασίας benchmarking ήταν να προσδιοριστεί ο στόχος, δηλαδή το πάχος του στρώματος χρυσού και τυχόν προσμίξεις. Αυτό πραγματοποιήθηκε προσομοιώνοντας το πειραματικό φάσμα ενέργειας $E_{d,lab}=1300$ keV και γωνίας σκέδασης 130° χρησιμοποιώντας Rutherford διαφορικές ενεργές διατομές για τον χρυσό και το πυρίτιο καθώς στην περίπτωση της ελαστικής σκέδασης δευτερίων από πυρίτιο ακολουθείται η σκέδαση Rutherford (εντός ~4%) σε αυτήν την ενέργεια. Αφού προσδιορίστηκε ο στόχος προσομοιώθηκαν τα υπόλοιπα φάσματα και κάποια παραδείγματα αυτής της διαδικασίας φαίνονται στο Σχήμα xxiv a-c. Θα πρέπει να σημειωθεί εδώ ότι ενέργειες υψηλότερες των 2000 keV απορρίφθηκαν καθώς η συμβολή των d-NRA αντιδράσεων ήταν σημαντική. όπως φαίνεται στα Σχήματα xxiv a-c η αναπαραγωγή των πειραματικών φασμάτων είναι πολύ καλή, με αποκλίσεις μέχρι 4-5% μέσα σε παράθυρο ολοκλήρωσης που περιλαμβάνει ~200 keV (~90 κανάλια) κάτω από την επιφάνεια του πυριτίου. below the surface of silicon, visible in the graphs.

Αναλυτικά τα αποτελέσματα βρίσκονται στον Πίνακα III. Όπως φαίνεται, η μεγαλύτερη διαφορά εντοπίζεται για την ενέργεια 1600 keV και την γωνία σκέδασης 140°. Οι αριθμοί αυτοί ωστόσο δεν υποδεικνύουν καμία αναγκαιότητα για να γίνει κάποιου είδους κανονικοποίηση στις τιμές των διαφορικών ενεργών διατομών εφόσον δεν εκδηλώνουν κάποια συστηματικότητα.



Σχήμα xxiv Πειραματικά και προσομοιωμένα φάσματα παχούς στόχου που αποκτήθηκαν σε ενέργειες και γωνίες (a) 150° και 1300 keV, (b) 160° και 1600 keV και (c) 130° και 1900 keV. Το παράθυρο ολοκλήρωσης επισημαίνεται με μπλε διακεκομμένες γραμμές και περιλαμβάνει ~230 keV (~90 κανάλια).

Energy (keV)	130°	140°	150°	160°
1300	1.2	-1.5	2.3	4.1
1600	-1.3	-5.4	1.8	0.2
1900	-0.6	-2.5	1.1	1.9

Πίνακας III Διαφορές (επί %) μεταξύ των προσομοιωμένων και των πειραματικών γεγονότων μέσα στο παράθυρο ολοκλήρωσης για κάθε συνδυασμό ενέργειας δέσμης/γωνία σκέδασης. Οι αρνητικοί αριθμοί

αντιστοιχούν σε λιγότερα προσομοιωμένα γεγονότα ενώ οι θετικές τιμές αντιστοιχούν σε περισσότερα προσομοιωμένα γεγονότα.

Μελέτη της ελαστικής σκέδασης $^{16}\text{O}(\text{d},\text{d}_0)^{16}\text{O}$

Στο παρόν κεφάλαιο μελετάται η ελαστική σκέδαση δευτερίων σε οξυγόνο. Αρχικά, περιγράφεται η μέτρηση της διαφορικής ενεργού διατομής, στη συνέχεια αναλύεται η διαδικασία του ελέγχου αξιοπιστίας και τα προβλήματα που προέκυψαν κατά την διαδικασία αυτή, και στην τελευταία ενότητα αναλύεται η θεωρητική μελέτη η οποία πραγματοποιήθηκε με τον κώδικα που αναπτύχθηκε από τον Dr. A. F. Gurbich, εφαρμόζοντας την θεωρία R-matrix μαζί με υπολογισμούς για το οπτικό μοντέλο. Η ελαστική σκέδαση των δευτερίων από οξυγόνο μελετήθηκε και θεωρητικά καθώς το οξυγόνο είναι το πιο σημαντικό στοιχείο από την άποψη εφαρμογών σε σύγκριση με τα υπόλοιπα στοιχεία που μελετήθηκαν στα πλαίσια αυτής της εργασίας.

Υπολογισμός διαφορικής ενεργού διατομής της ελαστικής σκέδασης $^{nat}\text{O}(\text{d},\text{d}_0)^{nat}\text{O}$

Η διαφορική ενεργός διατομή $^{nat}\text{O}(\text{d},\text{d}_0)^{nat}\text{O}$ μετρήθηκε στο ενεργειακό εύρος 1500 – 2500 keV με βήματα 10-20 keV και για τις γωνίες σκέδασης 130° , 140° , 150° , 160° and 170° . Το ενεργειακό διάγραμμα του σύνθετου πυρήνα που σχηματίζεται $^{18}\text{F}^*$ για το ισότοπο με την μεγαλύτερη αφθονία φαίνεται στο Σχήμα xxv. Αφού, όπως βλέπουμε στο Σχήμα xxv υπάρχουν ενεργειακές στάθμες με άγνωστα εύρη και τιμές J^π στην ενεργειακή περιοχή υπό μελέτη, τα ενεργειακά βήματα ήταν μεταβλητά και εξαρτώνταν από την ύπαρξη ενεργειακών σταθμών του σύνθετου πυρήνα ώστε να περιγραφούν με λεπτομέρεια τυχόν συντονισμοί στην δομή της διαφορικής ενεργού διατομής.

Στην συγκεκριμένη περίπτωση, εφόσον υπάρχει το θεωρητικό evaluation της ελαστικής σκέδασης $^{16}\text{O}(\text{d},\text{d}_0)^{16}\text{O}$ μέχρι την ενέργεια των 1980 keV, χρησιμοποιήθηκε στον υπολογισμό της διαφορικής ενεργού διατομής. Πιο συγκεκριμένα, για τον υπολογισμό των τελικών τιμών χρησιμοποιήθηκε η σχέση:

$$\left(\frac{d\sigma}{d\Omega}\right)_{\theta,E}^{natO} = \left(\frac{d\sigma}{d\Omega}\right)_{\theta,E'}^{Au} \times \frac{Y_{natO}}{Y_{Au}} \times F_\theta \quad (\text{xviii})$$

Ο παράγοντας κανονικοποίησης F_θ υπολογίστηκε από το ήδη υπάρχων SigmaCalc evaluation (2012) για κάθε γωνία και για όλες της τιμές ενέργειας στο διάστημα 1500 keV - 1980 keV, αντικαθιστώντας τον υπολογισμό του λόγου παχών. Πιο συγκεκριμένα, η αναλυτική διαδικασία ξεκίνησε με τον προσδιορισμό των δυο πρώτο όρων της εξίσωσης xviii, με υπολογισμό μέσω της σχέσης της σκέδασης Rutherford για τον πρώτο όρο και μέσω των πειραματικών φασμάτων για τον δεύτερο. Στη συνέχεια οι δυο πρώτοι όροι χρησιμοποιήθηκαν στο ενεργειακό διάστημα 1500-1980 keV, όπου υπάρχει ακόμα το evaluation, για τον υπολογισμό ενός παράγοντα κανονικοποίησης ώστε η πειραματική τιμή της ενεργού διατομής να συμπίπτει με την θεωρητική.

Αυτή η διαδικασία πραγματοποιήθηκε για κάθε ενέργεια (27 τιμές) και για όλες τις γωνίες. Η μέση τιμή αυτών των 27 ενεργειών αποτελεί τον παράγοντα κανονικοποίησης για κάθε γωνία. Οι τιμές αυτές, μαζί με τις αβεβαιότητες τους, παρουσιάζονται στον Πίνακα IV και συμφωνούν εντός $\pm 1\sigma$ εκτός από την τιμή των 130° , η οποία συμφωνεί εντός $\pm 2\sigma$ με αυτήν των 140° . Αυτή η τιμή εξαιρείται από τη σύγκριση των τιμών καθώς η μαθηματική διαδικασία που εξήχθησαν οι δυο πρώτοι όροι για αυτή τη γωνία ήταν λίγο διαφορετική όπως θα περιγραφεί παρακάτω. Παρόλο που η συμφωνία ήταν εντός $\pm 1\sigma$, παρατηρήθηκαν μικρές διαφορές στις μέσες τιμές (τάση μείωσης της μέσης τιμής καθώς η γωνία οπισθοσκέδασης γίνεται πιο απότομη) και επομένως προτιμήθηκε να χρησιμοποιηθεί διαφορετικός παράγοντας κανονικοποίησης για κάθε γωνία (οι τιμές του Πίνακα IV) αντί να χρησιμοποιηθεί ο ίδιος για όλες τις γωνίες σκέδασης. Αυτές οι μικρές διαφορές μπορεί να οφείλονται στο ήδη υπάρχον evaluation. Επίσης να σημειωθεί ότι οι διαφορές αυτές περιέχουν τις αβεβαιότητες της διαδικασίας ολοκλήρωσης των αντίστοιχων κορυφών (δηλαδή την επιλογή του υποβάθρου και την επιλογή των ορίων ολοκλήρωσης).

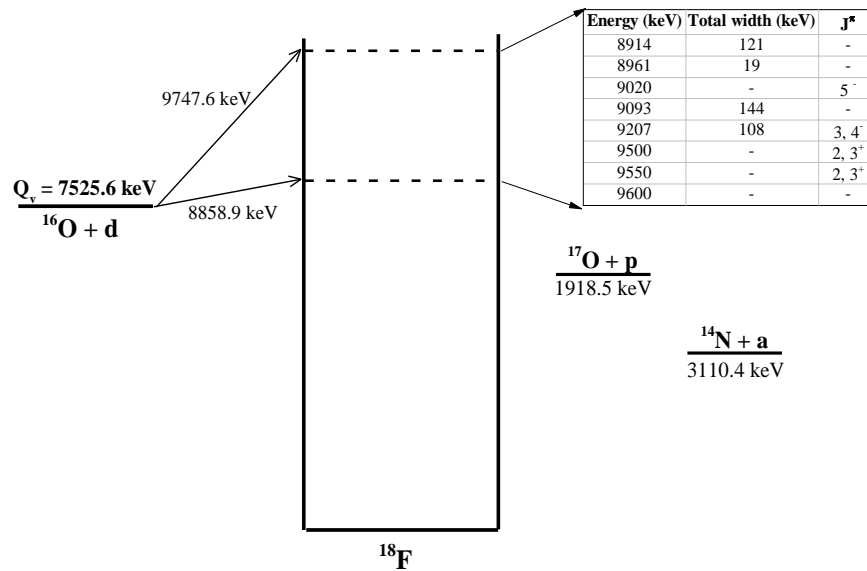
Για την γωνία σκέδασης των 130° και για χαμηλές ενέργειες η κορυφή της ελαστικής σκέδασης $^{197}\text{Au}(d,d_0)^{197}\text{Au}$ εμφάνιζε μια παρατεταμένη ουρά στην αριστερή πλευρά της κορυφής. Για να αποφευχθεί η ολοκλήρωση μια τέτοιας κορυφής, καθώς βασίζεται στον χρήστη, χρησιμοποιήθηκαν τα φάσματα των 160° μέσω της σχέσης: Therefore, a term needed to be inserted in Eq. 5.1 for the scattering angle of 130° in order to account for the different solid angle subtended by the two detectors set at 130° and 160° . This process was allowed only because the deuteron elastic scattering on gold follows the Rutherford formula and thus no anomalies are expected in the theta angular dependence. Thus, the differential cross section values for the scattering angle of 130° were calculated using the following equation:

$$\left(\frac{d\sigma}{d\Omega}\right)_{130^\circ,E}^{natO} = \left(\frac{d\sigma}{d\Omega}\right)_{160^\circ,E'}^{Au} \times \frac{Y_{oxyg,130^\circ}}{Y_{Au,160^\circ}} \times F_\theta \times \frac{\Omega_{160^\circ}}{\Omega_{130^\circ}} \quad (\text{xix})$$

Ο τελευταίος όρος εισήχθη για να συμπεριληφθεί η διαφορετική στερεά γωνία των 130° σε σχέση με τις 160° . Η χρήση αυτής της σχέσης ήταν δυνατή καθώς η ελαστική σκέδαση δευτερίων από χρυσό ακολουθεί την σκέδαση Rutherford και επομένως η μορφή της διαφορικής ενεργού διατομής είναι ομαλή. Για τον υπολογισμό του τελευταίου όρου χρησιμοποιήθηκε η σχέση:

$$\frac{\Omega_{160^\circ}}{\Omega_{130^\circ}} = \frac{\left(\frac{d\sigma}{d\Omega}\right)_{130^\circ,E}^{Au}}{\left(\frac{d\sigma}{d\Omega}\right)_{160^\circ,E}^{Au}} \times \frac{Y_{Au,160^\circ}}{Y_{Au,130^\circ}} \quad (\text{xx})$$

Για τον υπολογισμό του λόγου των στερεών γωνιών χρησιμοποιήθηκαν οι οκτώ μεγαλύτερες τιμές ενέργειας, ώστε ο διαχωρισμός των κορυφών να είναι βέλτιστος. Η τελική τιμή ήταν $\Omega_{160^\circ}/\Omega_{130^\circ} = 1.248 \pm 0.023$, δηλαδή 1.8% σχετικό σφάλμα το οποίο προέρχεται από την διαδικασία ολοκλήρωσης των κορυφών χρυσού.



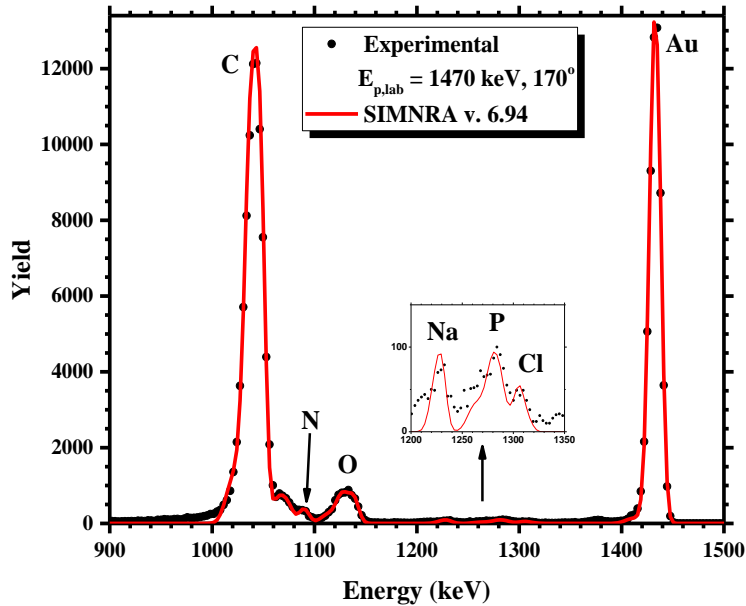
Σχήμα xxv Ενεργειακό διάγραμμα του συστήματος $d+^{16}\text{O}$ στο σύστημα αναφοράς μαζών

Scattering angle	Scaling factor	Relative uncertainty (%)
130°	0.275 ± 0.009	3.3
140°	0.248 ± 0.014	5.7
150°	0.237 ± 0.009	3.8
160°	0.231 ± 0.008	3.5
170°	0.227 ± 0.011	4.9

Πίνακας IV Τιμές του παράγοντα κανονικοποίησης για κάθε γωνία σκέδασης. Οι αβεβαιότητες για κάθε γωνία έχουν επίσης συμπεριληφθεί όπως προκύπτουν από την στατιστική μελέτη.

Το πάχος του στόχου, στην περίπτωση του οξυγόνου, ήταν απαραίτητο για τον υπολογισμό της αιώλειας ενέργειας της δέσμης μέσα στον στόχο. Για τον λόγο αυτό χρησιμοποιήθηκε η τεχνική p-EBS μέσω φάσματα πρωτονίων σε ενέργειες 1050 και 1470 keV και για γωνίες σκέδασης 160° και 170°. Για την προσομοίωση των κορυφών της ελαστικής σκέδασης δευτερίων από ^{nat}C , ^{nat}N , ^{nat}O , ^{23}Na και ^{31}P χρησιμοποιήθηκαν τα evaluated δεδομένα του SigmaCalc 2.0 ενώ για την ελαστική σκέδαση δευτερίων από Cl και Au χρησιμοποιήθηκαν οι αντίστοιχες τιμές Rutherford. Αφού χαρακτηρίστηκε ο στόχος έγινε ο υπολογισμός της απώλειας ενέργειας καθώς και του ενεργειακού διασκεδασμού της δέσμης μέσα στον στόχο για κάθε ενέργεια. Ένα τυπικό φάσμα

πρωτονίων μαζί με το προσομοιωμένο φαίνεται στο Σχήμα xxvi για την ενέργεια 1470 keV και για γωνία σκέδασης 170°.

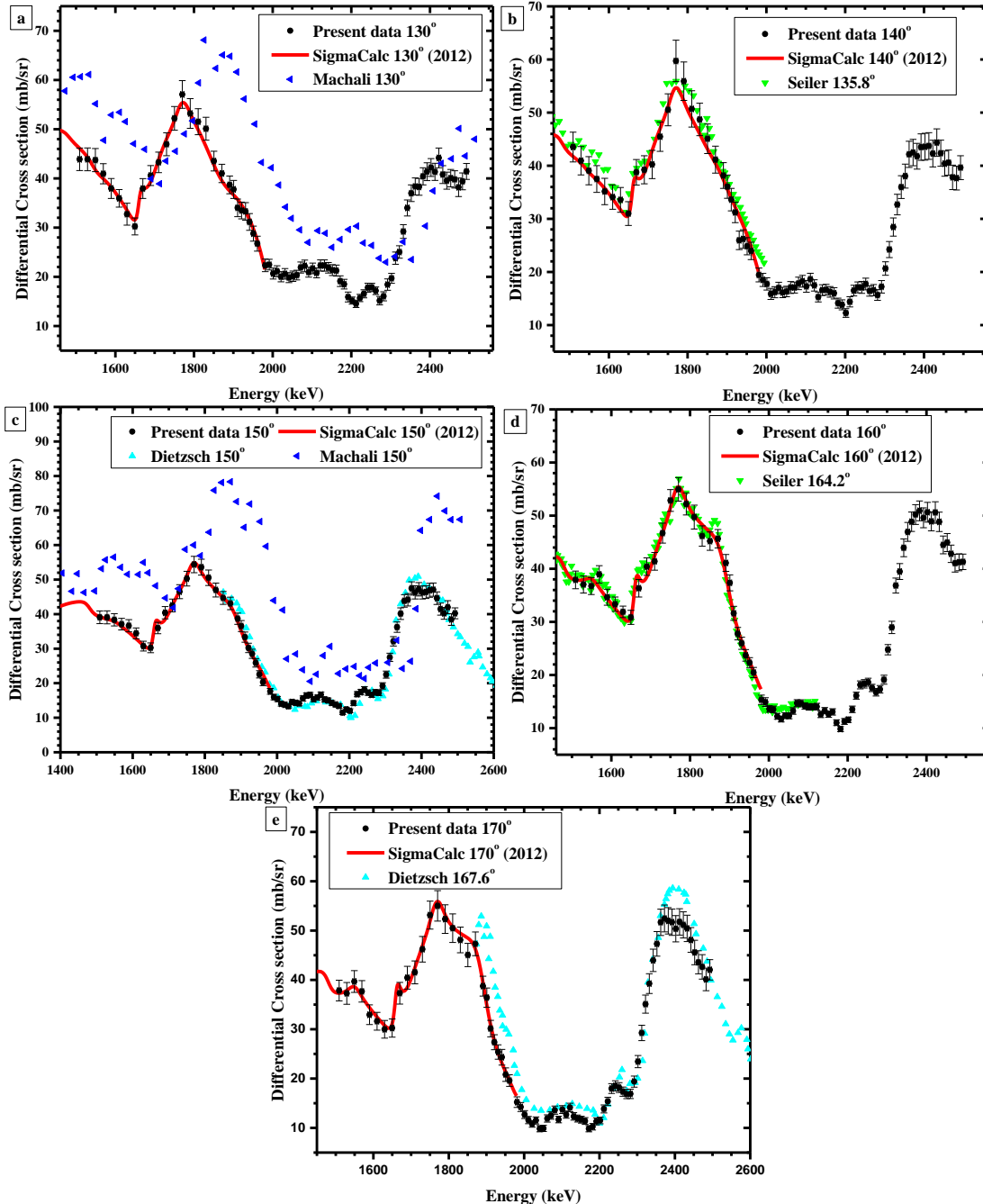


Σχήμα xxvi Πειραματικό και προσομοιωμένο φάσμα πρωτονίων με σκοπό τον χαρακτηρισμό του στόχου σε ενέργεια 1470 keV και για γωνία σκέδασης 170° μαζί με την αναγνώριση των αντίστοιχων κορυφών.

Οι τελικές τιμές της διαφορικής ενεργού διατομής της ελαστικής σκέδασης δευτερίων από οξυγόνο στο ενεργειακό εύρος 1500-2500 keV και για τις γωνίες σκέδασης 130°, 140°, 150°, 160° και 170° παρουσιάζονται σε γραφική μορφή στα Σχήματα xxvii a-e. Στα γραφήματα περιλαμβάνονται τα προϋπάρχοντα αποτελέσματα στη βιβλιογραφία καθώς και οι συνολικές στατιστικές αβεβαιότητες. Συγκεκριμένα οι συνολικές σχετικές αβεβαιότητες για κάθε γωνία ήταν: 130° μέχρι ~6.5%, 140° μέχρι ~7%, 150° και 160° έως ~5%, και 170° έως ~6.5%. Οι συστηματικές αβεβαιότητες των τιμών της ενεργού διατομής προέρχονται από τις διαφορές ανάμεσα στις θεωρητικές και τις πειραματικές τιμές των δεδομένων της ισχύς ανασχεσης και ήταν ~2.8% για το οξυγόνο και ~3.6% για τον χρυσό. Οι αβεβαιότητες στον οριζόντιο άξονα ήταν (~2 keV, από τη διαδικασία βαθμονόμησης του επιταχυντή και 4.6 keV από τον ενεργειακό διασκεδασμό της δέσμης μέσα στον στόχο.

Όπως φαίνεται στα Σχήματα xxvii a-e στην μορφή της διαφορικής ενεργού διατομής κυριαρχούν ένα έντονο ελάχιστο και ένα έντονο μέγιστο. Η μορφή αυτή θα μπορούσε να αποδοθεί στις ενεργειακές στάθμες του σύνθετου πυρήνα $^{19}\text{F}^*$, με ενέργειες 8.91 MeV, 8.96 MeV, 9.09 MeV και 9.20 MeV, τα οποία φαίνονται στο Σχήμα xxv. Συγκρίνοντας με τα προϋπάρχοντα δεδομένα των Machali et al. [28] παρατηρείται ίδια μορφή αλλά μετατοπισμένα πάνω και δεξιά. Τα δεδομένα των Machali et al. δεν υπήρχαν ούτε στην IBANDL ούτε στην EXFOR και ψηφιοποιήθηκαν από την δημοσίευση επομένως μπορεί να εμπεριέχουν σφάλματα. Σε κάθε

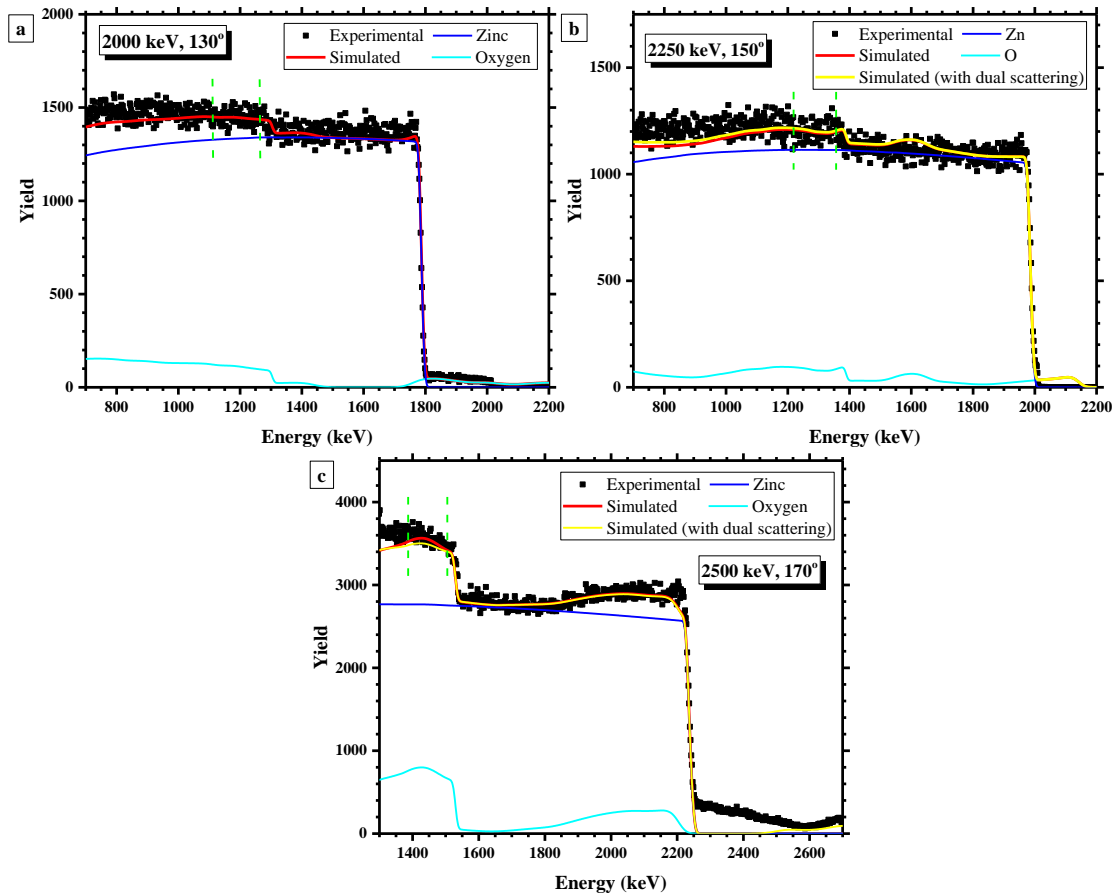
περίπτωση η μορφή είναι παρόμοια. Τα δεδομένα των Dietzsch et al. [29] συμφωνούν με τα παρόντα δεδομένα αλλά εμφανίζουν μια ενεργειακή μετατόπιση, η αιτία της οποίας δεν είναι ξεκάθαρη.



Σχήμα xxvii a-e Τιμές της διαφορικής ενεργού διατομής (mb/sr) της ελαστικής σκέδασης $^{nat}O(d,d_0)^{nat}O$ στο ενεργειακό εύρος $E_{d,lab} = 1500-2500$ keV για τις γωνίες σκέδασης 130°, 140°, 150°, 160° and 170° μαζί με τα δεδομένα της βιβλιογραφίας.

Έλεγχος αξιοπιστίας για την ελαστική σκέδαση $^{nat}\text{O}(\text{d},\text{d}_0)^{nat}\text{O}$

Για τον έλεγχο αξιοπιστίας των τιμών διαφορικής ενεργού διατομής της ελαστικής σκέδασης δευτερίων από οξυγόνο χρησιμοποιήθηκαν φάσματα από έναν παχύ στόχο ZnO τα οποία αποκτήθηκαν στον επιταχυντή Tandem IPPE στο Obninsk της Ρωσίας από τον Dr. A. F. Gurbich. Τα φάσματα των δευτερίων ήταν σε ενέργειες 2000 keV και 2250 keV για τις γωνίες σκέδασης 130° και 150° και 2000, 2250 και 2500 keV για τις γωνίες σκέδασης 170° . Η παράμετρος $Q \times \Omega$ προσαρμόστηκε στο σκαλοπάτι του Zn όπου η συνεισφορά της αντίδρασης $^{16}\text{O}(\text{d},\text{p}_1)^{15}\text{O}$ ήταν ελάχιστη για το οποίο χρησιμοποιήθηκαν Rutherford τιμές της ενεργού διατομής για κάθε συνδυασμό ενέργειας δέσμης/γωνίας σκέδασης. Το παράθυρο ολοκλήρωσης επιλέχθηκε να είναι ~ 100 keV (~ 65 κανάλια). Τα αποτελέσματα αυτής της διαδικασίας φαίνονται στα Σχήματα xxviii a-c. Η σημαντική συνεισφορά της αντίδρασης $^{16}\text{O}(\text{d},\text{p}_1)^{15}\text{O}$ υπολογίστηκε με χρήση των evaluated δεδομένων όπου αυτά ήταν διαθέσιμα (μέχρι 1650 keV), ενώ για υψηλότερες ενέργειες χρησιμοποιήθηκαν πειραματικά δεδομένα από την βιβλιογραφία. Πιο συγκεκριμένα, χρησιμοποιήθηκαν τα δεδομένα των Debras et al. [30] για την γωνία σκέδασης 130° , για τις 150° χρησιμοποιήθηκαν τα δεδομένα των Cavallaro et al. [31], ενώ για τις 170° επιλέχθηκαν τα δεδομένα των Seiler et al. [32] στις 164.25° . Ωστόσο το φάσμα του Σχήματος xxviii b, που αντιστοιχεί σε ενέργεια 2250 keV απορρίφθηκε καθώς η συνεισφορά της ελαστικής σκέδασης δευτερίων από οξυγόνο ήταν μόνο $\sim 30\%$ μεγαλύτερη από την συνεισφορά της αντίδρασης $^{16}\text{O}(\text{d},\text{p}_1)^{15}\text{O}$ εντός του παραθύρου ολοκλήρωσης για όλες τις μετρημένες γωνίες. Τα αποτελέσματα της διαδικασίας ελέγχου αξιοπιστίας φαίνονται στον Πίνακα V. Η μεγαλύτερη διαφορά είναι για την ενέργεια 2000 keV στις 170° (7.9%). Αυτή η τιμή, καθώς και όλες οι τιμές του Πίνακα V, υποδεικνύουν ικανοποιητική συμφωνία καθώς συμπεριλαμβάνουν τις αβεβαιότητες των πειραματικών μετρήσεων που χρησιμοποιήθηκαν ($\sim 5\%$ από τα δεδομένα των Seiler et al., $\sim 6\%$ για τα δεδομένα των Cavallaro et al.). Αξίζει να τονισθεί εδώ ότι παρόλο που το benchmarking πραγματοποιήθηκε σε λίγες ενέργειες και γωνίες, τα αποτελέσματα ανταποκρίνονται σε όλο το υπό μελέτη ενεργειακό εύρος.



Σχήμα xxviii a-c Πειραματικά και προσομοιωμένα φάσματα benchmarking από έναν στόχο ZnO σε ενέργεια και γωνία σκέδασης (a) 130° και 2000 keV, (b) 150° και 2250 keV και (c) 170° και 2500 keV. Το παράθυρο ολοκλήρωσης που χρησιμοποιήθηκε είναι μαρκαρισμένο με κάθετες διακεκομμένες γραμμές και περιλαμβάνει ~100 keV (~65 κανάλια).

Energy (keV)	130°	150°	170°
2000	3.1	4.4	7.9
2500	-	-	6.1

Πίνακας V Διαφορές (επί %) μεταξύ των πειραματικών και των προσομοιωμένων γεγονότων μέσα στο παράθυρο ολοκλήρωσης. Οι αριθμοί αντιστοιχούν σε υψηλότερο αριθμό προσομοιωμένων σε σύγκριση με τα πειραματικά γεγονότα.

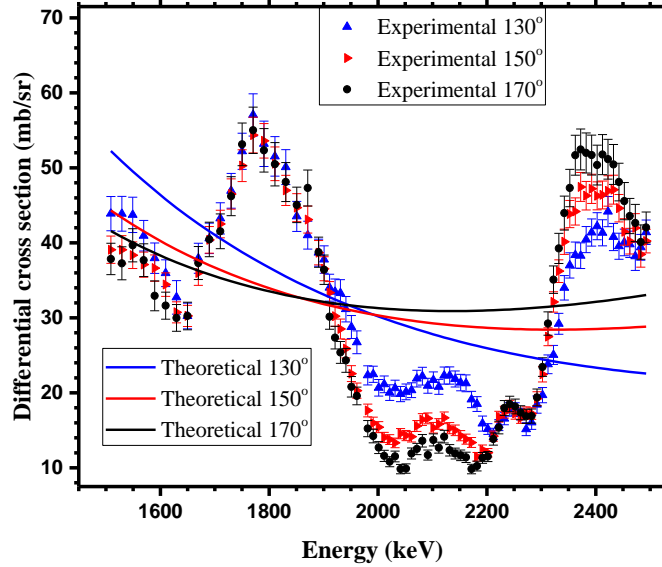
Θεωρητική μελέτη της ελαστικής σκέδασης $^{nat}\text{O}(d,d_0)^{nat}\text{O}$

Στην συγκεκριμένη περίπτωση χρησιμοποιήθηκε η θεωρία R-matrix για ένα κανάλι και πολλές ενεργειακές στάθμες ώστε να αναπαραχθεί θεωρητικά η μετρημένη διαφορική ενεργός διατομή της ελαστικής σκέδασης δευτερίων από οξυγόνο σε ενεργειακό εύρος 1.98-2.5 MeV. Οι υπολογισμοί πραγματοποιήθηκαν στα πλαίσια του μηχανισμού του σύνθετου πυρήνα αφού είναι ο κυρίαρχος μηχανισμός για τέτοιες χαμηλές ενέργειες δευτερίων και τόσο ελαφρύς πυρήνες όσο το οξυγόνο. Ο κώδικας που αναπτύχθηκε από τον Dr. A.F. Gurbich και χρησιμοποιήθηκε στα

πλαίσια της παρούσας διατριβής χρησιμοποιεί τις σχέσεις από την κλασική R-matrix θεωρία από τους Lane and Thomas [33].

Σύμφωνα με την κλασική θεωρία R-matrix το πλάτος σκέδασης υπολογίζεται χρησιμοποιώντας δύο διαφορές φάσης, την διαφορά φάσης συντονισμών (resonant phase shift) και την διαφορά φάσης λόγω του δυναμικού Coulomb. Η κλασική θεωρία R-matrix είναι ενσωματωμένη στους κώδικες ευρείας χρήσης για τον υπολογισμό διαφορικών ενεργών διατομών όπως π.χ. το AZURE [34] και το SAMMY [35]. Αντίθετα, όπως προτάθηκε από τον Johnson [36], η περιοχή σκέδασης εκτός συντονισμών (off resonant scattering) μπορεί να περιγραφεί από το οπτικό μοντέλο. Σε αυτήν την προσέγγιση το πλάτος σκέδασης υπολογίζεται από 3 συνεισφορές, την διαφορά φάσης συντονισμών (resonant phase shift), την διαφορά φάσης λόγω του δυναμικού Coulomb και την διαφορά φάσης της σκέδασης από το δυναμικό (potential scattering). Αυτή η εναλλακτική προσέγγιση εφαρμόζεται μέχρι στιγμής μόνο από τον κώδικα που χρησιμοποιήθηκε στα πλαίσια της παρούσας διατριβής. Επιπλέον λόγοι που επιλέχθηκε η προσέγγιση με το οπτικό δυναμικό είναι ότι μπορεί να προκύψουν συντονισμοί στην διαφορική ενεργό διατομή φυσικά μέσω των παραμέτρων του οπτικού μοντέλου χωρίς την προσθήκη ενεργειακών σταθμών στο σύνθετο πυρήνα και ότι μπορεί να οδηγήσει σε πληροφορίες σχετικά με τις τιμές των παραμέτρων του οπτικού μοντέλου.

Το πρώτο βήμα στη διαδικασία αναπαραγωγής της διαφορικής ενεργού διατομής είναι η πραγματοποίηση υπολογισμών μόνο με το οπτικό μοντέλο χωρίς την προσθήκη ενεργειακών στάθμεων του σύνθετου πυρήνα. Αυτοί οι υπολογισμοί έχουν ως αποτέλεσμα αργές και ομαλές μεταβολές της διαφορικής ενεργού διατομής χωρίς έντονα μέγιστα και ελάχιστα, όπως φαίνεται στο Σχήμα xxix για τρεις γωνίες σκέδασης (130° , 150° , και 170°). Στο γράφημα αυτό περιλαμβάνονται οι πειραματικές και οι θεωρητικές τιμές της ενεργού διατομής αλλά μόνο με την χρήση του οπτικού μοντέλου, χωρίς την προσθήκη ενεργειακών στάθμεων. Επομένως, με διαδικασίες δοκιμής οι οποίες δεν σταματούν καθ' όλη τη διαδικασία αναπαραγωγής των διαφορικών ενεργών διατομών οι βέλτιστες τιμές για τις παραμέτρους του οπτικού δυναμικού φαίνεται στον Πίνακα VI.



Σχήμα xxix Πειραματικές και θεωρητικές τιμές της ενεργού διατομής με τη χρήση μόνο υπολογισμών μέσω του οπτικού μοντέλου χωρίς την προσθήκη ενεργειακών στάθμεων του σύνθετου πυρήνα για τρεις γωνίες σκέδασης 130° , 150° και 170° .

r_0	a_c	V_{R0}	V_{R1}	V_{R2}	V_{R3}	W	V_{SO}	R_C
(fm)	(fm)	(MeV)	(MeV)	(MeV)	(MeV)	(MeV)	(MeV)	(fm)
1.56	0.55	66.31	71.90	62.74	85.41	0.16	9	2

Πίνακας VI Τιμές των παραμέτρων του οπτικού μοντέλου για τον υπολογισμό της διαφορικής ενεργού διατομής της ελαστικής σκέδασης δευτερίων από οξυγόνο. Ο συμβολισμός ακολουθεί τον συνήθη συμβολισμό που αναφέρεται στην 1^η ενότητα.

Στη συνέχεια στην μορφή της διαφορικής ενεργού διατομής που φαίνεται στο Σχήμα xxix προστέθηκαν συνεκτικά οι ενεργειακές στάθμες του σύνθετου πυρήνα. Οι παράμετροι αυτών των ενεργειακών στάθμεων βασίζονται στις πληροφορίες που υπάρχουν στην βιβλιογραφία για τις ενεργειακές στάθμες του σύνθετου πυρήνα. Οι τελικές τιμές που χρησιμοποιήθηκαν στους υπολογισμούς φαίνονται στον Πίνακα VII. Όπως φαίνεται από τον Πίνακα VII για τις ενεργειακές στάθμες με ενέργεια 2.242 MeV και 2.294 MeV οι τιμές των J^π είναι 2^- ενώ στην βιβλιογραφία οι τιμές αυτές έχουν ανατεθεί μόνο προσωρινά και είναι άγνωστο αν η πραγματική τιμή είναι 2^- ή 3^+ . Οι υπολογισμοί της παρούσας εργασίας υποδεικνύουν ότι η προσωρινή τιμή 2^- είναι πιο πιθανή σε σύγκριση με την εναλλακτική τιμή 3^+ .

E_d (MeV)	J^π	Γ (keV)	Γ_{el}/Γ	ψ
1.650	2^-	50	0.070	0
1.665	1^+	119	0.063	79
1.740	1^+	94	0.162	0
1.854	1^+	7.4	0.146	85
2.053	1^-	115	0.134	0
2.242	2^-	82	0.095	0
2.294	2^-	71.8	0.119	0
2.381	1^+	130	0.36	0

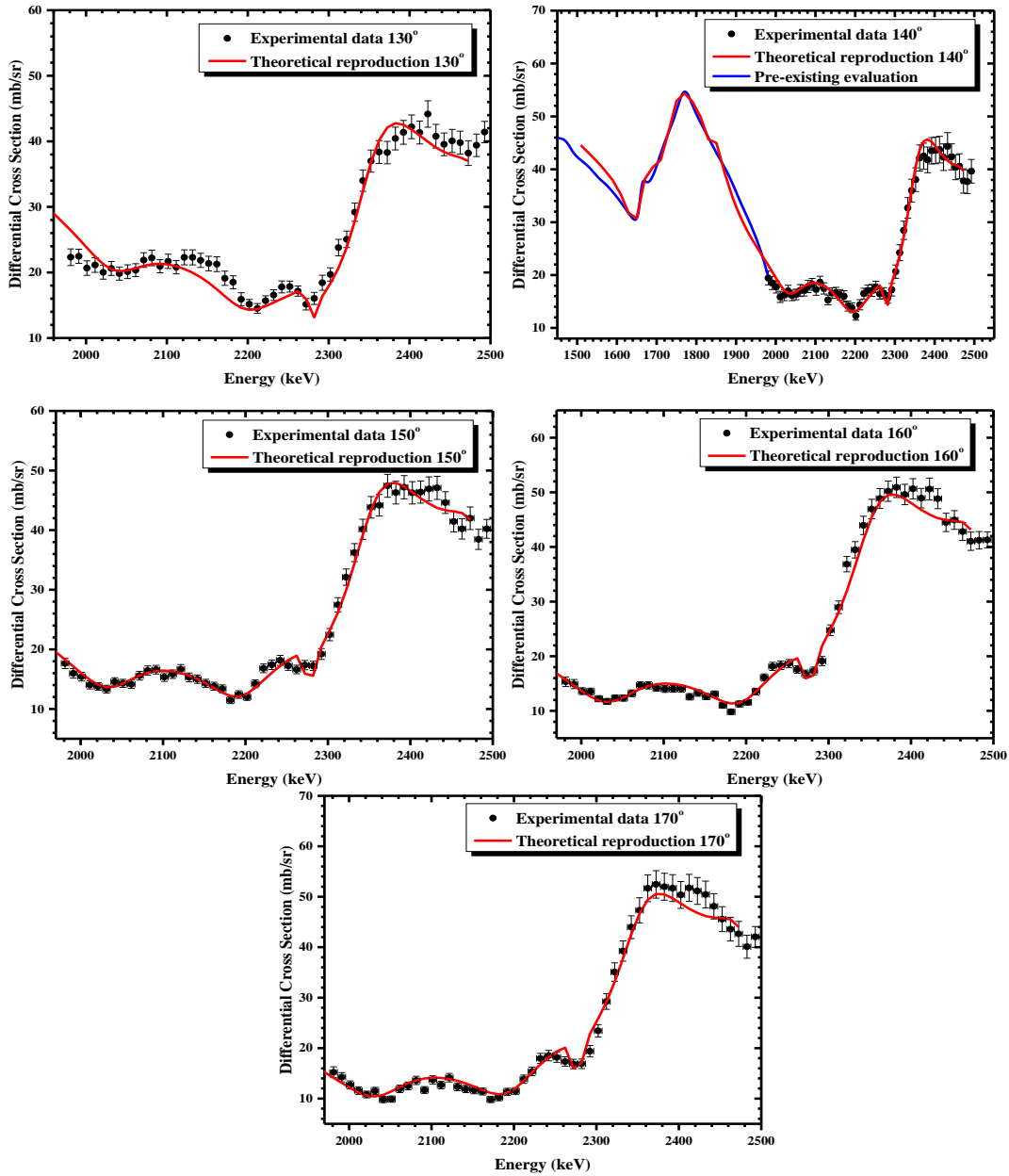
Πίνακας VII Παράμετροι των ενεργειακών στάθμεων που χρησιμοποιήθηκαν για τους υπολογισμούς της διαφορικής ενεργού διατομής στα πλαίσια της θεωρίας R-matrix.

Τα τελικά αποτελέσματα παρουσιάζονται στα Σχήματα xxx a-e μαζί με τα πειραματικά αποτελέσματα για τις πέντε γωνίες σκέδασης και για το ενεργειακό εύρος 1.98-2.5 MeV. Στο Σχήμα xxx b, για την γωνία σκέδασης των 140° παρουσιάζεται επίσης το προϋπάρχων ώστε να εξακριβωθεί ότι οι διαφορές ανάμεσα στο προϋπάρχων evaluation και στην θεωρητική μελέτη τη παρούσας εργασίας δεν είναι μεγάλες. Στο Σχήμα xxx a οι θεωρητικές καμπύλες αναπαράγουν επαρκώς τα πειραματικά δεδομένα εντός αβεβαιοτήτων. Οι πιο σημαντικές διαφορές παρατηρούνται στις ενέργειες ~ 1990 keV και ~ 2150 keV. Η κατάσταση στο Σχήμα xxx b βελτιώνεται υποδεικνύοντας πολύ καλή συμφωνία σε όλο το ενεργειακό εύρος υπό μελέτη, ωστόσο η διαφορά στην ενέργεια ~ 1990 keV παρατηρείται ακόμα. Στα Σχήματα xxx c-e είναι εξαιρετική εντός σφαλμάτων εκτός από την περιοχή κοντά στην ενέργεια ~ 2420 keV. Συνολικά η θεωρητική καμπύλες παρουσιάζουν πολύ καλή συμφωνία με τα πειραματικά δεδομένα.

Η λύση της παρούσας εργασίας περιλαμβάνει τις παραμέτρους του οπτικού μοντέλου και των παραμέτρων των ενεργειακών στάθμεων του σύνθετου πυρήνα, δηλαδή συνολικά 390 τιμές (78 σε κάθε γωνία σκέδασης) οι οποίες οδηγούν σε ίσο αριθμό εξισώσεων. Οι άγνωστοι παράμετροι που προσδιορίστηκαν ήταν 66 συνολικά (18 από το οπτικό μοντέλο και 48 από καθέναν από τους 8 συντονισμούς). Ένα τέτοιο σύστημα οδηγεί μαθηματικά σε μοναδική λύση. Ωστόσο η πιθανότητα να πραγματοποιηθούν οι ίδιοι υπολογισμοί με διαφορετικές τιμές για τις ενεργειακές στάθμες και διαφορετικές τιμές των παραμέτρων του οπτικού μοντέλου ή ακόμα και με χρήση της κλασικής R-matrix θεωρίας και να εξαχθούν εξίσου καλά αποτελέσματα δεν μπορεί να αποκλειστεί.

Σχετικά με την αξιοπιστία της θεωρητικής αναπαραγωγής, η επέκταση των αποτελεσμάτων σε ενδιάμεσες γωνίες θα οδηγήσει σε αξιόπιστα αποτελέσματα. Σχετικά με την επέκταση σε πιο μπροστινές γωνίες, η ακρίβεια των αποτελεσμάτων εξαρτάται από τα πολυώνυμα Legendre. Επομένως σε γωνίες όπου τα πολυώνυμα Legendre πλησιάζουν μηδενικές τιμές (όπως για

παράδειγμα σε γωνία $\theta=90^\circ$ όπου $\cos\theta=0$) θα υπάρχουν αποκλίσεις των θεωρητικών υπολογισμών και των πειραματικών δεδομένων.



Σχήμα xxx a-e Αποτελέσματα της θεωρητικής αναπαραγωγής μαζί με τις πειραματικές τιμές της διαφορικής ενεργού διατομής στο ενεργειακό εύρος 1.98-2.5 MeV για την ελαστική σκέδαση $^{16}\text{O}(d,d_0)^{16}\text{O}$ για τις γωνίες σκέδασης 130° , 140° , 150° , 160° , 170° . Στο γράφημα (b) συμπεριλαμβάνεται και το προϋπάρχων evaluation.

Προοπτικές

Η συνεισφορά της παρούσας εργασίας μέσω των μετρήσεων ελαστικής σκέδασης δευτερίων είναι σημαντική στον τομέα της ανάλυσης με δέσμες ιόντων και στον εμπλουτισμό της IBANDL. Ωστόσο, υπάρχει δυνατότητα να βελτιωθεί περαιτέρω η κατάσταση. Θα ήταν πολύ χρήσιμο να επεκταθεί η μελέτη στα υπόλοιπα ελαφρά στοιχεία (για παράδειγμα ^{10}B , ^{11}B , ^{27}Al) ώστε να ολοκληρωθεί αυτή η συστηματική μελέτη, ενισχύοντας της εφαρμογή του συνδυασμού των ιοντικών τεχνικών d-EBS και d-NRA ώστε να εξάγονται πιο ακριβή κατανομές βάθους των ελαφρών στοιχείων. Τέτοιες μετρήσεις έχουν ήδη προγραμματιστεί για το επόμενο χρονικό διάστημα. Επιπρόσθετα, θα μπορούσαν να πραγματοποιηθούν πειράματα ελέγχου αξιοπιστίας για τις περιπτώσεις που δεν πραγματοποιήθηκαν στα πλαίσια της παρούσας εργασίας ώστε οι διαφορικές ενεργές διατομές να επαληθευτούν με την χρήση παχέων στόχων, ιδανικά σε διαφορετικό εργαστήριο από αυτό που μετρήθηκαν οι διαφορικές ενεργές διατομές. Κατά τη διάρκεια τέτοιων μετρήσεων, οι επιπλοκές που προέκυψαν στα πλαίσια αυτής της εργασίας μπορούν να αποφευχθούν με την χρήση διαφορετικής πειραματικής διάταξης όπου θα μπορεί να διαχωρίσει τα δευτέρια από τα πρωτόνια και τα σωματίδια α.

Ενώ οι διαφορικές τιμές της ελαστικής σκέδασης πρωτονίων και τώρα των δευτερίων είναι μελετημένες για την πλειοψηφία των ελαφρών στοιχείων, η κατάσταση αλλάζει δραματικά στην ελαστική σκέδαση σωματιδίων ^3He από ελαφρά στοιχεία. Σε αυτήν την περίπτωση υπάρχουν μόνο αραιά και μεμονωμένα δεδομένα στην βιβλιογραφία. Η μέτρηση της ελαστικής σκέδασης των ελαφρών στοιχείων με χρήση δέσμης ^3He θα οδηγήσει σε μελέτες κατανομών βάθους εξαιτίας του καλύτερου διαχωρισμού μάζας και της καλύτερης ανάλυσης βάθους (depth resolution) σε σύγκριση με τα πρωτόνια και τα δευτέρια. Μια τέτοια μελέτη είναι σημαντική γιατί θα βοηθήσει όχι μόνο στην μελέτη των υλικών σύντηξης αλλά και στην μελέτη υπό εξέλιξη της πυρηνικής αστροφυσικής, για παράδειγμα στην rp διαδικασία.

Από την θεωρητική σκοπιά, θεωρητικές μελέτες θα μπορούσαν να πραγματοποιηθούν για τα ελαφρά στοιχεία που παρουσιάζουν μεγάλο τεχνολογικό ενδιαφέρον αλλά και για τα οποία υπάρχουν πληροφορίες στην βιβλιογραφία για τις ενεργειακές στάθμες του σύνθετου πυρήνα, όπως είναι για παράδειγμα το ^{14}N . Τέτοιες μελέτες θα οδηγούσαν σε συμπεράσματα σχετικά με το δυναμικό των πρωτονίων σε αυτές τις χαμηλές ενέργειες. Τέλος, η πειραματική και θεωρητική μελέτη όλων των αντιδράσεων του ^{16}O με δέσμη δευτερίων θα ήταν εξαιρετικά χρήσιμη καθώς οι παράμετροι των ενεργειακών στάθμων που προσδιορίστηκαν στα πλαίσια αυτής της εργασίας θα μπορούσαν να ελεγχθούν για διαφορετικά κανάλια. Η θεωρητική μελέτη θα οδηγούσε ακόμα στην μελέτη της συνεισφοράς του άμεσου μηχανισμού αντίδρασης. Συνοψίζοντας, παρά την εξαιρετική πρόοδο που πραγματοποιήθηκε και φαίνεται στις ιστοσελίδες της IBANDL και του SigmaCalc, υπάρχουν ακόμα πολλά ανοιχτά ζητήματα που χρήζουν περαιτέρω μελέτης.

Introduction

Ion Beam Analysis (IBA) techniques are universally used for analyzing elements and/or isotopes in the near-surface region of solids. More specifically, the implementation of such techniques includes the measurement of the number and the energy distribution of ions scattered from atoms in the near-surface layers of solid materials, and it provides a simple quantitative analysis, or it determines the depth profile of target elements. In the field of material analysis, in order for such results to be obtained via IBA techniques, the *a priori* knowledge of the corresponding differential cross section values is essential. However, the analytical calculation of the differential cross section values, for beam energies in the MeV range, is impossible since the physics concerning the interaction of the beam-target nucleons is only partially known. Therefore, the application of such analytical techniques is based on the existence of the corresponding experimental datasets in the literature.

At the same time, light elements find numerous technological applications in the industry. They are crucial in the field of material analysis due to their presence in ceramics, glasses, and polymers, while they are also frequently added in metallic alloys in order to improve their corresponding properties, such as, hardness, wear and heat resistance, or rigidity. Consequently, the accurate quantitative determination of light-element depth profile concentrations in a variety of matrices is of paramount importance in contemporary science and technology. Such information, concerning light elements, can be acquired via the implementation of IBA (Ion Beam Analysis) techniques and more specifically via ERDA (Elastic Recoil Detection Analysis), for ultra-thin surficial layers and NRA (Nuclear Reaction Analysis) due to the production of isolated peaks (high Q-values involved) with negligible background. At the same time, the use of a deuteron beam provides high depth resolution, deep layer analysis and allows for the simultaneous study of practically all the main light isotopes and/or elements coexisting in a target. The implementation of d-NRA could be further enhanced if one could also coherently analyze the elastic scattering spectra which are simultaneously acquired using the same experimental conditions. However, the general applicability of d-EBS is still limited nowadays, mostly because of the lack of reliable and coherent datasets of differential cross-sections in the literature for energies and angles suitable for IBA.

Hence, the contribution of the present thesis in the field of IBA is a comprehensive review of the differential cross section values of the deuteron elastic scattering on many important stable light elements and isotopes, such as ${}^6\text{Li}$, ${}^7\text{Li}$, ${}^9\text{Be}$, ${}^{14}\text{N}$, ${}^{\text{nat}}\text{O}$, ${}^{23}\text{Na}$ and ${}^{\text{nat}}\text{Si}$, at energies and angles suitable for analytical purposes. In several cases (${}^{\text{nat}}\text{O}$, ${}^{23}\text{Na}$, ${}^{\text{nat}}\text{Si}$) the obtained differential cross-section

datasets are also benchmarked using thick targets of known and accurate stoichiometry. All measurements were carried out at the 5.5 MV Tandem Accelerator of N.C.S.R. “Demokritos” in Athens, Greece. The experimental setup consisted of a high-precision goniometer, along with six silicon surface barrier (SSB) detectors (500 μm in thickness). Most of the obtained datasets are already available in IBANDL (Ion Beam Analysis Nuclear Data Library [38]) under the International Atomic Energy Agency auspices, in order to be used by the scientific community in basic research problems, as well as in technological applications in the field of material analysis.

Last but not least, in the context of the present thesis, the measured differential cross section values of the deuteron elastic scattering on oxygen were accompanied by theoretical calculations in order to extend the existing evaluation to higher deuteron beam energies. The theoretical calculations were accomplished in the framework of the R-matrix theory which is the most appropriate theoretical approach for calculating differential cross sections for resonant elastic scattering processes. The R-matrix theory takes into account the interaction of the projectile with the nucleus as a whole and the parameters of the used model were adjusted to the measured differential cross section values.

Chapter 1

Deuteron Physics & Basic Principles of Theory

The present chapter begins by mentioning a few crucial details for the elastic scattering properties of deuterons, and continues with the basic study of the formal quantum mechanical theory of scattering. Subsequently, the optical model for elastic scattering is described, followed by a review of the mechanisms of projectile-nucleus interaction. Finally, the basic principles of the R-matrix theory are illustrated, along with an example of the R-matrix derivation in the case of the elastic scattering of a spinless particle by a central potential.

Deuteron, consisting of one proton and one neutron, is the simplest bound state of nucleons found in nature and thus, over the years, has been extensively used for studying the interaction between two nucleons. The main drawback in understanding the deuteron structure through electromagnetic transitions is the lack of excited states, since the only possible “excited” states are a free proton and a neutron due to the low binding energy of deuteron (2.2246 MeV [39]) [2].

The deuteron total angular momentum \mathbf{J} is given by the equation:

$$\mathbf{J} = \boldsymbol{\ell} + \mathbf{s}_n + \mathbf{s}_p$$

It includes the individual spins of the proton ($s_p = 1/2$), the neutron ($s_n = 1/2$) and the orbital angular momentum $\boldsymbol{\ell}$ of the nucleons as they move about their common center of mass. The value of \mathbf{J} for the deuteron is measured to be equal to one (triplet state) and thus is a boson. Therefore, four ways exist to couple the \mathbf{s}_p and \mathbf{s}_n along with $\boldsymbol{\ell}$ in order to acquire a total \mathbf{J} of 1: if \mathbf{s}_p and \mathbf{s}_n are parallel and $\boldsymbol{\ell} = 0$, if \mathbf{s}_p and \mathbf{s}_n are antiparallel and $\boldsymbol{\ell} = 1$, if \mathbf{s}_p and \mathbf{s}_n are parallel and $\boldsymbol{\ell} = 1$ or if \mathbf{s}_p and \mathbf{s}_n are parallel and $\boldsymbol{\ell} = 2$. However, the combinations of spins which contain $\boldsymbol{\ell} = 1$ are eliminated since the deuteron parity is experimentally determined to be even. More specifically, the parity is associated with the orbital motion via a phase $(-1)^\ell$ and therefore the $\boldsymbol{\ell} = 0$ (s states) and $\boldsymbol{\ell} = 2$ (d states) result in an even parity leading to possible values of $\boldsymbol{\ell}$, whereas the $\boldsymbol{\ell} = 1$ (p states) results in an odd parity and is thus rejected.

The two possible values of $\boldsymbol{\ell}$ result in the wavefunction of the deuteron ground state being a quantum mechanical superposition of s and d wavefunctions in the form of $\Psi_d = \cos \omega |^3s_1\rangle + \sin \omega |^3d_1\rangle$. $|^3s_1\rangle$ and $|^3d_1\rangle$ are normalized s and d state wave functions and the terms $\cos \omega$ and $\sin \omega$ ensure that Ψ_d is normalized. Usually, it is assumed that for the ground state configuration of the deuteron the dominant component is $|^3s_1\rangle$ and $\sim 4\%$ is the $|^3d_1\rangle$ one. Such a mixed configuration is unexpected for the simple combination of a proton and a neutron [2], [3], [39].

Since this contribution is small, in the studied case, that is the deuteron elastic scattering on oxygen, only the s state wave functions were taken into account.

1.1 Theory of Elastic Scattering

When a beam of charged particles interacts with a target nucleus there is an interference between nuclear and Coulomb forces. Such an interference depends on the beam energy, the scattering angle and the target nucleus. The different ranges in which these two kinds of forces act, lead to regions where only long-range Coulomb forces, or only short-range nuclear forces operate, as the latter ones are at least 100 times greater than Coulomb forces at short distances of about 1 fm.

The atomic nucleus, a strongly bound system of nucleons located in a small domain, has a typical size of $r = r_0 A^{1/3}$ fm, where A is the mass number and $r_0 \approx 1.2$ fm [2] or $r_0 = (1.1-1.5)$ fm [1]. Assuming that the nucleus is a uniformly charged sphere of radius R , and Z and z are the charge numbers of the nucleus and projectile respectively, the dependence of the electrostatic potential energy on the distance r for the projectile-nucleus system is:

$$V_c(r) = \begin{cases} \frac{zZe^2}{r} & \text{for } r \geq R \\ \frac{zZe^2}{2R} \left(3 - \frac{r^2}{R^2} \right) & \text{for } r \leq R \end{cases} \quad (1.1)$$

The combination of Coulomb and nuclear potential, as shown in Fig. 1.1, could be illustrated as a well (40-50 MeV deep) with a narrow regime near the boundary of the nucleus in which the transition from repulsion to attraction is occurring.

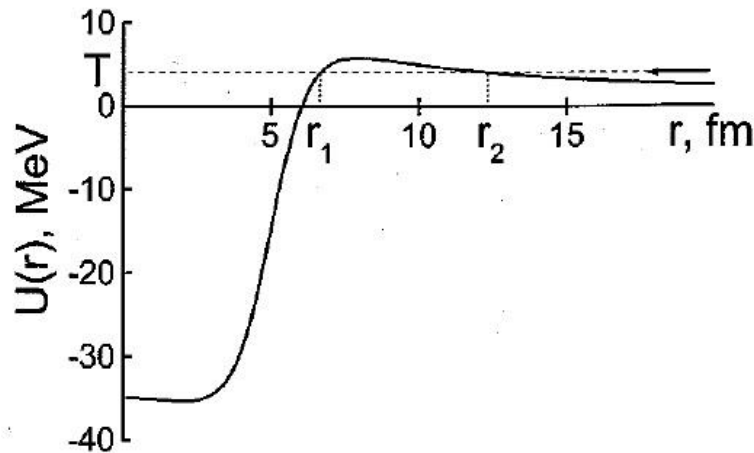


Figure 1.1 The combination of Coulomb and nuclear potential of a nucleus. The classical turning points for a particle with kinetic energy T are located at r_1 and r_2 [1].

A charged projectile will reach the attraction of the nuclear force, if it possesses a kinetic energy T sufficient to overcome the Coulomb potential barrier at height $B_c = zZe^2/R$. It should be noted here that the energy T is of the order of 1 MeV, even for the interaction of a single charged particle with the lightest nuclei. However, according to the basic principles of quantum mechanics, a particle having a lower kinetic energy could penetrate through the barrier via the tunneling effect. In this case, the transparency of the barrier is given by the formula:

$$D \approx \exp \left[-\frac{2}{\hbar} \int_{r_1}^{r_2} \sqrt{2\mu(V_c - T)} dr \right] \quad (1.2)$$

Where μ is the reduced mass ($\mu = M \cdot m / (M+m)$) and r_1, r_2 are the classical turning points indicated in Fig.1.1. Thus, reactions of the atomic nuclei with low-energy charged particles could still happen even for lower energies than the potential barrier [1].

At this point and in order to describe the cross section for the Coulomb and nuclear interactions, the Coulomb and the nuclear scattering will be examined separately.

1.1.1 Coulomb scattering

If the only forces operating in a projectile approaching a nucleus are the long-range electric ones (Coulomb) then the differential cross section can be derived from the principles of the conservation of energy and angular momentum along with the impact parameter b . The latter is defined as the perpendicular distance of the closest approach to the target nucleus in the absence of the repulsive force. The derived formula, called the Rutherford formula, describes the probability of a particle with mass M_1 , charge z and energy E to be scattered at an angle θ by a target nucleus with M_2, Z and is given (in the laboratory system) by:

$$\left(\frac{d\sigma_R}{d\Omega} \right)_{E,\theta} = \left(\frac{zZe^2}{4E} \right)^2 \frac{2[(M_2^2 - M_1^2 \sin^2 \theta)^{1/2} + M_2 \cos \theta]^2}{M_2 \sin^4 \theta (M_2^2 - M_1^2 \sin^2 \theta)^{1/2}} \quad (1.3)$$

As the energy of the projectile increases, a point will be reached in which the distance of closest approach will be equal to the nuclear radius and therefore the target and the projectile will start to feel each other's nuclear force. At this point, the Rutherford formula can no longer describe the interaction since it was derived with the assumption that only electric forces take place. Nuclear terms should then be included in the cross section due to the interference between Coulomb and nuclear scattering. However, at such short distances where the nuclear force is operating, simultaneous knowledge of the momentum and the position (thus the impact parameter) of the scattering particle is impossible according to Heisenberg's uncertainty principle. Consequently, in principle, nuclear forces cannot be incorporated into any theory that assumes the trajectory of the particle determined. Thus, quantum mechanics must be used instead of classical physics [2] [1].

1.1.2 Nuclear Scattering

The nuclear scattering of a projectile with no charge is going to be firstly examined, and subsequently the charged projectile case is going to be examined. The incident beam in the z axis is represented by a plane wave e^{ikz} with momentum $p=\hbar k$, where k is the propagation vector $k = \frac{p}{\hbar} = \frac{1}{\lambda}$.

As the scattering is taking place, the incident plane wave interacts with the potential of the nucleus $V(r)$, giving rise to a spherical divergent one from the center of the interaction. This wave has the form of:

$$f(\theta) \cdot e^{ikr} \quad (1.4)$$

Thus, after the scattering, the wave can be represented by a superposition of two waves, the incident plane wave and the spherical one in the form:

$$e^{ikz} + f(\theta) \cdot e^{ikr} \quad (1.5)$$

where $f(\theta)$ is the amplitude of the divergent wave and the term represents the decreasing of the flux.

However, the incident plane wave e^{ikz} can be represented as a superposition of spherical waves (since the outgoing particles are represented as spherical waves) by:

$$\Psi_{inc} = A e^{ikz} = A \sum_{\ell=0}^{\infty} i^{\ell} (2\ell + 1) j_{\ell}(kr) P_{\ell}(\cos\theta) \quad (1.6)$$

Where A is a normalization constant. The radial functions $j_{\ell}(kr)$ are spherical Bessel functions which are solutions to the radial part of the Schrödinger equation, in a region far from the target where the nuclear potential vanishes. The angular functions $P_{\ell}(\cos\theta)$ are the Legendre polynomials ($P_0(\cos\theta) = 1$, $P_1(\cos\theta) = \cos\theta$, $P_3(\cos\theta) = \frac{1}{2}(3\cos^2\theta - 1)$).

Equation (1.6) corresponds to the partial wave expansion of the incident wave, with each partial wave corresponding to a specific angular momentum ℓ . This expansion is only valid if the nuclear potential is assumed to be central.

When the wave is far from the nucleus, meaning that the free particle remains unaffected by the potential, ($kr \gg \ell$), the functions $j_{\ell}(kr)$ have the following expansion:

$$j_{\ell}(kr) = \frac{\sin(kr - \frac{1}{2}\ell\pi)}{kr} \quad \text{and since } kr \gg \ell \rightarrow j_{\ell}(kr) = i \frac{e^{-i(kr - \ell\pi/2)} - e^{+i(kr - \ell\pi/2)}}{2kr} \quad (1.7)$$

And by replacing the radial functions in Equation (1.6), the incident wave can be described by the following equation:

$$\Psi_{inc} = \frac{A}{2kr} \sum_{\ell=0}^{\infty} i^{\ell+1} (2\ell + 1) \left[e^{-i(kr - \frac{\ell\pi}{2})} - e^{+i(kr - \frac{\ell\pi}{2})} \right] P_{\ell} \cos\theta \quad (1.8)$$

Where the first term in the brackets, involving e^{-ikr} , represents an incoming spherical wave approaching the target, while the second term, involving e^{+ikr} , represents an outgoing spherical wave emerging from the target nucleus. The superposition of these two spherical waves, of course, gives the plane wave.

The scattering can affect the outgoing wave in either of two ways: through a change in phase (phase shift), and through a change in amplitude. The change in amplitude suggests inelastic scattering (or some other nuclear reaction) and the energy (or even the identity) of the outgoing particle may change. We account for the changes in the ℓ th outgoing partial wave by introducing the complex coefficient S_ℓ into the outgoing wave and thus the total wave after the scattering can be represented by:

$$\Psi = \frac{A}{2kr} \sum_{\ell=0}^{\infty} i^{\ell+1} (2\ell + 1) \left[e^{-i(kr - \frac{\ell\pi}{2})} - S_\ell e^{+i(kr - \frac{\ell\pi}{2})} \right] P_\ell \cos\theta \quad (1.9)$$

The complex coefficient S_ℓ includes the change in amplitude in the real part and the phase shift in the imaginary part. Equation (1.9) represents a superposition of the incident and scattered waves: $\Psi = \Psi_{inc} + \Psi_{scat}$. The scattered wave can be found by subtracting Equation (1.8) from Equation (1.9) ($\Psi_{scat} = \Psi - \Psi_{inc}$):

$$\Psi_{scat} = \frac{A}{2k} \frac{e^{ikr}}{r} \sum_{\ell=0}^{\infty} i (2\ell + 1) (1 - S_\ell) P_\ell \cos\theta \quad (1.10)$$

This equation includes the same wave number k as the incident wave, thus corresponds only to the elastic scattering. The current density of scattered particles per unit area can be calculated via:

$$j_{scat} = \frac{\hbar}{2mi} \left(\Psi_{scat}^* \frac{\partial \Psi_{scat}}{\partial r} - \frac{\partial \Psi_{scat}^*}{\partial r} \Psi_{scat} \right) \quad (1.11)$$

$$= |A|^2 \frac{\hbar}{4mkr^2} \left| \sum_{\ell=0}^{\infty} (2\ell + 1) i (1 - S_\ell) P_\ell \cos\theta \right|^2 \quad (1.12)$$

The current density of the incident wave is:

$$j_{inc} = \frac{\hbar k}{m} |A|^2 \quad (1.13)$$

This scattered current is uniformly distributed over a sphere of radius r . An element area of $r^2 d\Omega$ on the sphere subtends a solid angle of $d\Omega = \sin\theta d\theta d\phi$ at the scattering center. And since the differential cross section $d\sigma/d\Omega$ is the probability per unit solid angle for an incident particle to be scattered into the solid angle $d\Omega$; then the probability $d\sigma$ is the ratio of the scattered current through $d\Omega$ to the incident current:

$$d\sigma = \frac{(j_{scattered})(r^2 d\Omega)}{j_{incident}} \quad (1.14)$$

The differential cross section is given then by:

$$\frac{d\sigma}{d\Omega} = \frac{1}{4k^2} \left| \sum_{\ell=0}^{\infty} (2\ell + 1) i (1 - S_\ell) P_\ell \cos\theta \right|^2 \quad (1.15)$$

The most crucial terms in the above equation are the k and S_ℓ ones, since the potential which is used for solving the Schrödinger equation depends on these terms. In order to calculate the total cross section, we need to integrate Equation (1.15) over all angles using the integral of the Legendre polynomials:

$$\int P_\ell(\cos\theta)P_{\ell'}(\cos\theta) \sin\theta d\theta d\varphi = \begin{cases} \frac{4\pi}{2\ell+1} & \text{if } \ell = \ell' \\ 0 & \text{if } \ell \neq \ell' \end{cases} \quad (1.16)$$

And thus

$$\sigma_{scat} = \sum_{\ell=0}^{\infty} \pi\lambda^2 (2\ell+1) |1 - S_\ell|^2 \quad (1.17)$$

If the elastic scattering is the only occurring process, then $|S_\ell| = 1$ and it is common to write $S_\ell = e^{2i\delta_\ell}$, where δ_ℓ is the phase shift of the ℓ th partial wave (Fig. 1.2). For this case, $|1 - S_\ell|^2 = |1 - e^{2i\delta_\ell}|^2 = |1 - (\cos(2\delta_\ell) + i\sin(2\delta_\ell))|^2 = (1 - \cos(2\delta_\ell))^2 + (\sin(2\delta_\ell))^2 = 4 \sin^2\delta_\ell$ and the scattering cross section becomes:

$$\sigma_{scat} = \sum_{\ell=0}^{\infty} 4\pi\lambda^2 (2\ell+1) \sin^2\delta_\ell \quad (1.18)$$

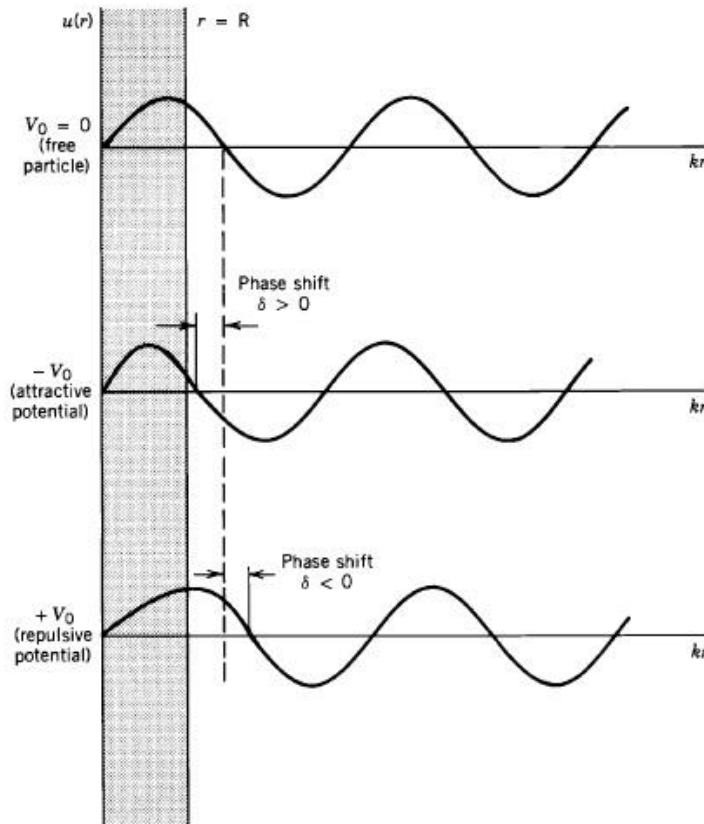


Figure 1.2 The scattering potential is shifting the phase of the scattered wave at points beyond the scattering regions [2].

If inelastic scattering or other reactions are occurring along with the elastic scattering, then Equation (1.18) is not valid, because $|S_\ell| < 1$. All the other processes' probabilities are grouped together under the term of the so called 'reaction cross section' σ_{react} . To find this cross section, Equation (1.9) must be examined in order to find the rate at which particles are "disappearing" from the channel with wave number k . Firstly, the current of the reaction is found using the difference between the incoming current and the outgoing current via, respectively, the first and second terms of Equation (1.9):

$$|j_{react}| = |j_{inc}| - |j_{out}| = \frac{|A|^2 \hbar}{4mkr^2} \left\{ \left| \sum_{\ell=0}^{\infty} (2\ell + 1) i^{\ell+1} e^{i\frac{\ell\pi}{2}} P_\ell(\cos\theta) \right|^2 - \left| \sum_{\ell=0}^{\infty} (2\ell + 1) i^{\ell+1} S_\ell e^{-i\frac{\ell\pi}{2}} P_\ell(\cos\theta) \right|^2 \right\} \quad (1.19)$$

And then the reaction cross section becomes:

$$\sigma_{react} = \sum_{\ell=0}^{\infty} \pi \lambda^2 (2\ell + 1) (1 - |S_\ell|^2) \quad (1.20)$$

The total cross section can now be calculated as:

$$\sigma_{total} = \sigma_{scat} + \sigma_{react} = \sum_{\ell=0}^{\infty} 2\pi \lambda^2 (2\ell + 1) (1 - \text{Re } S_\ell) \quad (1.21)$$

It should be noted here that it is possible to have only elastic scattering occurring in the absence of other processes; that is, if $|S_\ell| = 1$, then Equation (1.20) equals to zero. On the other hand, it is impossible, to have reactions without also having elastic scattering; that is, any choice of S_ℓ for which $\sigma_{react} \neq 0$ for a given partial wave automatically gives $\sigma_{scat} \neq 0$ from Eq. (1.17) for that partial wave.

In the case where the projectile is charged, it interacts with the combined Coulomb and nuclear potentials of the target nucleus. The equation for the scattering cross section is then derived from Eq. (1.21) along with Eq. (1.3), in order to account for the Coulomb scattering, as:

$$\frac{d\sigma}{d\Omega} = \left| f_c(\theta) + \frac{1}{2ki} \sum_{\ell=0}^{\infty} (2\ell + 1) (S_\ell - 1) e^{2i\sigma_\ell} P_\ell(\cos\theta) \right|^2 \quad (1.22)$$

Where $f_c(\theta)$ and σ_ℓ are the scattering amplitude and phase shift of the Coulomb scattering, respectively [1], [2].

In order to solve the Schrödinger equation and calculate S_ℓ , resulting in determining the elastic cross-section, it is essential to assume a form for the nuclear potential.

1.2 Optical Model for Elastic Scattering

Although the interaction of an incoming particle with an atomic nucleus can be described as the sum of the elementary interactions between the projectile and each of the nucleons of the nucleus, the potential of the scattering of one nucleon by another is not known. Moreover, the sum of these interactions would still not allow us to calculate the exact interaction, since it constitutes an unsolved many body problem. Therefore, in order to avoid these difficulties arising from the complicated interaction of a projectile with the nucleus, empirical optical potentials are used. The term ‘optical’ originates from the fact that the nucleus is a strong absorbing medium with respect to the incident nucleons, behaving similarly to an opaque glass sphere with respect to incoming light waves, causing reflection, absorption and interference effects.

In this section, the optical model is described. In the context of the optical model, the nucleus is represented by a potential $U(r)$ and thus it can be assumed that the projectile is interacting with the nucleus as a whole. This potential however, must display several characteristics arising from the nucleon-nucleon interaction. To begin with, it is mandatory to follow the nuclear matter distribution which reduces from its interior value close to the nuclear surface. It is expected that this reduction is performed exponentially as the nucleon-nucleon interaction. Moreover, the potential $U(r)$ should include a real part in order to account for the elastic scattering, as well as, a complex imaginary one, to account for the non-elastic processes (absorption effects). All these characteristics lead to the final equation for the optical model potential, which can be written as the sum of:

$$U(r) = U_R(r) + U_I(r) + U_D(r) + U_S(r) + U_C(r) \quad (1.23)$$

which contains parameters that can vary with the energy and the masses of the nuclei and their values can be chosen depending on the available experimental data. However, in order for the optical potential to make sense these values must not display large variations for close masses or neighboring energies.

The first term of Equation (1.23),

$$U_R(r) = -V f(r, R, a) \quad (1.24)$$

is the real one representing a nuclear well with depth V usually being multiplied by a Woods-Saxon form factor

$$f(r, R, a) = \{1 + \exp[(r - R)/a]\}^{-1} \quad (1.25)$$

where R is the radius of the nucleus, a is the diffuseness of the potential, meaning the width of the region where the function f ranges from 0 to 1. The Woods-Saxon factor produces a well with a smooth border, as shown in Fig. 1.3, which corresponds to reality better than the square well. The parameters V , R and a comprise adjustable parameters of the optical model.

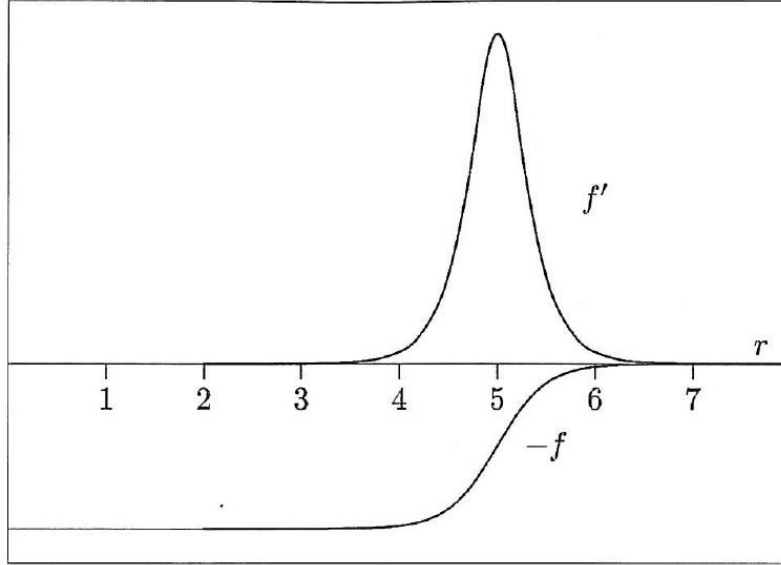


Figure 1.3 The Woods-Saxon factor which produces a well with round border and its derivative [4].

The next two terms $U_I(r)$ and $U_D(r)$ of Equation (1.23) account for the non-elastic processes, namely the absorption effects and therefore are imaginary. $U_I(r)$ corresponds to the absorption in the whole volume while $U_D(r)$ accounts for the absorption into the region close to the nuclear surface and can be written as:

$$U_I(r) = -i W f(r, R_I, a_I) \quad (1.26)$$

and

$$U_D(r) = 4i a_I W_D \frac{d}{dr} f(r, R_I, a_I) \quad (1.27)$$

These two terms ($U_I(r)$ and $U_D(r)$) act complementary to each other. That is, for high energies, the incident particle has a large penetration depth and the term $U_I(r)$ is dominant, whereas for low energies, the term $U_D(r)$ is important since the interactions occur essentially at the surface.

The fourth term of Equation (1.23) is a spin-orbit interaction term, loaned from atomic physics, which is usually written in the form:

$$U_S(r) = \mathbf{s} \cdot \boldsymbol{\ell} \left(\frac{\hbar}{m_\pi c^2} \right)^2 V_S \frac{1}{r} \frac{d}{dr} f(r, R_S, a_S) \quad (1.28)$$

containing a normalization factor which takes into account the mass of the pion; \mathbf{s} corresponds to the spin operator and $\boldsymbol{\ell}$ to the angular momentum one. The spin-orbit term is, like $U_D(r)$, only important in the surface of the nucleus, as it includes the derivative of the f factor. The values of the V_S , R_S , a_S parameters are adjusted to the experimental data in each case. The spin-orbit interaction may also result in an asymmetric scattering due to the possible different signs of the product $\mathbf{s} \cdot \boldsymbol{\ell}$, depending on which side of the nucleus the projectile passes by.

The necessity of this term in the optical potential equation lies in the fact that nucleons have spin $\frac{1}{2}$ and even if the incident beam is unpolarized, the scattered beam is polarized in the direction perpendicular to the scattering plane. Thus, the spin-orbit term accounts for the polarization and thus the optical model is in principle able to reproduce the experimental values of the polarization.

Last but not least, the final term of Equation (1.23), $U_C(r)$, corresponds to the Coulomb scattering in the case where charged particles are involved in the scattering. It can be written as:

$$U_C(r) = \begin{cases} \frac{Z_1 Z_2 e^2}{2R_C} \left(3 - \frac{r^2}{R_C^2} \right) & r \leq R_C \\ \frac{Z_1 Z_2 e^2}{r} & r > R_C \end{cases} \quad (1.29)$$

where the nucleus is considered to be a homogeneously charged sphere of radius equal to the Coulomb barrier radius (R_C) [1], [3], [4].

1.3 Reaction mechanisms

Nuclear interactions can proceed via several mechanisms. The mechanism characterizing each interaction depends on the incident energy, the incident angle and the kind of particles that are involved in the interaction. All the mechanisms are shown in Fig. 1 and the main ones, occurring when deuterons are the incident nuclei, are detailed below.

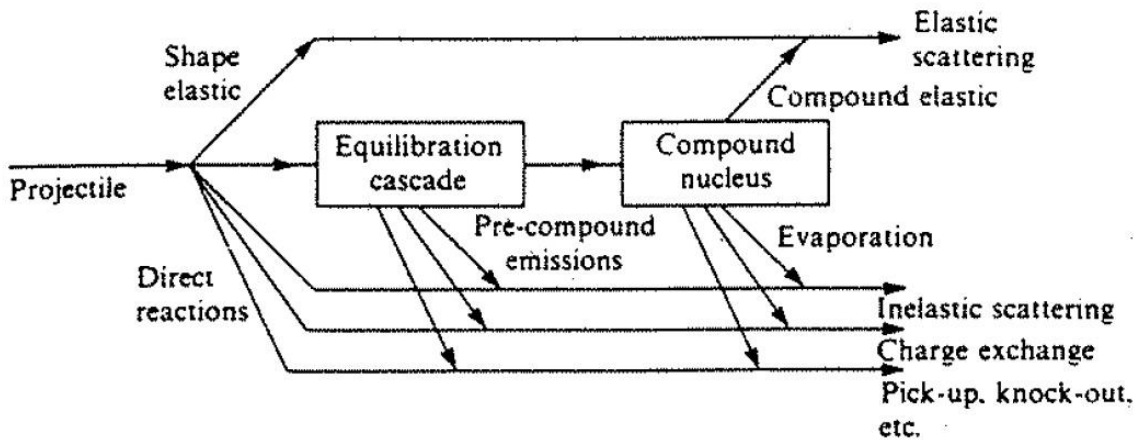


Figure 1.4 A sketch of the possible interaction scenarios emerging from a nucleon-nucleus collision [3].

1.3.1 Compound nucleus mechanism

If an incident particle enters a target nucleus with a small impact parameter compared to the nuclear radius, then it will, with a high probability, scatter and make successive collisions with other nucleons. In the course of such process one or more particles can be emitted and form, along with the residual nucleus, the products of a reaction which is called a pre-equilibrium one. If the particle is not emitted, it performs several interactions with the nucleons and afterwards the incident energy is randomly shared among many of the nucleons of the combined system of the projectile and the target. The average increase in energy of any single nucleon is not adequate to free it from the nucleus, since it is much smaller than the binding energy. However, as many more-or-less random collisions occur, there is a statistical distribution (Maxwell-Boltzmann) in energies and a small probability for a single nucleon to gain adequate energy to escape. This results in the relatively long-lived intermediate state of the compound nucleus $\sim 10^{-18} \text{ s} - 10^{-16} \text{ s}$, but also lifetimes as long as 10^{-14} s have been observed.

In such cases, where a definite intermediate state is created, after the absorption of the incident particle and before the emission of the outgoing particle (or particles), the reaction can be written as: $a + X \rightarrow C^* \rightarrow Y + b$, where C^* indicates the compound nucleus. Therefore, the compound nucleus reaction is a two-step process: the formation and the subsequent decay of the compound nucleus. A formed compound nucleus possesses a variety of possible decay modes (elastically, inelastically, reaction or gamma rays) and, according to Bohr-independence hypothesis, the relative probability of decaying into a specific set of final products is independent of the means of formation of the compound nucleus. The set of final products depends only on the energy acquired by the system; meaning that the compound nucleus "forgets" the process of its formation and decays, governed primarily by statistical rules and conservation laws.

Bohr-independence hypothesis, meaning the compound nucleus model, is best applied in cases where the incident energy is low (below 20 MeV) and therefore the projectile has a small possibility of escaping the nucleus, preserving both its energy and identity. Moreover, the compound nucleus model works best in cases of medium and heavy nuclei ($Z \geq 30$) where the interior of the nucleus is adequately large in order to absorb the energy of the projectile. An important characteristic of the compound nucleus model is the nearly isotropic angular distribution of the emitted particles, which originates from the random interactions among the nucleons and the Bohr-independence hypothesis. The compound nucleus mechanism is schematically illustrated in Fig. 1.5 [2].

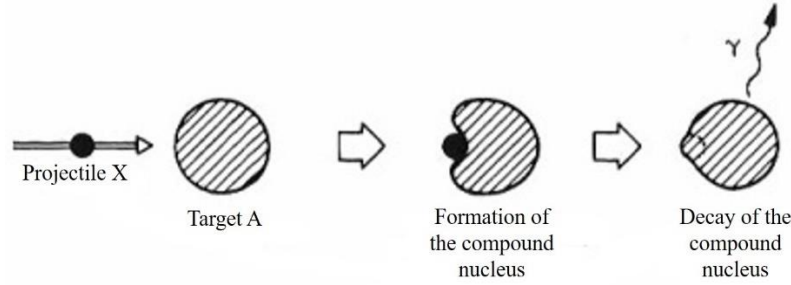


Figure 1.5 Formation of the compound nucleus (Based on [40]).

At this point, it should be noted that it was theoretically predicted by Ericson (1963) [41] that when a compound nucleus is formed at excitation energies such that its levels completely overlap, meaning it is no longer possible to distinguish individual resonances from each other, then the differential cross section is simultaneously dominated by a large number of resonances, the amplitudes of which interfere strongly. This interference between the different resonances displays largely a random nature and gives rise to fluctuations in the differential cross sections around an average value. The theory predicts that cross sections at any two energies differing by more than Γ and cross sections leading to different final levels are statistically independent. These fluctuations predicted by Ericson were experimentally verified by different authors e.g. [42], [43]. In the course of the present thesis, Ericson fluctuations may contribute to the differential cross-section behavior of the deuteron elastic scattering on silicon for deuteron energies above ~ 1600 keV, as discussed in Chapter 4.

1.3.2 Direct reaction mechanism

In direct or peripheral reactions, the incident particle interacts primarily at the surface of the target nucleus with one nucleon, very few valence nucleons or the whole nucleus. As the energy of the incident particle increases, its de Broglie wavelength (λ) decreases, until it becomes more likely to interact with a nucleon-sized object, than with a nucleus-sized one. A 1-MeV incident nucleon has a $\lambda \sim 4$ fm, and thus does not distinguish individual nucleons; it is more likely to interact through a compound-nucleus reaction. A 20-MeV nucleon, on the other hand, has $\lambda \sim 1$ fm and therefore could distinguish individual nucleons and thus participate in direct processes.

In some cases a reaction proceeds via both the compound nucleus and the direct reaction mechanisms and thus both mechanisms contribute to the cross section. These two contributions could be distinguished through two principal differences that can be experimentally observed:

- The time scale of the occurred reaction is very different between the two mechanisms. Direct processes occur very rapidly, in a time scale of the order of 10^{-22} s, while compound-nucleus processes typically take much longer, close to 10^{-16} - 10^{-18} s. Such a difference is

expected since in the compound nucleus mechanism a statistical equilibrium needs to be attained by the system. A few experimental techniques exist for distinguishing between these two incredibly short intervals of time.

- The second difference is related to the angular distribution of the outgoing particles. As mentioned above, the angular distributions of interactions proceeding via the compound nucleus mechanism are relatively isotropic, whereas in the case of direct reactions, more sharply peaked and forward angular distributions are produced.

The simplest direct reaction is the elastic scattering of a single bombarding particle from a potential well, representing the nucleus. In this case, the incident particle is directly scattered by the nuclear potential, without forming the resonant state and is called potential or shape elastic scattering. For deuterons at very low energies as projectiles and a heavy element as the target nucleus, the deuterons are repelled by the electrostatic field of the nucleus (Coulomb) and are scattered elastically with a cross section given by the Rutherford formula. This interaction is included in direct reactions.

Inelastic scattering could proceed via both reaction mechanisms, namely a direct process and a compound nucleus one, largely depending on the energy of the incident particle. In the cases where the projectiles are deuterons, the stripping reaction (d,n) proceeds via both mechanisms. Another stripping reaction, namely (d,p), is more likely to proceed via a direct process, since the “evaporation” of protons from the compound nucleus is partly inhibited by the Coulomb barrier. It should be mentioned here that when a deuteron is approaching a nucleus is oriented in such a way that the proton is further from the nuclear core than is the neutron, due to the electrical forces. Thus, taking into account the deuteron orientation, the deuteron small binding energy (2.2 MeV) and the relatively large diameter, it is more likely that the neutron is absorbed by the nucleus while the proton keeps moving in a forward direction.

Single-particle transfer reactions and especially the deuteron stripping ones, (d,p) and (d,n), are among the most important reactions since critical information about the nuclear structure has been obtained in the past through their implementation [44]. More specifically, such reactions allow the identification of the single-nucleon states of a nucleus. In the case of a (d,p) reaction, for instance, the neutron is captured into a vacant single-particle state and the detection of the energy of the outgoing proton determines the energy of the excited state of the residual nucleus. Moreover, the angular distribution and the polarization of the outgoing proton can determine the spin and the parity of the state in which the neutron was captured [1]–[3].

Illustrated in Fig. 1.6 are the contributions of the different reaction mechanisms of a proton beam inelastically scattered by ^{54}Fe at 40° scattering angle and for the proton energy of 29 MeV. Several differences exist between the scattering procedures studied in the present thesis and the $^{54}\text{Fe}(p,p_0)^{54}\text{Fe}$ scattering, for instance different projectiles, different beam energies and different scattering angles, however, it is included for the qualitative illustration of the dominant reaction mechanism at each energy region. At the highest energy part of the spectra the peaks correspond to particles with definite energies, which give the excitation energies of discrete low-lying states

of the residual nucleus. These particles originate from the direct reaction mechanism. At the lower energy part of the spectra a Maxwellian peak exists due to protons with energies only slightly greater than the Coulomb potential in the proximity of the iron nucleus, corresponding to the compound nucleus mechanism.

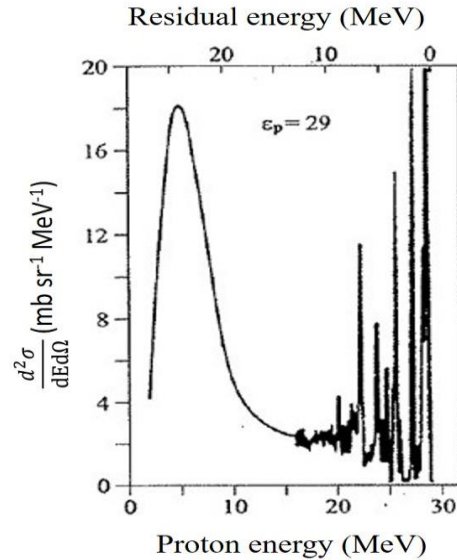


Figure 1.6 Spectrum of protons with 29 MeV incident energy inelastically scattered at 40° by ^{54}Fe (Part of [3]).

In the present dissertation only low deuteron beam energies were used and thus the dominant reaction mechanisms are the compound nucleus and the resonant one, detailed in the next section.

1.3.3 Resonant reactions

The compound nucleus model leads to reaction cross sections without sharp minima or maxima since the probed nuclear states form a structureless continuum, meaning a plethora of discrete nuclear states so close together that they form a continuum spectrum. On the other hand, the bound states are studied by direct reactions. Between these two extremes is the resonance region-discrete levels in the compound-nucleus region. These levels have large cross sections, meaning a high probability of formation, while their widths are usually small (implying relatively large lifetimes), and the quasibound state that is formed usually has only two modes of decay available to it; γ emission or re-ejecting of the incident particle, as in elastic or inelastic scattering.

In the case of the formation of a resonance, the incident particle interacts with the nuclear potential which is represented by a square well, in the simplest case. The oscillatory wave functions inside and outside the well must be matched smoothly at the nucleus surface ($r=R$). Fig. 1.7 displays three different cases of how this might occur. In case (a), where the amplitudes of the wavefunctions inside and outside the well match badly at the nucleus surface, the incident particle has relatively

little probability to penetrate the nucleus. In case (b) a higher probability for penetration exists while, in case (c), where the amplitudes match exactly, the incident particle easily penetrates the nucleus, forms a quasibound state, achieving the resonance, while the cross section reaches a maximum value. As the energy of the incident particle varies, the relative phase of the inner and outer wave functions varies; the location of the matching point and the relative amplitudes vary accordingly. The conditions shown in case (c) of Fig. 1.7 can be achieved only for certain incident energies, the energies of the resonances in the cross section.

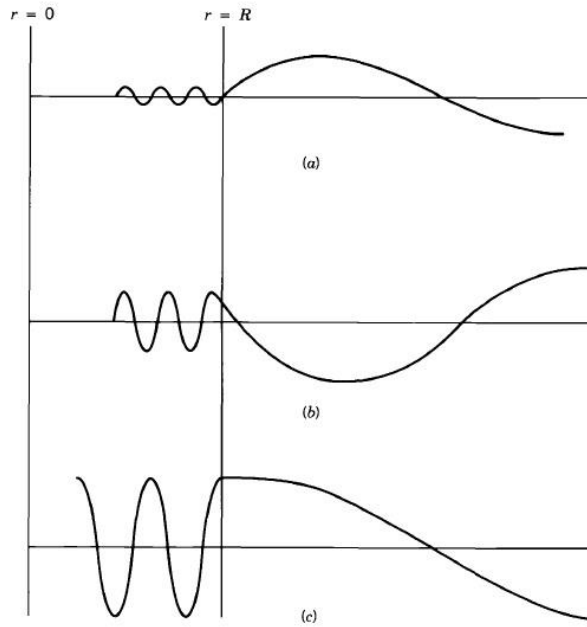


Figure 1.7 Three cases of a particle approaching a nucleus. In case (a) the wavefunctions match badly thus little probability of penetration exists, in case (b) higher probability for penetration exists and in case (c) the resonance case is displayed where the wavefunctions match exactly [2].

The cross-section for a single isolated resonance of energy E_R and width Γ , in the case of elastic scattering, is described by the Breit-Wigner formula:

$$\sigma = \frac{\pi}{k^2} g \frac{(\Gamma_{ax})^2}{(E - E_R)^2 + \Gamma^2/4} \quad (1.30)$$

where g is a general statistical factor accounting for the spins of the reacting particles. More specifically, if s_a and s_x are the spins of the incident and target particles, and if J is the total angular momentum of the resonant state (meaning that $J = s_a + s_x + \ell$) then g is: $g = \frac{2\ell+1}{(2s_a+1) \cdot (2s_x+1)}$.

For spinless particles ($s_a = s_x = 0$) then $g = (2\ell+1)$. Γ_{ax} is the partial width of the entrance and the exit channel, since Equation (1.30) describes the elastic scattering and Γ is the sum of all partial widths: $\Gamma = \sum_i \Gamma_i$. The Γ^2 factor in the denominator is related to the decay width of the resonant state and therefore to its lifetime: $\Gamma = \hbar/\tau$. Finally, k is the wave number of the outgoing scattered particle. Fig. 1.8 (b) shows the structure of a Breit-Wigner resonance. Moreover, a common elastic

scattering shape is the one shown in Fig. 1.8 (a). This originates from potential or shape elastic scattering. The interference between these two processes, namely the potential and the resonant scattering, can lead to smaller or higher values of the combined cross section than it would be for either process alone. Such an interference is shown in Fig. 1.8 (c). Thus, the contribution of the two processes should be calculated by writing the complex scattering amplitude as:

$$S_\ell = e^{2i(\delta_{\ell R} + \delta_{\ell P})} \quad (1.31)$$

where $\delta_{\ell R}$ is the resonant phase shift and $\delta_{\ell P}$ is an additional contribution to the phase shift due to potential scattering.

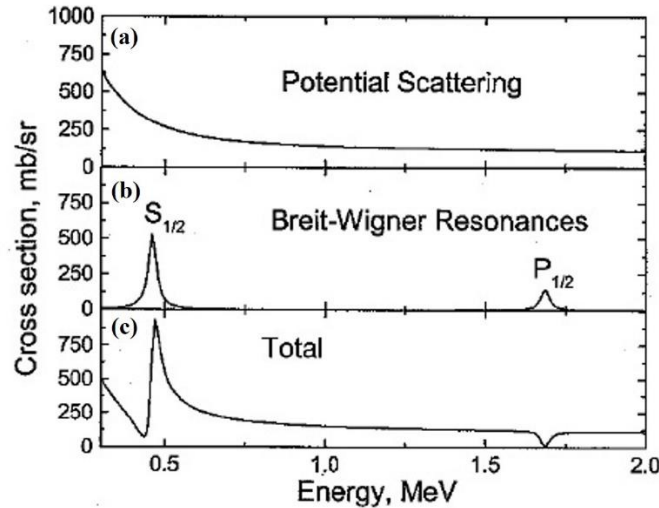


Figure 1.8 Interference of the potential and resonance scattering for $^{12}\text{C}(p,p_0)^{12}\text{C}$ [1].

In order to calculate the elastic scattering cross section, the determination of the phase shifts is necessary. This can be performed by a few phenomenological approaches. In the context of the phase shift analysis, for instance, one can calculate the phase shifts by directly fitting the cross section relations. A second approach is to solve the Schrödinger equation for partial waves, with the parameters of the nuclear potential being free. However, the applicability of the optical model near and below the Coulomb barrier is still debatable. Finally, the framework of the R-matrix theory [33], described in the next section, could be used by adjusting the compound nucleus level parameters and the boundary conditions [1].

1.4 R-Matrix theory

1.4.1 Introduction

The R matrix framework (1947, Wigner & Eisenbud [5]) is a theoretical approach for calculating differential cross sections mainly when the structure presents minima and maxima which correspond to discrete levels of the formed compound nucleus. It regards an interaction between a projectile and the nucleus as a whole, as a black box with an unknown internal structure. The

properties of the internal structure, which correspond to the elements of the R-matrix, are treated as adjustable parameters of the theoretical calculations to the available experimental cross section datasets [45].

The R-matrix approach is based on the assumption that the interaction between the projectile and the nucleus proceeds via the compound nucleus mechanism, as well as, that the cross section structure is governed by the interference between the resonant and the potential scattering. Since, in the case of deuterons (up to 2.5 MeV) impinging on a low/medium Z target, the dominant reaction mechanism is the compound nucleus one, the R-matrix theory is the most suitable approach for analyzing such elastic scattering cases. The basic principles of the R-matrix theory are described in the section below.

1.4.2 Basic principles

The basic concept of the R matrix theory is the division of the configuration space of the problem into an “internal” and an “external” region. The internal region corresponds to the compound nucleus, whereas the external one corresponds to the reaction alternatives, or channels, possible to reach the compound nucleus or emerge from it. An illustration in three dimensions of the internal and external regions of the space for resonance reactions can be found in Fig. 1.9.

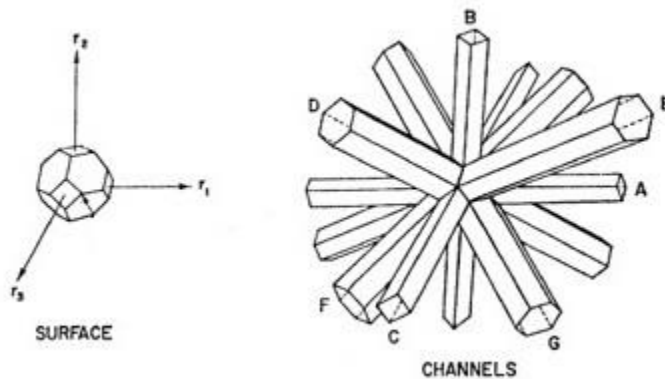


Figure 1.9 Schematic representation in three dimensions of the actual surface of the compound nucleus and the channels emerging from it (part of [46]).

Such division of the internal and the external region represents the radius of the atomic nucleus and it is accomplished via the choice of boundary conditions on the nuclear radius of the compound nucleus. Thus, for each reaction channel, a nuclear radius is chosen. The fact that the boundary conditions of the wavefunctions of the internal region and the external region must match on each nuclear radius, leads to resonances in the cross-section structure. The nuclear or internal parameters involved in the R-matrix framework are strongly tied to the basic nuclear physics properties, e.g. the nuclear radius which is used in the R-matrix framework originates from the

short range of nuclear forces, designating the R-matrix framework as the best one for the description of resonance properties.

1.4.3 Elastic scattering of a spinless particle by a central potential

The derivation of the R-matrix for the elastic scattering of a particle with a spin by a potential is highly complicated due to the involved spins, the Coulomb fields and the possibility of nuclear reactions. Therefore, in this section, the R-matrix will be derived for the simplest case of the elastic scattering of a spinless particle by a central potential $V(r)$. This interaction includes the centrifugal potential for each partial wave and the scattering of charged spinless particles by a nuclear potential well.

In the external region, the differential cross section for each partial wave was derived (Equation (1.15)), including the effects of partial waves and the Coulomb potential:

$$\frac{d\sigma}{d\Omega} = \frac{1}{4k^2} \left| \sum_{\ell=0}^{\infty} (2\ell + 1) i (1 - U_{\ell}) P_{\ell} \cos\theta \right|^2$$

The integrated cross section (Equation 1.17) was:

$$\sigma_{scat} = \sum_{\ell=0}^{\infty} \pi \lambda^2 (2\ell + 1) |1 - U_{\ell}|^2$$

where the collision functions $U_{\ell} = \exp(2i\delta_{\ell})$ are related to the phase shifts for each partial wave. Therefore, in order to calculate the cross section, the collision functions need to be determined.

In the internal region, meaning the compound nucleus, resonances or stationary states $X_{\lambda\ell}(r)$ exist for each partial wave. Thus, the Schrödinger radial equation for each partial wave is:

$$-\frac{\hbar^2}{2m} \left(\frac{d^2 X_{\lambda\ell}}{dr^2} \right) + V(r) X_{\lambda\ell} = E_{\lambda\ell} X_{\lambda\ell} \quad (1.32)$$

and the boundary condition at the nuclear radius is:

$$a_{\ell} \left. \frac{dX_{\lambda\ell}}{dr} \right|_{r=a} = b_{\ell} X_{\lambda\ell}(a_{\ell}) \quad (1.33)$$

where a_{ℓ} is the matching radius chosen for each partial wave to separate the internal from the external region and b_{ℓ} is the boundary condition number chosen for each partial wave. Thus, a boundary value problem for the resonant states emerges, where, if the boundary condition numbers are real, the problem is Hermitian.

The internal wave function, $\varphi_{\ell}(r)$, at energy E , satisfies the same Schrödinger equation:

$$-\frac{\hbar^2}{2m} \left(\frac{d^2 \varphi}{dr^2} \right) + V(r) \varphi = E \varphi \quad (1.34)$$

Multiplying Equation (1.34) by $X_{\lambda\ell}^*(r)$ and the complex conjugate of Equation (1.32) by $\varphi(r)$, subtract and integrate them, then apply Green's theorem, the logarithmic derivative at the matching radius is obtained as:

$$(\varphi'_\ell/\varphi_\ell)|_{r=a} = (1 + b_\ell R_\ell)/R_\ell \quad (1.35)$$

where the prime indicates the dimensionless derivative, $\varphi'_\ell = r \frac{d\varphi_\ell}{dr}$ and the R-function is defined as:

$$R_\ell = \sum_\lambda \gamma_{\lambda\ell}^2 / (E_{\lambda\ell} - E) \quad (1.36)$$

with the reduced width, $\gamma_{\lambda\ell}^2$ of level λ defined as:

$$\gamma_{\lambda\ell}^2 = (\hbar^2/2ma_\ell) X_{\lambda\ell}^2(a_\ell) \quad (1.37)$$

The external radial equation must include terms of the central and the Coulomb potential and is given by:

$$\frac{d^2\varphi_\ell}{dr^2} - \left[\frac{\ell(\ell+1)}{r^2} + \left(\frac{2m}{\hbar^2} \right) \left(\frac{-E + Z_1 Z_2 e^2}{r} \right) \right] \varphi_\ell = 0 \quad (1.38)$$

This equation has regular solutions F_ℓ , which are finite at $r = 0$ and irregular ones, G_ℓ , which are not finite at $r = 0$. At large r , their asymptotic behavior is:

$$F_\ell \sim \sin \left[kr - \eta \log(2kr) - \left(\frac{1}{2} \right) \ell \pi + \sigma_\ell \right] \quad (1.39)$$

and

$$G_\ell \sim \cos \left[kr - \eta \log(2kr) - \left(\frac{1}{2} \right) \ell \pi + \sigma_\ell \right] \quad (1.40)$$

where $k = mv/\hbar$ and the Coulomb phase shift (σ_ℓ) and the Coulomb parameter (η) are given by:

$$\sigma_\ell = \arg[1 + \ell + i\eta] \quad (1.41)$$

$$\eta = \frac{Z_1 Z_2 e^2}{\hbar v} \quad (1.42)$$

and the incoming (I_ℓ) and outgoing (O_ℓ) wave functions in the external region are:

$$I_\ell = (G_\ell - iF_\ell) \exp(i\omega_\ell) \quad (1.43)$$

$$O_\ell = (G_\ell + iF_\ell) \exp(-i\omega_\ell) \quad (1.44)$$

With $\omega_\ell = \sum_{n=1}^{\ell} \tan\left(\frac{\eta}{n}\right)$ being the Coulomb phase. The penetration factor (P_ℓ), the shift functions (S_ℓ) and the scattering phase shifts Ω_ℓ can now be written as:

$$P_\ell = \frac{kr}{(F_\ell^2 + G_\ell^2)} \quad (1.45)$$

$$S_\ell = \frac{(F'_\ell F_\ell + G'_\ell G_\ell)}{(F_\ell^2 + G_\ell^2)} \quad (1.46)$$

And $O_\ell^{-1} I_\ell = \exp(2i\Omega_\ell)$ with

$$\Omega_\ell = \omega_\ell - \tan\left(\frac{F_\ell}{G_\ell}\right) \quad (1.47)$$

where $-\tan(F_\ell/G_\ell)$ is the phase shift of the hard sphere. Such hard sphere phase shifts result from the division into external and internal quantities at the matching radius. The internal potential, $V(r)$, is assumed to be vanishing in the external region and thus the sudden change at the matching radius introduces square-well phase shifts.

The internal and external logarithmic derivatives are matched in the matching radii and the collision function is obtained as:

$$U_\ell = O_\ell^{-1}(1 - R_\ell L_\ell)^{-1}(1 - R_\ell L_\ell) * I_\ell \quad (1.48)$$

In which I_ℓ and O_ℓ correspond to the incoming and outgoing wave functions, as before and $L_\ell \equiv O'_\ell/O_\ell - b_\ell$. Through the above equations L_ℓ can be also written as:

$$L_\ell \equiv O'_\ell/O_\ell - b_\ell = S_\ell - b_\ell + iP_\ell \quad (1.49)$$

The R-function (Equation 1.36) along with the external functions I_ℓ , O_ℓ , L_ℓ (Equations 1.43, 1.44, 1.49 respectively) are inserted in the collision functions U_ℓ (Equation 1.48) and subsequently the collision functions are inserted in the cross section relation (Equation 1.17). Hence, the cross section is determined as:

$$\sigma = \left(\frac{\pi}{k^2}\right) (2\ell + 1) \left| -\exp(2i\Omega_\ell) \left\{ 1 + i\Gamma_{\lambda\ell} / \left[(E_{\lambda\ell} - E + \Delta_{\lambda\ell}) - \left(\frac{i}{2}\right)\Gamma_{\lambda\ell} \right] \right\} \right|^2 \quad (1.50)$$

where

$$\Gamma_{\lambda\ell} = 2P_\ell \gamma_{\lambda\ell}^2 \quad (1.51)$$

and

$$\Delta_{\lambda\ell} = (S_\ell - b_\ell) \gamma_{\lambda\ell}^2 \quad (1.52)$$

Therefore, an expression of the cross section (Equation 1.50) is deduced, which includes the interference between the potential and resonant scattering and contains all the essential elements of a resonance: The resonance can be very narrow by choosing its energy (via the choice of the potential well depth), $E_{\lambda\ell}$, to be sufficiently far below the Coulomb barrier; the level shift, $\Delta_{\lambda\ell}$, is energy dependent and also depends on the choice of the boundary condition number. Therefore, the obtained equation of the cross section contains most of the elements of the real nuclear problem except for the complications introduced by the spins, which were ignored here, and the complications introduced by the possibility of an additional occurring reaction. In this case the functions of (1.48) all become matrices.

One reason that the R-matrix framework was not, initially, as successful as it was afterwards, was that the channel parameters (matching radius and boundary condition numbers) were initially considered too artificial. In fact, the boundary condition numbers were often chosen to be zero for all channels. However, definitions containing physics do exist for these parameters and were analyzed later. More specifically, it is quite advantageous that the boundary condition numbers b_ℓ

correspond only to outgoing waves (since the resonances naturally decay) thus to be equal to $S_\ell + iP_\ell$. This equation originates from $L_\ell \equiv O'_\ell/O_\ell - b_\ell = S_\ell - b_\ell + iP_\ell$ (Equation 1.49), where O_ℓ corresponds to the outgoing wave function. Thus, if $L_\ell=0$ then $b_\ell = S_\ell + iP_\ell$ which correspond only to outgoing waves. However, in order to preserve the Hermitian nature of the problem, b_ℓ needs to be real, so the closest real value is selected, meaning $b_\ell = S_\ell$. The shift functions S_ℓ vary slowly with energy, and by choosing the $b_\ell = S_\ell$ equation to be valid for a value of energy within the energy interval in which the data is analyzed, then the level shifts $\Delta_{\lambda\ell} = (S_\ell - b_\ell) \gamma_{\lambda\ell}^2$ (Equation 1.52) are close to zero for all resonances in the energy interval. Therefore, in this case, the resonance energies $E_{\lambda\ell}$ slightly differ from the positions of the states of the nucleus. This means that the boundary condition numbers are physically compelling and also lead to close values of the level energies and level widths that arise from the shell model.

The situation is simpler for the choice of the matching radii; it must lead to reduced widths $\gamma_{\ell\lambda}$ readily comparable to the results of nuclear structure calculations. It is proven that the most suitable choice for a matching radius value is approximately one fermi larger than the mid-point radius of the mean field [46].

1.4.4 The single channel multi-level R-matrix

In the single channel multi-level approach [33], [47], [48], the R-matrix reduces to a simple R-function:

$$R_{\ell J} = \sum_{\lambda=1}^{\infty} \frac{\gamma_{\lambda\ell J}^2}{E_{\lambda\ell J} - E} \quad (1.53)$$

The relation between the R-function and the collision function U_ℓ is (based on [48]):

$$U_\ell = \exp(2i\Omega_{\ell P}) |(1 - 2i) P_\ell (R'_\ell / (1 + L'_\ell R'_\ell))| \quad (1.54)$$

In the present thesis the R-matrix theory will be employed for the theoretical reproduction of the cross sections of deuteron elastic scattering on oxygen in the energy range of 1.98-2.5 MeV. The main purpose of this project is to theoretically investigate the energy region where the present evaluation stops (1.98 MeV). The calculations are performed only for the elastic channel and a few levels of the compound nucleus. The details of this procedure and the results are analytically presented in Chapter 5.

Chapter 2

Motivation and IBA techniques

2.1 Light Elements

Light elements find numerous technological applications in the industry. Most of them are highly reactive, resulting to their presence practically everywhere. They are crucial in the field of material analysis due to their presence in ceramics, glasses, and polymers, while they are also frequently added in metallic alloys in order to improve their corresponding properties, such as, hardness, wear and heat resistance, or rigidity. Since each isotope/element investigated in this thesis has different applications in a variety of fields in the industry and in science, it is deemed important that each isotope/element is analyzed in detail separately.

In more details, ${}^6\text{Li}$, comprising 7.59 % of natural lithium, has a very high neutron absorption cross section (~ 940 barns) and thus readily fissions to yield tritium and helium. ${}^6\text{Li}$ has been the main source of tritium which is used in biochemical research, future controlled fission, thermonuclear weapons and fusion power reactors. The usage of ${}^6\text{Li}$ depends to a great extent upon its diffusion properties. Consequently, the knowledge of ${}^6\text{Li}$ concentration gradients in the matrices is an important requirement in the continued development of all relevant technology [49].

${}^7\text{Li}$ (92.41 % of natural lithium) is present in various materials, such as ceramics, glasses, lubricants, greases. Moreover, a common use includes lithium ion batteries which are one of the most widely used portable energy devices. In the field of research for lithium ion batteries, the mobility of lithium creates problems in which a comprehensive understanding of lithium transport, acquired by the determination of lithium concentration depth profile, is necessary to get a consistent picture of the problem [50] and eventually lead to a solution. In fact, after a successful usage of lithium ion batteries in consumer electronics, efforts are made to extend the application to electric vehicles [51].

Concerning beryllium (100% ${}^9\text{Be}$, with traces of ${}^7\text{Be}$ and ${}^{10}\text{Be}$), although it is a relatively rare element in the universe, it finds numerous applications in the industry. It is added as an alloying element to metals such as copper (beryllium copper), aluminum, nickel and iron, as it improves many physical properties. A few of its own physical properties, e.g. high metal flexural rigidity, thermal stability and conductivity, lead to the usage of beryllium in mechanical and defense applications, namely as aerospace material for aircraft components, guided missiles, satellites and

space crafts. Moreover, beryllium has a reasonably high melting point, an ability to getter or bury oxygen in the absence of chemical reactivity with hydrogen and a relatively high neutron scattering cross-section. These characteristics render beryllium one of the most crucial materials in plasma-facing components of magnetic fusion energy devices [52]. It is important to note here that the accurate quantitative determination of beryllium depth profile concentrations leads to the assessment of beryllium erosion, material migration and deposition processes which are interdependent with the safety of tokamak fusion reactors.

Nitrogen (99.63% ^{14}N , 0.37% ^{15}N) comprises, in molecular form, ~77% of the earth atmosphere. It is widely used in metallurgy and in the semiconductor and insulator technology. In metallurgy, it is implanted into metals, e.g. steels, titanium and titanium alloys, because it increases their hardness, toughness and wear resistance, important features for cutting tools. In fact, a heat treating process called nitriding takes advantage of nitrogen diffusion into the surface of a metal in order to create a case-hardened surface and to enhance its mechanical properties. Nitrogen is also used as a common dopant for the creation of n-type semiconductors. Moreover, nitrogen is incorporated into bulk ceramics, in order to modify the physical and the electrical properties in industrial glasses, polymers and biological samples.

Oxygen (99.76% ^{16}O , 0.04% ^{17}O , and 0.2% ^{18}O) is the third most abundant element by mass in the universe and it comprises ~21% of the earth's atmospheric volume in molecular form. Oxygen is used in the production of steel, plastics and textiles, brazing, welding and cutting of steels and other metals. Furthermore, as it is highly reactive, oxygen-induced corrosion, or even simple oxidization, is a well-known problem in most technological materials. Thus, the accurate quantitative determination of oxygen depth profile concentrations in various targets is deemed necessary.

Sodium (100% ^{23}Na) is the sixth most abundant element in the Earth's crust. Sodium is never found in nature in pure elemental form as it is readily oxidized. Its compounds are present in minerals, glasses, aerosol particles and pigments and are of great importance for material, environmental, earth sciences and for cultural heritage studies. Pure sodium is used in the industry in its liquid form as heat transfer fluid in certain types of nuclear reactors [53], due to its high thermal conductivity and low neutron absorption cross section. Moreover, corrosion phenomena which are unavoidably present in soda-lime glasses (sodium is a matrix element in these kinds of glasses) and in order to prevent the corrosion it is necessary to understand the applied corrosion mechanism and the composition of the corroded glass. Thus, it is deemed necessary to monitor the compositional changes that occur during the corrosion process via the determination of sodium depth profiling.

Silicon (92.23% ^{28}Si , 4.67% ^{29}Si , 3.10% ^{30}Si) is the second most abundant element in the Earth's crust, due to the various forms of silicon dioxide and silicates present in dust and sands. Silicon and its compounds form the basis of many modern technologies and have found their applications in industry. For example, silicon is used in semiconductor electronics and particularly for silicon wafers that constitute matrices on which the semiconductor structures are built and are essential to

the integrated circuits used in computers, cell phones and modern technology. Although, silicon applications dominate the wafer technology, it is also used in the field of building materials, ceramics and glasses (soda- lime silicate glasses).

From the above-mentioned applications, it becomes evident that the accurate quantitative determination of light-element depth profile concentrations is of paramount importance in contemporary technology and science. However, the existence of all these light elements in relatively complex matrices, along with several medium- or high-Z elements, leads to a rather complicated analytical problem. The determination of the depth profile concentrations can best be accomplished via the implementation of Ion Beam Analysis (IBA) techniques.

2.2 Ion Beam Analysis Techniques

IBA techniques for the determination of depth profile concentrations are divided into categories based on the studied interaction and are schematically represented in Fig. 2.1. Depth profiling without any standards and almost non-destructively have rendered the IBA techniques as the most commonly used tools for material analysis. The IBA techniques suitable for depth profiling are the Rutherford Backscattering Spectrometry (RBS)/ Elastic (non-Rutherford) Backscattering Spectrometry (EBS), the Elastic Recoil Detection Analysis (ERDA) and the Nuclear Reaction Analysis (NRA). The fundamental characteristics of each of these techniques are outlined below.

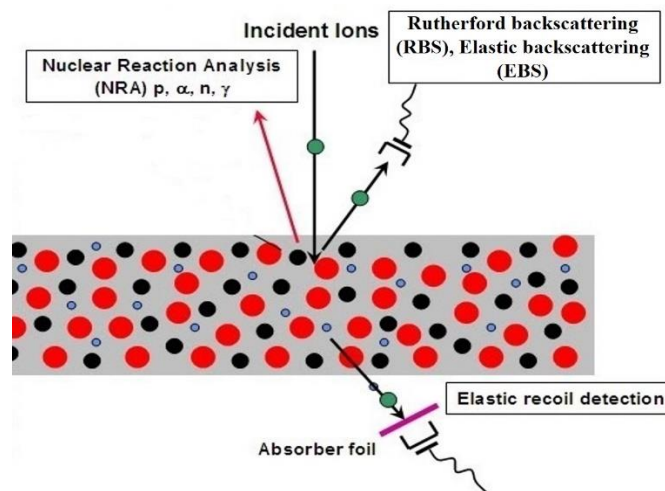


Figure 2.1 IBA techniques suitable for the determination of depth profile concentrations.

2.2.1 Rutherford Backscattering Spectrometry

RBS is the most widely used IBA technique for sample analysis since it provides elemental depth profiles non-destructively, with the use of a relatively simple experimental setup. The beam particle is scattered from the Coulomb potential of the target nucleus and the differential cross section follows the Rutherford formula (Equation 1.3) and can be analytically calculated. The kinematics of this interaction (conservation of energy and momentum) require that heavy (or light) target atoms scatter the primary ion beam at high (or low) energies. However, deviations from the Rutherford formula are observed at both low and high energies for all the beam-target combinations. For the low energies, these deviations are attributed to the screening effect of the beam particles due to the electrons surrounding both nuclei. Thus, a correction term $F_{LEcuycer}$ [54] is multiplied with the Rutherford cross-section value, which is given by:

$$F_{LEcuycer} = 1 - \frac{0.4873 Z_1 Z_2^{4/3}}{E_{CM}} \quad (2.1)$$

The screening effect is larger for heavier targets and heavier ions. For 1.5 MeV deuterons impinging on gold the correction term is ~1% whereas for 1.5 MeV deuterons impinging on lithium the correction term results to a practically zero correction in the cross-section values due to the screening effect. For high energies, the deviations are attributed to the nuclear forces present in the interaction. More specifically, as the beam energy increases and the target becomes lighter, the incident particle exceeds the Coulomb potential barrier and interacts with the nucleus, implying that the interaction is no longer purely Rutherford and thus cross-section measurements are deemed necessary for the implementation of the non-Rutherford EBS technique. Therefore, the RBS technique has been established as the standard analytical method for accurately measuring the depth concentration profiles of heavy elements in lighter matrices.

2.2.2 Elastic Recoil Detection Analysis

The ERDA technique is based on the elastic scattering, as the RBS one, but in this case the detected particle is the recoil nucleus which is scattered in the forward direction ($\theta < 90^\circ$) from the sample. The yield of the recoil particles is directly proportional to the amount of the corresponding element in the target layer. ERDA can yield quantitative depth profiles of any light element, using commonly a heavy ion beam and it is widely used for the depth profiling of hydrogen, deuterium and helium. The sensitivity of the ERDA technique is in the order of parts per million or even better and the depth resolution depends on the detector resolution and could be of the order of 1 nm. The main drawback in the implementation of the ERDA technique is that it provides depth information only for the near-surface target layers, due to the heavy ion beams used and the high stopping power values involved. The cross-section values are given by more or less the Rutherford cross-section (Equation 1.3), along with screening corrections (Equation 2.1) [4 - Chapter 5].

2.2.3 Elastic (non-Rutherford) Backscattering Spectroscopy

In several cases of elastic scattering the cross-section is not purely Rutherford, as described in section 1.1, due to the interference of the Coulomb and the nuclear potential. In these cases the cross-section values have to be measured. The implementation of the EBS technique is based on the usage of these experimental cross-section measurements and can provide accurate results for light elements. EBS is presented in detail in the section 2.4.

2.2.4 Nuclear Reaction Analysis

Concerning the NRA technique; it is similar to the RBS one from the experimental point of view, but in the NRA technique the detected particles are ejected from the inelastic reaction of the beam with the target and not from elastic scattering. NRA is analyzed in detail in the next section. Moreover, it is possible that the detected particles are γ -rays. In this case, the technique is called Particle Induced Gamma ray Emission (PIGE). These γ -rays originate from the excited nucleus, as it de-excites by emitting γ -rays. The acquisition of a depth profile with the PIGE technique could be achieved through the shifting of a sharp resonance along the thickness of the target (the so-called resonant-PIGE). The PIGE technique is not frequently implemented for the acquisition of the depth profile of light elements, since resonances are usually very wide and limit the resolution of the technique. However, several cases exist where resonant PIGE is implemented with high precision, especially via the reactions $^1\text{H}(^{15}\text{N},\alpha\gamma)^{12}\text{C}$ (4.43 MeV γ -ray [55]) , $^1\text{H}(^{19}\text{F},\alpha\gamma)^{16}\text{O}$ (6-7 MeV γ -rays [55]), $^{19}\text{F}(p,\alpha\gamma)^{16}\text{O}$ (6-7 MeV γ -rays [56]) and $^{23}\text{Na}(p,\alpha\gamma)^{20}\text{Ne}$ (using the 440 keV γ -ray [57], [58]).

2.2.5 Parameters for choosing the most suitable IBA technique for each case

In order to choose the most suitable IBA technique for each specific case, a number of parameters have to be examined. The ion beam and the beam energy, the emitted ejectile and the scattering angle, the elements/isotopes existing in the under-study sample and whether the desired result is a simple quantitative analysis or a depth profile determination, are among the most important ones. For example, higher beam energies (used for thick targets) allow for the analysis of deep layers at the expense of depth resolution, since the stopping power is reduced as the beam energy increases. Depth resolution can be improved by using a heavy ion beam for thin samples or by increasing the outgoing particle path by tilting the target or by changing the detector angle. Hence, all this information must be taken into account before deciding which is the most suitable IBA technique

for each case. Moreover, another crucial parameter for choosing the most suitable IBA technique is the availability of the specific cross section dataset in the literature. Except for the RBS and the ERDA techniques, in which the cross-section is analytically derived (Eq. 1.3), the implementation of the EBS and the NRA techniques completely relies on the available cross-section datasets. Thus, the cross-section datasets should be available, but should also be accurate and reliable, because the final results are based on these values. Since all the available datasets in literature are either measured or evaluated, with the latter being also based on measurements (as described in Chapter 5), the only way to test their accuracy and reliability is via a benchmarking experiment [23]. A benchmarking experiment is performed in order to validate a specific differential cross section dataset. Thus, with the use of a thick target containing the element/isotope of interest at a known composition, the experimental spectrum is simulated using the cross-section data to be checked. This whole procedure determines the error margin of the benchmarked data. The benchmarking procedure is analyzed in more detail in Chapter 4. For the easier implementation of the IBA techniques a data library has recently been created at the International Atomic Energy Agency (IAEA) called IBANDL (Ion Beam Analysis Nuclear Data Library) [38], in which measured and evaluated cross-section datasets are included. The evaluated cross-sections are provided by the online calculator SigmaCalc [59], developed by Dr. A. F. Gurbich.

2.3 Deuteron Nuclear Reaction Analysis Technique

As already mentioned, in the NRA technique the detected particles originate from inelastic processes with high Q-values. These offer the significant advantage of having emitted particles with high energies (higher than the elastically scattered ones), appearing in the high energy region of the experimental spectrum, where little or no background due to the target matrix exists. Moreover, NRA provides high isotopic selectivity and the possibility of the simultaneous analysis of more than one light elements in near surface analysis for the determination of non-destructive depth profiles. Hence, these significant advantages render the NRA technique a very useful tool for the detection and concentration depth profiling of light elements/isotopes in heavy, complicated matrices. Especially in the cases where the incident beam is deuterons, the simultaneous analysis of most of the light elements/isotopes is possible, since deuterons excite most of the main light isotopes coexisting in a target; in some cases though, an increased background is created. Furthermore, d-NRA is characterized by the relatively high cross-section values involved, which lead to enhanced sensitivity and accuracy, especially in the depth profiling of light isotopes present in small concentrations. In fact, these are the reasons why the $^{12}\text{C}(d,p_0)$, $^{14}\text{N}(d,p_0)$, $^{16}\text{O}(d,p_{0,1})$ and $^{23}\text{Na}(d,p_0)$ reactions constitute flagships in the determination of depth profile concentrations of the corresponding light elements. It should be noted though, that when the deuteron-induced NRA technique is implemented, neutrons are also emitted due to (d,n) reactions on the target elements and materials along the beam path as well as from the deuteron breakup (for deuteron beam energies higher than 2.2 MeV) and thus radiation safety precautions are obligatory. However, the

emitted neutrons usually do not cause problems at the low energies and currents (of the order of nA) typically employed during NRA studies.

2.4 Deuteron Elastic Backscattering spectroscopy

In the above section the outstanding advantages of the d-NRA technique in the analysis of light elements have been illustrated. The implementation of the d-NRA technique could be greatly enhanced if the ever-existing elastic peaks appearing in the low-energy part of the experimental spectrum, could also be analyzed. This simultaneous analysis of the elastic and the inelastic peaks, implying the simultaneous implementation of both the EBS and the NRA techniques, could lead to the full analysis of the target matrix. However, the cross-section values required for the EBS technique are usually a combination of the Coulomb, the nuclear potential and the resonant scattering, as already mentioned, and hence there is no analytical way to calculate the values *ab initio*; thus, measurements are required. Unfortunately, the significant lack of such experimental data in literature is the main reason why the simultaneous application of the d-NRA and the d-EBS techniques is impeded. The experimental measurement of the cross-section values of deuterons elastically scattered from most of the light elements is a rather challenging task, however it is essential from the experimental point of view, as well as the theoretical one. From the theoretical aspect, unfortunately, for the d-EBS case the only existing theoretical evaluations concern carbon and oxygen, the latter up to 1.98 MeV. From the experimental point of view, deuteron elastic scattering cross sections of light elements are important, since the EBS technique offers high sensitivity and accuracy, as well as superior depth resolution with respect to the d-NRA one. More specifically, the use of measured cross section values which are frequently many times greater than the corresponding Rutherford ones leads to increased sensitivity and accuracy for the determination of light elements. Concerning the depth resolution; depth information originates from the energy loss of the outgoing particles. Hence, a particle with lower energy loses more energy as it traverses through the target compared with an identical particle with higher energy for the same analyzing depth. Therefore, combining the NRA and the EBS techniques one could obtain a very useful tool for the simultaneous, coherent analysis of the light elements coexisting in a target. Furthermore, if heavy elements also exist in the target the RBS technique could also be simultaneously employed with the use of the same experimental setup.

However, a serious problem that was encountered in the present dissertation arises from the benchmarking procedure. Especially for higher beam energies (above ~ 2 MeV) the contribution of the levels of the (d,p_x) and (d,α_x) reactions becomes more significant. Such contribution creates a “tail” even in the low energy part of the experimental spectrum of a thick target and consequently under the light element elastic scattering edge. In such complicated cases a solution could be the use of a magnetic spectrometer for the separation of the deuterons, protons and alpha particles,

however this situation constitutes a well-known problem in the scientific community. In the present dissertation this problem was only partly addressed.

At this point, the comparison of the deuteron beam, for the simultaneous implementation of the EBS and the NRA techniques, with proton and alpha beams for the same techniques is deemed necessary since protons and alphas are the most widely used beams for the determination of the depth profile concentrations of light elements up to now.

As evident in IBANDL, the p-EBS technique is widely implemented because of the high cross section values involved and due to the existence of evaluated and benchmarked differential cross-section datasets for the most important light elements. However, the major drawback of the p-EBS technique is that the simultaneous implementation of p-EBS and p-NRA (when complex matrices are involved) is impeded since the reactions (p, α), (p,d) and (p, ^3He) are in several cases strongly endothermic (e.g. for ^{14}N , ^{16}O , ^{28}Si). Even in the cases where the reactions are exothermic (e.g. $^6\text{Li}(p,^3\text{He})$, $^9\text{Be}(p,d_0)$), the p-NRA Q-values involved have usually relatively low values and the corresponding cross-sections have more complicated structures, than the corresponding d-NRA ones. This situation usually impedes their use in applications. Moreover, due to the kinematics, deuterons offer better mass separation and resolution from protons, without a significant loss in the maximum analyzing depth for the same beam energy, creating spectra with more distant peaks and thus more easily manageable for subsequent analysis.

The α -EBS technique on the other hand, displays undoubtedly the advantage of better mass separation and resolution than deuterons and, of course, protons. However, the α -NRA technique is rarely used due to the existence of negative Q-values in most cases and the rather low cross-section values involved. Thus, the simultaneous implementation of the α -EBS and the α -NRA techniques is rather hindered for analytical purposes.

Last but not least, it should be noted here that only a ^3He beam can lead to similar results with those obtained with a deuteron beam, regarding the excitation of most of the light elements, while it produces – on average - one hundred times fewer neutrons than the (d,p) and (d, α) reactions. Moreover, reactions induced by ^3He beams display better mass separation and resolution, due to the higher stopping power compared with deuterons of the same energy. On the other hand, the involved cross-section values are significantly lower [60] and for most of the light isotopes have not yet been measured. Another drawback in the implementation of the ^3He -EBS technique is that the production of the ^3He beam from the accelerator source is considerably more costly.

2.5 Content and goals of the present work

The widespread use of light elements in the industry, as well as in science, indicates the necessity of the determination of light element depth profile concentrations in a variety of complex matrices. The advantages of the simultaneous implementation of the d-NRA and d-EBS techniques

mentioned above, render this combination as the most suitable one for such cases. However, concerning the d-EBS cross-section datasets, for several light elements only a few datasets exist presenting many discrepancies among them, as evidenced in literature. Therefore, the present doctoral thesis aims at contributing in the field of Ion Beam Analysis via the differential cross-section measurements of elastically scattered deuterons from selected, technologically important light elements. More specifically, the differential cross section measurements include: ${}^6\text{Li}(d,d_0){}^6\text{Li}$, ${}^7\text{Li}(d,d_0){}^7\text{Li}$, ${}^9\text{Be}(d,d_0){}^9\text{Be}$, ${}^{14}\text{N}(d,d_0){}^{14}\text{N}$, ${}^{16}\text{O}(d,d_0){}^{16}\text{O}$, ${}^{23}\text{Na}(d,d_0){}^{23}\text{Na}$ and ${}^{\text{nat}}\text{Si}(d,d_0){}^{\text{nat}}\text{Si}$ in the deuteron energy range of 0.9–2.2 MeV, using a variable energy step and for the detection angles between 120° and 170° in steps of 10° (in most cases). In order to validate the results, in three cases, namely ${}^{16}\text{O}$, ${}^{23}\text{Na}$ and ${}^{\text{nat}}\text{Si}$, benchmarking data were also acquired, as detailed in Chapter 4. The last part of this dissertation, Chapter 5, concerns an attempt to theoretically investigate the cross-section of the deuteron elastic scattering on oxygen for energies higher than 1.98 MeV, where the current evaluation of SigmaCalc stops.

Chapter 3

Experimental Setup

3.1 5.5 MV Tandem Accelerator

All the experiments were performed at the 5.5 MV HV TN11 Tandem accelerator located at the Tandem accelerator laboratory of the Institute of Nuclear and Particle Physics of the National Center for Scientific Research “Demokritos” in Athens, Greece.

The accelerator is shown in Fig. 3.1 while the major components are sketched in Fig. 3.2. To begin with, the sources are a duoplasmatron one, from which the protons and deuterons are produced and a caesium sputter source for the production of heavier ion beams (${}^7\text{Li}$, ${}^{12}\text{C}$ etc). After the sources, the negatively charged ions that are produced at ground potential get pre-accelerated and subsequently enter the main beam line towards the acceleration tube. This acceleration is caused by the Van de Graaff generator which is a positive high-voltage terminal (metallic sphere) located in the center of a pressure tank. In order to achieve high voltage values, the system must be able to hold the entire high voltage between the terminal and the ground, hence a gradual increase of the voltage value from zero to the needed final value is ensured by the acceleration tube. The tank surrounding the main accelerator parts is filled with SF_6 gas at high pressure in order to ensure electronegativity and to inhibit electrical breakdown (sparking) of the power motor responsible for the rotating charging belt. The acceleration tube must be kept under high vacuum ($<10^{-6}$ Torr) in order to reduce the corresponding energy losses in the residual gas. A corona feedback system also exists in order to stabilize the voltage. The stripping of the negatively charged ions from their electrons is performed via thin carbon stripping foils located in the center of the tube. After the stripping the positively charged ions are repulsed due to the positive polarity of the terminal and are subsequently accelerated for a second time (the name tandem originates from this subsequent acceleration). The ion beam which contains a range of energies is then guided to the 90° analyzing magnet where the desired beam energy is selected by choosing a specific q/m ratio (i.e. value of the magnetic field). The feedback system which controls the magnetic field of the analyzing magnet is based on a Nuclear Magnetic Resonance (NMR) probe. Following the analyzing magnet, analyzer slits are installed; their aperture determines the range of the beam energy around the desired central value. Subsequently the beam enters the switching magnet which directs it towards the desired beam line. Each beam line is selected depending on the experimental purposes, since at the end of each beam line chambers containing the necessary detection systems and the under-

study targets are mounted. As the beam traverses through the beamline it is properly guided to its destination by a series of optical components (like dipole lenses, electrostatic steerers and magnetic quadrupoles) which are implemented in order to guide and focus the beam along the desired path. The acceleration tube and the beam lines are kept under high vacuum $\sim 10^{-6}$ - 10^{-7} Torr, using a combination of diffusion and thermomolecular pumps.



Figure 3.1 Panoramic view of the Tandem Accelerator of N.C.S.R. "Demokritos", Athens, Greece.

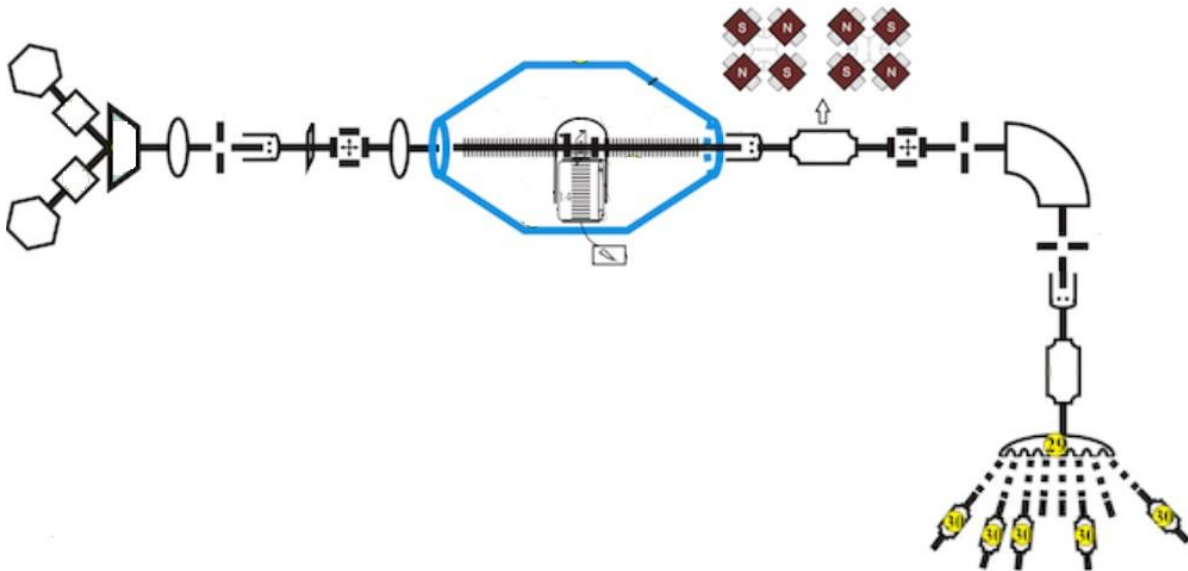


Figure 3.2 A schematic diagram of the accelerator along with the beam line.

In the present work deuterons and protons from the duoplasmatron source were used, and their energy was selected via a 90° analyzing magnet controlled through a Nuclear Magnetic Resonance (NMR) probe, along with a high-accuracy electronic feedback system. However, due to remanence

and the fact that the NMR probe is not located in the absolute center of the magnet, resulting to not exactly measuring the precise value of the field, the beam energy, along with its spread (largely defined by the aperture of the slits) had to be determined and verified. In order to achieve this goal, an accurate accelerator energy calibration procedure was carried out before every experiment implementing resonance reactions. More specifically, the resonance of the $^{27}\text{Al}(p,\gamma)$ reaction corresponding to the proton energy of 991.9 keV with $\Gamma = 100$ eV [61] and/or the resonance of the $^{13}\text{C}(p,\gamma)$ reaction corresponding to the proton energy of 1747.6 keV with $\Gamma = 122$ eV [61] were used, as will be thoroughly described in the next chapter.

3.2 Scattering chamber

At the Tandem accelerator laboratory, the beamline that was used for all the experiments of the present dissertation ends up in a large-size, cylindrical scattering chamber with a radius of 40 cm, equipped with a high precision goniometer. The interior of the scattering chamber is shown in Fig. 3.3 and illustrated in a schematic diagram in Fig. 3.4. There is a collimator/antiscatterer system set at the entrance of the scattering chamber. The antiscatterer (2.5 mm in diameter) was located 40 cm before the target holder and the distance between the collimator (2 mm in diameter) and the antiscatterer was ~ 4 cm. The antiscatterer, as suggested by its name, is practically a second larger collimator set up to partially impede the large-angle scattered ions from the first collimator to continue their course along the beamline. Such a system results in a beam spot of about $\sim 2 \times 2$ mm² on the target. In cases where the active area of the target was too small, an additional collimator (1 mm in diameter) was mounted at ~ 10 cm from the target holder, resulting in a beam spot size of $\sim 1 \times 1$ mm². Inside the scattering chamber, the target holder was placed perpendicularly to the beam axis and in the center of the goniometer. The target holder allows for the simultaneous mounting of five targets. Two independently rotating tables exist with the possibility of mounting detectors per 5° (lower table) or per 10° (upper table). Four motors with micrometric precision permit the control of both the rotating tables and the target holder without opening the chamber. For the latter there exist only two degrees of freedom, namely a vertical one along the y-axis and a rotational one along the x-axis. The motors which are controlling the rotating tables result to an uncertainty in the detector scattering angle of 0.1° . The detector signals are guided out of the chamber through BNC vacuum feedthrough connectors. The same cabling system is responsible for the voltage biasing of the detectors as well. Finally, a Faraday cup is mounted at the end of the beam line, at a distance of ~ 1.3 meters from the target holder in order to measure the charge (charge collection and current integration). The vacuum inside the scattering chamber is of the order of 10^{-6} - 10^{-7} mbar via the use of a rotary and a turbomolecular pump.

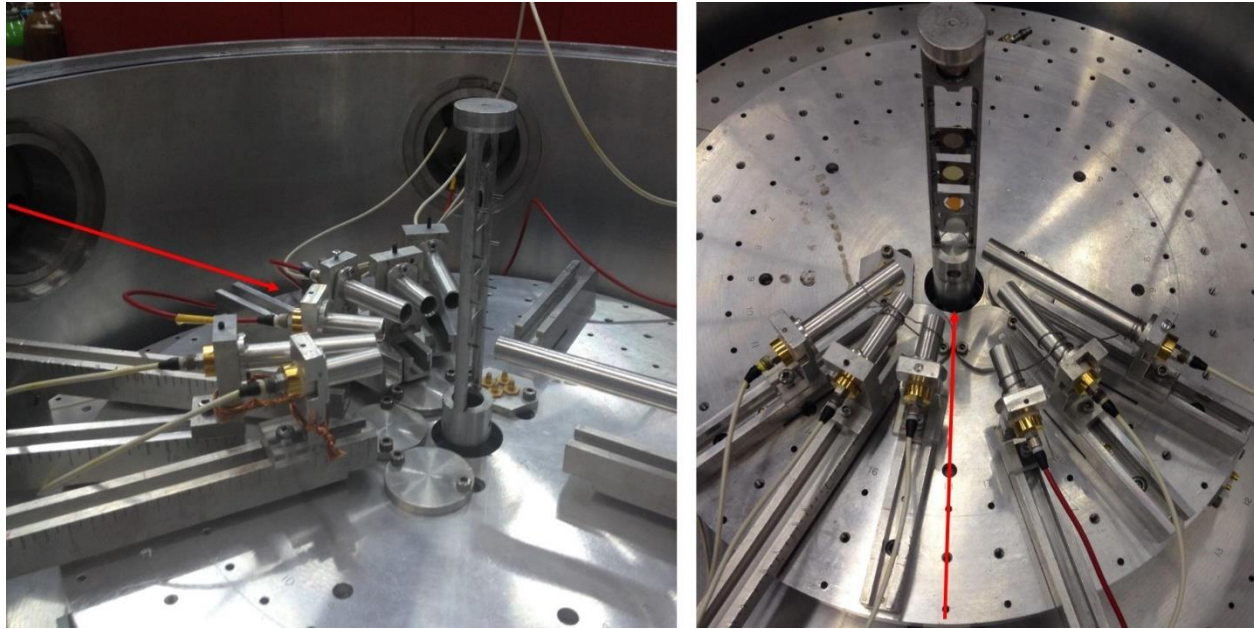


Figure 3.3 The interior of the scattering chamber prepared for an experiment. The red arrow in both pictures indicates the direction of the impinging ions.

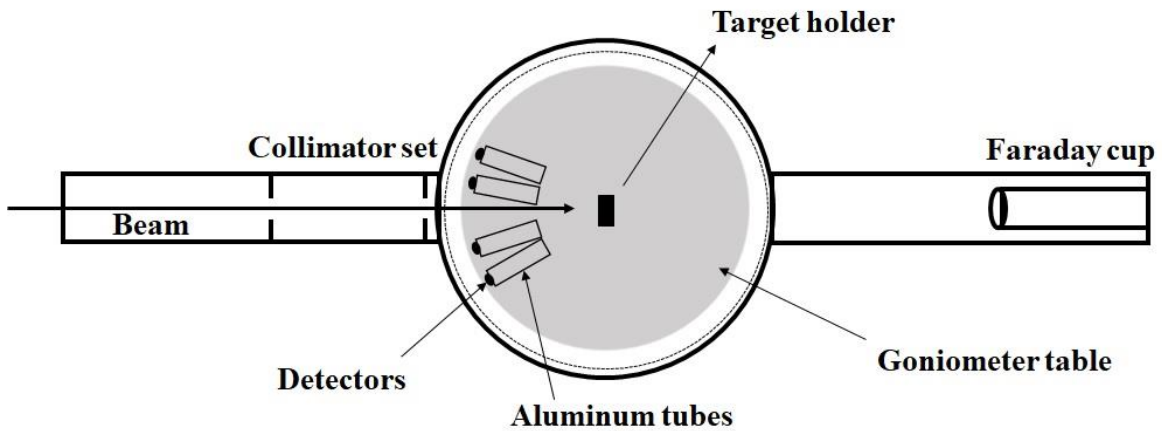


Figure 3.4 Schematic diagram of the scattering chamber and the Faraday cup assembly for cross-section measurements. The diagram is not scaled.

3.3 Detection System

The detection system consisted of four, five or six Silicon Surface barrier (SSB) detectors (provided by Dr. N. Patronis, property of the department of Physics at the University of Ioannina), depending on the studied case, having thicknesses of 500 μm , carefully selected so that the scattered deuterons or protons deposit all their energy in the detector. The detectors were mounted

in the goniometer at the corresponding backscattering angles varying from 120° (or 125°) to 170° with steps of 10° . Orthogonal slits with variable sizes (e.g. $\sim 3 \times 6 \text{ mm}^2$, $4 \times 8 \text{ mm}^2$, $4 \times 7 \text{ mm}^2$) were placed in front of each detector in order to minimize the angular uncertainty to less than 1° , while subtending a sufficient solid angle for the detectors. The solid angle obtained by all the detectors ranged between 2 and 4 msr. At the same time, cylindrical aluminum tubes with variable lengths $\sim 30 - 70 \text{ mm}$, having a diameter of 10 mm were placed in front of each detector in order to reduce the contribution of the elastically scattered particles from the goniometer walls and/or the faraday cup in the spectrum background under the studied elastic peaks. These tubes were also connected to ground via wires so that the beam is not deflected as it traversed the chamber due to any possible charging of the tubes. Such aluminum tubes are visible in both pictures of Fig. 3.3 while the slits are shown in Fig 3.5. The detectors were mounted at a distance of 10-12 cm from the target holder and their resolution (for protons and deuterons) varied from 8.5 keV to 13 keV in the energy range of 1-3 MeV. These values were experimentally determined by irradiating a polished thick silicon target with protons at $E_p = 1.8 \text{ MeV}$ and were deemed stable. During the course of every experiment the leakage current of the detectors was monitored, hence ensuring the proper operation of the detectors, and it displayed values up to 100 nA.

It should be noted here that no correction was deemed necessary concerning the pulse height defect (PHD) of the detectors since the experimental spectra were in all cases collected at an energy range of maximum 1.5 MeV, usually from $\sim 1 \text{ MeV}$ to $\sim 2.2 \text{ MeV}$ [1], taking into account the relatively small stopping powers of protons and deuterons with respect to alpha particles.

The detector signals were collected and processed via suitable, standard spectroscopy electronics, as presented in the following section.

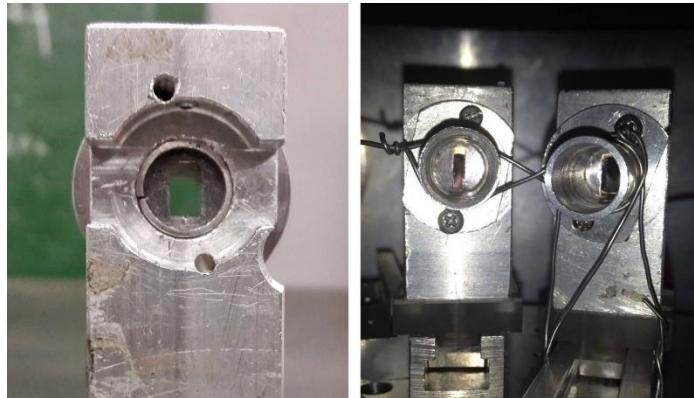


Figure 3.5 Orthogonal slits placed in front of the detectors. In the left image the detector is removed so that only the slit is visible, whereas in the right image the detector is on the back side of the holder, so that both the slits and the aluminum tubes are visible.

3.4 Electronics

The signal obtained from each detector was properly processed via a sequence of NIM spectroscopy electronics, schematically represented in Fig. 3.6. The signal originating from the silicon detector was processed primarily from the preamplifier which was located as close as possible to the detector. The preamplifier maximized the signal-to-noise ratio and its output was a linear tail pulse, shown in Fig. 3.6. Moreover, through the preamplifier the detector was supplied with the required voltage bias in order to be fully depleted from charge carriers. Such a linear tail pulse was used as input to the shaping (RC-CR) amplifier, which produced an approximately Gaussian shaped pulse with an amplitude proportional to the input pulse. Afterwards, the analog signal was converted to digital via an analog-to-digital (ADC) converter coupled to a multichannel analyzer (MCA) responsible for the histogram (spectrum) creation. For silicon detectors the number of required channels was limited to 1024/2048. The specific implemented amplifiers allowed for the adjustment of several important parameters like the shaping time, the pole zero cancellation, the polarity and the shape of the output signal (bipolar or unipolar). The shaping time usually was set at 2 μ s, which constitutes a reasonable compromise for the reduction of pile up, without critically affecting the resolution of the detection system. Concerning pole zero cancellation, adjustments were performed in order to minimize the effect but retain a slight undershoot during the electronic setup at the beginning of each experiment. The output signals were adjusted to a unipolar shape. Pile-up rejection was not deemed necessary since the current was kept relatively low (below 100 nA for the ultra-thin targets used in the differential cross section measurements) in order to avoid overheating. The adjustment of the amplification (gain) depended on the specific experiment and the elements/isotopes present in the target [62].

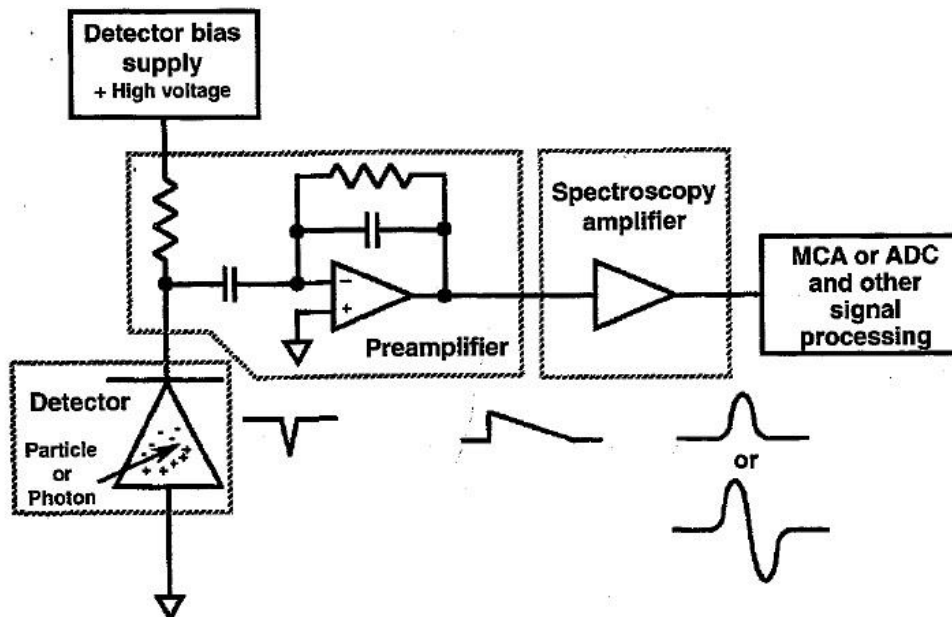


Figure 3.6 Schematic of the used electronics [4].

3.5 Target Preparation

The targets used for all the experiments in the context of the present thesis were either purchased or manufactured at the Tandem laboratory using the evaporator or the high-pressure system. Within the evaporator two kinds of techniques can be performed, the thermal evaporation and the electron-gun technique. The selection of the appropriate technique depends only on the properties (physical and chemical) of the material to be evaporated.

3.5.1 Targets manufactured using the evaporation procedure for cross section measurements

The thin targets for the differential cross section measurements of deuteron elastic scattering on ${}^6\text{Li}$, ${}^7\text{Li}$, ${}^{\text{nat}}\text{O}$ and ${}^{23}\text{Na}$ were manufactured using the evaporator, shown in Fig. 3.7, at the Tandem laboratory of the N.C.S.R. “Demokritos”. As displayed in Fig. 3.7 the evaporator is essentially a chamber operating in high vacuum ($\sim 10^{-6}$ mbar), achieved via a rotary and a turbomolecular pump. Both thermal evaporation and electron gun techniques were implemented for the manufacturing of all the targets. Thermal evaporation is achieved via a gradually applied high current on a thin metal sheet (boat), on which the material to be evaporated is placed, located at the center and bottom of the chamber. Substrates are placed above the boat, at a distance ranging from 10 to 20 cm, with the help of a mechanical frame (visible in the right picture of Fig. 2.7). Thus, due to the heating, the material on the boat is evaporated, transported to the substrates and is finally condensed, forming a solid film on each substrate. The method with the electron gun utilizes the same geometry, but instead of the boat, a pellet manufactured from the material to be evaporated is used. More specifically, an electron beam is being generated via the heating of a resistor and directed towards the evaporation material using an appropriate magnetic field. The thermal energy that is produced when electrons are striking the evaporation material, heats the material locally, causing its melting and subsequent vaporization. The resulting vaporized material forms a solid film on the substrate located above. The application of the electron gun is generally necessary when the melting point of the desired substance is quite high. Such high temperatures cannot be achieved using the standard thermal evaporation technique.

One of the most important parameters in the target manufacturing procedure is the choice of the substrate. For all the thin targets manufactured in the Tandem laboratory in the context of the present thesis the selected substrate was carbon. Since carbon is evaporated using an electron gun, a carbon pellet was placed in the evaporator and glasses with a mixture of soap (10% betadine and 90% sugar water) on top were placed at ~ 15 cm, depending on the case, from the carbon pellet. Subsequently, the electron beam impinged on the pellet, causing the formation of a carbon layer on top of the soap-covered substrates. The glasses were then sunk in water and since soap is a dissolvent, each carbon foil floated on the water surface and was ready to be adjusted on a frame, thus creating a self-supported thin carbon target. This is in fact the same process used for the

manufacturing of the stripping carbon foils used inside the accelerator, as described in section 3.1, only in this case the foils needed to be thinner ($\sim 10 \mu\text{g}/\text{cm}^2$).

The next step included the evaporation of the element/isotope under-study. As a typical example, the procedure of manufacturing the target for the $^{23}\text{Na}(d,d_0)^{23}\text{Na}$ experiment will be analyzed. The selected powder was Na_2O since it contains a high amount of sodium with a relatively low melting point ($1132 \text{ }^\circ\text{C}$). The areal density (ρ) of the powder was calculated with the help of the SRIM2013 [63] code so that the deuteron beam loss at 1 MeV was $\sim 10 \text{ keV}$ as it traversed through the target. The calculated areal density is related to the amount (m-mass) of the powder and the distance R in which the carbon foils are placed via the equation: $m = \rho \cdot 2\pi R^2$, since the evaporation is performed in the upper part of the chamber (i.e. with a corresponding 2π solid angle). The distance $R=17 \text{ cm}$ was deemed preferable in order to achieve a relatively isotropic evaporation resulting in a uniform distribution of the sodium films on top of the carbon foils. Thus, the proper amount of Na_2O ($m \approx 82 \text{ mgr}$) was weighted on a high-accuracy scale and was subsequently placed on a metallic boat made of tantalum. Tantalum is among the most common materials that are used for manufacturing boats since it has a high melting point ($2996 \text{ }^\circ\text{C}$), as well as, proper physical properties (electrical conductivity, possession of low vapor pressures). Alternatively, molybdenum and tungsten boats can be used, with the choice depending on the chemical affinity of the metallic base with the evaporated substance. In the case of sodium oxide as primary material a standard tantalum boat was deemed adequate. Thus, as the high current was applied on the boat, the powder was melted, vaporized and deposited on the carbon foils forming a thin layer of Na_2O on top of carbon.

The same procedure was followed for the evaporation of gold. A small quantity of gold (30 mgr in order for the energy loss of 1 MeV deuterons in the gold layer to be $\sim 1\text{-}1.5 \text{ keV}$ or less) was placed on the tantalum boat, while the carbon foils with the Na_2O layer were again placed on top. After the evaporation an ultra-thin gold layer was deposited on top of the Na_2O one for the protection of the target, as well as for normalization processes (as described in the next chapter). The final layering of the obtained target can be seen in a schematic diagram in Fig. 3.8.

It should be noted here that in some cases the obtained layers and elements in a target were not exactly as represented in Fig. 3.8 and displayed differences. More specifically, the mixture of soap used for the manufacturing of self-supporting carbon foils may cause a minor contamination of chlorine and nitrogen, as observed in the experimental spectra of the obtained targets. An asymmetry (tail at the left side) in the experimental peaks has also been observed and may be attributed to the coating for the creation of the carbon foils. Moreover, the evaporation procedure itself may cause an oxygen contamination. The contribution of each of such contaminants will be thoroughly discussed in the next chapter for every manufactured target separately.

Furthermore, of great importance are the cases where the evaporated substance is a compound. In such cases the stoichiometry is usually not retained during the evaporation process (due to e.g. a possible break of the chemical bonds followed by rapid oxidization when the targets are removed from the evaporator etc.). Since in the present dissertation compounds and not chemical elements

were used for all the manufactured targets, the experimental determination (along with the corresponding verification of the target thickness) is absolutely mandatory. Several techniques can be implemented for the full characterization of the obtained targets. A very common technique for the thickness determination of heavy elements is XRF. However, in the course of this dissertation, due to the study of low- and medium-Z elements which are expected to present strong deviations from the Rutherford formula when studied with deuterons over the whole energy range covered in the present work, the EBS technique with protons was implemented for the full target characterization and the determination of the target thickness in each case. Moreover, for beryllium, the ERDA technique using an oxygen beam was also implemented in order to acquire a supplementary value of the target thickness. The corresponding beam energies and the whole procedure are analyzed in detail in the following chapter.

The materials used for each one of the manufactured targets can be found in Table 3.1. The melting point of each powder along with the suitable boats [64] are also included in the table.

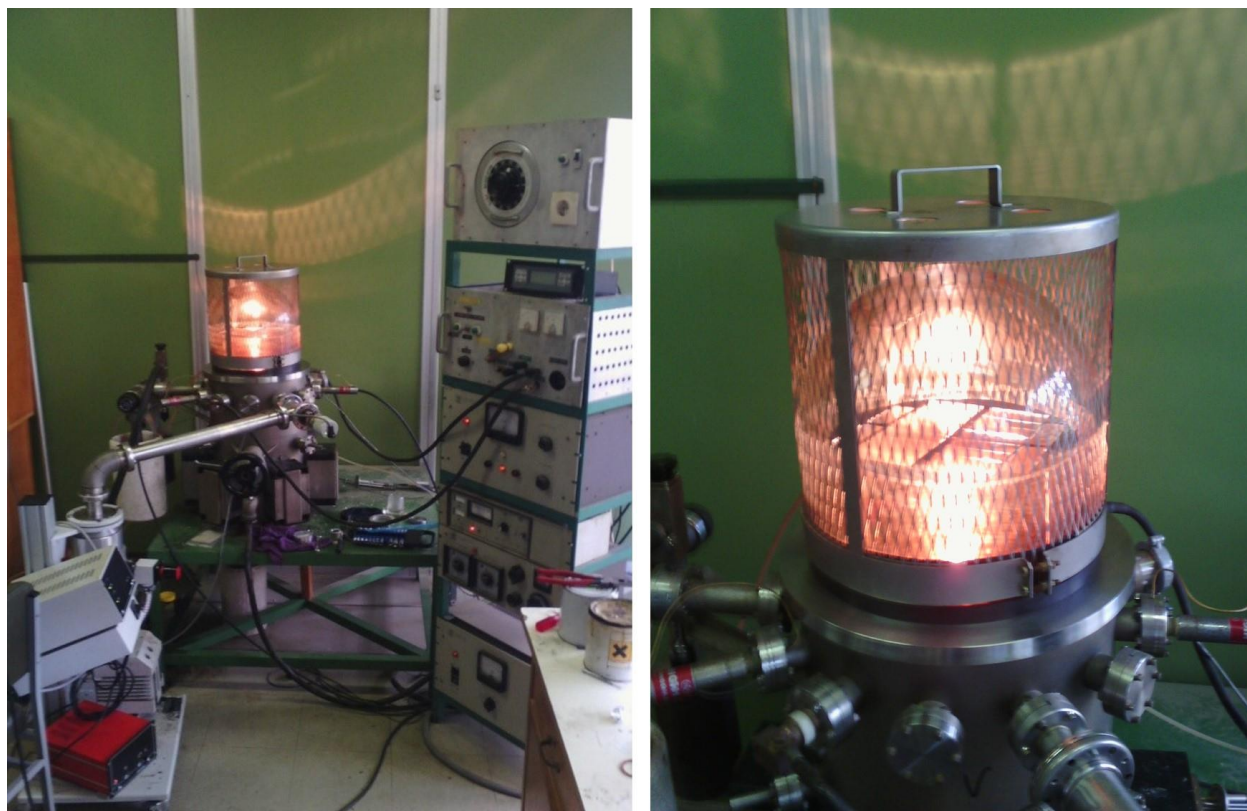


Figure 3.7 The evaporator of the Tandem laboratory of the N.C.S.R. “Demokritos” during an evaporation process. In the left picture the rotary and the turbo pump are visible, as well as the power supply of the electron gun and the system for thermal evaporation.



Figure 3.8 Schematic diagram of the obtained target. The red arrow indicates the direction of the beam. The diagram is not scaled.

Table 3.1 Materials used for the target manufacture procedure.

Cross section measurement	Substrate	Powder evaporated on top of the substrate	Powder melting point (°C)	Top layer	Suitable Boats
${}^6\text{Li}(d,d_0){}^6\text{Li}$	C	${}^6\text{LiF}$ enriched 97%	841	Au	Ni, Ta, Mo, W
${}^7\text{Li}(d,d_0){}^7\text{Li}$	C	${}^{\text{nat}}\text{LiF}$	841	Au	Ni, Ta, Mo, W
${}^{\text{nat}}\text{O}(d,d_0){}^{\text{nat}}\text{O}$	C	Na_2HPO_4	250	Au	
${}^{23}\text{Na}(d,d_0){}^{23}\text{Na}$	C	Na_2O	1132	Au	

3.5.2 Purchased targets for cross section measurements

Concerning specific differential cross-section measurements, targets were also purchased that included beryllium (highly toxic), nitrogen and silicon. More specifically, differential cross-sections of the deuteron elastic scattering on nitrogen and silicon were accomplished using ultra-thin, high-purity silicon nitride membranes manufactured by Silson Ltd. Such self-supporting membranes had a nominal thickness of 75 nm and their square-shape active area was rather small ($5 \times 5 \text{ mm}^2$), thus necessitating the implementation of a third collimator inside the scattering chamber, as described in the previous section. Moreover, for normalization purposes (described in section 4.1), on top of the Si_3N_4 membrane a small quantity of gold was evaporated using the standard thermal evaporation technique with tantalum boats, as described above. It should be mentioned here that, according to the manufacturer, the stoichiometry in these silicon nitride targets may vary between 3:4 and 1:1. This excludes from the differential cross section values calculation the possible use of the nominal stoichiometry. For the deuteron elastic scattering on beryllium, these identical high purity, ultra-thin self-supporting Si_3N_4 membranes (Silson Ltd.) were used as substrates, with the deposition of a thin ${}^9\text{Be}$ layer on top being carried out by means of magnetron sputtering.

3.5.3 Targets for the benchmarking experiments

For the validation of the obtained cross-section values, benchmarking experiments were performed for the selected cases of ^{23}Na and $^{\text{nat}}\text{Si}$. For the sodium case, the used thick target was manufactured by using the high-pressure system for manufacturing pellets located at the Tandem laboratory. More specifically, the NaCl target was manufactured by pressing a small quantity of high purity, fine-mesh NaCl powder at ~ 8 tn. The formed target was pressed for at least half an hour, in order for the pellet to be homogeneously formed, through a reduction of the air inclusions. However, the surface roughness of the created pellet is relatively high. Polished crystalline wafers, when available, do not present this problem when used in benchmarking experiments; thus for the silicon case a thick Si polished wafer was used. For charge normalization purposes, an additional gold layer was evaporated on top of the Si target. However, it should also be pointed out here that in the case of thick crystalline targets channeling perturbations near the surface might occur. This phenomenon might seriously affect the experimental spectra and thus the obtained results. A more detailed discussion will be presented in a following chapter in cases where channeling was possible.

It should be noted here that during the benchmarking experiments, unlike the differential cross-section measurements, the current on each thick target was kept very low (1-2 nA) in order to significantly reduce pile-up effects in the experimental spectra.

Chapter 4

Methodology, Data Analysis, Results and Discussion

In the present chapter the methodology and the necessary steps for obtaining the final differential cross section values, as well as the validation procedure, will be thoroughly analyzed (sections 4.1 and 4.2 respectively). Subsequently, each case of the deuteron elastic scattering on ${}^6\text{Li}$, ${}^7\text{Li}$, ${}^9\text{Be}$, ${}^{14}\text{N}$, ${}^{23}\text{Na}$ and ${}^{\text{nat}}\text{Si}$ is described in detail separately, along with the benchmarking process in the cases of ${}^{23}\text{Na}$ and ${}^{\text{nat}}\text{Si}$.

4.1 Differential cross section determination – Methodology

In general, the determination of the differential cross section values for the elastic scattering of a deuteron from a light element at energy E and for the scattering angle θ could be achieved by implementing an ultra-thin target containing the isotope/element of interest using the absolute measurement technique via the equation:

$$\left(\frac{d\sigma}{d\Omega}\right)_{E,\theta}^{light\ isot} = \frac{Y_{light\ isot}}{Q \cdot \Omega \cdot N_t^{light\ isot}} \quad (4.1)$$

Where $Y_{light\ isot}$ corresponds to the number of detected particles scattered from the light isotope/element under-study, Q corresponds to the number of impinging deuteron ions in each measurement, Ω corresponds to the detector solid angle subtended by the detector set at angle θ (in sr) and $N_t^{light\ isot}$ is the light isotope target thickness calculated in atoms/cm². The obtained units of the differential cross section values are mb/sr. It should be noted here that E represents the energy at the half of the target's thickness (see section 4.1.1.2).

In order to calculate the differential cross section, the parameters in Eq. 4.1 need to be determined. Y can be easily obtained by processing the corresponding peak in the experimental spectra, as described below. The determination of the target thickness, $N_t^{light\ isot}$, is among the most challenging parameters since it should be obtained from an independent measurement with high accuracy, as analyzed in section 4.1.3. The collected charge Q can be measured by adding the charge from the Faraday cup and the charge induced in the target, using a current integrator. However, as the beam impinges on the target a large number of secondary electrons and photons (X-rays) are emitted. Such secondary electron current could be comparable or even higher than the

incident beam current, depending on the beam-target combination [1]. Possible solutions to this problem could be the installation of a suppression system for these electrons, or the installation of a Faraday cup in close distance from the target or the use of the whole chamber as a Faraday cup. In principle, the latter solution could lead to a better collection of the charge, however, it is rather difficult to be performed since the scattering chambers used for differential cross section measurements have usually large dimensions in order to allow for the simultaneous mounting of multiple detectors and act as charge collectors from the surrounding environment, thus impeding the accurate measurement of the charge. Past measurements have pointed out that the Faraday cup located in the scattering chamber at Demokritos, where all the experiments of the present thesis were performed, leads to an accuracy of ~7-14% for deuterons at the energy range of 1-2 MeV depending also on the target thickness. Thus, Q is difficult to determine with high accuracy and frequently leads to a high percentage of uncertainty, in the absence of a sophisticated faraday cup with a suppression system. At the same time, the detector solid angle Ω , is also rather difficult to be calculated with high accuracy. An accurately calibrated alpha source emitting alpha particles at a solid angle of 4π could be placed at the position of the target, thus leading to the determination of Ω . The main problems of this method are the different dimensions of the source compared to the beam spot, as well as the difficulty in mounting the source in the exact position of the target [1].

Therefore, Q and Ω are quantities that are hard to measure with high accuracy and the use of equations for relative measurements for the cross sections could in principle provide results with high accuracy, as it bypasses the calculation of these two coupled parameters. More specifically, the differential cross section values for a heavy element at the energy E' and at the scattering angle θ could be found by using the following equation, similar to Eq. 4.1:

$$\left(\frac{d\sigma}{d\Omega}\right)_{E',\theta}^{heavy\ elem} = \frac{Y_{heavy\ elem}}{Q' \cdot \Omega' \cdot N_t^{heavy\ elem}} \quad (4.2)$$

The values of the differential cross section for each beam energy and scattering angle combination can be analytically calculated using the Rutherford formula (Eq. 1.3). In this case, the beam energy E' represents the energy at the half of the gold layer thickness. All the parameters of the right part of Eq. 4.2 correspond to the same quantities as for Eq. 4.1, but in this case regarding a heavy element and can be calculated with the same methodology. If the heavy element and the light isotope are both present in the target during a measurement, then the impinging number of ions and the solid angle for a specific measurement and for each detector are equal ($Q=Q'$, $\Omega=\Omega'$). Thus, if Eq 4.1 is divided with Eq. 4.2 then the following equation is derived:

$$\left(\frac{d\sigma}{d\Omega}\right)_{E,\theta}^{light\ isot} = \left(\frac{d\sigma}{d\Omega}\right)_{E,\theta}^{heavy\ elem} \cdot \frac{Y_{light\ isot}}{Y_{heavy\ elem}} \cdot \frac{N_t^{heavy\ elem}}{N_t^{light\ isot}} \quad (4.3)$$

In the present thesis Eq. 4.3 was used for the determination of the differential cross section values in all cases with the heavy element frequently being gold. Gold was chosen since it is a malleable and ductile metal, has a relatively low melting point (1064.18 °C) while it displays good conductivity and general resistance to oxidation and corrosion. Unfortunately, in the beryllium

cross section measurement the target did not contain gold or any other heavy element, requiring the use of the following equation where the beryllium differential cross section values were obtained compared to the ones of the $^{nat}\text{Si}(d,d_0)^{nat}\text{Si}$ elastic scattering, which does not deviate from the Rutherford formula at $E_{d,lab} = 1000$ keV [6], for the same scattering angle:

$$\left(\frac{d\sigma}{d\Omega}\right)_{E,\theta}^{9Be} = \left(\frac{d\sigma}{d\Omega}\right)_{1000,\theta}^{Si,Ruth} \cdot \frac{Y_{9Be}}{Y_{natSi}} \cdot \frac{Q_{Ruth}^{1000}}{Q_{9Be}} \cdot \frac{N_t^{Si}}{N_t^{9Be}} \quad (4.4)$$

In this case, the calculation of the relative charge of both measurements could not be avoided. This case is analyzed in section 4.5.

Therefore, after the completion of each experiment, the procedure in order to obtain the final differential cross section values includes the analysis of the recorded spectra, the determination of the target thickness and, with the target thickness known, the final beam energy can be calculated via the accelerator calibration and the energy loss in the target. With all these parameters set, the unknown differential cross section values can eventually be determined at each energy step.

4.1.1 Spectrum analysis

A typical spectrum of deuterons having an energy of 1290 keV impinging on a Na_2O target and scattered at 170° is shown in Fig. 4.1 along with the corresponding peak identification (procedure and discussion below). The obtained spectra are technically histograms showing the number of deuterons scattered at a certain angle after interacting with the isotopes/elements present in the target, with respect to the channels of the ADC, coupled with the MCA. In order to obtain the number of counts of each of the isotopes/elements of interest from the spectra, the peaks need to be identified. Thus, the calibration of each one of the ADCs, namely the procedure determining the relation between the channel in the spectra and the energy of the scattered ion, leads to the peak identification process which is rather essential. This relation is different for each one of the ADCs since the detector, the amplification gain and the cables are different. Subsequently, the peaks which correspond to the elastic scattering of interest should be integrated in order to obtain the yield parameters $Y_{light\ isot}$ and $Y_{heavy\ elem}$ of Eq. 4.3 needed for the determination of the cross section.

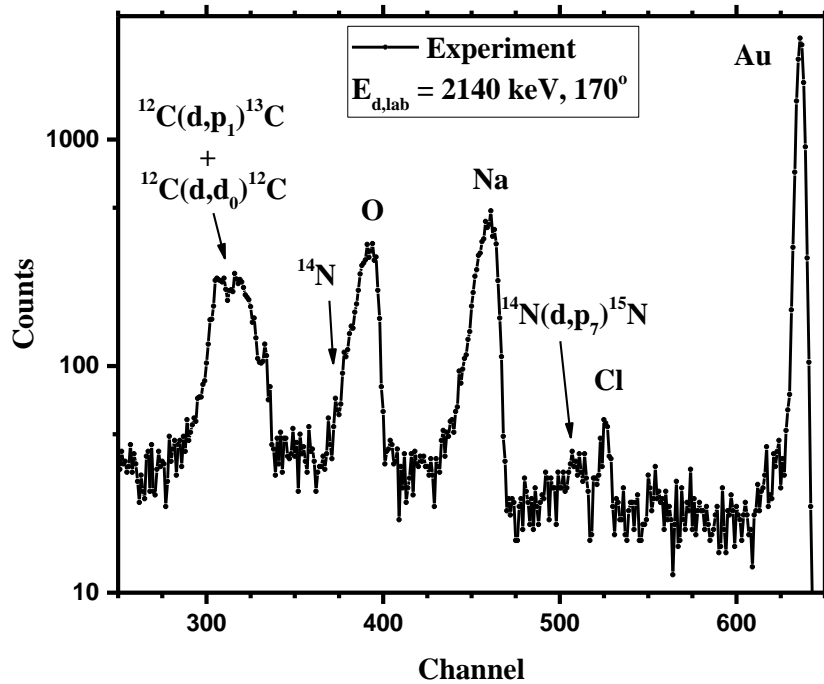


Figure 4.1 A typical spectrum of the Na_2O target for the deuteron energy 2140 keV and for the scattering angle of 170° along with the corresponding peak identification.

4.1.1.1 Peak Identification – Calibration ADC

The spectra obtained from all the experiments are frequently composed of multiple peaks, as observed in Fig. 4.1. In order to identify such peaks, the calibration of the ADC, namely the relation between the channel visible in the experimental spectrum and the energy of the scattered ion from the specific isotope/element of interest needs to be determined. The ADC calibration can be performed either via the use of calibrated sources or via the use of standard samples with at least two elements (both high and low Z) at the surface, or by using a target with one surface element at multiple beam energies. In the latter two procedures surface elements are usually preferred in order to avoid the uncertainty introduced by the calculation of the beam energy loss between the surface and the depth in which the element is located. In the present thesis the ADC calibration for all the experiments was performed using one surface element at multiple energies. Generally, the ADC calibration procedure involves the identification of channel numbers corresponding to well-known energies. The channel can be easily obtained from the experimental spectra; in cases of very thin layers (FWHM less than the detector resolution) the signal peak is chosen, whereas for thick layers the signal half-height is chosen. The energy of the surface element, since it is

characteristic of the struck particle in the target, can be analytically calculated, for the elastic scattering, via the kinematics of the corresponding scattering ($E_e = k_e E_0$, where E_0 is the incident beam energy and k_e is the kinematic factor of the corresponding element), for instance via CATKIN [65]. In the case of a reaction, the Q-value and the levels of the residual nucleus should also be taken into account. After the channel and energy values are determined and plotted, a linear regression is performed to obtain the gain a (in keV/ch) and the offset b (in keV) values: $E_c = a C + b$, e.g. the energy E_c is represented by a channel C . With the relation of channel number to energy established, the conversion of a backscattering spectrum from channel numbers to particle energies and the subsequent identification of all present peaks is possible.

At the Tandem Accelerator Laboratory, where all the experiments were performed, the accurate ADC calibration was achieved by using the surface gold evaporated on top of all the targets (except for the case of the beryllium). Since the thin layer of gold existed in all the cross-section measurement targets, all the obtained spectra over the whole energy range could be used for the ADC calibration. In the beryllium case, a target of thick silicon with a thin layer of Au evaporated on top was also irradiated at several beam energies (in steps of 100 keV) over the whole energy range under-study for the determination of the ADC calibration. In most cases, since the layer of gold was ultra-thin, the chosen channel was the signal peak. Thus, after the channel and the corresponding energy of gold were determined, the linear graph of the energy with regard to the channels was obtained and a least square fit was performed. The graph of the ADC calibration procedure for the scattering angle of 170° and for the differential cross section measurement of sodium is visible in Fig. 4.2. The obtained values were $\alpha = (3.187 \pm 0.004)$ keV/ch and $b = (32.4 \pm 1.8)$ keV. These values are valid until a change in the amplification gain for any reason occurs. In order to decrease the statistical uncertainties of the parameters obtained from the least square fit procedure the number of experimental points could be increased. The goodness of the fitting procedure, is described by the chi-squared value; in the case of Fig. 4.2 a figure of merit of the linear fit is 0.99999, implying an almost perfect linearity of the system. With the calibration parameters known (namely α and b) the conversion of the horizontal axis of a spectrum from channels to energies, as shown in Fig. 4.3, can be performed.

The accurate calibration of the ADC is a rather important procedure, especially in cases like the one shown in Fig. 4.3 where the spectrum includes multiple peaks either from the elements existing intentionally in the target or from the ones existing in small amounts and originating from parasitic contributions. In Fig. 4.3 for instance, chlorine and nitrogen are present, which were introduced in the target during the manufacturing process, as discussed in section 3.5.1. Moreover, the accurate ADC calibration allows also for the identification of reaction channels of one or more isotopes/elements (e.g. $^{14}\text{N}(d,p_7)^{15}\text{N}$ in Fig. 4.3). However, in cases with complex targets containing many elements, the phenomenon of overlapping peaks is not rare. In fact, in Fig 4.3, the overlapping peaks of $^{12}\text{C}(d,d_0)^{12}\text{C}$ and $^{12}\text{C}(d,p_1)^{13}\text{C}$ are displayed. In such cases the spectrum analysis must be performed very carefully, especially if the overlapping peaks include the peaks of interest. In the context of the present thesis overlapping peak phenomena occurred and will be discussed in detail in the following sections.

Generally, the accuracy of the obtained ADC calibration depends on the accelerator calibration (section 4.1.4.1), on the accurate knowledge of the detector entrance window and dead layer (pulse height defect (PHD) of the detector), since semiconductor detectors are known to respond in a non-linear way to particle energy, species, and to the detector resolution [1]. However, as mentioned in section 3.3, the PHD is not affecting the linearity of the ADC, as displayed in Fig. 4.2, in the energy range of maximum 2.5 MeV of protons and deuterons, used in the present thesis.

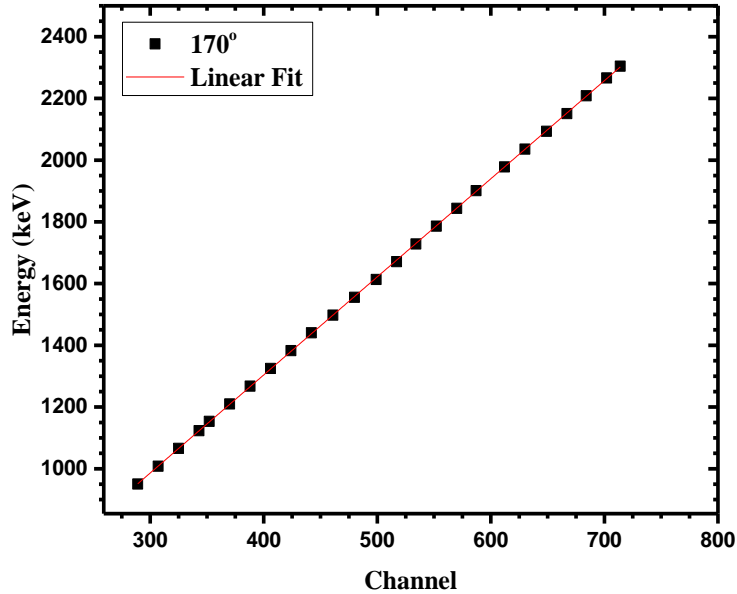


Figure 4.2 Calibration of the ADC connected with the detector mounted at 170°.

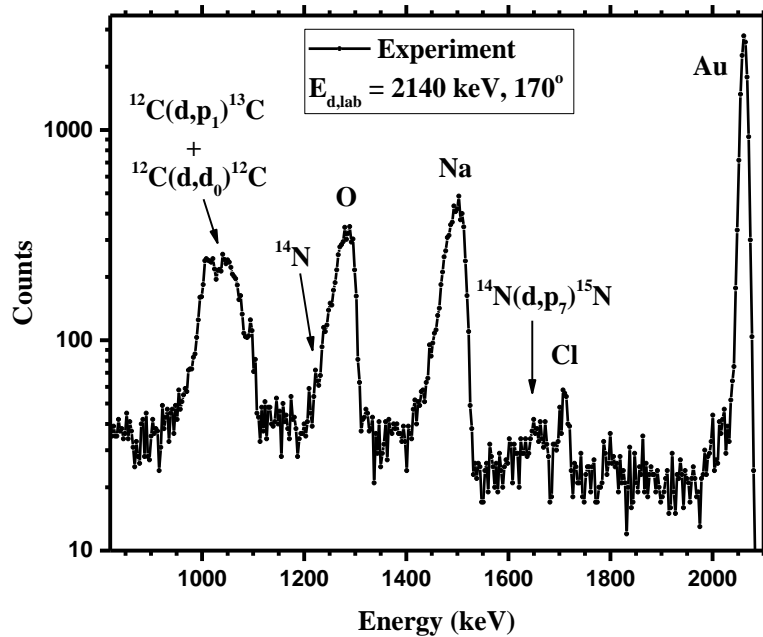


Figure 4.3 Calibrated typical spectrum of the Na_2O target for the deuteron energy 2140 keV and for the scattering angle of 170° along with the corresponding peak identification.

4.1.1.2 Peak integration

After all the peaks are properly identified in the experimental spectra the yield parameters in Eq. 4.3 should be determined. In the cases where the peaks of the elements of interest are well separated and the counts can be accurately determined from the spectra, the peak integration method can be applied. The programs used for spectra analysis in the present thesis were the SpectrW [7] and the Tv spectroscopy code [8], depending on the case. The two programs were compared prior to their use and the differences in the acquired integrals were well below 1%. Generally, the deuteron-induced EBS spectra are relatively rich, especially in the cases where nitrogen is involved, due to the excitation of several levels, however in the obtained experimental spectra there was no significant background under the peaks of elements of interest. A linear background was subtracted (no substantial loss of signal is caused) from the under-study peaks prior to the integration procedure. The statistical uncertainties of this procedure were obtained from the analysis program. The uncertainties in the SpectrW code are calculated for the sum over all the channels in the integration region as the square root of the counts of all channels plus the counts of the corresponding background. For the gold peak the statistical uncertainty remained

usually below 1%, whereas for the under-study elements it was usually higher. The specific values of the statistical uncertainties are mentioned below for each case separately.

In the cases where the under-study peaks were overlapping, the peak integration method could not be applied. In the far-fetched scenario where peaks were fully overlapping no results could be produced. Although fully overlapping peaks of elastic scattering cannot occur, with the given thin targets and the detectors with good resolution, as far as reactions are concerned caution is needed. These cases should be identified by keeping track of the closest peaks to the studied ones at each scattering angle and energy combination. Moreover, these cases should be predicted before the experiment by studying the kinematics of the anticipated reactions via e.g. CATKIN. In the cases where the peaks were partially overlapping, the use of a fitting method to separate the contributions of different elements to the total counts in the overlapping peaks was deemed necessary. Thus, the least square fitting procedure with Gaussian functions was applied in the experimental spectra, when needed, via the use of the SpectrW or the Tv codes. The two codes were again compared and the differences were below 2%. Since, as already discussed in section 3.5.1, the peaks in certain cases display a tail on the left side, during the fitting process the application of an asymmetry to the left side of the Gaussian fit was required and was thus used. The results of the fitting process provide the counts in the desired peak along with the appropriate values of uncertainties, which are usually higher compared with the integration method. The statistical uncertainties in the fitting method in the SpectrW code are calculated following the Levenberg–Marquardt method for chi-square minimization [66].

4.1.2 Target thickness calculation

The accurate determination of the $N_t^{heavy\ elem} / N_t^{light\ isot}$ ratio is probably the most crucial parameter in Eq. 4.3 for the determination of the differential cross section values using the relative technique. Since deuteron elastic scattering from the under-study elements was *a priori* expected to display deviations from the Rutherford formula over the whole deuteron beam energy range covered in the present dissertation, measurements with protons as projectiles, at several different beam energies were also acquired during all the experiments. The proton energy values were carefully selected in all cases in order to be far from the existing Breit-Wigner resonances to maximize accuracy. Proton elastic scattering in most of the studied cases ($^{nat}N(p,p_0)^{nat}N$, $^{23}Na(p,p_0)^{23}Na$, $^{nat}Si(p,p_0)^{nat}Si$) has been evaluated [59] and benchmarked in the cases of $^{nat}N(p,p_0)^{nat}N$ [67], $^{23}Na(p,p_0)^{23}Na$ [22] and $^{nat}Si(p,p_0)^{nat}Si$ [68]. In order to calculate the target thickness ratio, the following equation could be used:

$$\frac{N_t^{Au}}{N_t^{light\ isot}} = \frac{\left(\frac{d\sigma}{d\Omega}\right)_{light\ isot}}{\left(\frac{d\sigma}{d\Omega}\right)_{Au}} \cdot \frac{Y_{Au}}{Y_{light\ isot}} \quad (4.5)$$

However, Eq. 4.5 calculates the target thickness ratio for a specific value of the incident energy without taking into account the changes in the cross-section structure as the beam traverses through the target and loses energy. In order to address this problem the obtained proton spectra were analyzed using the SIMNRA (v. 6.94) code [9]. The followed procedure included: The choice of a specific energy value and scattering angle and the double fitting of the product $Q \cdot \Omega$ and the thickness of gold using the corresponding (or any heavy element which is used for normalization) peak. For this fitting Rutherford cross section datasets were used. Subsequently, while keeping the gold thickness constant for all the remaining beam energy/scattering angle combinations, the product $Q \times \Omega$ was fitted in the gold or any other heavy element peak. After this procedure was completed, the total areal density of the under-study element (in atoms/cm²) could be determined by slightly varying the under-study element composition in each case for every proton beam/scattering angle combination. Thus, the final value (in atoms/cm²) of the target thickness ratio was calculated as the mean value of the different beam energy/scattering angle combinations. Only the spectra corresponding to the backscattering angles of 150°, 160° and 170° were used in the target thickness ratio calculation process in order to avoid uncertainties due to the larger straggling caused by the larger exit path of the beam in the most forward angles (120°, 130°, 140°). Moreover, only the spectra where the under-study peaks were well separated were included in the analysis process in each case. Therefore, the average value along with the relative statistical uncertainty were obtained from this procedure. However, the determined statistical uncertainty did not include any systematic uncertainties, mainly due to the accuracy of implemented stopping power compilations, possible lateral inhomogeneities in the target composition as well as carbon buildup effects. The values of the systematic and statistical uncertainties differed for every case and are mentioned below, in the devoted sections for each specific case.

For the analysis of the proton spectra at every experiment the exact detector geometry was used along with the effect of multiple scattering. Moreover, a very small energy step in the incoming and outgoing protons was adopted at least in one spectrum and the differences were negligible for all the tests. For the stopping power the ZBL compilation was used along with the corrections for silicon [69], [70] and for the straggling Chu and Yang's model was adopted, as implemented in the code.

The method described above was used for most of the cases of the present dissertation. The adjustments of this method according to the requirements of each specific case will be discussed in the corresponding section devoted to each experiment.

4.1.3 Differential cross section calculation for the heavy element

In order to determine the $\left(\frac{d\sigma}{d\Omega}\right)_{E,\theta}^{heavy\ elem}$ parameter in Eq. 4.3 the differential cross section of the heavy element existing in the implemented target e.g. gold or gallium needs to be calculated. The

gold as well as the gallium differential cross section follows the Rutherford formula at these low deuteron incident energies and for backscattering angles. Thus, it is analytically calculated using Eq. 1.3, along with the corresponding correction for the screening effect. The beam energy at which the differential cross section of gold is calculated corresponds to the energy after the accelerator calibration procedure (see below). It should also be noted here that the values corresponding to the differential cross section in the surface of the target and in the middle of the Au layer were compared and, due to the fact that the difference was well below 1%, no uncertainty needed to be included in the final uncertainty budget of the obtained differential cross section due to the differential cross section value of the heavy element parameter.

4.1.4 Energy determination

The true beam energy E that corresponds to a specific value of the cross section should be accurately determined since it is important for the obtained results, especially in cases where resonances are present in the cross-section structure. The procedure in order to obtain the energy of the beam particles entering the scattering chamber, the so-called accelerator calibration, is followed by a proper correction of the obtained energy values since not all interactions are occurring on the surface of the target. Thus, the energy loss as the beam traverses through the target until the interaction occurs at a random depth should be taken into account. In order to account for this phenomenon, the convention of attributing the differential cross section value to the half of the target's thickness was followed, as analyzed below.

4.1.4.1 Accelerator calibration

The beam energy value frequently slightly differs from the value provided by the accelerator operator. This is due to the remanence and the fact that the NMR probe is not located in the center of the magnet, as described in section 3.1, and thus the careful calibration of the analyzing magnet of the accelerator is necessary for conducting cross-section measurements. The energy calibration of the accelerator is equivalent with calibrating the field of the magnet in terms of energy, so that it bends the desired q/m ratio at the corresponding required energy. The needed values that should be obtained from the machine calibration procedure are the offset, namely the numerical difference between the nominal value (set by the operator) and the true one, as well as the uncertainty (ripple) of the energy, since the beam displays a gaussian distribution around its central value. The ripple directly depends on the aperture of the analyzing slits. For the experiments of the present thesis the aperture of the slits was either 5 or 8 mm, depending on the experiment.

Several techniques exist in order to calculate the accelerator energy. For example via resonances in elastic scattering e.g. $^{12}\text{C}(p,p_0)^{12}\text{C}$, although the maximum of the yield does not correspond to

the energy of the resonance since an interference exists between the nuclear and potential scattering, or by using a threshold reaction with neutrons in the exit channel (e.g. ${}^7\text{Li}(p,n){}^7\text{Be}$ at 1881 keV [71]). These two calibration techniques lead to accurately determining the energy offset, without obtaining the beam energy ripple with high precision, and also in the case of emitted neutrons radiation safety precautions are necessary. If available, a time of flight (ToF) system could also be used. Furthermore, RBS measurements constitute a competitive technique although with a mediocre energy resolution, since the implementation of charged particle detectors is necessary [72]. However, the most commonly implemented technique is the use of sharp, narrow (commonly with a width Γ of a few hundred eV) resonances of proton induced reactions. This technique is preferred, since it offers better resolution compared with the ones using charged particles. In the present dissertation, where deuteron elastic scattering on light elements is discussed, a reaction with deuterons as the incident beam could avoid the necessity of measuring a narrow proton resonance before switching to a deuteron beam. In the past, the ${}^{16}\text{O}(d,n){}^{17}\text{F}$ reaction at the energy of 1829.2 ± 0.6 [73] has been used for the precise absolute energy calibration of accelerators. Moreover, in a recent work, Csedreki et al. [74] determined with high accuracy the beam energy and the level width of the ${}^{12}\text{C}(d,p\gamma){}^{13}\text{C}$ reaction emitting an intense gamma ray with $E_\gamma = 3089$ keV. The deuteron energy was measured 1446.9 ± 0.2 keV while the width was measured as 5.3 ± 0.6 keV. This is among the strongest and narrowest resonances in the field of the deuteron induced reactions, however it still displays a large value of the width Γ , compared to the ones obtained from (p,γ) reactions, which evidently leads to a limited accuracy. Generally, deuteron induced reactions lead to higher levels with larger widths in the formed compound nucleus and therefore are not frequently implemented for precise accelerator calibrations. Since this is the situation, and taking into account that the accelerator calibration technically means calibrating the field of the magnet in terms of energy, the use of proton induced reactions for the calibration of the analyzing magnet is preferred concerning cross section measurements with deuterons.

The most suitable (p,γ) reactions implemented in the present work are the ${}^{27}\text{Al}(p,\gamma){}^{28}\text{Si}$, the ${}^{13}\text{C}(p,\gamma){}^{14}\text{N}$ and the ${}^{32}\text{S}(p,\gamma){}^{32}\text{S}$ ones, corresponding to the proton energies: (991.9 ± 0.04) keV [61], (1747.6 ± 0.9) keV [61] and 3379 keV [75] having widths $\Gamma = (100 \pm 20)$ eV, $\Gamma = 122$ eV and $\Gamma = 700$ eV, respectively. These resonances provide an accelerator calibration with high accuracy up to 3.4 MeV, sufficient for the present dissertation. In cases where higher beam energies are required, the reaction ${}^{14}\text{N}(p,\gamma){}^{14}\text{N}$ which displays resonances up to 6 MeV could be implemented, but only for very practical ion beam applications, since the widths of the associated levels are quite large ($\Gamma = 106, 27, 17$ keV [76]). It should be mentioned here that at the Tandem laboratory, in the past, the main three reactions mentioned above have been sequentially implemented and the magnet displayed a linear behavior in this energy range. In the context of the present thesis the resonance of the ${}^{27}\text{Al}(p,\gamma){}^{28}\text{Si}$ reaction or the ${}^{13}\text{C}(p,\gamma){}^{14}\text{N}$ reaction, depending on the case, were used for the accelerator calibration in the beginning of all the experiments. The procedure will be described in detail for the ${}^{27}\text{Al}(p,\gamma){}^{28}\text{Si}$ reaction performed prior to the ${}^{\text{nat}}\text{Si}(d,d_0){}^{\text{nat}}\text{Si}$ experiment.

A thick aluminum target was placed in front of the faraday cup, at the end of the beamline, and a 18% HPGe detector was placed behind the beamline at a distance of 1 cm between the front face of the crystal and the target. The used proton beam energies were in the energy range of 980-1006 keV with a variable energy step; in the energy range of 988-1000 keV the energy step was 1 keV in order to properly scan the resonance. In this case the impinging charge was the same for every beam energy, whereas in several cases, the impinging charge of every proton energy differed, thus the acquired yield needed to be normalized over the charge. The produced gamma-rays were recorded in a spectrum with the utilization of standard spectroscopy electronics namely a preamplifier, an amplifier and an ADC coupled with an MCA adjusted to 4096 channels. In order to identify the aluminum peak, the gamma ray with the energy of 661.7 keV emitted by a Cs-137 source and the gamma rays with energies 1173.2 keV and 1332.5 keV emitted by a Co-60 gamma ray source were used for the calibration of the obtained spectra. Thus, the aluminum peak at the energy of 1779.03 keV was identified and integrated. The normalized yield is plotted in Fig. 4.4 as a function of the proton energy. A sigmoidal Boltzmann function was fitted in order to determine the beam offset and the ripple. The offset is determined by the mid-point of the sigmoidal rise which corresponds to 995.2 keV resulting to an offset of 3.3 keV, while the ripple is the width from the 12% up to 88% [1] of the maximum yield, as shown in Fig. 4.4 and it was determined to be 2.7 keV (0.27% of the incident beam energy).

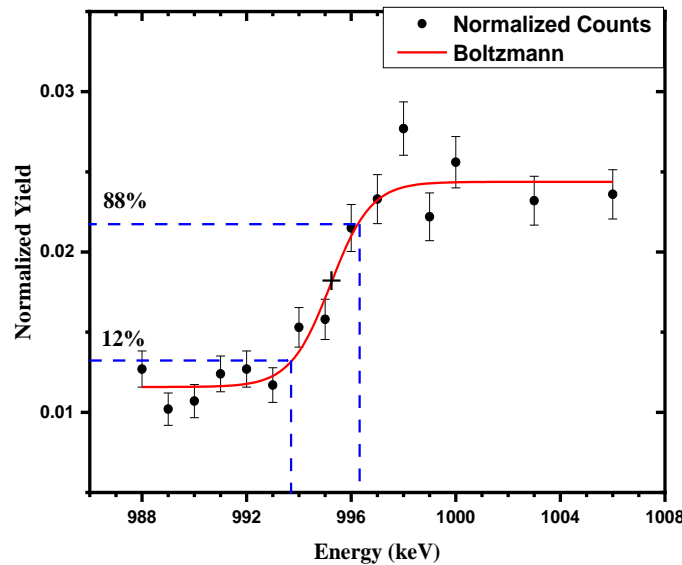


Figure 4.4 Normalized thick target yield of the $^{27}\text{Al}(p,\gamma)^{28}\text{Si}$ reaction in the energy range of 988-1006 keV.

4.1.4.2 Energy loss - Mean Energy Approximation

Following the accelerator calibration, the obtained energy values need to be corrected in order to account for the energy loss as the beam traversed through the target until the interaction occurred. The amount of the energy loss per traversed distance Δx depends on the identity of the projectile, on the density and composition of the target and on the initial incident energy. Since the composition of the target is a crucial parameter, the energy loss should be separately studied for each of the isotopes/elements that are present in the target. The isotopes/elements are structured in layers inside the target (analyzed in section 3.5) and since the used targets are thin, the energy loss in a layer is minimal and can be approximately considered as constant over the whole layer's thickness. This approximation is only valid in the cases of thin targets (as well as Eq. 1.4), where the cross section does not display any sharp resonances.

Moreover, the cross section values are attributed to the energy that corresponds to the mean target thickness (mean energy approximation [77]). This is a common convention and can be used in cases of ultra-thin targets, but also taking into account the cross-section structure. The targets used in the present thesis had a variety of thicknesses ranging from ~ 10 to 30 keV. Nevertheless, the mean energy approximation can be applied since the cross-section do not display any sharp resonances with widths of a few keV. The thickness of each one of the used targets is analyzed in detail in the following sections along with the energy loss values.

Therefore, after the target thickness ratio was determined and the simulation of the target layers was performed in the SIMNRA program, the differential cross section values were attributed to the beam energy E after the accelerator calibration minus the energy that the beam loses as it progresses up to the mean thickness of the under-study element. More specifically, the energy E was obtained by using the following equation: $E = E_1 - \Delta E_{Au} - \Delta E_{N/2}$, where E_1 corresponds to the beam energy after the accelerator calibration, ΔE_{Au} to the energy loss in the surface gold layer and $\Delta E_{N/2}$ is the energy loss taking into account half of the target thickness of the layer where the under-study element is located. These values also correspond to the incident beam energy in the cases where ratio to Rutherford plots are shown. The settings of the parameters in SIMNRA for such calculations are the same, as described in section 4.1.2.

The uncertainty obtained from the whole procedure of calculating the final energy in which the cross-section values were attributed involves the ripple value of the accelerator, as well as the energy straggling in the target, value obtained from the target thickness calculation procedure via SIMNRA. Since the used targets are not ultra-thin, the dominant parameter in the assessment of the beam energy uncertainty is the energy straggling, as it becomes obvious in the sections where the specific cases are analyzed.

4.2 Validation procedure – Benchmarking methodology

As discussed above, the only way to test the accuracy and the reliability of a specific differential cross section dataset is by using the benchmarking procedure. In the present dissertation, in certain cases (^{16}O , ^{23}Na , $^{\text{nat}}\text{Si}$), benchmarking experiments of the acquired datasets followed the differential cross section measurements. Such a validation process includes the irradiation of a thick target containing the under-study element/isotope at a known composition, using the same incident beam as the tested cross section dataset. The obtained experimental spectra are subsequently simulated in detail, by implementing the cross-section dataset to be checked using an appropriate program capable of taking into account any possible sharp narrow resonances displayed in the cross section, such as e.g. the SIMNRA code. Up to now SIMNRA, as all the widespread analytical codes, does not take into account the uncertainties when using experimental datasets, while the evaluated ones do not include any uncertainties either. The obtained result of the whole benchmarking procedure is the error margin of the benchmarked data.

It should be pointed out here that the key points of a benchmarking experiment are the target selection and the integrated window. The target ideally needs to be polished and to contain a medium-Z element besides the element under-study, for charge normalization and in order to avoid a huge background contribution from the matrix which would need to be subtracted in case of the presence of a heavy element. The integrated window is a region below the surface of the under-study element in the target, in which the comparison between the simulated and the experimental counts is performed. Usually it is chosen to be $\sim 150\text{-}200$ keV below the target surface in order to avoid differences due to straggling and plural scattering (in the case of heavy elements).

The most important parameters of benchmarking measurements are the stopping power compilation and the straggling models (the latter have only a minimal contribution due to the choice of the integration window) used, the resolution of the detectors, the beam energy, the ADC calibration and the target roughness [22]. The stopping power and the straggling models are the same as the ones used for the target thickness ratio calculation mentioned in section 4.1.2. Moreover, different stopping power models (Ziegler-Biersack [78] and Andersen-Ziegler) were tested in the integrated window and the differences in the benchmarking procedure were below 1%. All the experimental parameters (detector resolution, beam energy and ADC calibration) were determined as discussed in the previous sections. Concerning the target roughness, in the cases where the implemented target is not a crystal, the edge of the target surface in the experimental spectra is not so steep. Corrections could be applied after the measurements in the simulated spectra in order to account for the target surface asperities [22]. However, in the course of the present thesis where a NaCl pellet was used for the benchmarking of the $^{23}\text{Na}(d,d_0)^{23}\text{Na}$, the obtained spectra did not indicate any severe effects of surface roughness and thus no corrections were applied, as discussed in the dedicated section. On the other hand, the crystalline targets usually display channeling perturbations near the surface. One way to impede such perturbations and obtain a truly random spectrum is the tilting and rotating of the target during the acquisition. However, in the used experimental chamber this was not possible. Thus, following the completion of the measurements, the obtained spectra were carefully re-examined for a decrease in the number of the counts near the surface edge and for a change in the detector resolution (different slope),

that is, for experimental effects related to channeling effects. After the examination, the used spectra were very strictly selected; if doubts existed the spectrum was not used, in order to ensure that the spectra did not contain any channeling perturbations.

As the benchmarking is an integral experiment, it contains its own uncertainties and limitations. Concerning the uncertainties, the main parameters are the stopping power systematics, the pulse height defect, the counting statistics and the correct determination of the $Q \cdot \Omega$ parameter in the used spectra [22]. Since the use of different stopping power compilations results to effects in the benchmarking process below 1%, no systematic uncertainty is obtained. However, the issue of the accuracy of the available stopping power compilations remains unresolved and thus it cannot be somehow accounted in the final calculated uncertainty budget. The statistical uncertainty of the stopping power in each case depends on the element and it is examined separately. The pulse height defect had a negligible effect on the analysis for the studied deuteron energy range. The counting statistics and the determination of the $Q \cdot \Omega$ factor are strongly related to the isotopes/elements in the target and more specifically to the presence of medium or high Z elements and are discussed in each specific case.

The major problem of the benchmarking procedure that is more profound in the d-EBS spectra and inserts extra uncertainties and may even exclude spectra from the benchmarking process is the contribution of the d-NRA levels under the elastic ones, as mentioned in section 2.4. Especially for higher beam energies (above ~ 2 MeV), where additional levels of the (d,p_x) and (d,α_x) reactions are excited and may contribute to the experimental spectra under the elastic scattering edge. One way to resolve the problem of the combined NRA/EBS benchmarking contribution is, as mentioned before, the use of a magnetic spectrometer for the separation of the deuterons, protons and alpha particles. In the absence of such a magnetic spectrometer the implementation of very thin ΔE -E telescopes could in principle separate alpha particles and deuterons. In the case of protons however, since the differences between the stopping power of protons and deuterons in the d-EBS energy range between 1-2 MeV are relatively small, thick ΔE -E telescopes would be required. Such thick telescopes would result to a large dependence on the proper straggling model, leading to large uncertainties in the benchmarking procedure. In the context of the present thesis none of these methods was possible and thus no results were obtained in the cases where the background attributed to the (d,p_x) levels was significant.

All the details concerning the particularities of each case are analyzed in the specific sections devoted to each element/isotope under study.

4.3 Cross section measurements for the ${}^6\text{Li}(d,d_0){}^6\text{Li}$ elastic scattering

The differential cross section of deuteron elastic scattering on ${}^6\text{Li}$ were studied in the energy range of 940-2000 keV with a variable energy step (~ 20 -30 keV) and for the scattering angles of 125° , 140° , 150° , 160° , 170° . Since the structure of the under-study cross section cannot be *a priori*

known, especially in the case where it has never been measured before in the selected energy range, the theoretical study of the levels of the formed compound nucleus before the experiment is essential. From such a study the required energy steps depending on the level density in the studied energy range, along with the proper thickness of the measured target are obtained. The level scheme of the system ${}^6\text{Li}+d$ is shown in Fig. 4.5 along with the possible reaction channels. The levels of the compound nucleus included in the level scheme are the ones close to the studied energy region. The formed compound nucleus is ${}^8\text{Be}$ and one level lays in the studied energy range with energy $E_x^* = 22980$ keV and amplitude $\Gamma = 230$ keV. Moreover, the levels with energies $E_x^* = 22240$ keV, $E_x^* = 23980$ keV and amplitudes $\Gamma = 800$ keV and $\Gamma \approx 7\text{MeV}$ respectively are included in the level scheme since the cross-section structure could be affected due to their large amplitudes. The information concerning the energy of the levels and the widths were obtained in all cases from the National Nuclear Data Center website [79], unless it is reported otherwise.

The implemented target had a thin gold layer on top of an enriched ${}^6\text{LiF}$ layer, evaporated on top of a self-supporting carbon foil (details on section 3.5.1). A typical spectrum is shown in Fig. 4.6 for the deuteron energy of 1820 keV and the scattering angle of 150° . The parasitic contribution of oxygen and nitrogen, inserted in the target during the evaporation process, was observed, as it creates two partially overlapping wide peaks. The width of such peaks was probably caused by the existence of nitrogen and oxygen in all the target layers. In the carbon elastic peak, as well as in the ${}^{12}\text{C}(d,p){}^{13}\text{C}$ peak, a second peak is also formed in the right side of the main peaks that could be attributed to the possible partially diffused LiF in the carbon foil and was enhanced due to the carbon buildup effect during the measurements. However, none of these effects impeded the analysis of the experimental spectra, since the under-study peaks of ${}^6\text{Li}$ and Au remained unaffected. Equation 4.3 for the ${}^6\text{Li}$ case is transformed to the following:

$$\left(\frac{d\sigma}{d\Omega}\right)_{\theta,E}^{6\text{Li}} = \left(\frac{d\sigma}{d\Omega}\right)_{\theta,E'}^{\text{Au}} \times \frac{Y_{6\text{Li}}}{Y_{\text{Au}}} \times \frac{N_{t,\text{Au}}}{N_{t,6\text{Li}}} \quad (4.6)$$

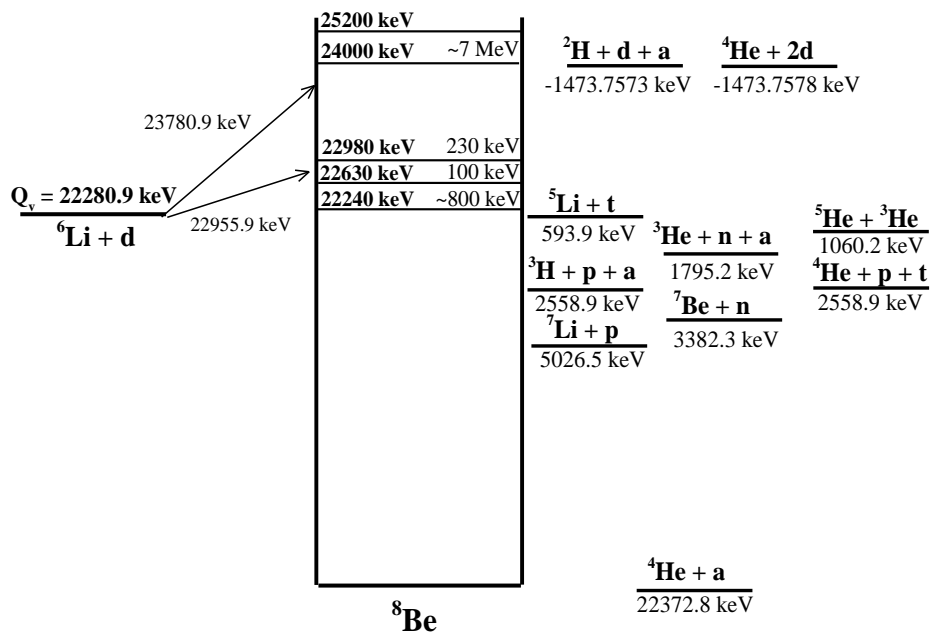


Figure 4.5 Level scheme of the ${}^6\text{Li}+\text{d}$ system in the CM reference frame.

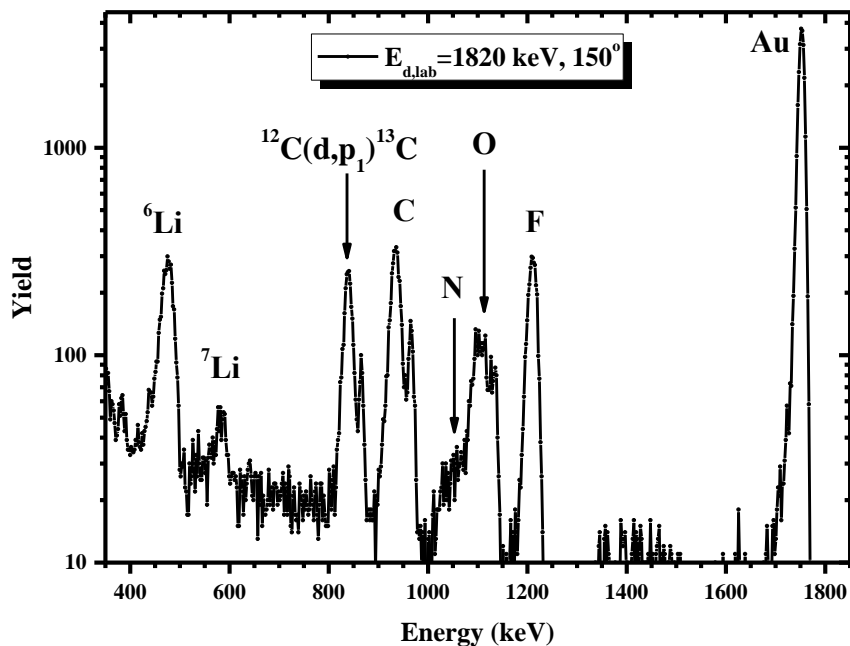


Figure 4.6 Typical deuteron experimental spectrum of a ${}^6\text{LiF}$ layer on top of a carbon foil, along with a ${}^{197}\text{Au}$ layer on top acquired at 1820 keV and for the scattering angle of 150° along with the corresponding peak identification.

4.3.1 Target characterization

In order to calculate the target thickness ratio $N_{\text{Au}}/N_{{}^6\text{Li}}$, the enrichment factor of ${}^6\text{Li}$ in the target (f_{enr}) was used via the equation $\frac{N_{t,\text{Au}}}{N_{t,{}^6\text{Li}}} = \frac{N_{t,\text{Au}}}{f_{\text{enr}} \cdot N_{t,\text{natLi}}}$. For the calculation of the $\frac{N_{t,\text{Au}}}{N_{t,\text{natLi}}}$ ratio the assumption that lithium and fluorine retain their respective elemental ratio during the evaporation procedure was used and thus the equality $\frac{N_{t,\text{Au}}}{N_{t,\text{natLi}}} = \frac{N_{t,\text{Au}}}{N_{t,\text{F}}}$ holds. This assumption is justified by the strong ionic bonding between alkaline/halogen salts like LiF that retain their stoichiometry under extreme circumstances. In chemistry, the bigger the difference between the electronegativity of the elements in the bond the stronger the ionic bonding is. The electronegativity value for lithium is 0.98, while the corresponding one for fluorine is 3.98. This difference is among the highest in the periodic table of elements. Moreover, this assumption has also been verified in the past in our laboratory [10] and the obtained results based on this assumption were also benchmarked. Consequently, the following equation: $\frac{N_{t,\text{Au}}}{N_{t,{}^6\text{Li}}} = \frac{N_{t,\text{Au}}}{f_{\text{enr}} \cdot N_{t,\text{natLi}}} = \frac{N_{t,\text{Au}}}{f_{\text{enr}} \cdot N_{t,\text{F}}}$ holds and it was used for the target thickness calculation. Since the deuteron elastic scattering on fluorine is described by the Rutherford formula for energies up to ~ 1200 keV, for the scattering angles of 140° and 150° , (deviations are less than 2%) as shown in [11], the low-energy deuteron spectra at the scattering angles of 140° and 150° were used. The fitting of the corresponding spectra at 1160 keV and 1200 keV using the SIMNRA program was performed by implementing Rutherford cross section values for both fluorine and gold and the results are shown in Fig. 4.7 for the $E_{\text{d,lab}}=1200$ keV and for 140° . This procedure led to a mean value of $\frac{N_{t,\text{Au}}}{N_{t,\text{natLi}}} = 0.091 \pm 0.004$.

For the determination of the enrichment factor f_{enr} proton spectra of the enriched ${}^6\text{LiF}$ and a thin ${}^{\text{nat}}\text{LiF}$ (prepared in a similar way) target were acquired at $E_{\text{p,lab}}=1600$ keV and 1700 keV for the scattering angles of 125° , 140° , 150° , 160° , 170° . The ratios of counts of F and ${}^6\text{Li}$ in both the enriched and the natural target were determined ($Y_{\text{nat}}^{\text{F}}:Y_{\text{enr}}^{\text{F}}$ and $Y_{\text{nat}}^{6\text{Li}}:Y_{\text{enr}}^{6\text{Li}}$), afterwards the numbers corresponding to the enriched target were normalized over the charge. The charge normalization number was obtained by the ratio of the charge of the two measurements using the current integrator and subsequently a second normalization was performed over the counts of ${}^6\text{Li}$ in the enriched target due to the different target thicknesses. The normalization number was the ratio $\left(\frac{Y_{\text{nat}}^{\text{F}}}{Y_{\text{enr}}^{\text{F}}}\right)$ which expressed the ratio of the equivalent target thicknesses of lithium in the natural

and in the enriched target. Thus, by taking into account that the abundance of ${}^6\text{Li}$ in the natural target is 7.5%, the value of the enrichment factor was acquired. This procedure was repeated for both proton energies (1600 keV and 1700 keV) and for the five scattering angles and the average value of the enrichment factor was 97%, with a statistical error of $\sim 2\%$. This experimentally obtained value was in excellent agreement with the nominal one supplied by the manufacturer and it was therefore adopted for the determination of the differential cross-section values.

The target thickness ratio $N_{t,Au} : N_{t,{}^6\text{Li}}$ was also calculated straightforward, as an alternative means of checking the obtained value, using the proton spectrum of the ${}^6\text{LiF}$ target for the energy of 1600 keV at 170° . More specifically, a dataset from literature should be implemented in the simulation of the experimental spectrum and the one measured by Fasoli et al. [12] at 166.4° was chosen, due to the fact that it was obtained with a small energy step. The results of this simulation led to a good agreement, as shown in Fig. 4.8. However, the obtained ${}^6\text{Li}:\text{Au}$ areal surface density ratio differed by more than 10% from the one determined with the deuterons. Moreover, since Fasoli et al. has also measured differential cross-section datasets for proton elastic scattering on ${}^7\text{Li}$ [80] and spectra from the thin ${}^{\text{nat}}\text{LiF}$ target were also obtained during measurements, the simulation of both ${}^6\text{Li}$ and ${}^7\text{Li}$ peak was deemed crucial and thus it was performed using the Fasoli et al. datasets. An overestimation of 11% occurred in the ${}^6\text{Li}$ integral when the ${}^7\text{Li}$ peak was fitted, as shown in Fig. 4.9. It is not clear whether the problem lies in the dataset of ${}^6\text{Li}$ or ${}^7\text{Li}$ and in fact this situation is common in non-benchmarked and non-evaluated cross section datasets. Additionally, the datasets by Baskin et al. for ${}^6\text{Li}$ and ${}^7\text{Li}$ [81] were used, which are the only existing ones along with data by Fasoli et al. for both isotopes in IBANDL, and the situation deteriorated (deviations were higher than 15%). Such systematic divergences ($\sim 11\%$ and $>15\%$) could not be considered negligible and thus the target thickness ratio determined with deuterons, by using the Rutherford fluorine data, was considered more reliable and was subsequently adopted in the differential cross section values calculation.

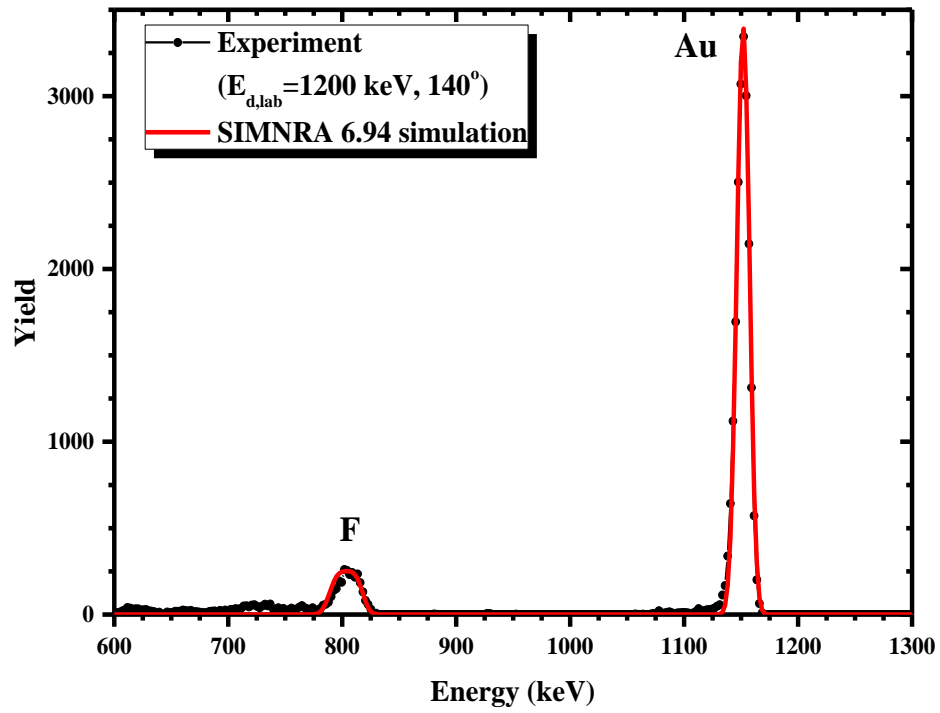


Figure 4.7 Experimental and simulated spectra at the deuteron energy 1200 keV and for the scattering angle of 140° acquired for the target thickness ratio calculation, along with the corresponding peak identification.

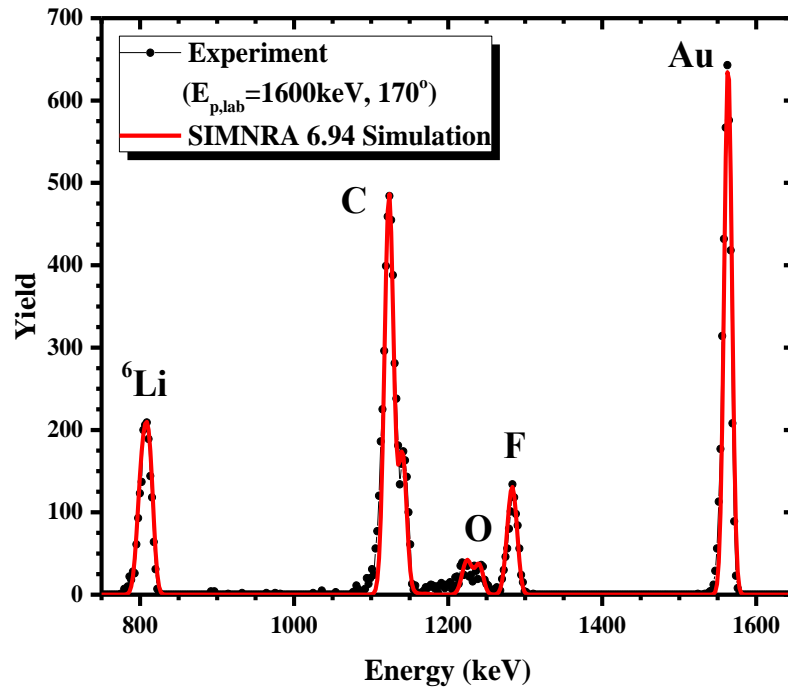


Figure 4.8 Experimental and simulated proton spectra at $E_{p,lab} = 1600$ keV and 170° , along with the corresponding peak identification, using the Fasoli et al. [12] differential cross-section values for proton elastic scattering from ${}^6\text{Li}$.

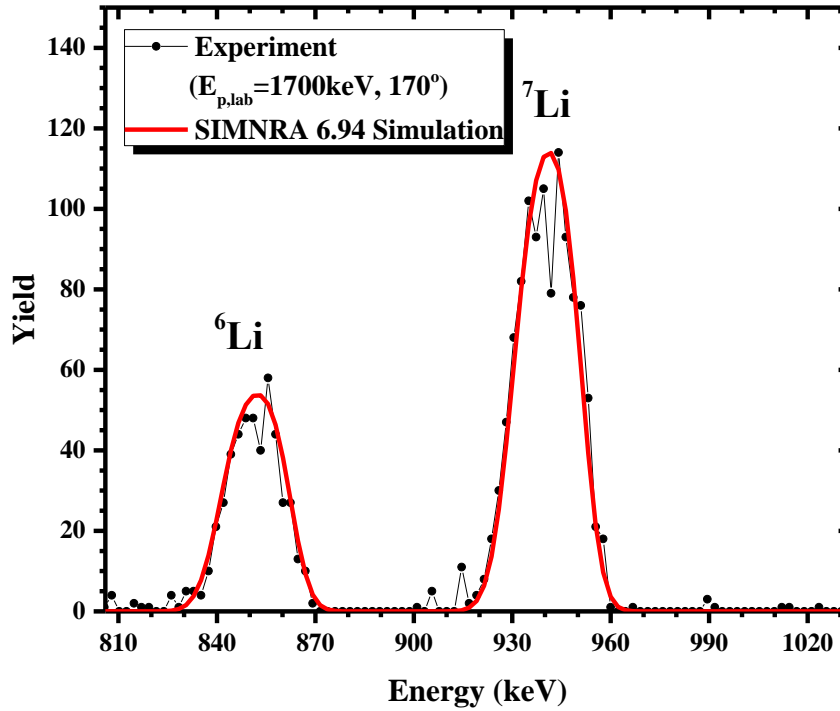


Figure 4.9 Experimental and simulated proton spectra at $E_{p,lab} = 1700$ keV and 170° of the thin ^{nat}Li target, along with the corresponding peak identification, using the Fasoli et al. differential cross-section datasets for proton elastic scattering on ^6Li [12] and ^7Li [80]. An overestimation of more than 10% in the integrated counts of the ^6Li peak is obtained.

4.3.2 Uncertainties

The integration process of the ^6Li and Au peaks yielded a statistical uncertainty below 1%. The target thickness ratio calculation inserted a higher statistical uncertainty of 4.4% originating mainly from the mean value determination process of the ratio $N_{t,Au} : N_{t,^6\text{Li}}$ along with ~2% obtained from the enrichment factor determination process due to the integration of the ^6Li and F peaks in the corresponding spectra. In this calculation the use of ratios was indeed intended to avoid the insertion of any additional uncertainties in this process. It should also be pointed out that during the course of the determination of the $^6\text{Li}:\text{Au}$ ratio different stopping power compilations were also implemented in SIMNRA and the discrepancies were always below 1%. The sum of these values according to the error propagation formula yielded a statistical uncertainty of the order of 5%, adopted in the determined cross section values.

Systematic uncertainties were inserted in the final cross section values due to the deviation between the SRIM compilation and the existing experimental stopping power data; for lithium a value of 9.6 % was obtained, while for fluorine there was no information available (as shown in the SRIM website, <https://www.srim.org>). However, testing neighbouring nuclei like oxygen and neon differences up to 2.8% were observed for both. For the gold case the differences were up to 3.6%.

The uncertainties in the deuteron beam energy originated from the energy calibration process and the energy straggling inside the determined target. In this specific case, the energy calibration was accomplished using the proton resonances with energies 1.737 MeV ($\Gamma = 47$ keV) and 2.08 MeV ($\Gamma = 15.6$ keV) of the $^{12}\text{C}(p,p_0)^{12}\text{C}$ [82] and $^{28}\text{Si}(p,p_0)^{28}\text{Si}$ [27] elastic scattering respectively which are described via evaluated differential cross section values. As mentioned in section 4.1.4.1, with the implementation of this method for energy calibration the determination of the ripple is not possible and the accuracy cannot be better than one channel in the experimental spectra corresponding to ~ 3 keV. The straggling was determined to be 3.4-3.6 keV for all beam energy values.

4.3.3 Results and Discussion

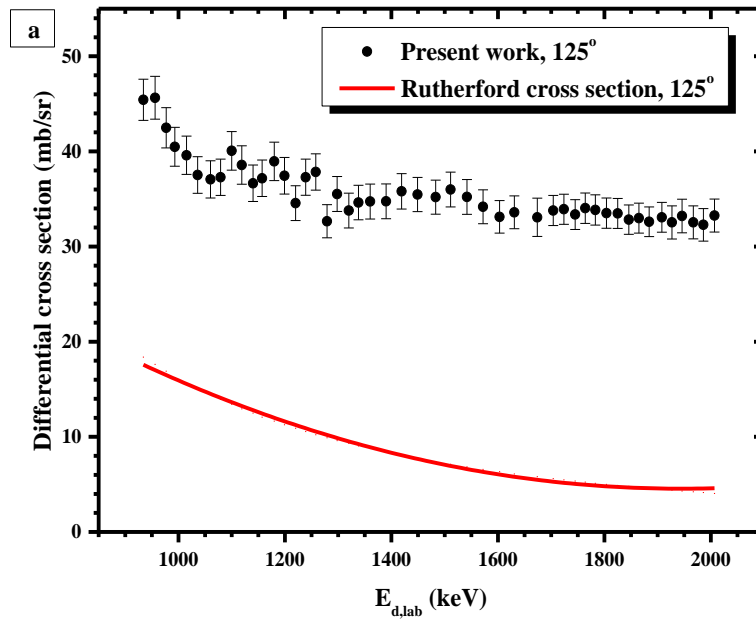
The differential cross-section values of the deuteron elastic scattering on ^6Li , $^6\text{Li}(d,d_0)^6\text{Li}$, in the energy range 940 – 2000 keV for the backscattering angles of 125° , 140° , 150° , 160° and 170° are presented in graphical form in Figs. 4.10 a–e and in tabulated form in Table 4.1, along with the corresponding statistical uncertainties. The plotted uncertainties are only the statistical ones, according to the common convention, while the uncertainties concerning the deuteron beam energy are not visible in the horizontal axis due to the adopted scale.

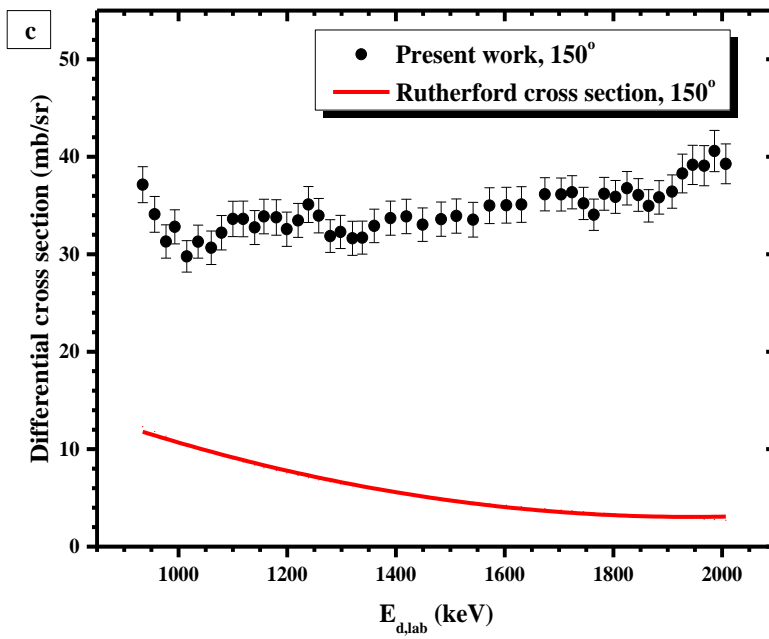
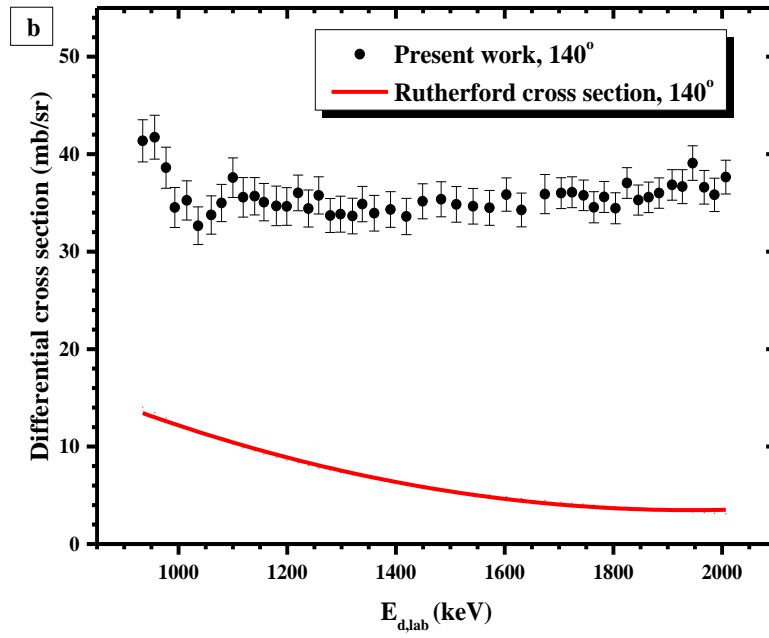
The final cross section values are considerably higher than the corresponding Rutherford ones, up to a factor of ~ 18 . The whole cross section structure is influenced by the overlapping levels of the compound nucleus ^8Be , shown in Fig. 4.5 with energies $E_x^* = 22240$ keV, 22980 keV, and 24000 keV and amplitudes $\Gamma = 800$ keV, 230 keV and 7000 keV respectively. More specifically, the structure revealed in the low energy part (930-980 keV) resembles the tail of a resonance and could be attributed to the level with energy $E_x^* = 22240$ keV and $\Gamma = 800$ keV of the compound nucleus ^8Be . Even though this level is below the studied energy range it might have affected the cross section. These broad overlapping states could in principle have caused the small variation of the differential cross section values at such a broad energy range of ~ 1.1 MeV.

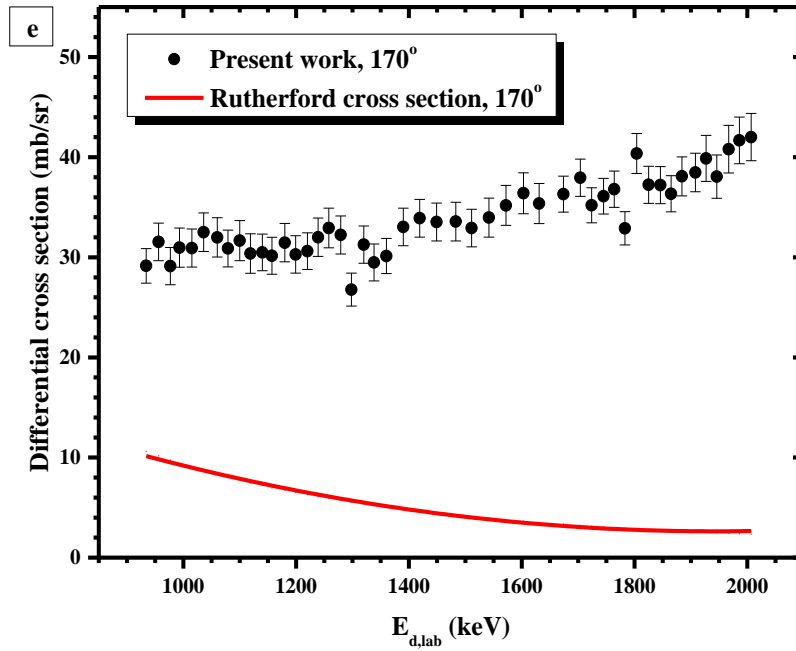
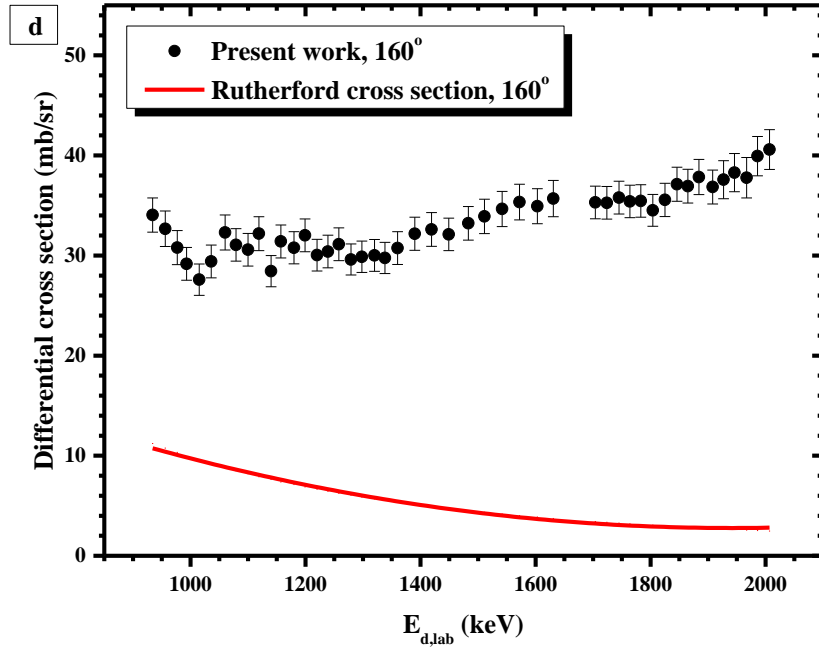
Regarding the angular dependence of the obtained differential cross sections of deuteron elastic scattering on ^6Li , as shown in Fig. 4.11, a region exists (~ 1400 - 1800 keV) where the changes in both the angle as well as the energy are minimal. Such a characteristic could be very useful for applications of determining ^6Li depth profile concentrations when the beam energy and/or the scattering angle are not known with high precision. It should also be pointed out that in the low

energy region (below 1400 keV) the more forward backscattering angles displayed higher cross section values, whereas in the high energy region (above 1800 keV) the opposite behavior was observed, with the more backscattering angles displaying higher values. This could be attributed to the differences in the angular dependence of the resonances at low and high energies of the compound nucleus ^8Be .

The problem of benchmarking the obtained d–EBS differential cross–sections, especially in the case of ^6Li , which is a relatively low–abundance isotope, is rather important; however, it was not addressed in the present dissertation since it required a more sophisticated target e.g. a metallic, enriched in ^6Li , one.







Figures 4.10 a-e. Differential cross-section values (mb/sr) of the ${}^6\text{Li}(d,d_0){}^6\text{Li}$ elastic scattering, measured at $E_{d,lab} = 940\text{--}2000$ keV and for the scattering angles of 125° , 140° , 150° , 160° , 170° , in variable energy

steps ~20-30 keV. The total estimated statistical uncertainties are included in the graphs; in the x-axis, the uncertainties are not visible due to the selected scale.

Table 4.1 Tabulated differential cross sections (mb/sr) of the ${}^6\text{Li}(d,d_0){}^6\text{Li}$ elastic scattering, measured for $E_{d,\text{lab}}=940\text{--}2000$ keV, in variable energy steps (20-30 keV) at backscattering angles 125° , 140° , 150° , 160° , 170° . The corresponding combined cross-section statistical uncertainties are also included.

$E_{d,\text{lab}}$ (keV)	$dE_{d,\text{lab}}$ (keV)	$(\sigma \pm d\sigma)$ (mb/sr)									
		125°		140°		150°		160°		170°	
930	5	45.4	2.2	41.4	2.2	37.1	1.8	34.0	1.7	29.1	1.7
950	5	45.6	2.3	41.7	2.3	34.1	1.8	32.7	1.8	31.5	1.9
970	5	42.5	2.1	38.6	2.2	31.3	1.7	30.8	1.7	29.1	1.9
990	5	40.5	2.0	34.5	2.0	32.8	1.7	29.2	1.6	31.0	2.0
1010	5	39.6	2.0	35.3	2.0	29.8	1.6	27.6	1.6	30.9	1.9
1031	5	37.5	1.9	32.7	2.0	31.3	1.7	29.4	1.6	32.5	1.9
1051	5	37.1	2.0	33.8	2.0	30.7	1.7	32.3	1.7	32.0	2.0
1071	5	37.3	1.9	35.0	2.1	32.2	1.8	31.1	1.6	30.9	1.8
1091	5	40.1	2.0	37.6	2.2	33.6	1.8	30.6	1.6	31.7	2.0
1111	5	38.6	2.0	35.6	2.1	33.6	1.8	32.2	1.7	30.4	2.0
1131	5	36.7	1.9	35.7	2.1	32.7	1.7	28.4	1.6	30.5	1.8
1151	5	37.2	1.9	35.1	2.0	33.9	1.8	31.4	1.6	30.2	1.8
1171	5	39.0	2.0	34.7	2.0	33.8	1.8	30.8	1.6	31.5	1.9
1192	5	37.4	1.9	34.6	2.0	32.6	1.8	32.0	1.6	30.3	1.9
1212	5	34.6	1.8	36.0	2.1	33.5	1.7	30.0	1.6	30.6	1.8
1232	5	37.3	1.9	34.4	2.1	35.1	1.8	30.4	1.6	32.0	1.9
1252	5	37.8	1.9	35.8	2.1	34.0	1.8	31.1	1.6	32.9	2.0
1272	5	32.7	1.7	33.7	2.0	31.9	1.7	29.6	1.5	32.2	1.9
1292	5	35.5	1.8	33.8	2.0	32.3	1.7	29.9	1.6	26.8	1.6
1312	5	33.8	1.8	33.7	1.9	31.6	1.7	30.0	1.6	31.3	1.9
1332	5	34.6	1.8	34.9	2.0	31.7	1.7	29.8	1.6	29.5	1.8
1352	5	34.7	1.8	33.9	1.9	32.9	1.7	30.7	1.6	30.1	1.8

1383	5	34.7	1.8	34.3	2.0	33.7	1.7	32.2	1.7	33.0	1.9
1413	5	35.8	1.9	33.6	1.9	33.9	1.8	32.6	1.7	33.9	1.9
1443	5	35.5	1.8	35.2	2.0	33.0	1.7	32.1	1.6	33.5	1.9
1473	5	35.2	1.8	35.4	2.0	33.6	1.8	33.2	1.7	33.6	1.9
1503	5	36.0	1.8	34.9	2.0	33.9	1.8	33.9	1.7	32.9	1.9
1533	5	35.2	1.8	34.7	1.9	33.5	1.8	34.7	1.8	34.0	2.0
1563	5	34.2	1.8	34.5	2.0	35.0	1.8	35.3	1.8	35.2	2.0
1593	5	33.1	1.7	35.9	2.0	35.0	1.8	34.9	1.8	36.4	2.0
1623	5	33.6	1.7	34.3	2.0	35.1	1.8	35.7	1.8	35.4	2.0
1664	5	33.1	2.0	35.9	1.8	36.2	1.7	-	-	36.3	1.8
1694	5	33.8	1.6	36.0	1.8	36.1	1.7	35.3	1.6	37.9	1.9
1714	5	33.9	1.6	36.1	1.8	36.4	1.7	35.3	1.6	35.2	1.7
1734	5	33.4	1.6	35.8	1.8	35.2	1.7	35.8	1.6	36.1	1.8
1754	5	34.0	1.6	34.6	1.7	34.1	1.6	35.4	1.6	36.8	1.8
1774	5	33.8	1.6	35.6	1.8	36.2	1.7	35.4	1.6	32.9	1.7
1794	5	33.5	1.6	34.5	1.7	35.9	1.7	34.5	1.6	40.4	2.0
1814	5	33.5	1.6	37.0	1.8	36.8	1.7	35.6	1.7	37.2	1.9
1834	5	32.8	1.5	35.3	1.8	36.1	1.7	37.1	1.7	37.2	1.9
1854	5	33.0	1.6	35.6	1.8	35.0	1.7	36.9	1.7	36.3	1.8
1874	5	32.6	1.6	36.0	1.8	35.8	1.7	37.8	1.8	38.1	1.9
1894	5	33.1	1.6	36.8	1.8	36.4	1.7	36.8	1.7	38.5	1.9
1914	5	32.5	1.7	36.7	2.1	38.3	2.0	37.6	1.9	39.9	2.3
1934	5	33.2	1.8	39.1	2.2	39.2	2.0	38.3	1.9	38.1	2.2
1954	5	32.5	1.7	36.6	2.1	39.1	2.1	37.8	2.0	40.8	2.4
1975	5	32.3	1.7	35.8	2.1	40.6	2.1	39.9	2.0	41.7	2.3
1995	5	33.3	1.7	37.7	2.1	39.3	2.0	40.6	2.0	42.0	2.4

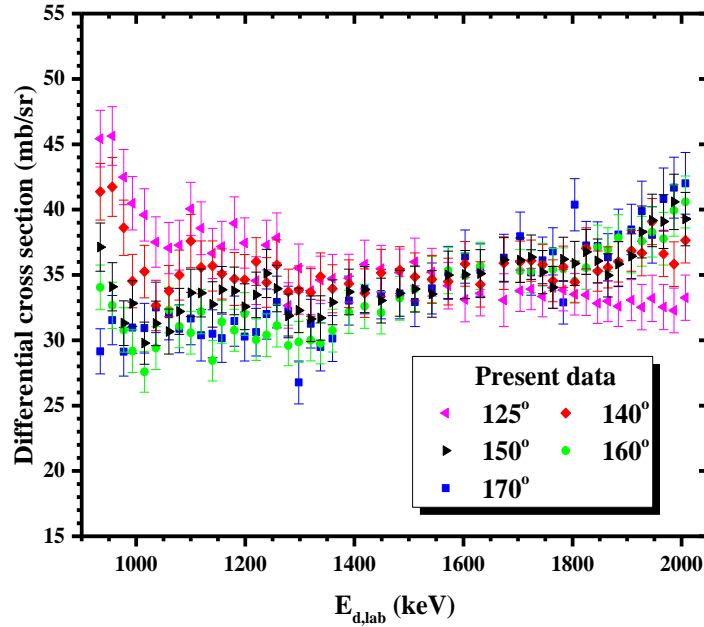


Figure 4.11 Differential cross-section values (mb/sr) for the ${}^6\text{Li}(d,d_0){}^6\text{Li}$ elastic scattering at different angles, measured at $E_{d,\text{lab}}=940\text{--}2000$ keV and for all the scattering angles measured in the present work.

4.4 Cross section measurements for the ${}^7\text{Li}(d,d_0){}^7\text{Li}$ elastic scattering

The differential cross section values of the ${}^7\text{Li}(d,d_0){}^7\text{Li}$ elastic scattering were measured in the deuteron energy range of 940-2000 keV with a variable energy step (5-50 keV) and for the backscattering angles of 125° , 140° , 150° , 160° and 170° . The level scheme along with the reaction channels is displayed in Fig. 4.12. The formed compound nucleus is ${}^9\text{Be}$ and the levels included in the study energy range were $E_x^*=17495$ keV with $\Gamma=47$ keV and the $E_x^*=18020$ keV with unknown amplitude. Moreover, the ones outside the studied energy range but with the possibility of affecting the cross section due to their large amplitude were the ones corresponding to $E_x^*=17300$ keV with $\Gamma=95$ keV and $E_x^*=18580$ keV also with unknown amplitude.

The implemented target consisted of a thin ${}^{\text{nat}}\text{LiF}$ layer on top of a self-supporting carbon foil with a thin layer of gold on top. An experimental spectrum at the deuteron energy of 1700 keV for the scattering angle of 150° is shown in Fig. 4.13a. However, at certain energies and angles, a full or partial overlap between the elastic scattering on ${}^7\text{Li}$ with the reaction channels ${}^7\text{Li}(d,p_0){}^6\text{Li}$ ($Q_v = -191.95$ keV) and ${}^{12}\text{C}(d,p_1){}^{13}\text{C}$ was observed, as shown in Fig. 4.13b.

Since for the case of ${}^7\text{Li}$ Eq. 4.3 is transformed to:

$$\left(\frac{d\sigma}{d\Omega}\right)_{\theta,E}^{7Li} = \left(\frac{d\sigma}{d\Omega}\right)_{\theta,E'}^{Au} \times \frac{Y_{7Li}}{Y_{Au}} \times \frac{N_{t,Au}}{N_{t,7Li}} \quad (4.7)$$

the determination of the Y_{7Li} is essential for the calculation of the cross section values. Thus, in the cases where the fitting process could not be accomplished due to the overlap, the sum peak containing the contributions of ${}^7\text{Li}(d,d_0){}^7\text{Li}$, ${}^7\text{Li}(d,p_0){}^6\text{Li}$ and ${}^{12}\text{C}(d,p_1){}^{13}\text{C}$ was initially integrated. Afterwards, the calculation of the contribution of the ${}^{12}\text{C}(d,p_1){}^{13}\text{C}$ reaction in the sum peak was performed using the carbon amount in the target obtained for the experimental spectra and the SIMNRA program. More specifically, the carbon amount was calculated through the deuteron spectra and the implementation of the evaluated ${}^{12}\text{C}(d,d_0){}^{12}\text{C}$ elastic scattering datasets in the SIMNRA program and through the proton spectra, via the ${}^{12}\text{C}(p,p_0){}^{12}\text{C}$ evaluated ones. Afterwards, the verification of the calculated carbon amount was deemed necessary and thus in the energies without the overlap where the peak induced by the ${}^{12}\text{C}(d,p_1){}^{13}\text{C}$ reaction could be properly integrated, the experimental counts were compared with the simulated ones acquired using the Kokkoris et al. dataset [13] for the ${}^{12}\text{C}(d,p_1){}^{13}\text{C}$ reaction. After the verification of the carbon amount and via the implementation of the ${}^{12}\text{C}(d,p_1){}^{13}\text{C}$ dataset for the energies with the peak overlapping, the counts induced by this reaction were calculated and subsequently subtracted from the sum peak counts at each of the energies demonstrating such an overlap. This procedure was not implemented for the scattering angle of 125° , since the used ${}^{12}\text{C}(d,p_1){}^{13}\text{C}$ datasets did not include measurements for this scattering angle and thus the experimental cross section values for 125° were initiated at 1420 keV. Moreover, in the case of 140° , since no measurements exist for the ${}^{12}\text{C}(d,p_1){}^{13}\text{C}$ reaction at this exact angle, the dataset for 145° was used due to the relative invariance of the angular distribution (within $\pm 10^\circ$) of the ${}^{12}\text{C}(d,p_1){}^{13}\text{C}$ reaction at low deuteron beam energies.

Unfortunately, a similar procedure for the ${}^7\text{Li}(d,p_0){}^6\text{Li}$ reaction could not be accomplished, since there is a complete lack of associated datasets in literature. Thus, the obtained cross section measurements refer to the combination of ${}^7\text{Li}(d,d_0){}^7\text{Li}$ and ${}^7\text{Li}(d,p_0){}^6\text{Li}$ for the particular energies where the overlap between the two peaks occurred. This situation, however, does not render the obtained cross section values useless, since in thick target measurements, where no mass spectrometer or ToF technique is employed, resulting to no possibility of distinguishing protons from deuterons, this overlap would also appear in the experimental spectra.

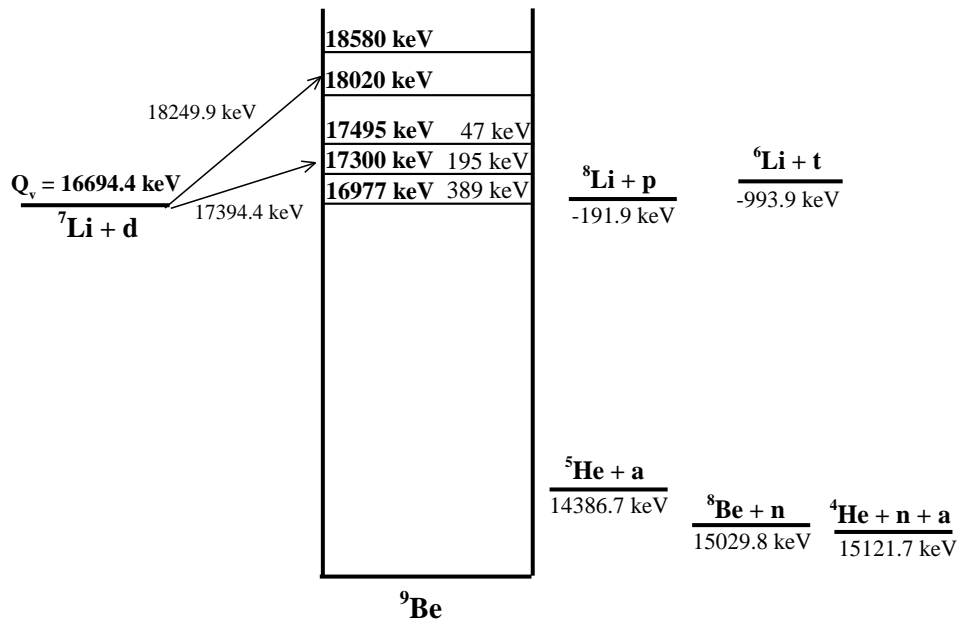
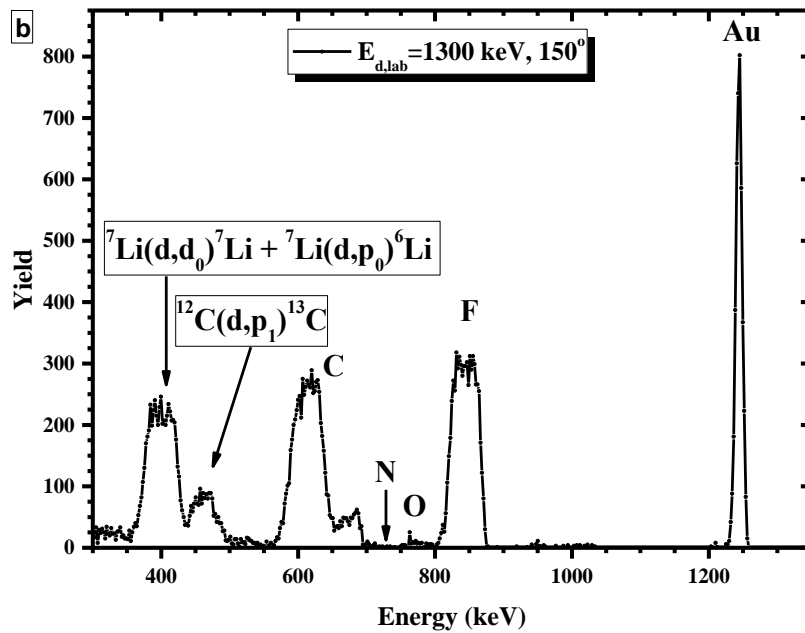
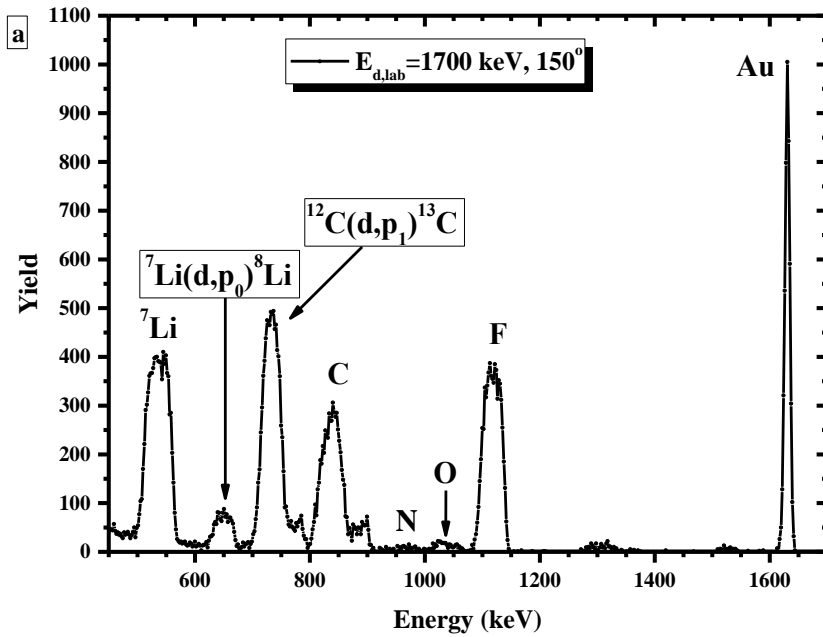


Figure 4.12 Level scheme of the ${}^7\text{Li}+d$ in the CM reference frame.



Figures 4.13 (a) An experimental spectrum of a ${}^{nat}\text{LiF}$ layer on top of a carbon foil, with a Au layer on top taken at the deuteron energy 1700 keV at 150° along with the corresponding peak identification (b) An experimental spectrum of the same target at the deuteron energy 1300 keV at 150° along with the corresponding peak identification.

4.4.1 Target characterization

For the determination of the $N_{t,Au} : N_{t, {}^7Li}$ term of Eq 4.6 the assumption of the retention of the stoichiometry between fluorine and lithium during the evaporation process was used, as in the case of 6Li , and thus the equation $\frac{N_{t,Au}}{N_{t, {}^7Li}} = \frac{N_{t,Au}}{0.9241 \cdot N_{t,natLi}} = \frac{N_{t,Au}}{0.9241 \cdot N_{t,F}}$ was deemed valid. In this case,

since the target consisted of natural LiF, the enrichment factor was not an unknown quantity; it was simply the abundance of 7Li in natural lithium (that is 0.9241). Thus, in order to calculate the term $N_{t,Au} : N_{t,F}$ the low energy deuteron spectra were used, taking into account that fluorine follows the Rutherford scattering formula for deuteron energies lower than ~ 1200 keV at 140° and 150° within 2%, as presented by Foteinou et al. [11], as discussed above. More specifically, the used deuteron energies were 1000, 1050, 1100, 1150, 1200 keV for the scattering angles of 125° , 140° , 150° , 160° and 170° and the mean value of the target thickness ratio $N_{t,Au} : N_{t, {}^7Li}$ was calculated to be (0.0084 ± 0.0004) . A spectrum at the deuteron energy of 1000 keV and 140° is shown in Fig. 4.14. For the simulation of the deuteron energy spectra, Rutherford cross section values were used for the fluorine and gold peaks, whereas for the carbon [14] and oxygen [14] ones the evaluated data existing in SigmaCalc 2.0, as implemented in SIMNRA 6.94, were used.

Moreover, the proton spectra acquired at the energies of 1600 keV and 1700 keV were used as an alternative means of obtaining the $N_{t,Au} : N_{t, {}^7Li}$ value. In order to effectively utilize the proton spectra, datasets from literature were tested for the proton elastic scattering on 7Li . The dataset by Fasoli et al. [80] was the first one tested since it was in good agreement with Malmberg et al. [83], had a small energy step and was accompanied by measurements for 6Li [12]. The results of the simulation are shown in Fig. 4.15 for the proton energy of 1600 keV and at 170° . The cross-section values used for the simulation of the ${}^{12}C(p,p_0){}^{12}C$ [82], ${}^{16}O(p,p_0){}^{16}O$ [84] and ${}^{19}F(p,p_0){}^{19}F$ [85] were obtained from SigmaCalc 2.0, as implemented in SIMNRA 6.94, despite the fact that for the fluorine case a more recent evaluation existed [10]. The mean value of the ratio $N_{t,Au} : N_{t, {}^7Li}$ acquired with this method was 0.0082, which has a $\sim 2.4\%$ deviation from the first method. However, by implementing the dataset by Paneta et al. [10] in the proton spectra simulation this deviation increased, as discrepancies up to $\sim 11\%$ were observed between the datasets from Fasoli et al. and Paneta et al. Taking these discrepancies into account, the value obtained from the low energy deuteron spectra was deemed more reliable and was subsequently used in the cross section values calculation.

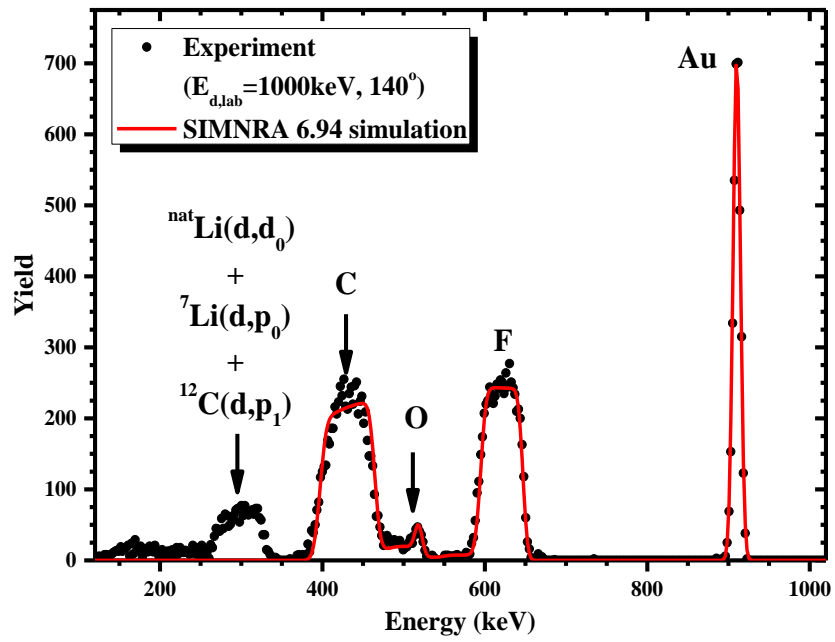


Figure 4.14 Experimental and simulated spectra for the deuteron energy $E_{d,lab} = 1000 \text{ keV}$ at 140° along with the corresponding peak identification.

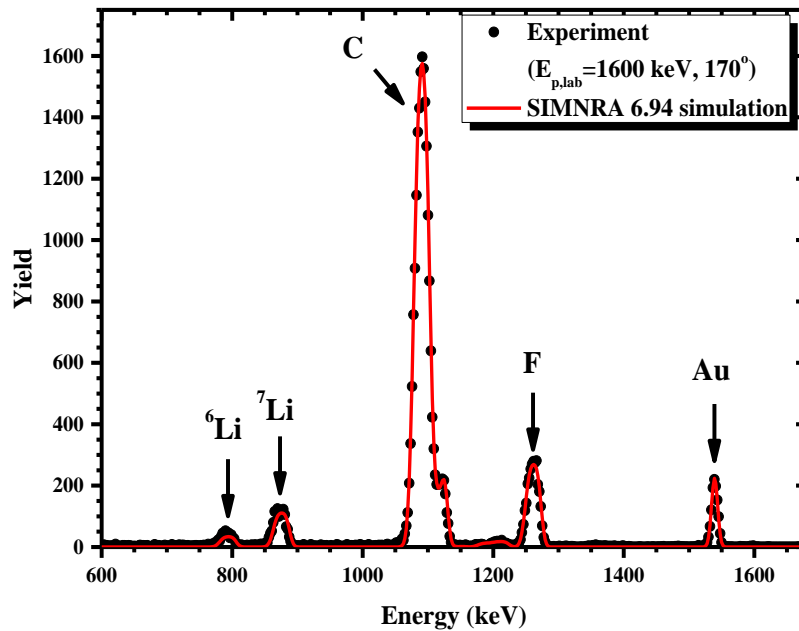


Figure 4.15 Proton experimental and simulated spectrum at the $E_{p,lab} = 1600$ keV and for 170° along with the corresponding peak identification.

4.4.2 Uncertainties

The statistical uncertainties in the differential cross section values included the statistical uncertainty in the determination of the target thickness, which was $\sim 4.8\%$ and the uncertainties in the peak integration method, which were $\sim 1\%$ in the cases where no overlap was observed. However, in the cases with an existing partial or full overlap between the ${}^7\text{Li}(d,d_0){}^7\text{Li}$, ${}^7\text{Li}(d,p_0){}^6\text{Li}$ and ${}^{12}\text{C}(d,p_1){}^{13}\text{C}$ peaks, the statistical uncertainties increased due to the much larger uncertainty of the ${}^{12}\text{C}(d,p_1){}^{13}\text{C}$ cross section values, obtained by Kokkoris et al. [13], which were introduced in the calculations through the error propagation formula. Such calculations led to the combined statistical uncertainties in the differential cross section values of $\sim 5\%$ for the higher beam energies and 6–14% for the lower ones, where the ${}^{12}\text{C}(d,p_1){}^{13}\text{C}$ reaction peak has been subtracted and the combined differential cross sections for both ${}^7\text{Li}(d,d_0){}^7\text{Li}$ and ${}^7\text{Li}(d,p_0){}^6\text{Li}$ reactions have been determined.

Systematic uncertainties were considered, as before, in the final cross section values due to the deviation between the SRIM compilation and the existing experimental stopping power data. These deviations were found at the SRIM website (<https://www.srim.org>) and for the lithium case a value of 9.6 % was obtained, for the gold case a 3.6% deviation was obtained, while for the

fluorine case no information was available. Therefore values for the neighbouring nuclei can be used, which are ~2.8% for oxygen and neon.

The uncertainties in the deuteron beam energy included the accuracy of the energy calibration, which as mentioned above for the ${}^6\text{Li}$ case, was ~3 keV, whereas the energy straggling in the determined target was 4.2 keV for all beam energy values.

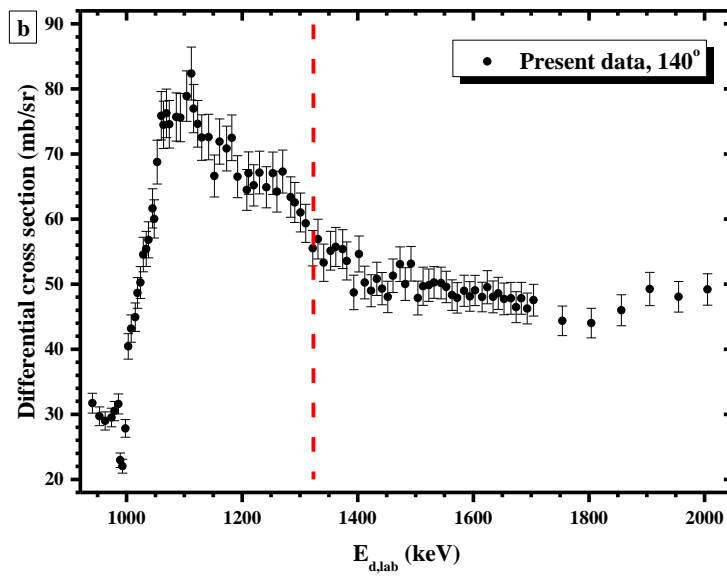
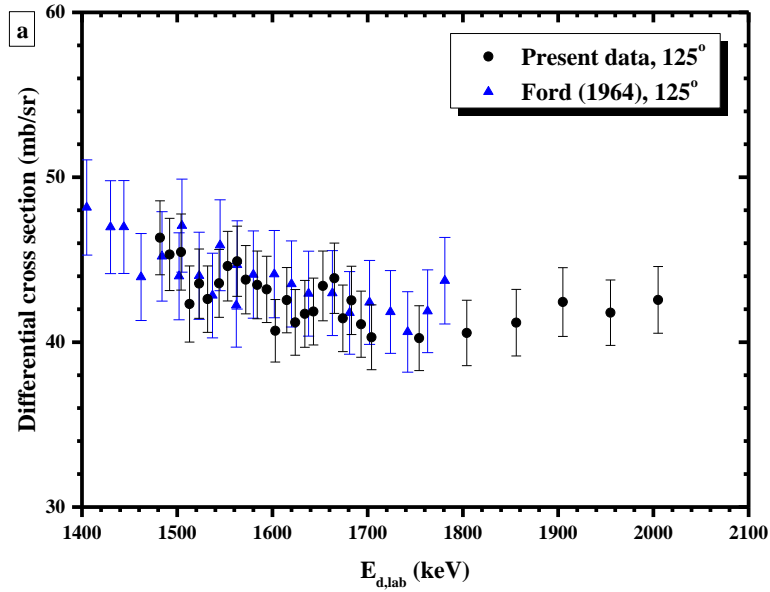
4.4.3 Results and Discussion

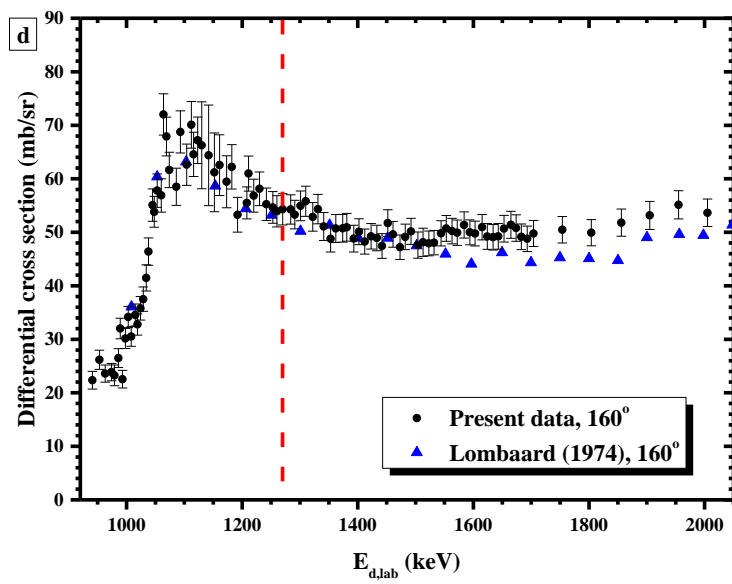
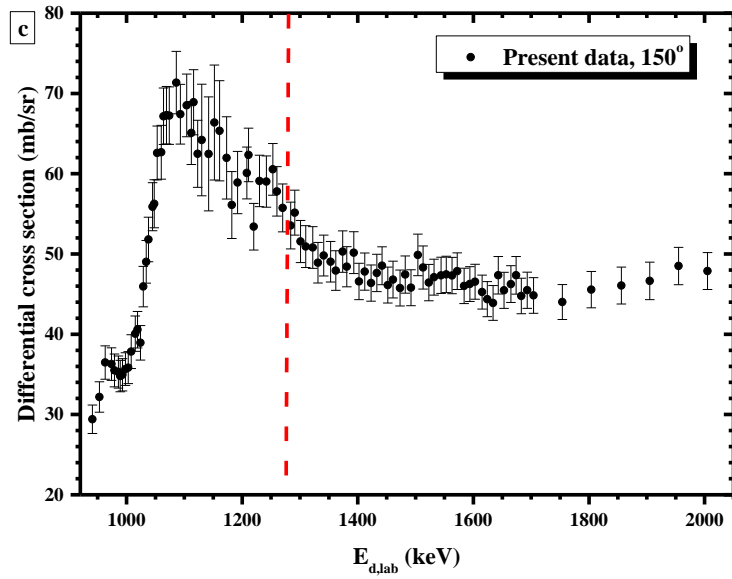
The final cross section values of ${}^7\text{Li}(d,d_0){}^7\text{Li}$ elastic scattering for higher energies and the final cross section values of the sum of the ${}^7\text{Li}(d,d_0){}^7\text{Li}$ and ${}^7\text{Li}(d,p_0){}^6\text{Li}$ reactions for lower energies are shown in graphical form in Figs. 4.16 a-e and in tabulated form in Table 4.2. In Table 4.2 the two regions of the results, corresponding to different reactions, are marked with a dashed horizontal line for every angle. The x-uncertainties are not visible in the graphs due to the adopted scale. The vertical dashed line in Fig. 4.16 b-e divides to two regimes of results. As discussed above, for 125° (Fig. 4.16 a) no data exist in literature for the contribution of ${}^{12}\text{C}(d,p_1){}^{13}\text{C}$ reaction and thus no results were obtained for the low energy region. For higher energies, in Fig. 4.16a the determined cross section values are compared with the ones existing in literature by Ford [15] resulting to a good agreement within errors, up to 5%. In figures 4.16b-e a distinct resonance is displayed in the energy region of 1000 keV and it could be attributed to the superposition of the resulting yields of both ${}^7\text{Li}(d,d_0){}^7\text{Li}$ and ${}^7\text{Li}(d,p_0){}^6\text{Li}$ reactions due to the level of the compound nucleus ${}^9\text{Be}$ at $E_x^* = 17495$ keV with $\Gamma = 47$ keV corresponding to a deuteron beam energy of 1027 keV (in the lab system of reference). In Fig. 4.16d the previously measured data by Lombaard et al. [16], corresponding only to the ${}^7\text{Li}(d,d_0){}^7\text{Li}$ elastic scattering in the whole energy range are also included in the graph. In the latter work the overlap between the peaks of the reactions ${}^7\text{Li}(d,d_0){}^7\text{Li}$, ${}^7\text{Li}(d,p_0){}^6\text{Li}$ and ${}^{12}\text{C}(d,p_1){}^{13}\text{C}$ also existed (due to the lack of a mass separation system). The contribution of the ${}^{12}\text{C}(d,p_1){}^{13}\text{C}$ reaction was calculated from the number of elastically scattered deuterons by the carbon contamination, as in the present work, whereas in the ${}^7\text{Li}(d,p_0){}^6\text{Li}$ case, as the proton peak moved through the desired elastic peak, its contribution was approximated by taking the average of the proton yields determined on either side of the overlapping region. In the whole energy region under-study, the agreement is satisfactory, within uncertainties.

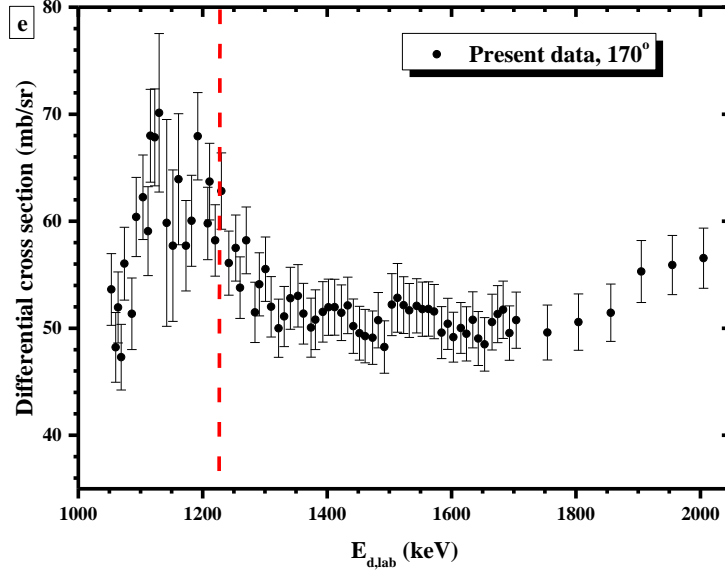
It was also noticed that in the high energy region the differential cross section at each measured angle is relatively stable for small energy steps, namely a few keV, especially for the deuteron energies from 1500 to 1700 keV. This characteristic could be useful for analytical purposes, in the cases where the accelerator beam energy is not so well defined and/or the ripple may not be negligible.

It should be pointed out here that the obtained cross section values were extremely enhanced compared to the corresponding Rutherford ones, especially at higher energies and large angles where the determined values were ~23 times greater relative to the Rutherford ones, as displayed

in Fig. 4.17. Moreover, concerning the angular dependence of the elastic scattering differential cross sections of ${}^7\text{Li}$, it is not particularly strong, as shown in Fig. 4.17 and within 10° no significant variations between the obtained cross sections were observed.







Figures 4.16 a) Differential cross sections of the elastic ${}^7\text{Li}(d,d_0){}^7\text{Li}$ scattering at 125° from the present work along with the dataset by Ford, b,c) Differential cross section at 140° and 150° respectively of the elastic ${}^7\text{Li}(d,d_0){}^7\text{Li}$ scattering for deuteron beam energies higher than $E_{d,\text{lab}} = \sim 1300$ keV (red vertical line) and for both ${}^7\text{Li}(d,d_0){}^7\text{Li}$ and ${}^7\text{Li}(d,p_0){}^6\text{Li}$ reactions at lower energies, d) Differential cross section at 160° of the elastic ${}^7\text{Li}(d,d_0){}^7\text{Li}$ scattering for deuteron beam energies higher than $E_{d,\text{lab}} = 1270$ keV (red vertical line) and for both ${}^7\text{Li}(d,d_0){}^7\text{Li}$ and ${}^7\text{Li}(d,p_0){}^6\text{Li}$ reactions at lower energies along with the data by Lombaard et al. corresponding only to ${}^7\text{Li}(d,d_0){}^7\text{Li}$ in the whole energy range e) Differential cross section at 170° of the elastic ${}^7\text{Li}(d,d_0){}^7\text{Li}$ scattering for deuteron beam energies higher than $E_{d,\text{lab}} = 1220$ keV (red vertical line) and for both ${}^7\text{Li}(d,d_0){}^7\text{Li}$ and ${}^7\text{Li}(d,p_0){}^6\text{Li}$ reactions at lower energies.

Table 4.2 Tabulated differential cross sections (mb/sr) of the ${}^7\text{Li}(d,d_0){}^7\text{Li}$ elastic scattering for higher beam energies ($> \sim 1300$ keV) and the combined ${}^7\text{Li}(d,d_0){}^7\text{Li}$ and ${}^7\text{Li}(d,p_0){}^6\text{Li}$ for lower energies, in variable energy steps (5-50 keV) for the backscattering angles of 125° , 140° , 150° , 160° , 170° . The dashed line in the columns of the table divides the two regimes of the results for each measured angle. The corresponding combined cross-section statistical uncertainties are also included.

$E_{d,\text{lab}}$ (keV)	$dE_{d,\text{lab}}$ (keV)	$(\sigma \pm d\sigma)$ (mb/sr)									
		125°		140°		150°		160°		170°	
941	5	-	-	31.7	1.5	29.4	1.8	22.4	1.6	-	-
953	5	-	-	29.7	1.4	32.2	1.9	26.2	1.8	-	-
963	5	-	-	29.0	1.4	36.5	2.1	23.6	1.6	-	-
974	5	-	-	29.5	1.4	36.3	2.0	23.9	1.6	-	-

979	5	-	-	30.5	1.5	35.5	2.0	23.3	1.9	-	-
986	5	-	-	31.6	1.5	35.3	2.0	26.5	1.8	-	-
989	5	-	-	22.9	1.1	34.8	2.0	32.0	1.9	-	-
993	5	-	-	22.0	1.1	34.9	2.0	22.6	1.7	-	-
998	5	-	-	27.8	1.4	35.7	2.0	30.2	1.9	-	-
1003	5	-	-	40.4	2.0	35.8	2.0	34.2	2.0	-	-
1008	5	-	-	43.2	2.1	37.8	2.1	30.5	1.8	-	-
1015	5	-	-	44.9	2.2	40.1	2.2	34.5	2.0	-	-
1019	5	-	-	48.7	2.4	40.6	2.3	32.8	2.0	-	-
1024	5	-	-	50.3	2.4	38.9	2.1	35.8	2.2	-	-
1029	5	-	-	54.6	2.7	45.9	2.5	37.5	2.3	-	-
1034	5	-	-	55.4	2.7	49.0	2.7	41.5	2.5	-	-
1038	5	-	-	56.8	2.8	51.8	2.8	46.4	2.6	-	-
1045	5	-	-	62	3	56	3	55	3	-	-
1048	5	-	-	60	3	56	3	53.8	2.9	-	-
1053	5	-	-	69	3	63	3	58	3	54	3
1060	5	-	-	76	4	63	3	57	3	48	3
1064	5	-	-	74	4	67	4	72	4	52	3
1069	5	-	-	76	4	67	4	68	4	47	3
1074	5	-	-	75	4	67	4	62	3	56	3
1086	5	-	-	76	4	71	4	59	3	51	3
1093	5	-	-	76	4	67	4	69	4	60	4
1104	5	-	-	79	4	69	4	63	4	62	4
1112	5	-	-	82	4	65	4	70	4	59	4
1116	5	-	-	77	4	69	4	65	4	68	4
1123	5	-	-	75	4	62	4	67	4	68	5
1130	5	-	-	73	3	64	7	66	8	70	7
1142	5	-	-	73	3	62	7	64	9	60	10
1152	5	-	-	67	3	66	7	61	7	58	7

1161	5	-	-	72	3	65	6	63	6	64	6
1173	5	-	-	71	3	62	5	59	5	58	4
1182	5	-	-	72	4	56	4	62	4	60	4
1192	5	-	-	67	3	59	4	53	3	68	4
1208	5	-	-	64	3	60	3	55	3	60	3
1211	5	-	-	67	3	62	3	61	3	64	4
1220	5	-	-	65	3	53.4	2.9	57	3	58	3
1230	5	-	-	67	3	59	3	58	3	63	4
1242	5	-	-	65	3	59	3	55	3	56	3
1253	5	-	-	67	3	61	3	55	3	57	3
1260	5	-	-	64	3	58	3	53.9	2.9	53.8	2.9
1270	5	-	-	67	3	56	3	54.3	2.9	58	3
1284	5	-	-	63	3	53.5	2.9	54.3	2.7	51.5	2.8
1291	5	-	-	63	3	55.1	2.8	53.3	2.7	54.1	2.9
1301	5	-	-	61	3	51.6	2.6	54.9	2.8	56	3
1310	5	-	-	59	3	50.9	2.6	55.8	2.8	52.0	2.8
1322	5	-	-	55.5	2.7	50.8	2.6	52.9	2.7	50.0	2.7
1331	5	-	-	57	3	48.9	2.5	54.3	2.8	51.1	2.8
1341	5	-	-	53.3	2.9	49.8	2.5	51.1	2.6	52.8	2.9
1353	5	-	-	55	3	49.0	2.5	48.8	2.5	53.0	2.9
1362	5	-	-	56	3	47.9	2.5	50.7	2.6	51.4	2.8
1374	5	-	-	55	3	50.3	2.6	50.8	2.6	50.1	2.8
1381	5	-	-	53.6	2.9	48.4	2.5	50.9	2.6	50.8	2.8
1393	5	-	-	48.7	2.7	50.2	2.6	48.8	2.5	51.5	2.8
1402	5	-	-	54.6	2.8	46.6	2.3	50.1	2.4	52.0	2.6
1412	5	-	-	50.3	2.5	47.8	2.3	48.3	2.3	52.0	2.6
1423	5	-	-	49.0	2.5	46.4	2.3	49.2	2.4	51.4	2.6
1433	5	-	-	50.8	2.6	47.6	2.3	48.9	2.4	52.1	2.6
1442	5	-	-	49.3	2.5	48.5	2.4	47.4	2.3	50.2	2.5

1452	5	-	-	48.0	2.4	46.1	2.2	51.7	2.5	49.5	2.5
1461	5	-	-	51.3	2.6	46.8	2.3	49.6	2.4	49.3	2.5
1473	5	-	-	53.1	2.7	45.8	2.2	47.2	2.3	49.1	2.5
1482	5	46.3	2.2	50.0	2.5	47.4	2.3	49.1	2.4	50.8	2.6
1492	5	45.3	2.2	53.1	2.7	45.8	2.2	50.2	2.4	48.2	2.4
1504	5	45.5	2.3	47.9	2.6	49.9	2.6	47.6	2.4	52.2	2.9
1513	5	42.3	2.3	49.7	2.9	48.3	2.7	48.1	2.6	52.8	3.2
1523	5	43.5	2.1	49.8	2.5	46.4	2.3	47.9	2.3	52.2	2.7
1532	5	42.6	2.0	50.3	2.4	47.1	2.2	48.1	2.3	51.7	2.5
1544	5	43.6	2.1	50.2	2.4	47.3	2.3	49.8	2.4	52.1	2.5
1553	5	44.6	2.1	49.6	2.4	47.5	2.3	50.7	2.4	51.8	2.5
1563	5	44.9	2.1	48.3	2.4	47.3	2.3	50.2	2.4	51.8	2.5
1572	5	43.8	2.1	47.9	2.3	47.9	2.3	49.9	2.4	51.6	2.5
1584	5	43.5	2.1	49.0	2.4	46.0	2.2	51.4	2.4	49.6	2.4
1594	5	43.2	2.0	48.1	2.3	46.3	2.2	50.0	2.3	50.4	2.4
1603	5	40.7	1.9	49.0	2.3	46.5	2.2	49.8	2.3	49.2	2.3
1615	5	42.5	2.0	48.0	2.3	45.3	2.1	51.0	2.4	50.0	2.4
1624	5	41.2	2.0	49.5	2.5	44.4	2.2	49.2	2.4	49.5	2.5
1634	5	41.7	2.0	48.1	2.4	43.9	2.2	49.1	2.4	50.8	2.6
1643	5	41.9	2.0	48.6	2.5	47.3	2.3	49.3	2.4	49.0	2.5
1653	5	43.4	2.1	47.7	2.4	45.5	2.2	50.7	2.5	48.5	2.5
1665	5	43.9	2.1	47.8	2.4	46.2	2.3	51.4	2.5	50.6	2.6
1674	5	41.4	2.0	46.5	2.4	47.3	2.3	50.8	2.5	51.3	2.7
1683	5	42.5	2.1	47.8	2.4	44.8	2.2	49.2	2.4	51.7	2.7
1693	5	41.1	2.0	46.3	2.4	45.5	2.3	48.8	2.4	49.5	2.5
1704	5	40.3	2.0	47.5	2.4	44.8	2.2	49.8	2.4	50.8	2.6
1754	5	40.2	2.0	44.4	2.3	44.0	2.2	50.5	2.5	49.6	2.6
1804	5	40.6	2.0	44.0	2.3	45.6	2.3	49.9	2.5	50.6	2.6
1856	5	41.2	2.0	46.0	2.4	46.1	2.3	51.8	2.5	51.4	2.7

1905	5	42.4	2.1	49.3	2.6	46.6	2.3	53.2	2.6	55.3	2.9
1955	5	41.8	2.0	48.1	2.4	48.5	2.3	55.1	2.6	55.9	2.8
2005	5	42.6	2.0	49.2	2.4	47.9	2.3	53.6	2.6	56.5	2.8

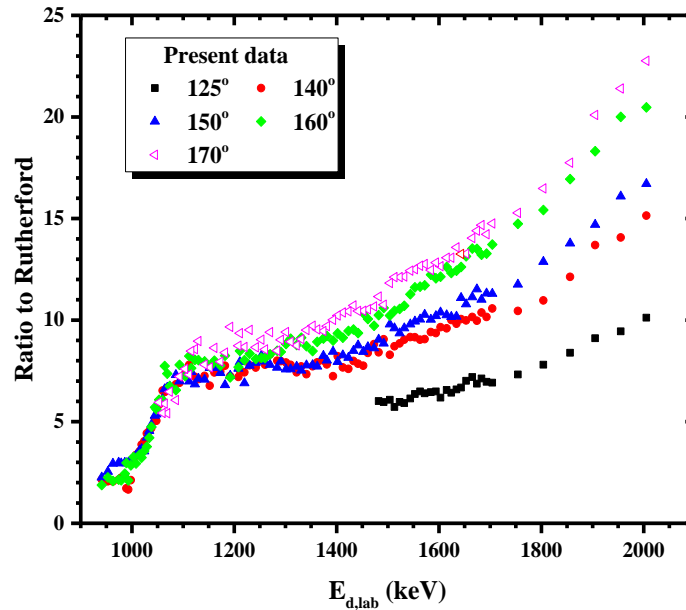


Figure 4.17 Ratio to Rutherford of the elastic ${}^7\text{Li}(d,d_0){}^7\text{Li}$ scattering for the deuteron energy range 940-2000 keV for all the measured backscattering angles.

4.5 Cross section measurements for the ${}^9\text{Be}(d,d_0){}^9\text{Be}$ elastic scattering

The differential cross section values of deuteron elastic scattering on ${}^9\text{Be}$ in the energy range of 1600 - 2200 keV, with a 20 keV energy step, and for the scattering angles of 120° , 140° , 150° , 160° , 170° was studied. The level scheme of the $d+{}^9\text{Be}$ system is shown in Fig. 4.18, along with the possible reaction channels. In the studied energy range the levels of the formed compound nucleus ${}^{11}\text{B}$ have energies of $E_x^* = 17310$ keV and $E_x^* = 17500$ keV with $\Gamma \approx 1$ MeV and $\Gamma = 116$ keV, respectively. Moreover, the level with energy $E_x^* = 18000$ keV and $\Gamma = 870$ keV might affect the studied cross section due to its large amplitude.

The implemented target was a self-supporting thin Si_3N_4 foil with a beryllium layer on top. A typical experimental spectrum at the deuteron energy of 1960 keV for the scattering angle of 170° is shown in Fig. 4.19. The obtained spectra were quite rich and the parasitic contributions of carbon

and oxygen, originating from the magnetron sputtering procedure, were obvious in the experimental spectra. It should also be noted here that deuteron measurements were also acquired at lower energies (~1000-1600 keV), however the problem of overlapping peaks between the elastic one of ${}^9\text{Be}$ and the ${}^{12}\text{C}(\text{d},\text{p}_1){}^{13}\text{C}$ was again present. In this case, the subtraction of the carbon counts, as achieved in the ${}^7\text{Li}(\text{d},\text{d}_0){}^7\text{Li}$ case, could not be appropriately performed since the contribution of the ${}^{12}\text{C}(\text{d},\text{p}_1){}^{13}\text{C}$ reaction was higher than the one from the ${}^9\text{Be}(\text{d},\text{d}_0){}^9\text{Be}$ elastic scattering, leading to unreliable results. Therefore, the final cross section values correspond only to deuteron energies between 1600 – 2200 keV, depending on the scattering angle, where the ${}^9\text{Be}(\text{d},\text{d}_0){}^9\text{Be}$ elastic peak was not overshadowed.

The differential cross section values were calculated using the Eq. 4.4, as discussed in section 4.1.

$$\left(\frac{d\sigma}{d\Omega}\right)_{E,\theta}^{9\text{Be}} = \left(\frac{d\sigma}{d\Omega}\right)_{1000,\theta}^{\text{Si,Ruth}} \cdot \frac{Y_{9\text{Be}}}{Y_{\text{nat}_{\text{Si}}}} \cdot \frac{Q_{\text{Ruth}}^{1000}}{Q_{9\text{Be}}} \cdot \frac{N_t^{\text{Si}}}{N_t^{9\text{Be}}} \quad (4.4)$$

The term $\left(\frac{d\sigma}{d\Omega}\right)_{1000,\theta}^{\text{Si,Ruth}}$ was calculated using the Rutherford formula along with a correction factor due to the screening effect since, as mentioned before, it does not deviate from the Rutherford formula for the nominal deuteron beam energy of 1000 keV [6]. The deuteron beam energy which was used to calculate this term corresponded to the energy at the half of the Si_3N_4 target, including the energy loss in the overlaying Be layer.

The charge terms Q_{Ruth}^{1000} and $Q_{9\text{Be}}$ were determined using the current integrator that was employed during the measurements. The systematic error of the current integrator is expected to be cancelled out in the ratio, since the relative technique was implemented.

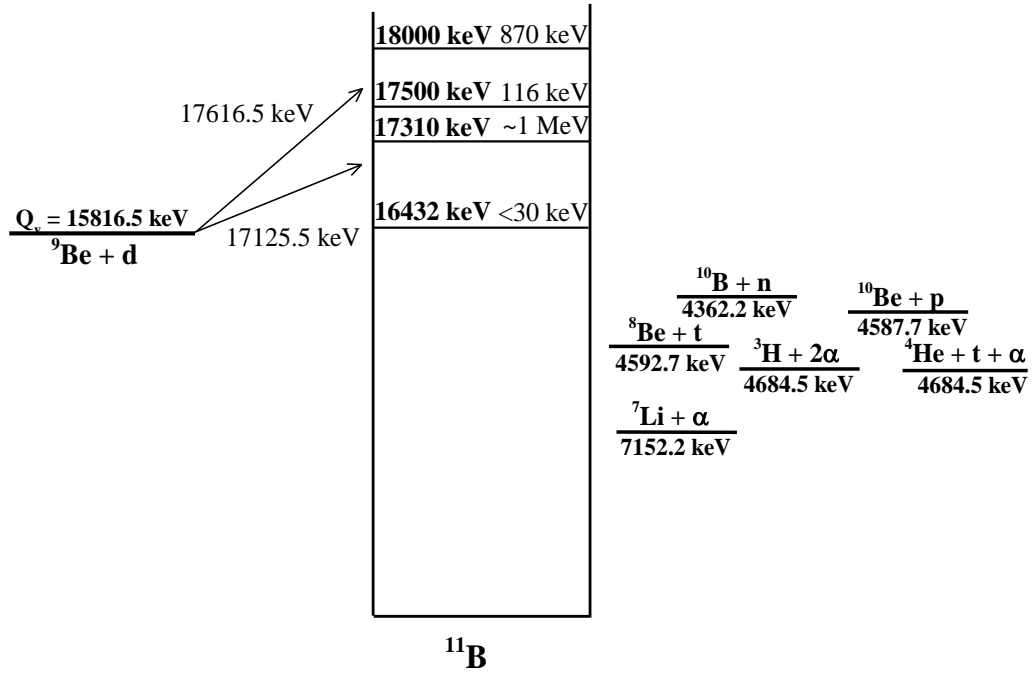


Figure 4.18 Level scheme of the $d+{}^9\text{Be}$ system in the CM reference frame.

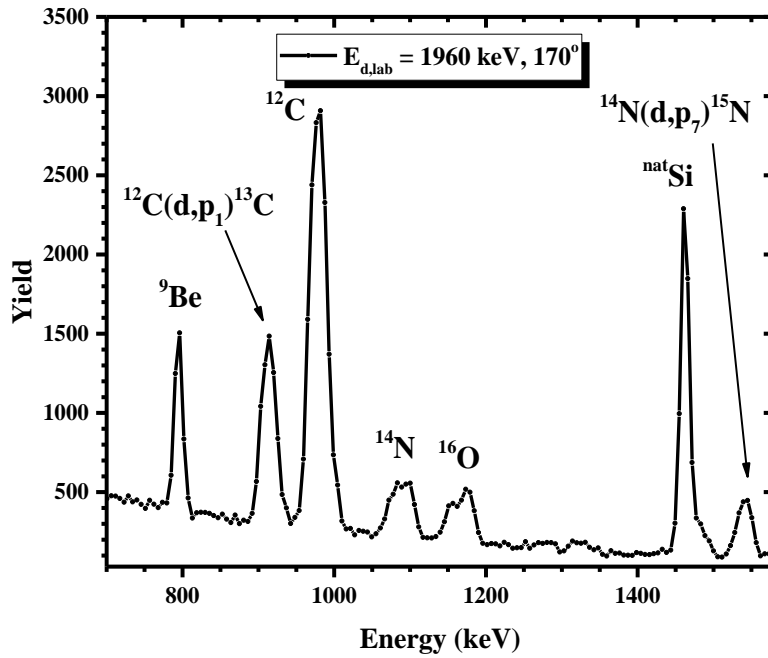


Figure 4.19 Typical experimental spectrum of the silicon nitride membrane with beryllium on top acquired at $E_{d,\text{lab}}=1960 \text{ keV}$ and for 170° along with the corresponding peak identification.

4.5.1 Target characterization

In order to calculate the term $\frac{N_t^{Si}}{N_t^{Be}}$, two independent techniques were used; the p-EBS and the transmission ERDA one. For the EBS technique proton spectra were acquired at the energies 1200 keV and 1500 keV and at the scattering angles of 150°, 160° and 170°. The target thickness determination and the proton spectra simulation was accomplished using the evaluated data for the $^{12}\text{C}(p,p_0)^{12}\text{C}$ [82], $^{14}\text{N}(p,p_0)^{14}\text{N}$ [26], $^{16}\text{O}(p,p_0)^{16}\text{O}$ [84] and the $^{nat}\text{Si}(p,p_0)^{nat}\text{Si}$ [27] elastic scattering as calculated through the online calculator SigmaCalc 2.0, implemented in SIMNRA v. 6.94. For the simulation of the $^9\text{Be}(p,p_0)^9\text{Be}$ peak, in the absence of evaluated or benchmarked data, measured data were used and more specifically the data by Liu et al. [17] at 170°, which were in agreement, within 4%, with the data by Krat et al. [18] at 165°. An experimental spectrum, along with the simulated one, are shown in Fig. 4.20 for the proton energy of 1500 keV at 170°. In this case, the simulation procedure included keeping constant the thickness of silicon and slightly changing the $Q \times \Omega$ product in order to achieve differences below 1% in the integral of the $^9\text{Be}(p,p_0)^9\text{Be}$ peak between the simulated and the experimental spectrum for every beam energy/scattering angle combination. This procedure led to a mean value of the term $N_t^{Si} : N_t^{Be}$ equal to 0.200 ± 0.010 , implying a relative statistical error of 5%.

The transmission ERDA technique was performed using an oxygen beam at 11.75 MeV and the detector was set at 30°. For the simulation of the obtained spectrum Rutherford cross section values were implemented in the SIMNRA code for all the peaks, except for the oxygen one. The values for the $^{16}\text{O}(^{16}\text{O},^{16}\text{O})$ peak simulation were calculated using the Mott formula via the <http://nuclearphysics.ntua.gr/downloads.php> website and were subsequently implemented in the SIMNRA code. The used value of the gain (keV/ch) was determined by the carbon spectra, via the carbon and the hydrogen peaks, acquired for this exact purpose at the oxygen energy of 11.75 MeV and at 30°. The results of the simulation procedure are visible in Fig. 4.21 and the obtained target thickness ratio $N_t^{Si} : N_t^{Be}$ was 0.221. Since the resolution is different for every element, it should be mentioned here that in the presented simulation the integral of the integrated and the simulated counts in the obtained peaks was the same (within 1%), in order to lead to a correct value of the target thickness ratio. The determined target thickness ratio leads to <10% differences between the transmission ERDA and the p-EBS technique. However, in the determination of the final cross section values, namely, in the subsequent calculations, the number obtained from the p-EBS technique was used due to the lower reliability of the transmission ERDA technique, since according to Bass [86] the interaction barrier for the beryllium case is at $E_{cm}=5.367$ MeV ($E_{lab}=14.9$ MeV), value obtained by the <http://nrv.jinr.ru/nrv/webnrv/qcalc/> website, which is rather close to the used oxygen beam energy value, although no data exist in literature revealing deviations from the Rutherford formula. At the same time, the choice of an even lower oxygen beam energy would lead to peak overlapping.

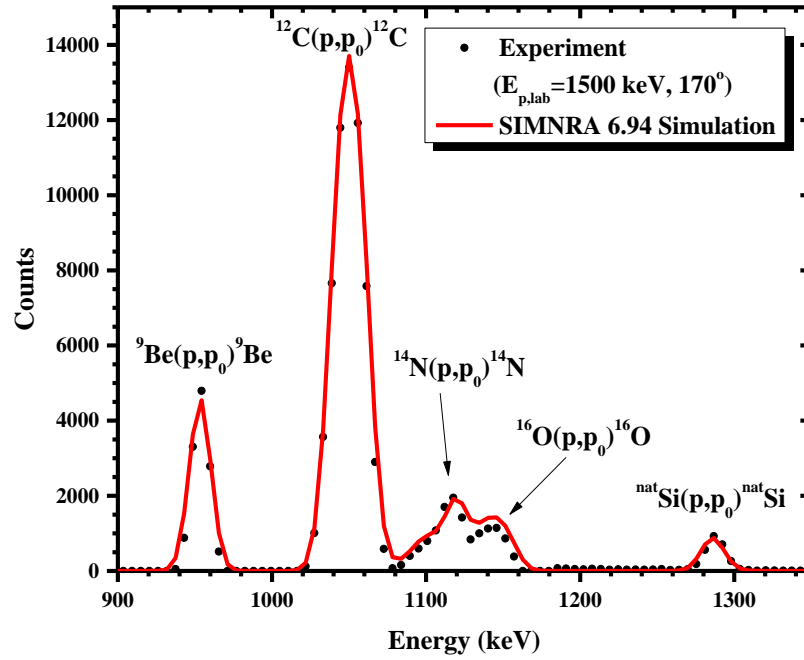


Figure 4.20 Proton experimental and simulated spectra acquired for the target thickness ratio calculation at $E_{p,\text{lab}}=1500$ keV and 170° along with the corresponding peak identification.

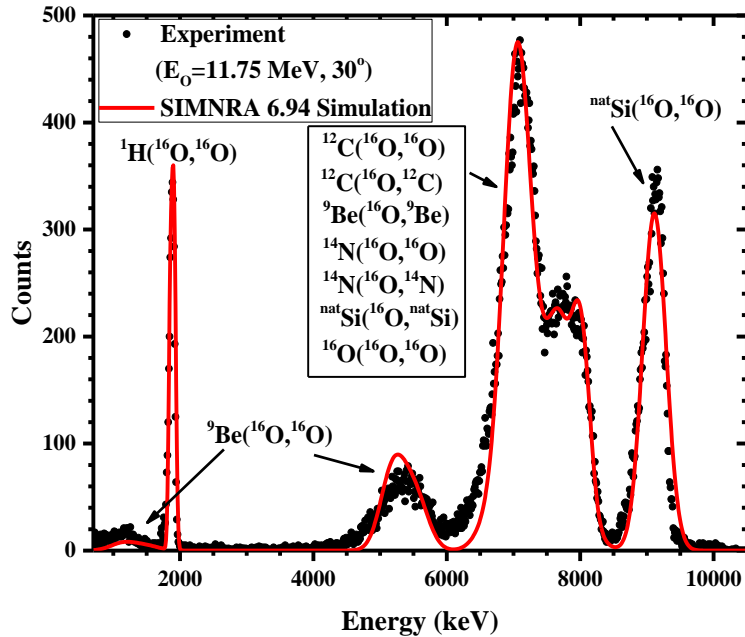


Figure 4.21 Experimental and simulated transmission ERDA spectra acquired at the oxygen energy 11.75 MeV at 30° along with the corresponding peak identification.

4.5.2 Uncertainties

The statistical uncertainty of the integration procedure for the determination of the terms Y_{9Be} and Y_{natSi} was below ~1%. The target thickness ratio calculation inserted a relative statistical uncertainty of 5%, originating from the p-EBS calculation. Therefore, the statistical uncertainty of the final cross section values, calculated using the error propagation formula, did not exceed ~5% in all cases.

Systematic uncertainties originate from the deviation of the target thickness ratio values calculated through the p-EBS and the transmission ERDA technique (<10%) and the systematic uncertainty in the charge calculation (~6% in all cases). Moreover, deviations between the theoretical and the experimental stopping power data for protons scattered from silicon and from beryllium are also present. More specifically, these deviations are ~4% for silicon and ~3.4% for beryllium, according to the SRIM website (<http://www.srim.org/>).

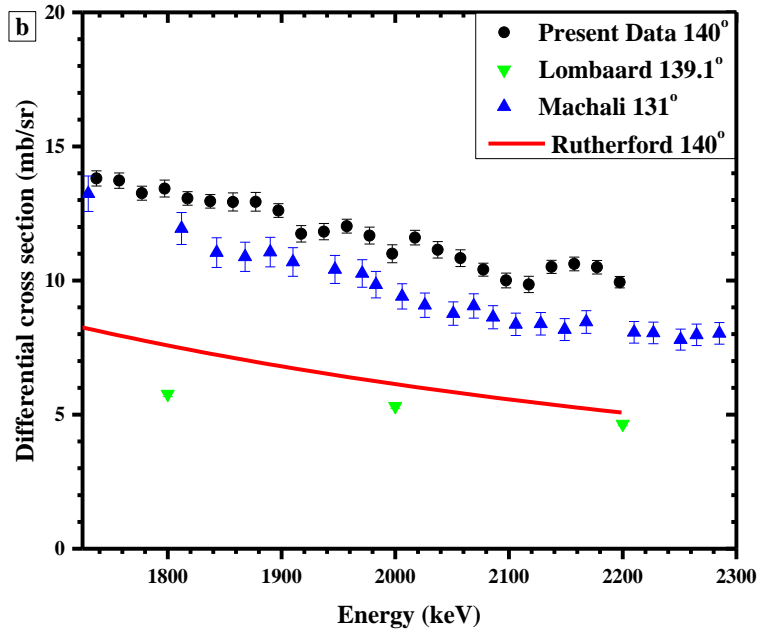
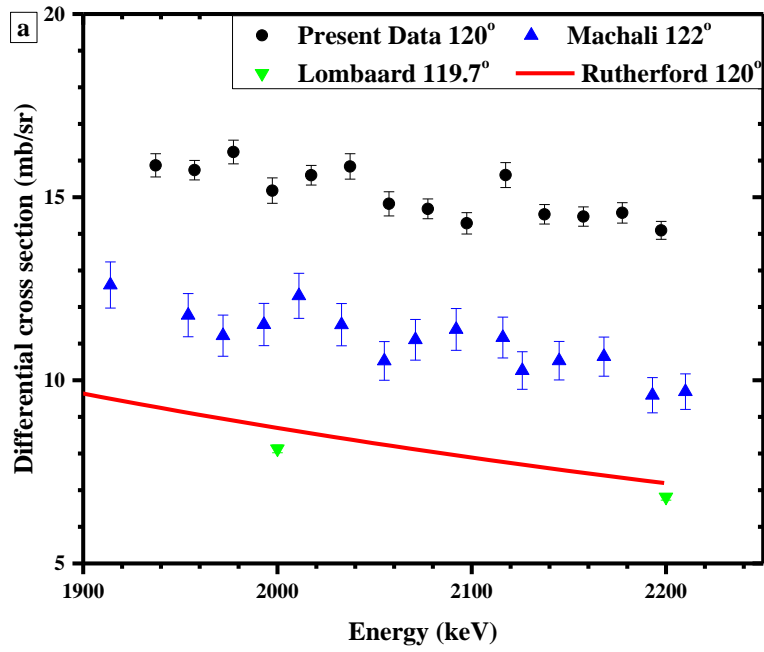
The uncertainties in the beam energy calculation include the ripple of the accelerator (~3 keV) and the energy straggling, acquired from the SIMNRA program, inside the determined target (~2.2 keV in all the beam energies).

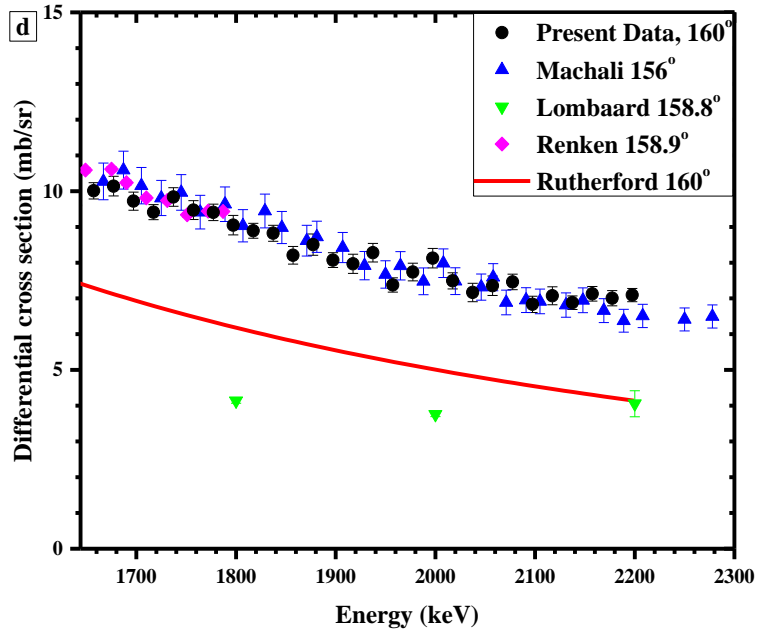
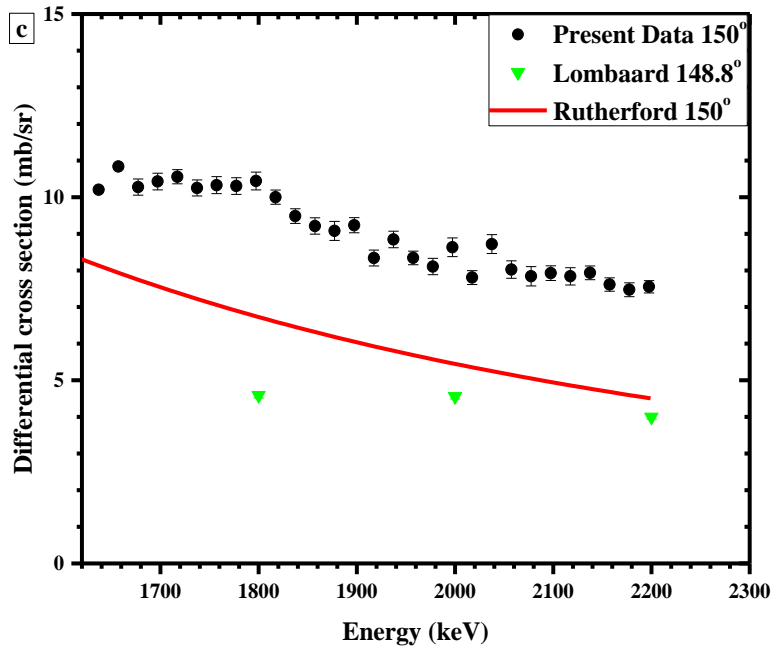
4.5.3 Results and Discussion

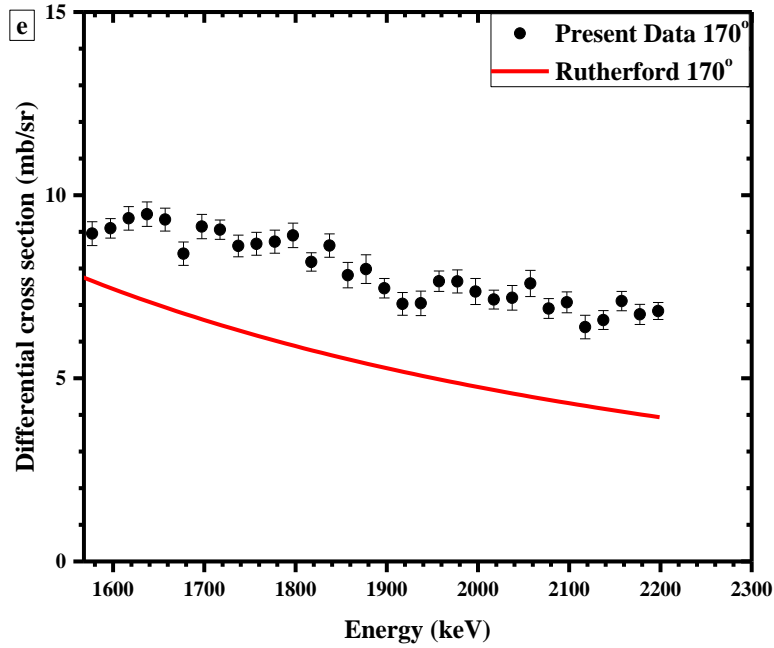
The final values of the differential cross section for the deuteron elastic scattering on beryllium ${}^9\text{Be}(d,d_0){}^9\text{Be}$ in the energy range $E_{d,\text{lab}}=1600\text{--}2200$ keV, depending on the scattering angle, with a 20 keV energy step, for the scattering angles of 120° , 140° , 150° , 160° and 170° are presented in graphical form in Figs. 4.22a–e, along with the preexisting measurements available in literature and in tabulated form in Table 4.3. The systematic uncertainties are excluded from the calculation of the total statistical uncertainty budget and thus from the presented figures.

The structure of the obtained data could be attributed to the overlapping levels of the compound nucleus ${}^{11}\text{B}$, with energies $E_x^*=17310$ keV ($\Gamma\approx 1$ MeV), $E_x^*=17500$ keV ($\Gamma=116$ keV) and $E_x^*=18000$ keV ($\Gamma=870$ keV), as previously discussed. Large deviations were observed in Figs. 4.22a–d between the present dataset and the dataset by Lombaard et al. [19] over the whole energy range and for all scattering angles, although no clear reason exists. A possible explanation though could be associated with the energy range in which Lombaard et al. corrected the contribution of the ${}^{12}\text{C}(d,p_1){}^{13}\text{C}$ counts in the ${}^9\text{Be}(d,d_0){}^9\text{Be}$ peak. Comparing the present dataset with the one by Machali et al. [20], for the scattering angle 160° good agreement was observed whereas for 120° and 140° discrepancies were recorded and this dataset seems to be systematically lower. Actually, a clear trend was revealed, since, as the scattering angle was increasing (moving to more steep backscattering angles) the discrepancies decreased. These discrepancies in the most forward backscattering angles (120° and 140°) could be caused due to the dead time of the multichannel analyzer which, as reported in [20], was the main source of uncertainty for the forward angles and it could justify the observed trend. It should also be noted that in Fig. 4.22b the data by Machali et al. were measured at 131° but are compared with the present ones at 140° , since it is the closest experimental angle measured. For the only common scattering angle of 160° good agreement within the quoted errors was observed with the dataset by Renken [21], although the latter cross section dataset corresponds to $\theta=158.9^\circ$.

Moreover, discrepancies were observed between the measured cross section values and the corresponding Rutherford ones, with the measured ones being up to 2 times higher, as shown in Fig. 4.23. In fact, a strong angular variation was observed between the two most forward measured angles (120° and 140°) and the most backward ones. This phenomenon could be attributed to the angular dependence of the overlapping energy levels in the prompt energy range of the compound nucleus.







Figures 4.22 a-e Differential cross-section values (mb/sr) of the ${}^9\text{Be}(d,d_0){}^9\text{Be}$ elastic scattering, measured at $E_{d,\text{lab}} \sim 1600\text{--}2200$ keV and for the scattering angles of 120° , 140° , 150° , 160° and 170° , in energy steps of ~ 20 keV, along with data from literature.

Table 4.3 Tabulated differential cross sections (mb/sr) of the ${}^9\text{Be}(d,d_0){}^9\text{Be}$ elastic scattering in the deuteron energy range of $\sim 1600\text{--}2200$ keV with 20 keV energy step for the backscattering angles of 120° , 140° , 150° , 160° , 170° . The corresponding combined cross-section statistical uncertainties at $\pm 1\sigma$ accuracy are also included.

$E_{d,\text{lab}}$ (keV)	$\delta E_{d,\text{lab}}$ (keV)	$(\sigma \pm d\sigma)$ (mb/sr)									
		120°		140°		150°		160°		170°	
1577.1	2.4	-	-	-	-	-	-	-	-	8.9	0.3
1597.1	2.4	-	-	-	-	-	-	-	-	9.1	0.3
1617.1	2.4	-	-	-	-	-	-	-	-	9.4	0.3
1637.1	2.4	-	-	-	-	10.2	0.1	-	-	9.5	0.3
1657.2	2.4	-	-	-	-	10.8	0.1	10.0	0.2	9.3	0.3
1677.2	2.4	-	-	-	-	10.3	0.2	10.1	0.3	8.4	0.3
1697.2	2.4	-	-	-	-	10.4	0.2	9.7	0.3	9.1	0.3
1717.2	2.4	-	-	-	-	10.6	0.2	9.4	0.2	9.1	0.3

1737.2	2.4	-	-	13.8	0.3	10.3	0.2	9.8	0.3	8.6	0.3
1757.2	2.4	-	-	13.7	0.3	10.3	0.2	9.5	0.3	8.7	0.3
1777.2	2.4	-	-	13.3	0.3	10.3	0.2	9.4	0.2	8.7	0.3
1797.3	2.4	-	-	13.4	0.3	10.4	0.2	9.1	0.3	8.9	0.3
1817.3	2.4	-	-	13.1	0.3	10.0	0.2	8.9	0.2	8.2	0.3
1837.3	2.4	-	-	13.0	0.3	9.5	0.2	8.8	0.2	8.6	0.3
1857.3	2.4	-	-	12.9	0.3	9.2	0.2	8.2	0.2	7.8	0.3
1877.3	2.4	-	-	12.9	0.3	9.1	0.3	8.5	0.3	8.0	0.4
1897.3	2.4	-	-	12.6	0.3	9.2	0.2	8.1	0.2	7.5	0.3
1917.3	2.4	-	-	11.7	0.3	8.3	0.2	8.0	0.3	7.0	0.3
1937.3	2.4	15.9	0.3	11.8	0.3	8.8	0.2	8.3	0.3	7.0	0.3
1957.3	2.4	15.7	0.3	12.0	0.3	8.3	0.2	7.4	0.2	7.7	0.3
1977.4	2.4	16.2	0.3	11.7	0.3	8.1	0.2	7.7	0.2	7.6	0.3
1997.4	2.4	15.2	0.3	11.0	0.3	8.6	0.3	8.1	0.3	7.4	0.4
2017.4	2.4	15.6	0.3	11.6	0.3	7.8	0.2	7.5	0.2	7.1	0.3
2037.4	2.4	15.8	0.3	11.1	0.3	8.7	0.3	7.2	0.3	7.2	0.3
2057.4	2.4	14.8	0.3	10.8	0.3	8.0	0.2	7.4	0.3	7.6	0.4
2077.4	2.4	14.7	0.3	10.4	0.2	7.8	0.3	7.5	0.2	6.9	0.3
2097.4	2.4	14.3	0.3	10.0	0.3	7.9	0.2	6.8	0.2	7.1	0.3
2117.4	2.4	15.6	0.3	9.9	0.3	7.8	0.2	7.1	0.3	6.4	0.3
2137.4	2.4	14.5	0.3	10.5	0.2	7.9	0.2	6.9	0.2	6.6	0.3
2157.5	2.4	14.5	0.3	10.6	0.3	7.6	0.2	7.1	0.2	7.1	0.3
2177.5	2.4	14.6	0.3	10.5	0.3	7.5	0.2	7.0	0.2	6.7	0.3

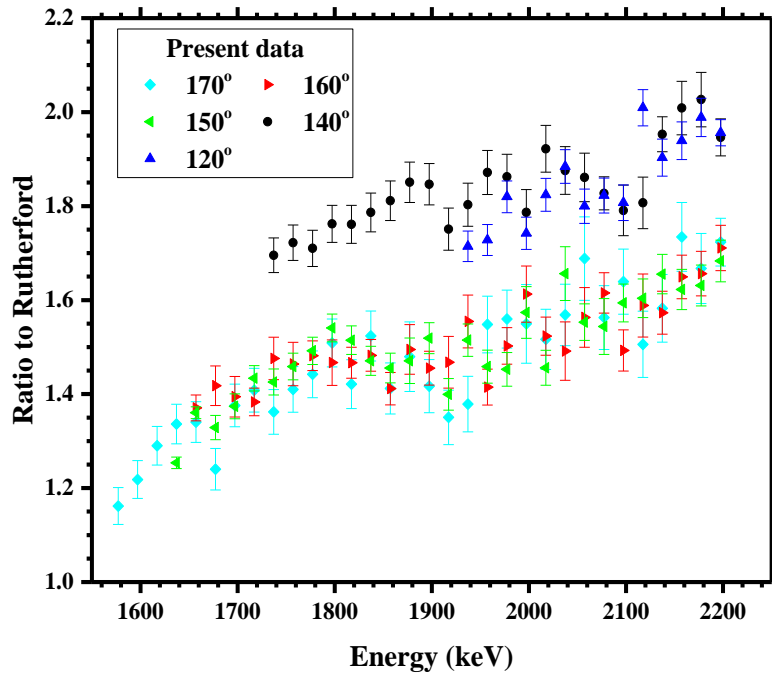


Figure 4.23 Ratio to Rutherford of the obtained differential cross section values of the elastic ${}^9\text{Be}(d,d_0){}^9\text{Be}$ scattering for the deuteron energy range 1600-2200 keV for all the measured backscattering angles.

4.6 Cross section measurements for the ${}^{\text{nat}}\text{N}(d,d_0){}^{\text{nat}}\text{N}$ elastic scattering

The deuteron elastic scattering on ${}^{\text{nat}}\text{N}$ was measured in the energy range 1000 – 2200 keV in steps of ~ 10 keV and for the backscattering angles of 120° , 130° , 140° , 150° , 160° and 170° . The level scheme of the under-study system, $d+{}^{14}\text{N}$, concerning the most abundant isotope of nitrogen, ${}^{14}\text{N}$ (99.634% in ${}^{\text{nat}}\text{N}$), is displayed in Fig. 4.23, along with the possible reaction channels. The prompt energy region includes multiple levels of the compound nucleus ${}^{16}\text{O}$ that are included in Fig. 4.24, along with the ones that could, due to their energy or their width, affect the cross-section structure.

The implemented target was a thin self-supporting silicon nitride membrane with Au evaporated on top. A typical spectrum is shown in Fig. 4.25a at the deuteron energy of 1500 keV acquired at 150° , along with the corresponding peak identification. The carbon, chlorine and oxygen unavoidable parasitic contributions, due to the evaporation of Au on top of the silicon nitride membrane, were clearly separated from the nitrogen peak. The presence of carbon was also enhanced during the measurements due to the carbon buildup effect. Concerning the levels of nitrogen, mainly the ${}^{14}\text{N}(d,p_x)$ and ${}^{14}\text{N}(d,\alpha_x)$ reactions, although at higher energies e.g. Fig. 4.25b

they appeared in the experimental spectra, there was no peak overlap, or enhanced background under the ^{nat}N and Au elastic peaks for the whole energy range under study.

The obtained cross section values were calculated via Eq. 4.3 for the nitrogen case:

$$\left(\frac{d\sigma}{d\Omega}\right)_{\theta,E}^{nat_N} = \left(\frac{d\sigma}{d\Omega}\right)_{\theta,E'}^{Au} \times \frac{Y_{nat_N}}{Y_{Au}} \times \frac{N_{t,Au}}{N_{t,nat_N}} \quad (4.8)$$

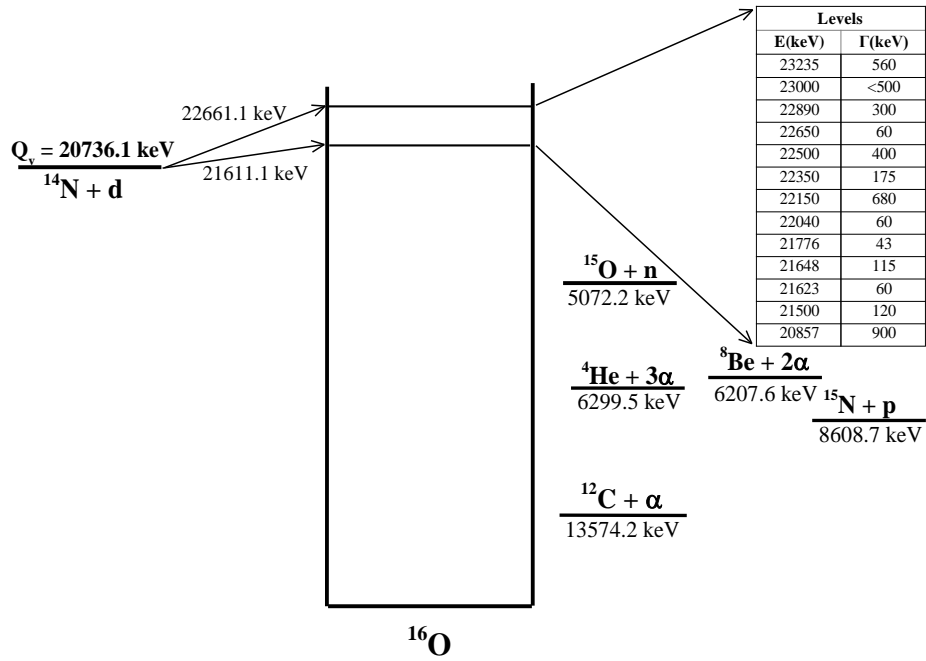


Figure 4.24 Level scheme of the $d+^{14}\text{N}$ system in the CM reference frame.

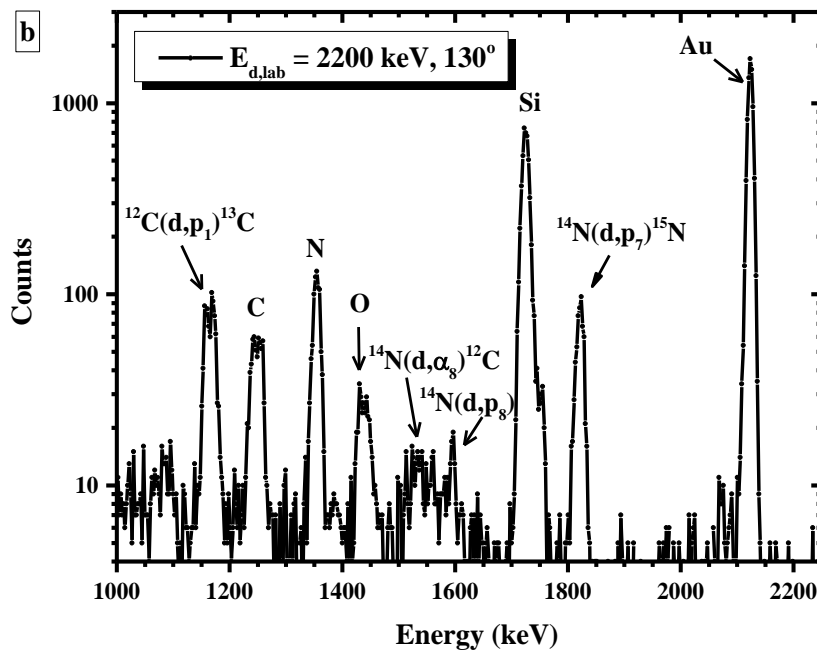
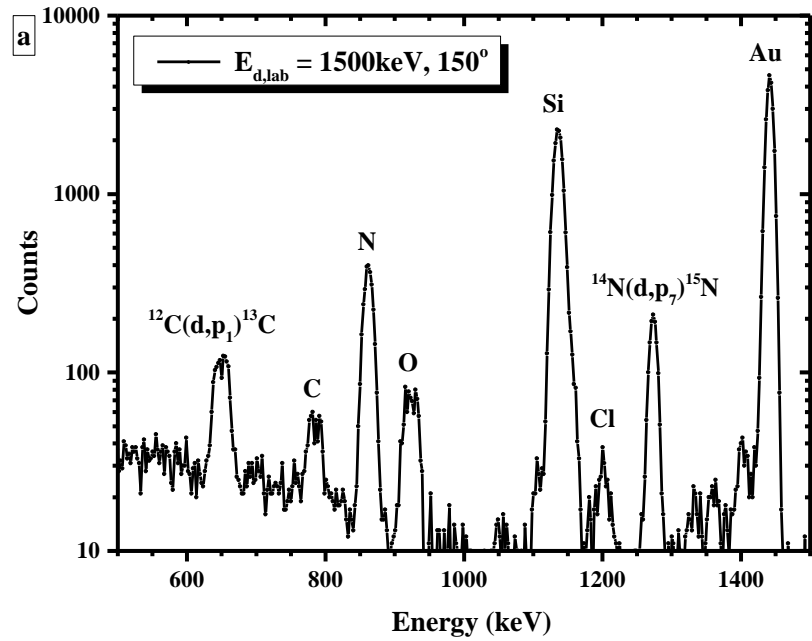


Figure 4.25 a) Experimental spectrum of the silicon nitride membrane with a gold layer on top acquired at the deuteron energy 1500 keV at 150° , along with the corresponding peak identification. b) Experimental spectrum of the same target taken at the deuteron energy 2200 keV at 130° , along with the corresponding peak identification.

4.6.1 Target characterization

The determination of the N_{Au}/N^{nat}_N ratio was accomplished using protons as projectiles at the beam energies of 980, 1200 and 1300 keV. The implementation of the p-EBS technique was deemed appropriate, since proton elastic scattering on nitrogen has been evaluated and benchmarked [26]. In this case, for the simulation of the acquired proton spectra using SIMNRA v. 6.94, the procedure originated with the determination of the $Q \times \Omega$ product using the proton elastic scattering on ^{nat}Si peak, as well as the evaluated data [27], using SigmaCalc 2.0 as implemented in SIMNRA. The simulation of the proton elastic scattering on carbon [82] and oxygen [84] was accomplished by using the evaluated data from SigmaCalc 2.0, whereas for the chlorine peak Rutherford data were used, since no measurements exist in literature that display differences from the Rutherford values. Subsequently, for every proton beam/ scattering angle combination, the total Au and N thicknesses (in atoms/cm²) were determined, by slightly varying the target composition in each case. The obtained average value of the $N_{Au}:N^{nat}_N$ ratio was 0.0423 ± 0.0011 , implying a relative statistical error of 2.6%. An example is shown in Fig. 4.26 for the proton energy of 1300 keV at 170°, along with the corresponding peak identification.

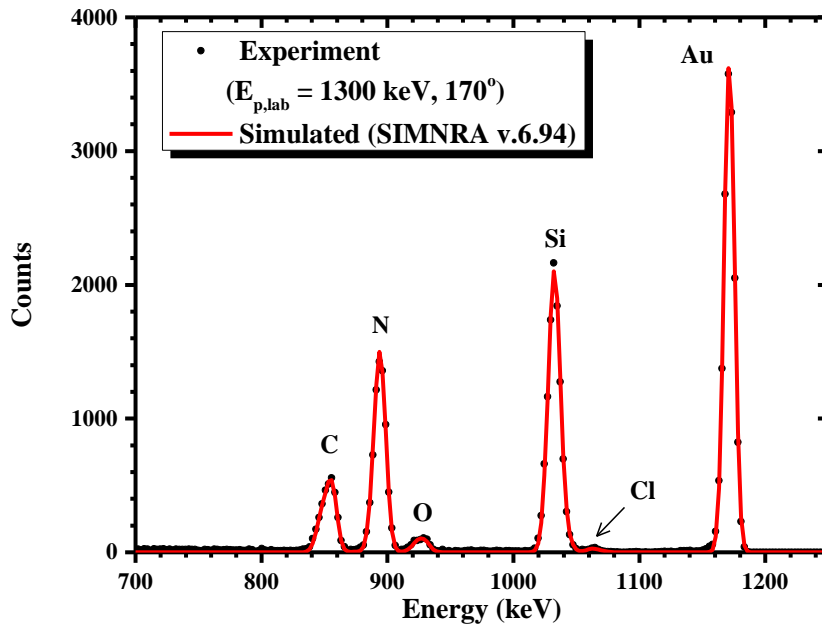


Figure 4.26 Experimental and simulated proton spectra acquired at 1300 keV at 170° in order to characterize the target, along with the corresponding peak identification.

4.6.2 Uncertainties

The statistical uncertainties originated from the integration procedure, which for the gold peak was always below 1%, while for the nitrogen one did not exceed 3.5%. The relative statistical uncertainty from the target thickness ratio calculation was 2.6%. Thus, through the error propagation formula the combined statistical uncertainty did not exceed 5.3% in all cases.

The systematic uncertainties of the obtained cross section values originated from the accuracy of the implemented stopping power compilations. Especially in the case of protons impinging on silicon, the deviations between compiled and experimental stopping-power data can be as high as 4%, whereas for protons impinging on nitrogen the deviations were ~2.9%, as reported in the SRIM website.

The uncertainties in the beam energy calculation included the ripple of the accelerator (3 keV) and the energy straggling, acquired from the SIMNRA program, inside the determined target (2.3-2.4 keV for all incident energies).

4.6.3 Results and Discussion

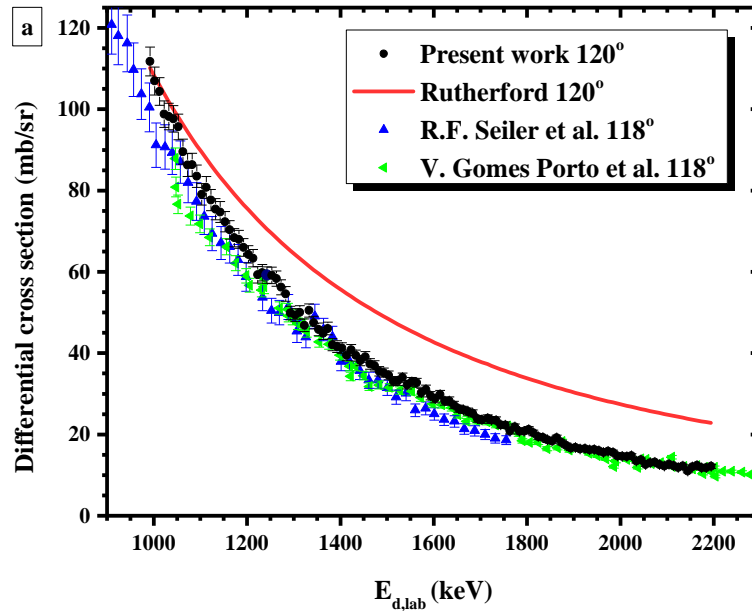
The final cross section values of the $^{nat}\text{N}(d,d_0)^{nat}\text{N}$ elastic scattering in the energy range of 1000-2200 keV for the scattering angles of 120°, 130°, 140°, 150°, 160° and 170° are presented in Figs. 4.27 a-f and in tabulated form in Table 4.4, along with the corresponding uncertainties. In Figs. 4.27 a-f all the preexisting datasets from literature are also included for the closest scattering angle (if not identical), for comparison purposes.

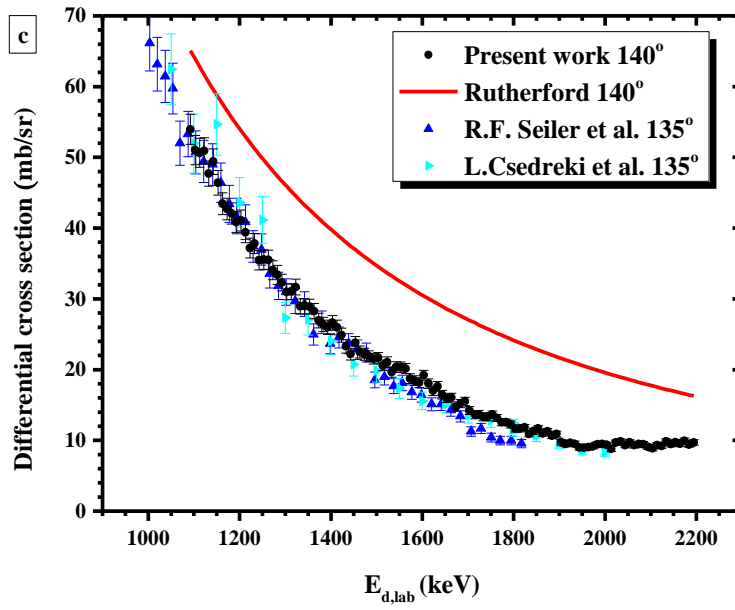
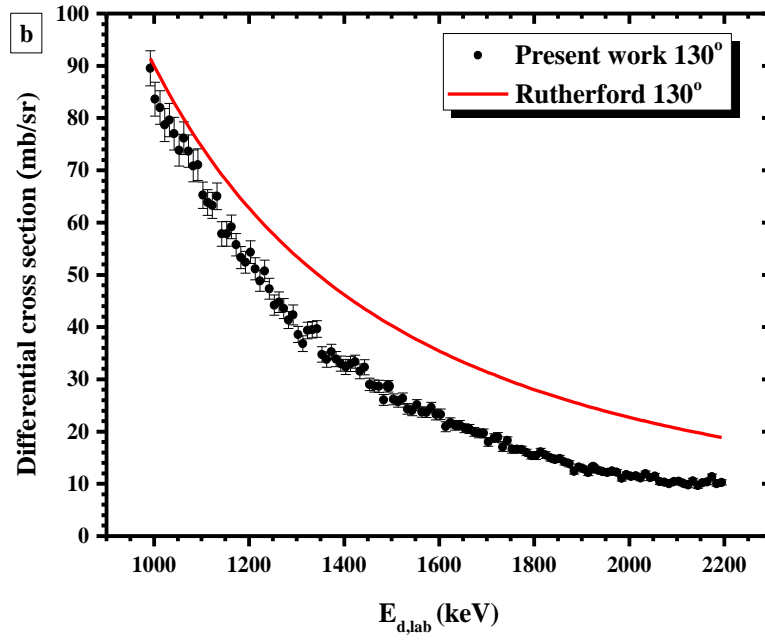
In Fig. 4.27a, the obtained results were in good agreement for most of the energy values, mainly the high ones, with the datasets from Seiler et al. [23] and Gomes Porto et al. [24] both measured at 118°, whereas for the low beam energies, the previously measured datasets displayed lower values. The same situation was observed in Fig. 4.27f; excellent agreement within the quoted errors was observed between the present dataset and the measured one from Gomes Porto et al. at 167° for higher energies (above 1500 keV), whereas for lower ones the deviations increased. For the scattering angle of 140°, Fig. 4.27 b, the situation was reversed, implying a good agreement within the quoted errors with Seiler et al. for the low energies, whereas for the high deuteron energies the latter dataset seems to be lower than the present data. For the scattering angle of 160°, the dataset by Seiler et al., measured at 164°, seems to be systematically lower over the whole energy range under study. Moreover, at the scattering angle of 140°, the agreement with Csedreki et al. [25] seems to be good within errors, as displayed in Fig. 4.27c. It should be mentioned here that the quoted errors for the Csedreki et al. dataset were directly acquired from the publication. All these discrepancies seem angularly uncorrelated. It should be mentioned here that in cases where gaseous targets and absolute measurement techniques are employed, like in both [23] and [24], the

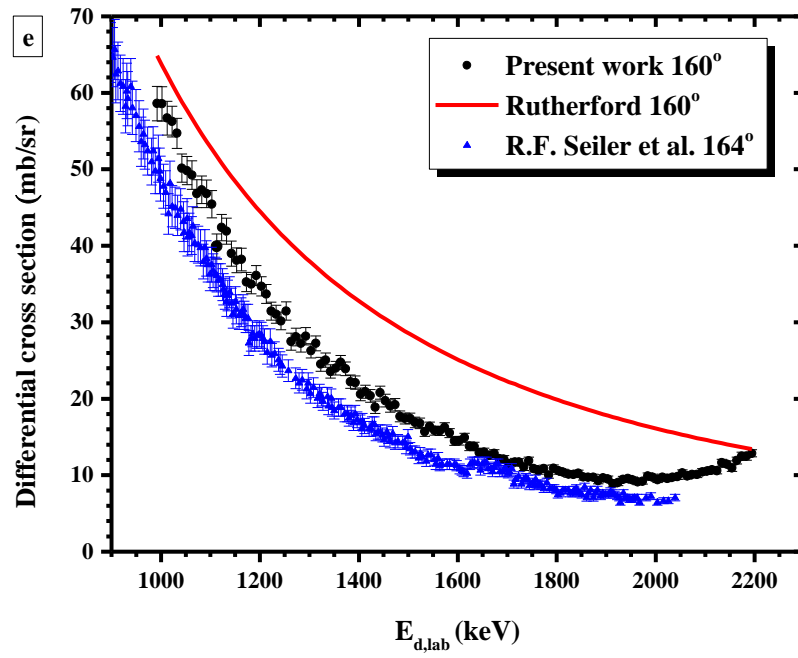
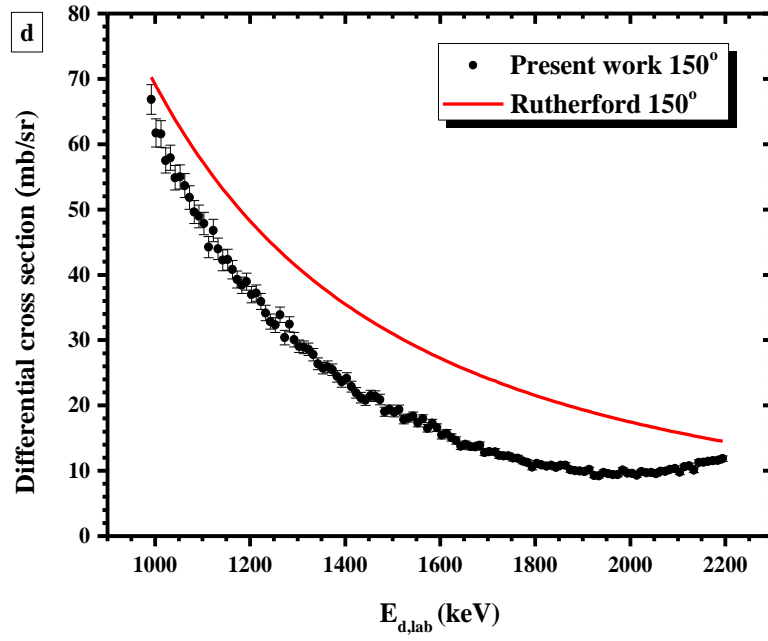
resulting uncertainties tend to be larger. On the other hand, the present measurement with a solid target and the employment of the relative measurement technique has led to a coherent cross section dataset ensemble, eliminating the effect of the $Q \times \Omega$ product and limiting the systematic uncertainties of the target thickness calculation.

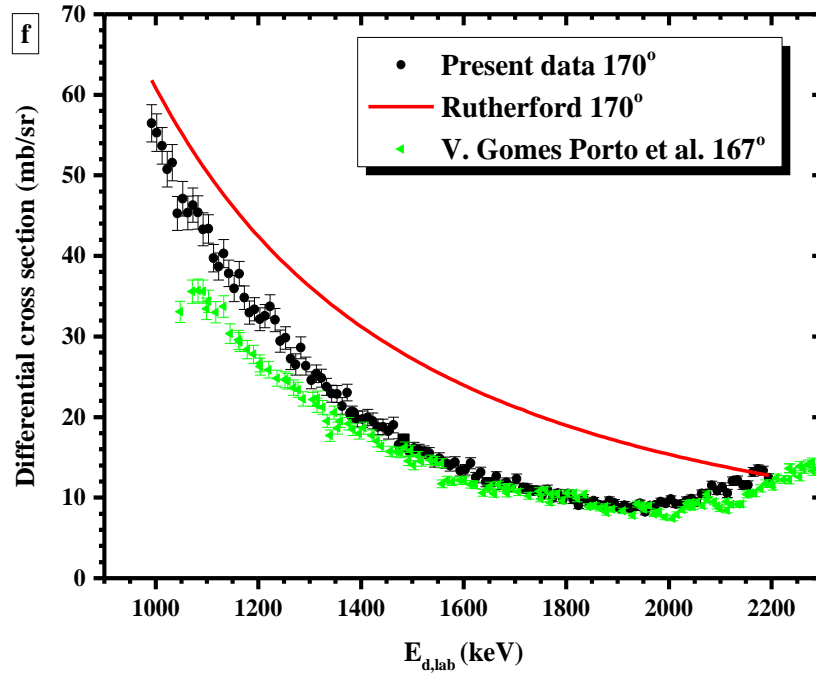
The effect of the energy levels of the compound nucleus ^{16}O in the prompt energy region, implying the effect of the resonant reaction mechanism, was examined through Fig. 4.28, which includes the ratio to Rutherford measured cross section values for all the measured scattering angles. It can be observed that the measured cross section values remain lower than the corresponding Rutherford ones over the whole energy range under study, although there is a strong increasing trend for higher energies and for steeper backscattering angles. This behavior could be attributed to the multiple broad overlapping levels of the compound nucleus ^{16}O in the prompt energy region, along with the ones with higher or lower energies which might affect the cross section due to their large widths, displayed in Fig. 4.24. The effect of all these overlapping resonances could in principle lead to the absence of strong, sharp maxima and minima in the observed yield and to the existence of a rather smooth energy variation, along with a strong angular one, evident in Fig. 4.28, for higher energies and steep backscattering angles.

It should also be pointed out here that the benchmarking of the obtained d-EBS cross section values was not performed due to the multiple levels originating from the $^{14}\text{N}(d,p_x)^{15}\text{N}$ and $^{14}\text{N}(d,a_x)^{12}\text{C}$ reaction channels and contributing under the elastic nitrogen edge, thus impeding the benchmarking procedure.









Figures 4.27 a-f Differential cross-section values (mb/sr) of the $^{14}\text{N}(d,d_0)^{14}\text{N}$ elastic scattering, measured at $E_{d,\text{lab}} \sim 1000\text{--}2200$ keV and for the scattering angles of 120° , 130° , 140° , 150° , 160° and 170° , in energy steps of ~ 20 keV, along with the available data from literature.

Table 4.4 Tabulated differential cross sections (mb/sr) of the $^{14}\text{N}(d,d_0)^{14}\text{N}$ elastic scattering in the energy range of $\sim 1000\text{--}2000$ keV in energy steps of ~ 10 keV for the backscattering angles of 120° , 130° , 140° , 150° , 160° , 170° . The corresponding combined cross-section statistical uncertainties at $\pm 1\sigma$ accuracy are also included.

$E_{d,\text{lab}}$ (keV)	$dE_{d,\text{lab}}$ (keV)	$(\sigma \pm d\sigma)$ (mb/sr)											
		120°		130°		140°		150°		160°		170°	
992	6	112	4	90	3	-	-	66.8	2.3	58.6	2.2	56.5	2.3
1002	6	107	3	84	3	-	-	61.7	2.1	58.6	2.3	55.3	2.3
1012	6	104	3	82	3	-	-	61.6	2.0	56.7	2.2	53.7	2.3
1022	6	99	3	79	3	-	-	57.5	1.9	56.2	2.0	50.8	2.2
1032	6	98	3	80	3	-	-	57.9	1.9	54.7	2.0	51.6	2.3
1042	6	98	3	77	3	-	-	54.9	1.9	50.2	1.9	45.3	2.1

1052	6	96	3	74	3	-	-	55.0	1.9	49.8	1.8	47.1	2.1
1063	6	90	3	76	3	-	-	53.7	1.8	49.2	1.9	45.3	2.1
1073	6	86.3	2.8	73.7	3	-	-	51.8	1.8	46.8	1.8	46.3	2.1
1083	6	86.3	2.8	70.8	3	-	-	49.6	1.8	47.3	1.8	45.4	2.1
1093	6	83.5	2.7	71.1	3	54.0	2.1	48.9	1.7	46.8	1.8	43.3	2.0
1103	6	79.1	2.6	65.2	2.5	51.0	2.1	47.8	1.7	45.4	1.8	43.4	1.8
1113	6	80.8	2.7	63.9	2.5	50.6	2.0	44.2	1.6	39.9	1.6	39.7	1.7
1123	6	77.7	2.6	63.3	2.5	50.9	1.9	46.8	1.7	42.4	1.7	38.7	1.7
1133	6	75.4	2.6	65.0	2.5	47.7	1.8	44.0	1.7	41.9	1.7	40.3	1.7
1143	6	74.7	2.6	57.8	2.3	49.4	1.8	42.2	1.6	39.0	1.6	37.8	1.6
1153	6	72.3	2.5	57.8	2.4	46.4	1.7	42.3	1.6	38.1	1.6	36.0	1.6
1163	6	70.3	2.3	59.2	2.2	43.5	1.5	40.8	1.4	38.2	1.5	37.8	1.5
1173	6	68.4	2.2	55.8	2.2	42.7	1.5	39.3	1.3	35.3	1.3	34.8	1.5
1183	6	68.0	2.2	53.3	2.1	42.1	1.5	38.4	1.3	35.0	1.3	33.0	1.4
1193	6	66.0	2.2	52.4	2.1	40.9	1.5	38.9	1.3	36.1	1.3	33.4	1.4
1203	6	64.3	2.1	54.3	2.2	41.1	1.5	37.0	1.2	34.7	1.3	32.1	1.4
1213	6	63.4	2.1	51.2	2.1	39.4	1.4	37.2	1.2	33.7	1.2	32.5	1.4
1223	6	59.3	2.0	48.8	2.0	37.2	1.4	35.9	1.2	31.5	1.2	33.7	1.5
1233	6	59.8	2.0	50.7	2.1	37.8	1.4	34.2	1.2	31.0	1.2	32.0	1.5
1243	6	59.2	2.0	47.3	2.0	35.5	1.4	32.8	1.2	30.2	1.2	29.4	1.4
1253	6	59.1	2.0	44.2	1.9	35.5	1.4	32.3	1.1	31.5	1.2	29.8	1.4
1263	6	58.3	1.9	44.8	2.0	35.5	1.4	33.9	1.2	27.5	1.1	27.3	1.3
1273	6	56.2	1.8	43.5	1.9	34.0	1.3	30.4	1.1	28.1	1.1	26.5	1.3
1283	6	54.6	1.8	41.4	1.6	33.4	1.3	32.4	1.2	27.2	1.1	28.6	1.4
1293	6	49.9	1.7	42.3	1.9	32.3	1.2	30.1	1.1	28.2	1.1	26.3	1.1
1303	6	49.4	1.6	38.6	1.5	31.0	1.1	29.1	1.0	26.3	0.9	24.6	1.1
1313	6	50.0	1.6	36.8	1.5	31.0	1.1	28.9	1.0	27.2	1.0	25.4	1.1
1323	6	46.8	1.6	39.3	1.6	31.7	1.1	28.6	1.0	24.5	0.9	24.8	1.1

1333	6	50.5	1.6	39.5	1.6	28.9	1.1	27.8	0.9	25.0	0.9	23.7	1.1
1343	6	47.5	1.6	39.6	1.6	29.0	1.1	26.4	0.9	23.6	0.9	22.9	1.1
1353	6	45.9	1.5	34.8	1.5	28.9	1.1	25.7	0.9	24.0	0.9	22.9	1.1
1363	6	44.9	1.5	33.8	1.5	28.3	1.1	25.9	0.9	24.7	0.9	21.4	1.0
1373	6	46.0	1.6	35.2	1.5	26.9	1.0	25.5	0.9	23.9	0.9	23.0	1.0
1383	6	42.1	1.5	33.9	1.5	26.4	1.0	24.5	0.9	22.2	0.9	20.4	1.0
1393	6	41.6	1.5	33.0	1.5	26.0	1.0	23.6	0.8	22.1	0.9	19.8	1.0
1403	6	41.2	1.4	32.4	1.5	26.6	1.0	24.1	0.9	20.6	0.8	19.7	1.0
1413	6	39.5	1.3	32.9	1.5	26.0	1.0	22.9	0.8	20.9	0.8	20.0	1.0
1423	6	40.8	1.4	33.4	1.3	24.9	1.0	21.9	0.8	20.4	0.8	19.5	1.0
1433	6	39.4	1.3	31.5	1.4	23.3	1.0	21.2	0.8	18.9	0.8	18.8	1.0
1443	6	38.2	1.3	32.3	1.5	22.2	0.8	20.8	0.8	20.8	0.8	18.8	1.0
1453	6	39.1	1.3	29.0	1.2	23.8	0.9	21.5	0.8	19.8	0.8	18.2	1.0
1463	6	37.4	1.3	28.7	1.2	22.5	0.8	21.4	0.8	19.0	0.8	19.0	1.0
1473	6	36.9	1.3	28.7	1.2	22.2	0.8	20.9	0.8	19.2	0.8	16.5	0.8
1483	6	35.5	1.1	26.1	1.0	21.9	0.8	19.0	0.7	17.7	0.7	17.2	0.7
1493	6	35.2	1.1	28.7	1.1	21.5	0.8	19.4	0.7	17.4	0.7	15.8	0.7
1503	6	34.5	1.1	26.2	1.0	21.7	0.8	18.9	0.7	17.4	0.7	16.1	0.7
1513	6	33.1	1.1	25.7	1.0	20.6	0.7	19.4	0.7	16.9	0.7	15.9	0.7
1523	6	33.1	1.1	26.3	1.1	21.0	0.7	17.8	0.6	16.8	0.7	15.7	0.7
1533	6	34.0	1.1	24.3	1.0	19.7	0.7	18.1	0.6	15.7	0.6	15.5	0.7
1543	6	32.2	1.1	24.0	1.0	20.4	0.7	18.4	0.6	16.4	0.6	14.5	0.7
1553	6	32.9	1.1	25.1	1.0	20.3	0.7	17.3	0.6	15.8	0.6	14.9	0.7
1563	6	32.7	1.1	23.7	1.0	20.2	0.7	18.0	0.6	15.8	0.6	14.4	0.7
1573	6	30.3	1.0	23.7	1.0	18.7	0.7	16.5	0.6	16.3	0.6	14.0	0.7
1583	6	31.1	1.1	24.6	1.0	18.4	0.7	17.3	0.6	15.5	0.6	14.4	0.7
1593	6	29.5	1.0	23.3	1.0	18.2	0.7	16.6	0.6	14.5	0.6	13.3	0.7
1603	6	28.8	1.0	23.3	1.0	19.2	0.7	15.5	0.6	14.5	0.6	13.4	0.7

1613	6	29.8	1.0	20.9	0.9	18.0	0.7	15.7	0.6	14.9	0.6	14.3	0.7
1623	6	28.2	1.0	21.7	1.0	17.0	0.7	15.1	0.6	13.8	0.6	12.5	0.7
1633	6	28.2	1.0	21.2	0.9	17.6	0.7	14.6	0.5	13.8	0.6	13.1	0.7
1643	6	27.2	0.9	21.3	0.9	16.5	0.6	13.8	0.5	12.9	0.5	11.9	0.6
1653	6	26.3	0.9	20.6	0.9	16.0	0.6	14.1	0.5	13.0	0.5	11.9	0.6
1663	6	26.1	0.9	20.5	0.9	16.0	0.6	13.7	0.5	12.6	0.5	12.6	0.6
1674	6	25.6	0.9	19.9	0.8	14.7	0.6	13.7	0.5	12.8	0.5	11.6	0.6
1684	6	25.2	0.9	19.7	0.8	15.2	0.6	13.9	0.5	12.1	0.5	11.9	0.6
1694	6	23.9	0.8	19.7	0.8	15.5	0.6	12.8	0.5	12.1	0.5	11.4	0.6
1704	6	23.6	0.8	18.0	0.8	14.2	0.6	12.9	0.5	11.5	0.5	12.3	0.6
1716	6	24.0	0.8	18.8	0.8	13.6	0.6	12.9	0.5	11.7	0.5	11.2	0.6
1724	6	23.6	0.8	18.9	0.8	13.7	0.6	12.4	0.5	11.7	0.5	11.1	0.6
1734	6	23.5	0.8	17.0	0.8	13.3	0.5	12.3	0.5	11.1	0.5	10.9	0.6
1744	6	22.3	0.8	18.3	0.7	13.3	0.5	12.3	0.5	11.9	0.5	10.9	0.6
1754	6	22.3	0.8	16.6	0.7	13.7	0.5	11.9	0.4	10.9	0.4	10.3	0.5
1764	6	20.8	0.7	16.6	0.7	13.2	0.5	11.9	0.4	10.6	0.4	11.0	0.5
1774	6	21.9	0.7	16.6	0.6	12.5	0.5	11.5	0.4	10.9	0.4	10.0	0.5
1784	6	20.8	0.7	16.0	0.6	12.6	0.4	11.3	0.4	10.0	0.4	10.5	0.5
1794	6	20.8	0.7	15.4	0.6	12.2	0.5	10.5	0.4	10.9	0.4	9.8	0.5
1804	6	21.2	0.7	15.4	0.7	11.7	0.5	11.1	0.4	10.6	0.4	10.5	0.5
1814	6	20.4	0.7	16.1	0.7	11.7	0.5	10.9	0.4	10.4	0.4	9.8	0.5
1824	6	19.4	0.6	15.5	0.6	11.8	0.4	10.7	0.4	10.1	0.4	9.0	0.4
1834	6	19.2	0.6	15.0	0.6	10.9	0.4	10.9	0.4	10.1	0.4	9.9	0.5
1844	6	18.7	0.6	14.7	0.6	11.3	0.4	10.5	0.4	10.3	0.4	9.5	0.5
1854	6	18.4	0.6	14.8	0.6	11.7	0.4	10.8	0.4	9.8	0.4	9.6	0.4
1864	6	19.2	0.6	14.2	0.6	11.0	0.4	10.9	0.4	9.7	0.4	9.1	0.5
1874	6	18.0	0.6	13.9	0.6	11.3	0.4	10.2	0.4	9.7	0.4	9.0	0.5
1884	6	17.3	0.6	12.4	0.6	10.7	0.4	10.0	0.3	9.3	0.4	9.6	0.5

1894	6	16.6	0.6	13.2	0.6	10.9	0.4	10.0	0.4	9.7	0.4	9.3	0.4
1904	6	16.8	0.6	12.8	0.6	9.7	0.4	9.8	0.3	9.5	0.4	8.7	0.4
1914	6	16.4	0.6	12.2	0.6	9.5	0.4	10.2	0.4	8.9	0.4	9.0	0.5
1924	6	16.5	0.6	13.1	0.6	9.6	0.4	9.3	0.3	9.0	0.4	8.7	0.4
1934	6	16.2	0.6	12.6	0.6	9.5	0.4	9.2	0.3	9.4	0.4	8.9	0.5
1944	6	16.3	0.6	12.4	0.6	9.0	0.4	9.7	0.4	9.6	0.4	9.3	0.4
1954	6	16.0	0.6	12.2	0.6	9.0	0.4	9.5	0.4	9.4	0.4	8.2	0.4
1964	6	15.6	0.5	12.5	0.5	9.0	0.4	9.4	0.4	9.1	0.4	9.0	0.4
1974	6	15.9	0.6	12.2	0.6	9.2	0.4	9.4	0.3	9.2	0.4	9.1	0.4
1984	6	15.6	0.5	11.1	0.5	9.5	0.4	10.1	0.4	9.9	0.4	9.5	0.4
1994	6	14.7	0.5	11.7	0.6	9.5	0.4	9.6	0.3	9.7	0.4	9.3	0.4
2004	6	14.7	0.5	11.4	0.5	9.4	0.4	9.6	0.4	9.4	0.4	9.8	0.4
2014	6	14.5	0.5	11.5	0.5	8.8	0.4	9.3	0.3	9.7	0.4	9.2	0.4
2024	6	14.8	0.5	11.1	0.5	9.7	0.4	9.9	0.4	9.6	0.4	9.2	0.4
2034	6	13.4	0.5	11.9	0.5	9.8	0.4	9.7	0.3	9.7	0.4	9.6	0.5
2044	6	13.7	0.5	11.2	0.5	9.3	0.4	9.7	0.3	9.8	0.4	9.9	0.5
2054	6	12.6	0.5	11.5	0.6	9.7	0.4	9.5	0.3	10.3	0.4	9.4	0.4
2064	6	13.0	0.5	10.4	0.5	9.3	0.4	9.9	0.4	9.9	0.4	10.5	0.4
2074	6	13.2	0.5	10.3	0.4	9.5	0.4	9.9	0.3	10.1	0.4	10.5	0.5
2084	6	12.6	0.5	10.0	0.4	9.5	0.4	10.2	0.4	10.1	0.4	11.5	0.5
2094	6	12.2	0.4	10.4	0.4	9.1	0.4	10.3	0.4	10.4	0.4	10.9	0.5
2104	6	12.7	0.5	10.5	0.4	8.9	0.4	9.8	0.3	10.5	0.4	11.3	0.5
2114	6	12.3	0.5	10.1	0.5	9.3	0.4	10.6	0.4	10.7	0.4	10.5	0.5
2124	6	11.9	0.5	9.8	0.5	9.2	0.4	10.8	0.4	10.6	0.4	12.0	0.5
2134	6	12.2	0.4	10.6	0.5	9.8	0.4	10.1	0.4	11.6	0.4	12.2	0.5
2144	6	11.0	0.4	9.6	0.5	9.5	0.4	11.2	0.4	11.4	0.4	11.5	0.5
2154	6	12.0	0.4	10.2	0.5	9.7	0.4	11.3	0.4	10.9	0.4	11.6	0.5
2164	6	12.4	0.5	10.3	0.5	9.5	0.4	11.4	0.4	11.9	0.4	13.2	0.6

2174	6	11.8	0.4	11.4	0.5	9.9	0.4	11.5	0.4	12.5	0.5	13.5	0.6
2184	6	11.8	0.4	10.0	0.5	9.4	0.4	11.6	0.4	12.5	0.5	13.3	0.6
2194	6	12.1	0.4	10.3	0.5	9.7	0.4	11.9	0.4	12.9	0.5	12.5	0.5

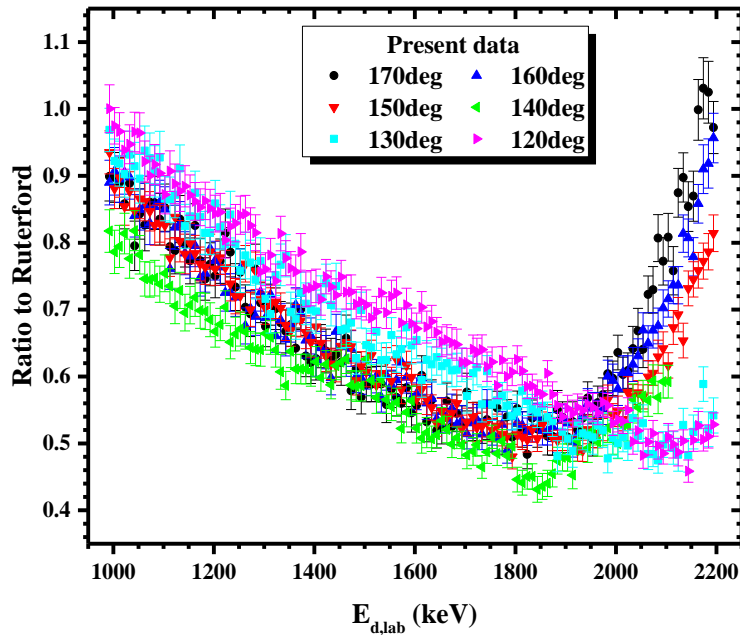


Figure 4.28 Ratio to Rutherford of the obtained differential cross section measurements of the $^{14}\text{N}(d,d_0)^{14}\text{N}$ in the deuteron energy range 1000-2200 keV for all the measured scattering angles.

4.7 Cross section measurements for the $^{23}\text{Na}(d,d_0)^{23}\text{Na}$ elastic scattering

The differential cross section of deuteron elastic scattering on ^{23}Na was studied in the energy range of $E_{d,\text{lab}} = 1060\text{-}2400$ keV with energy steps of $\sim 20\text{-}30$ keV and for the scattering angles of 140° , 150° , 160° and 170° . The level scheme of the $d+^{23}\text{Na}$ system is displayed in Fig. 4.29, along with the possible reaction channels. However, in the studied energy region no known levels of the compound nucleus ^{25}Mg exist and thus a nominal energy step of 20-30 keV was adopted in the present cross section measurements.

The implemented target was a Na_2O layer on top of a carbon foil with an Au layer on top. A typical experimental spectrum is shown in Fig. 4.30 for the deuteron energy of 2200 keV and for 170° . The minor contribution of nitrogen and chlorine were visible in the experimental spectra due to

the coating used for the manufacturing of carbon foils, although without interfering with the peaks under study.

The differential cross section values were determined using the Eq. 4.3 for the sodium case as:

$$\left(\frac{d\sigma}{d\Omega}\right)_{\theta,E}^{Na} = \left(\frac{d\sigma}{d\Omega}\right)_{\theta,E'}^{Au} \times \frac{Y_{Na}}{Y_{Au}} \times \frac{N_{t,Au}}{N_{t,Na}} \quad (4.9)$$

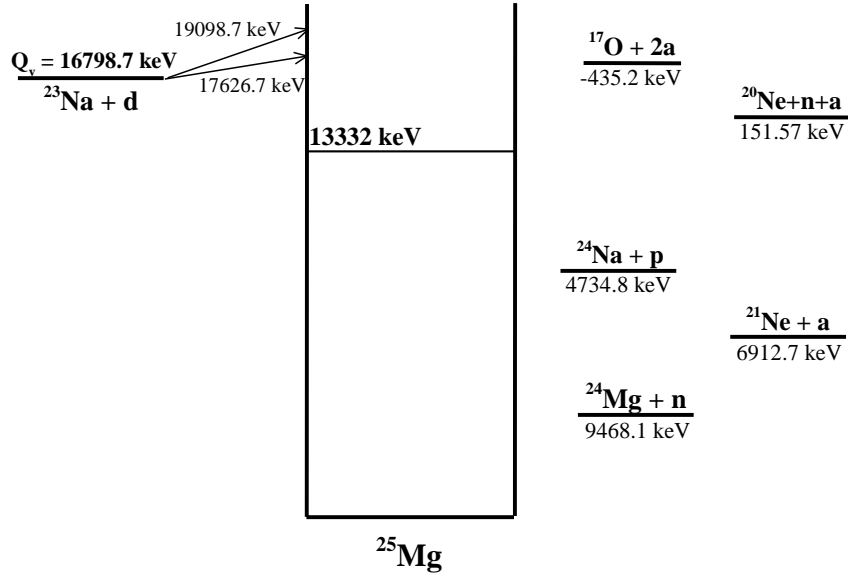


Figure 4.29 Level scheme of the $^{23}\text{Na}+d$ system in the CM reference frame.

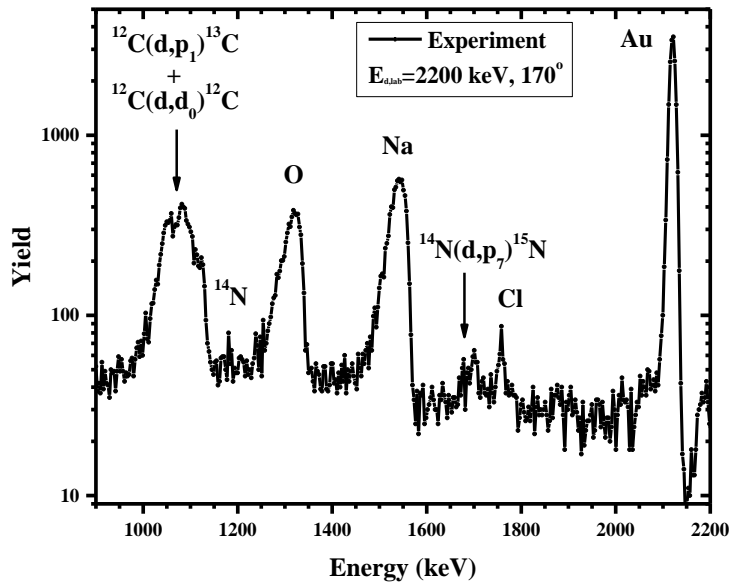


Figure 4.30 Typical experimental spectrum acquired from the irradiation of the target consisting of a Na_2O layer on top of carbon foil along with a Au layer on top at the deuteron energy 2200 keV at 170° along with the corresponding peak identification.

4.7.1 Target characterization

The target thickness ratio of $^{197}\text{Au}:^{23}\text{Na}$ was determined using proton spectra acquired at $E_{p,\text{lab}}=1200, 1360, 1430$ keV and for the scattering angles of $170^\circ, 160^\circ$ and 150° , in order to avoid the uncertainties introduced by the effect of straggling. In the case of sodium, the selection of proton energies far from the existing sharp, Breit-Wigner type resonances was rather difficult, because of the existing multiple resonances in the structure of the $^{23}\text{Na}(p,p_0)^{23}\text{Na}$ elastic scattering differential cross-sections. The simulation of the obtained spectra was accomplished by using the evaluated cross section datasets on proton elastic scattering on ^{12}C [82], ^{14}N [26], ^{16}O [84] and ^{23}Na [85] (for the sodium case the datasets were also benchmarked [22]) calculated using SigmaCalc 2.0 as implemented in the SIMNRA program. Rutherford cross section values were used for the deuteron elastic scattering on ^{197}Au . The acquired mean value of the $N_{t,\text{Au}}/N_{t,\text{Na}}$ was found to be 0.038 ± 0.001 , implying a 2.6% relative statistical uncertainty. It should also be pointed out here that the spectrum at 1200 keV and 150° was not included in the calculation of the mean target thickness ratio value since there was a partial overlap between the elastic peaks of sodium and oxygen. Nevertheless, the results of such a procedure are shown in Fig. 4.31 for the proton energy of 1360 keV and for the 160° scattering angle.

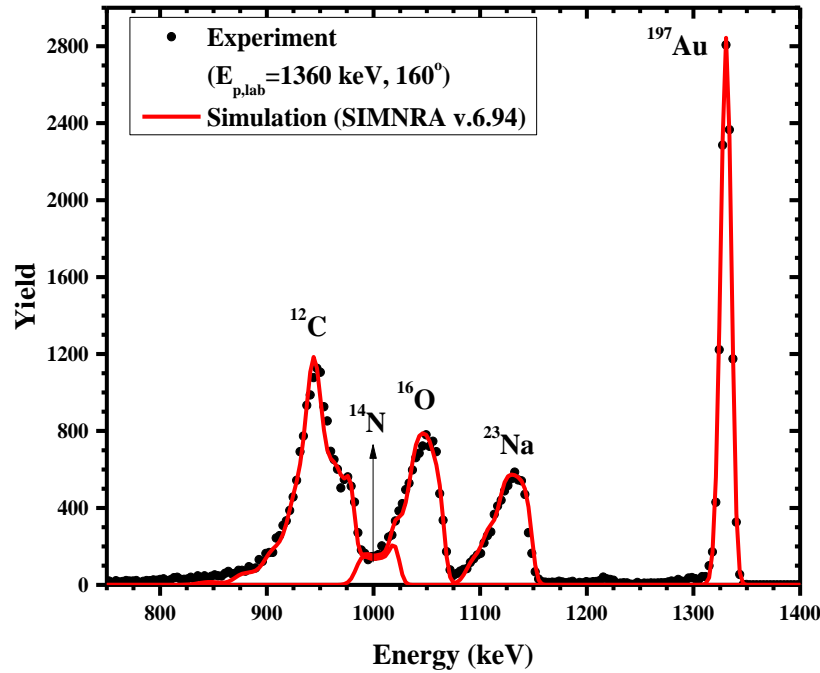


Figure 4.31 Experimental and simulated proton spectra acquired for the target thickness ratio calculation at 1360 keV at 160° along with the corresponding peak identification.

4.7.2 Uncertainties

The integration or fitting process (when necessary) of the ^{197}Au and ^{23}Na peaks, following the background subtraction, led to a relative statistical uncertainty of the order of 1–2%, while the target thickness ratio calculation yielded a 2.6% relative statistical uncertainty. Therefore, the implementation of the error propagation formula indicated a total statistical uncertainty in the cross-section values below ~4% in all cases.

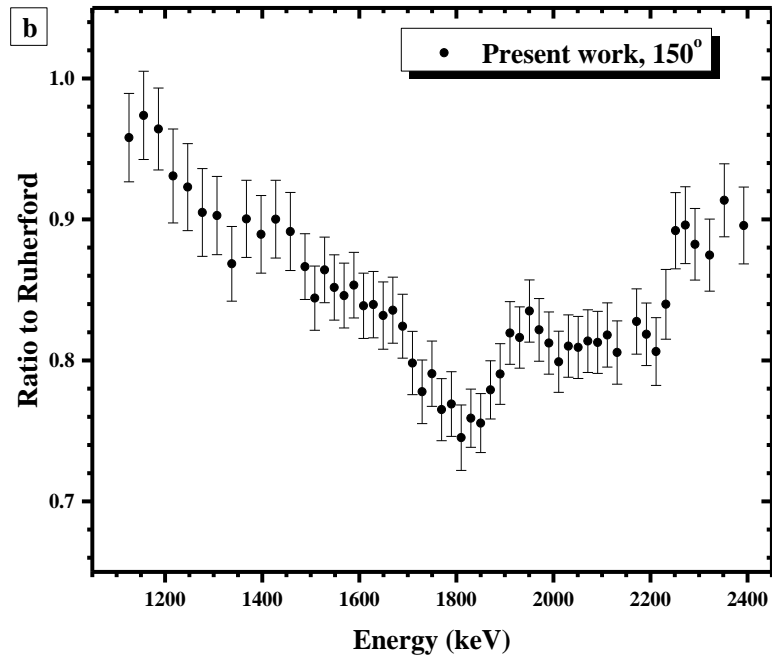
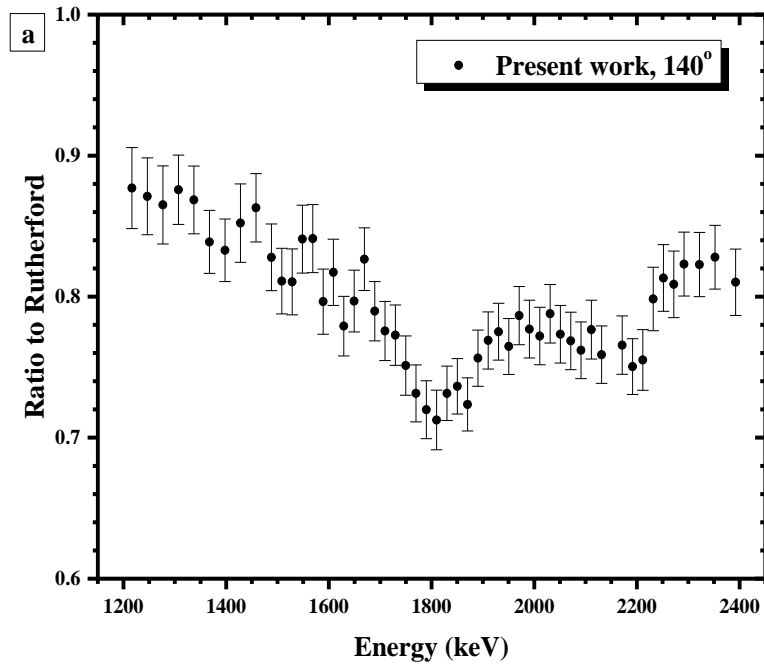
The systematic uncertainties in the cross-section values originated only from the deviations of the compiled and the experimental stopping power data and for the gold case were ~3.6%, whereas for the sodium case are unknown. However, testing neighbouring nuclei, namely neon and aluminum, discrepancies up to 2.8% were observed. Therefore, the adopted systematic uncertainty for this procedure should be at least equal to 3.6%.

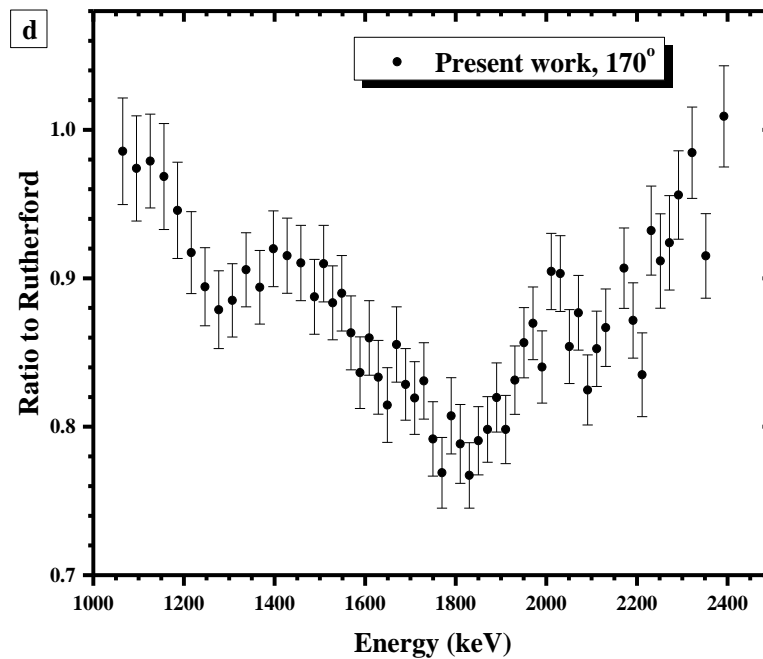
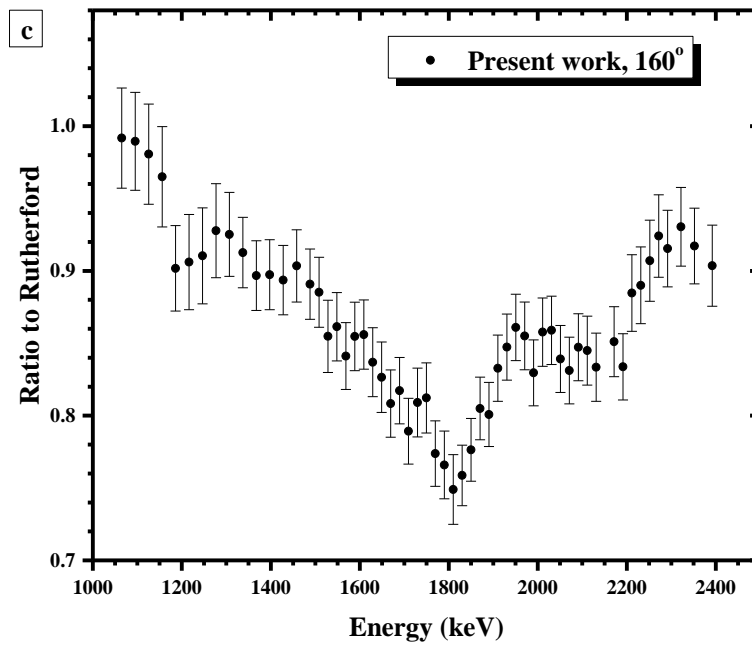
The uncertainties in the deuteron energy included the energy ripple acquired from the accelerator calibration procedure (~1 keV) and the energy straggling in the calculated target (5.1 keV).

4.7.3 Results and Discussion

The ratio to Rutherford of the obtained differential cross-section values for the deuteron elastic scattering on ^{23}Na in the energy range of 1060-2400 keV with energy steps of ~20-30 keV for the four measured backscattering angles of 140° , 150° , 160° and 170° are presented in both graphical form in Fig. 4.32 a–d and in tabulated form in Table 4.5. In Figs. 4.32 a-d the uncertainties concerning the deuteron beam energy are not visible in the x-axis due to the adopted scale.

Strong deviations from the corresponding Rutherford values are displayed in Figs 4.32a-d especially at high energies, in some cases up to 35%. The measured cross sections display values lower than the Rutherford ones over the whole studied energy range, as it was also observed in the $^{\text{nat}}\text{N}(d,d_0)^{\text{nat}}\text{N}$ elastic scattering. In fact, in the lower energy region (up to 1450 keV) the measured values are 10% lower than the Rutherford ones, except for 140° where they are 15% lower, while for higher energies these deviations increased. Moreover, a structure could be observed in the measured cross section values with a significant minimum in the deuteron energy of ~1800 keV. Due to the lack of spectroscopic information in the prompt energy region of the compound nucleus ^{25}Mg , the presence of such a structure could not be unambiguously associated with the resonant mechanism. However, the presence of the minimum in all the measured scattering angles, indicating a strong angular correlation, as well as the existence of a structure in the same energy in the $^{23}\text{Na}(d,p_0)^{24}\text{Na}$ channel [87] excluded the presence of Ericson fluctuations and indicated the possible influence of the compound nucleus mechanism. Moreover, it should be pointed out that the origin of this structure could be attributed to the possible competition with the (d,p) and especially the (d,n) reaction channels. From Fig. 4.33, where all the measured angles are presented in one graph, the displayed distribution was rather smooth.





Figures 4.32 a-d Ratio of the obtained differential cross section values to the ones calculated using the Rutherford formula for the $^{23}\text{Na}(d,d_0)^{23}\text{Na}$ elastic scattering in the energy range $E_{d,\text{lab}}=1060\text{-}2400$ keV in

steps of ~20-30 keV for the scattering angles of 140°, 150°, 160°, 170°. The total estimated statistical uncertainties are included in the graphs.

Table 4.5 Tabulated differential cross sections (mb/sr) of the $^{23}\text{Na}(d,d_0)^{23}\text{Na}$ elastic scattering in the deuteron energy range of 1060-2400 keV with energy steps of ~20-30 keV for the backscattering angles of 140°, 150°, 160°, 170°. The corresponding combined cross-section statistical uncertainties are also included.

$E_{d,\text{lab}}$ (keV)	$\delta E_{d,\text{lab}}$ (keV)	$d\sigma/d\Omega$ (mb/sr)							
		140°		150°		160°		170°	
1065	5	-	-	-	-	144	5	136	5
1095	5	-	-	-	-	135	5	127	5
1126	5	-	-	134	4	127	4	121	4
1156	5	-	-	129	4	119	4	114	4
1186	5	-	-	122	4	105	3	105	4
1216	5	118	4	112	4	101	4	97.1	2.9
1247	5	111	3	105	4	96	4	90.2	2.7
1277	5	105	3	99	3	93	3	84.5	2.5
1307	5	101.8	2.9	93.8	2.9	88.9	2.8	81.2	2.3
1337	5	96.4	2.7	86.2	2.6	83.8	2.2	79.4	2.2
1367	5	89.1	2.4	85.5	2.6	78.7	2.1	74.9	2.1
1398	5	84.6	2.3	80.9	2.5	75.4	2.0	73.8	2.1
1428	5	83.0	2.7	78.4	2.4	72.0	1.9	70.3	1.9
1458	5	80.6	2.3	74.5	2.3	69.8	1.9	67.1	1.9
1488	5	74.2	2.1	69.5	1.9	66.0	1.8	62.8	1.8
1508	5	70.8	2.0	65.9	1.8	63.9	1.7	62.7	1.8
1528	5	68.9	2.0	65.7	1.8	60.1	1.8	59.3	1.7
1549	5	69.6	2.0	63.1	1.7	59.0	1.6	58.1	1.7
1569	5	67.9	1.9	61.1	1.7	56.1	1.5	55.0	1.6
1589	5	62.6	1.8	60.0	1.6	55.6	1.5	51.9	1.5

1609	5	62.7	1.8	57.5	1.6	54.3	1.5	52.0	1.5
1629	5	58.3	1.6	56.2	1.6	51.8	1.5	49.2	1.5
1649	5	58.2	1.6	54.3	1.6	49.9	1.5	46.9	1.4
1669	5	58.9	1.6	53.3	1.5	47.6	1.4	48.1	1.4
1689	5	54.9	1.5	51.3	1.4	47.0	1.3	45.5	1.3
1709	5	52.7	1.4	48.5	1.4	44.3	1.3	43.9	1.3
1730	5	51.3	1.4	46.2	1.3	44.4	1.3	43.5	1.3
1750	5	48.7	1.4	45.9	1.3	43.6	1.3	40.5	1.3
1770	5	46.4	1.3	43.4	1.2	40.6	1.2	38.5	1.2
1790	5	44.6	1.3	42.6	1.3	39.3	1.2	39.5	1.3
1810	5	43.2	1.3	40.4	1.3	37.5	1.2	37.7	1.3
1830	5	43.4	1.1	40.3	1.1	37.2	1.0	35.9	1.0
1850	5	42.7	1.1	39.2	1.1	37.2	1.0	36.2	1.1
1870	5	41.1	1.1	39.6	1.0	37.8	1.0	35.8	1.0
1890	5	42.0	1.1	39.3	1.1	36.8	1.0	35.9	1.0
1910	5	41.8	1.1	39.9	1.1	37.5	1.0	34.3	1.0
1930	5	41.3	1.1	38.9	1.0	37.3	1.0	35.0	1.0
1951	5	39.9	1.0	39.0	1.0	37.2	1.0	35.3	1.0
1971	5	40.2	1.1	37.6	1.0	36.2	1.0	35.1	1.0
1991	5	38.9	1.0	36.4	1.0	34.4	0.9	33.2	1.0
2011	5	37.9	1.0	35.1	1.0	34.8	1.0	35.1	1.0
2031	5	37.9	1.0	34.9	1.0	34.2	0.9	34.3	1.0
2051	5	36.5	1.0	34.2	0.9	32.8	0.9	31.8	0.9
2071	5	35.6	0.9	33.7	0.9	31.8	0.9	32.0	0.9
2091	5	34.6	0.9	33.0	0.9	31.8	0.9	29.6	0.8
2111	5	34.6	0.9	32.6	0.9	31.1	0.9	30.0	0.9
2131	5	33.2	0.9	31.5	0.9	30.1	0.9	29.9	0.9
2171	5	32.2	0.9	31.2	0.9	29.6	0.8	30.1	0.9

2191	5	31.0	0.8	30.3	0.8	28.5	0.8	28.4	0.8
2212	5	30.7	0.9	29.3	0.9	29.7	0.9	26.8	0.9
2232	5	31.8	0.9	30.0	0.9	29.3	0.9	29.3	0.9
2252	5	31.9	0.9	31.3	0.9	29.4	0.9	28.2	1.0
2272	5	31.1	0.9	30.8	0.9	29.4	0.9	28.1	1.0
2292	5	31.1	0.9	29.8	0.9	28.6	0.8	28.5	0.9
2322	5	30.3	0.8	28.8	0.8	28.3	0.8	28.6	0.9
2352	5	29.7	0.8	29.3	0.8	27.2	0.8	25.9	0.8
2392	5	28.1	0.8	27.8	0.8	25.9	0.8	27.6	0.9

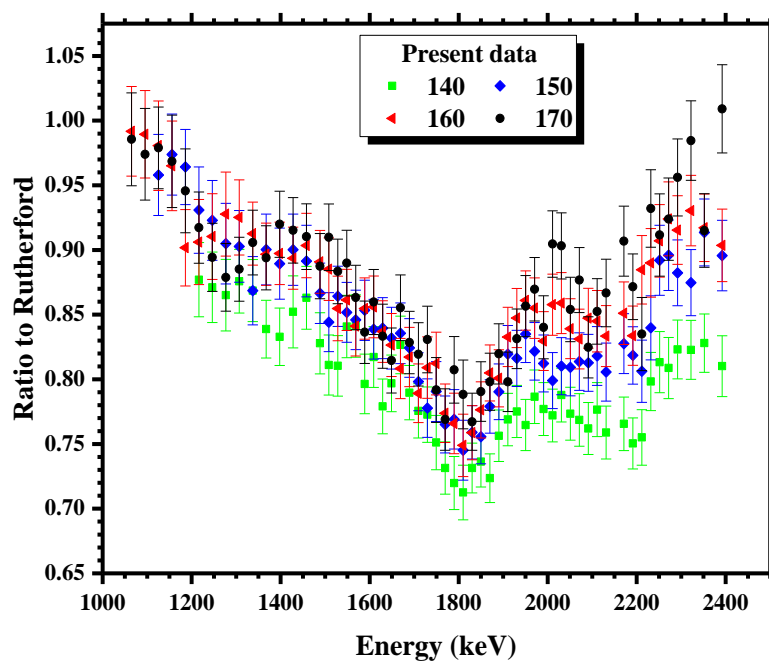


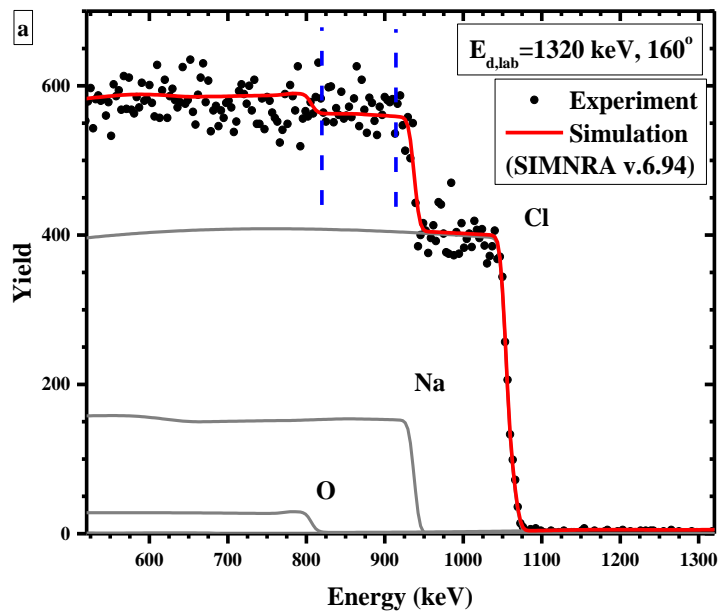
Figure 4.33 Ratio to Rutherford of the obtained differential cross section measurements of the $^{23}\text{Na}(d,d_0)^{23}\text{Na}$ in the deuteron energy range 1060-2400 keV for all the measured scattering angles.

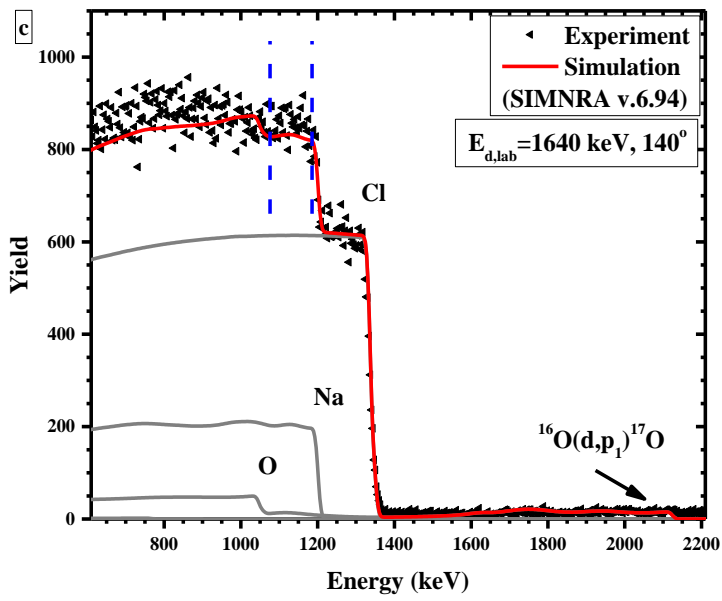
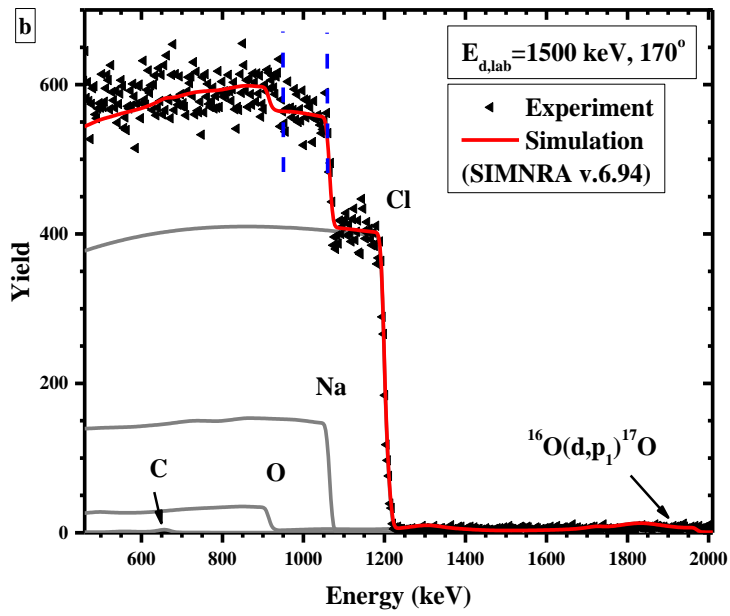
4.7.4 Benchmarking of the obtained $^{23}\text{Na}(d,d_0)^{23}\text{Na}$ differential cross section values

The validation of the obtained differential cross section values for the deuteron elastic scattering on ^{23}Na was performed by bombarding a NaCl pellet with deuterons at $E_{d,\text{lab}}=1110, 1320, 1500, 1640, 1820, 2060$ and 2300 keV for all the measured scattering angles namely $140^\circ, 150^\circ, 160^\circ$ and 170° . For the simulation of the thick target spectra in the case of chlorine (both natural isotopes ^{35}Cl and ^{37}Cl) Rutherford cross sections along with the screening effect factor were implemented in the SIMNRA program. For the simulation of the parasitic edges of oxygen and carbon, evaluated datasets from SigmaCalc 2.0 were used for the carbon and oxygen elastic scattering, $^{12}\text{C}(d,d_0)^{12}\text{C}$ [14] and $^{16}\text{O}(d,d_0)^{16}\text{O}$ [14] as well as for the $^{16}\text{O}(d,p_1)^{17}\text{O}$ and $^{16}\text{O}(d,a_0)^{14}\text{N}$ [14] reaction channels visible in the experimental spectra. Due to the highly hygroscopic nature of the NaCl powder, carbon and especially oxygen were unavoidably present in the formed pellet. It should be noted here that the deuteron elastic scattering on chlorine was deemed to follow the Rutherford formula, since no measurements indicating otherwise existed in literature for the present energy range. However, proton elastic scattering on chlorine was reported [88] to present differences up to 20% from the corresponding Rutherford values for energies higher than ~ 2100 keV, thus, as the beam energy increased, the chlorine edge became more unreliable for normalization. Nevertheless, the NaCl constitutes a reasonable choice for the benchmarking experiment, since if a target containing a higher-Z element - for instance NaBr or NaI - or compounds containing oxygen in their chemical formula (e.g. Na_2O or NaOH) were implemented, the heavy-Z element would have created a significant background under the Na edge, thus leading to a higher statistical uncertainty in the Na yield and the same applies to any possible strong contribution from the oxygen reaction channels.

The benchmarking procedure was initiated with the accurate description of the implemented target through the 1110 keV and 170° experimental spectrum, since sodium follows the Rutherford formula in this case within 2-3%. Subsequently, all the experimental spectra were simulated, while the chlorine edge was used for the determination of the $Q \times \Omega$ product for every beam energy/scattering angle combination. A few examples can be found in Figs. 4.34a-e for several beam energy/scattering angle combinations, along with the corresponding edge identification. As it is shown in the graphs, the presence of oxygen via the reaction $^{16}\text{O}(d,p_1)^{17}\text{O}$, induced a significant background, especially for higher beam energies, while it displayed resonances over the whole studied energy range, as evident in SigmaCalc 2.0. More specifically, in the experimental spectra with energies 1640 keV and 2060 keV, the contribution of this reaction increased significantly under the sodium edge (Figs. 4.34c and e) and thus these energies were excluded from the benchmarking procedure. Moreover, it is evident in the figures that the background was increasing as the beam energy increased and for energies above 2000 keV the induced background could not be accurately reproduced by the $^{16}\text{O}(d,p_1)^{17}\text{O}$ reaction, indicating the possible additional contribution of $^{23}\text{Na}(d,p_x)^{24}\text{Na}$ reaction channels. Thus, the experimental spectra for energies above 2000 keV were also excluded from the benchmarking process. The integrated window, in which the comparison between the simulated sodium counts and the experimental sodium ones (the simulated counts from oxygen and chlorine were subtracted) was performed, is denoted in the figures and included ~ 180 keV (~ 60 channels) below the sodium edge. The low energy limit of the integrated window was selected in order to avoid the contribution of

the deuteron elastic scattering on oxygen. Therefore, the results of the benchmarking process within the integrated window are presented in Table 4.6. The worst difference included in Table 7 is the 13.6% one for the deuteron energy of 1320 keV and 170°. However, these numbers indicate a fair agreement between the simulated and the experimental results, since it should be taken into account that these differences include the uncertainty of the $^{16}\text{O}(d,p_1)^{17}\text{O}$ reaction which - at least partly - is unavoidably included in the integrated window. Moreover, the obtained numbers in Table 7 did not reveal a coherent behavior for all scattering angles, therefore any type of renormalization of the determined cross section values based solely on the benchmarking experiment was not deemed advisable.





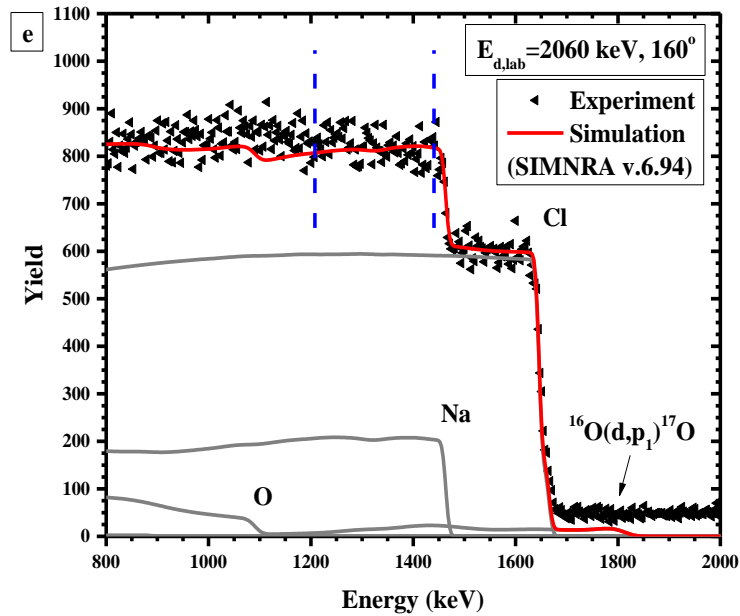
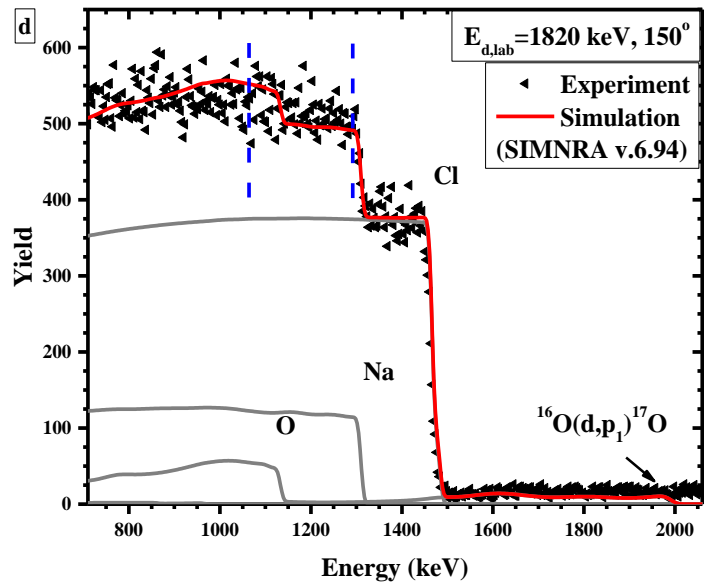


Figure 4.34 a-e Typical experimental and simulated thick target spectra (NaCl) at different beam energy/scattering angle combinations along with the corresponding edge identification. As denoted in the figures by blue dashed lines, the integrated window used in the benchmarking procedure included, depending on the beam energy, ~ 180 keV (~ 60 channels) below the sodium edge.

Table 4.6 Differences (in %) between the simulated and the experimental counts within the integrated window for every beam energy/scattering angle combination. The negative values correspond to a lower

value of the integral for the simulated spectrum than the integral of the experimental spectrum whereas the positive ones correspond to a higher integral for the simulated spectrum than the integral of the experimental spectrum.

Energy (keV)	140°	150°	160°	170°
1110	-	-	+6.7	-
1320	-13.1	-12.9	+1.2	-13.6
1500	-11.4	-9.9	-7.6	-3.0
1820	-12.6	-12.0	+6.5	-10.4

4.8 Cross section measurements for the $^{nat}\text{Si}(d,d_0)^{nat}\text{Si}$ elastic scattering

The deuteron elastic scattering on ^{nat}Si was studied in the energy range $E_{d,lab} = 1000\text{--}2200$ keV in energy steps of 10 keV and for the scattering angles of 120° , 130° , 140° , 150° , 160° and 170° . The level scheme, shown in Fig. 4.35 for the most abundant isotope ^{28}Si (92.23% in ^{nat}Si), reveals the lack of known energy levels of the compound nucleus ^{30}P in the prompt energy region. Due to the lack of such information the adopted energy step during the measurements was set to 10 keV.

The implemented target was a silicon nitride membrane with evaporated gold on top. A typical spectrum for the deuteron energy of 1420 keV and for 160° is presented in Fig. 4.36 along with the corresponding peak identification. The parasitic contribution of carbon, oxygen and chlorine has also been displayed in the experimental spectra, although without any interference with the peaks under study over the whole energy range.

The obtained cross section values of the $^{nat}\text{Si}(d,d_0)^{nat}\text{Si}$ elastic scattering were calculated via Eq. 4.3 for the silicon case:

$$\left(\frac{d\sigma}{d\Omega}\right)_{\theta,E}^{natSi} = \left(\frac{d\sigma}{d\Omega}\right)_{\theta,E'}^{Au} \times \frac{Y_{natSi}}{Y_{Au}} \times \frac{N_{t,Au}}{N_{t,natSi}} \quad (4.10)$$

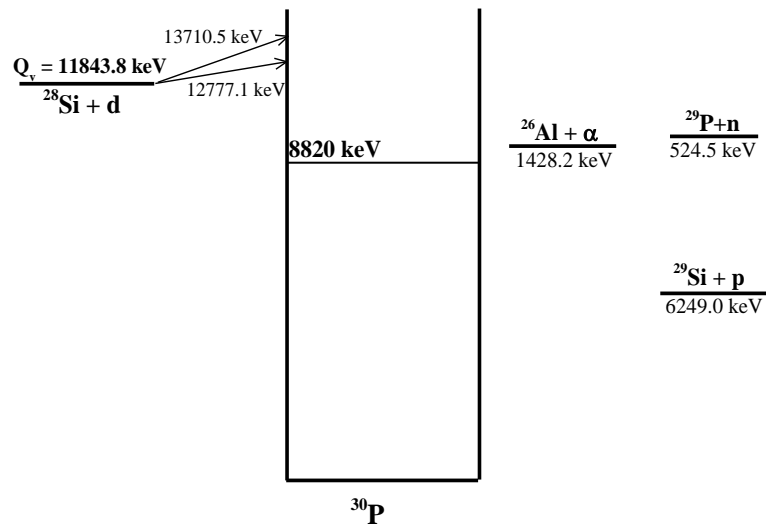


Figure 4.35 Level scheme of the $^{28}\text{Si} + \text{d}$ system in the CM reference frame.

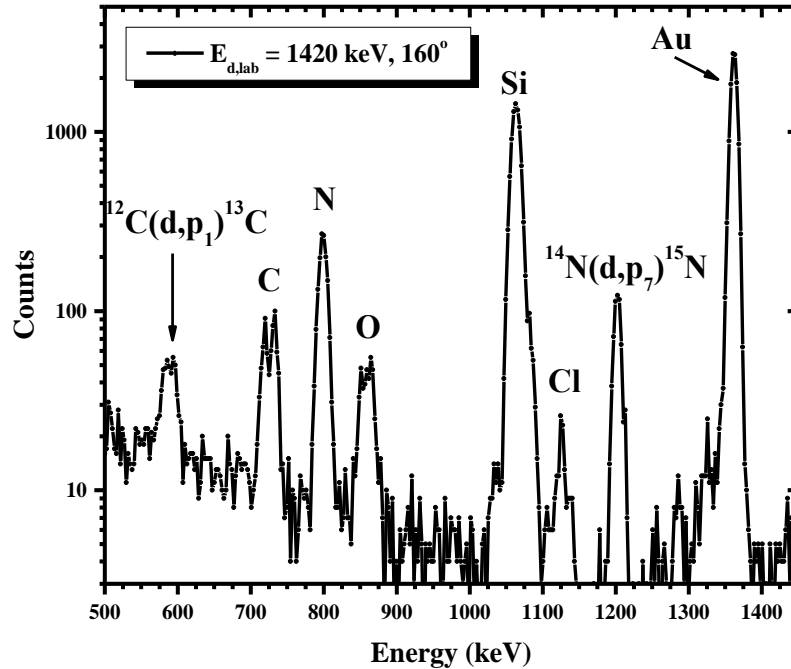


Figure 4.36 Typical experimental spectrum acquired from the implemented target which consisted of a silicon nitride membrane with a layer of gold on top at the deuteron energy 1420 keV taken at 160° along with the corresponding peak identification.

4.8.1 Target characterization

The thickness ratio $N_{t,Au}:N_{t,Si}$ was calculated using the proton spectra at the energies of 1200 and 1300 keV at six backscattering angles (120° , 130° , 140° , 150° , 160° , 170°). The analysis of the proton spectra was accomplished using the Rutherford formula for ^{197}Au and the non-Rutherford evaluated data for proton elastic scattering on ^{12}C [82], $^{\text{nat}}\text{N}$ [26], ^{16}O [84], and $^{\text{nat}}\text{Si}$ [27], as obtained via the online calculator SigmaCalc 2.0. The average $N_{t,Au}:N_{t,Si}$ ratio value obtained from the simulation procedure via the SIMNRA program was 0.0431 ± 0.0005 with a relative statistical error of 1.1%. The simulation of the experimental spectrum at the proton energy of 1300 keV and for the 150° scattering angle is shown in Fig. 4.37, along with the corresponding peak identification.

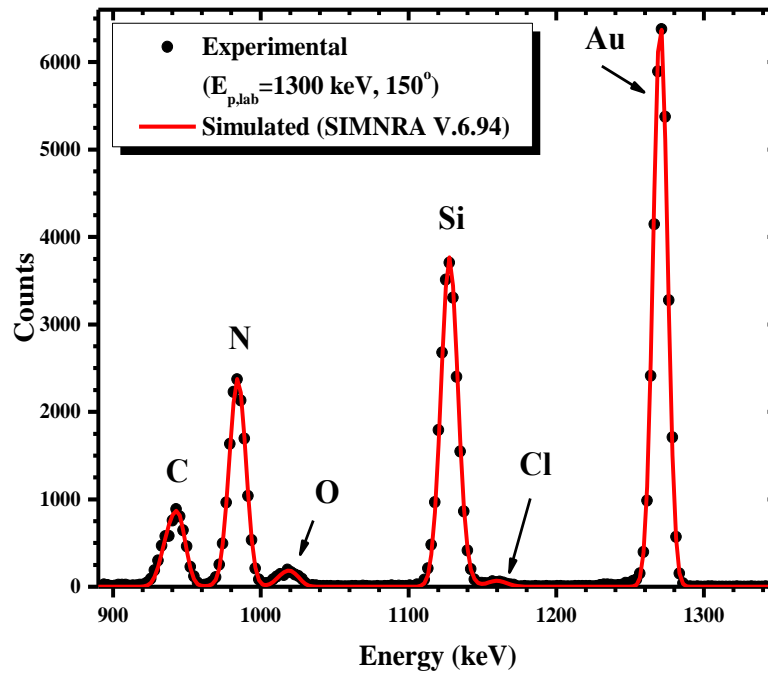


Figure 4.37 Experimental and simulated proton spectra taken from the target characterization procedure at 1300 keV and at the scattering angle of 150° along with the corresponding peak identification.

4.8.2 Uncertainties

The statistical uncertainty obtained by the integration/fitting process of the Si and Au peaks, after the background subtraction, was below 1%, while the statistical uncertainty originating from the target thickness ratio calculation was 1.1%. The addition of these values using the error propagation formula resulted in the total statistical uncertainty of the obtained cross section values being below 2.3% in all cases.

However, this statistical error does not include any systematic uncertainties e.g. deviations between compiled and experimental stopping power data for protons impinging on silicon which are evident in SRIM (<http://www.srim.org/>) and can be as high as ~4% while for protons impinging on gold the deviations are up to 3.6%.

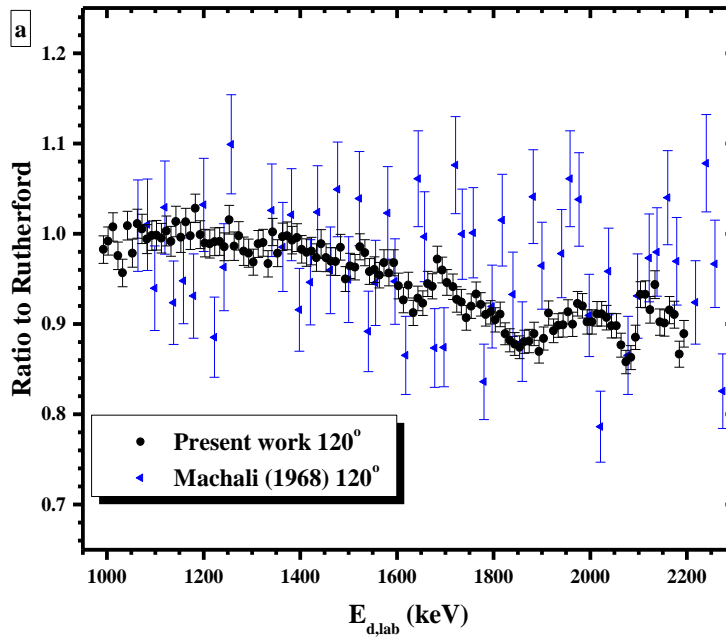
The uncertainties in the energy was the accelerator ripple (~3 keV) and the energy straggling in the obtained target (~2.4 keV). These two values were quadratically added and resulted in a total error in the x-values of ~4 keV in all cases.

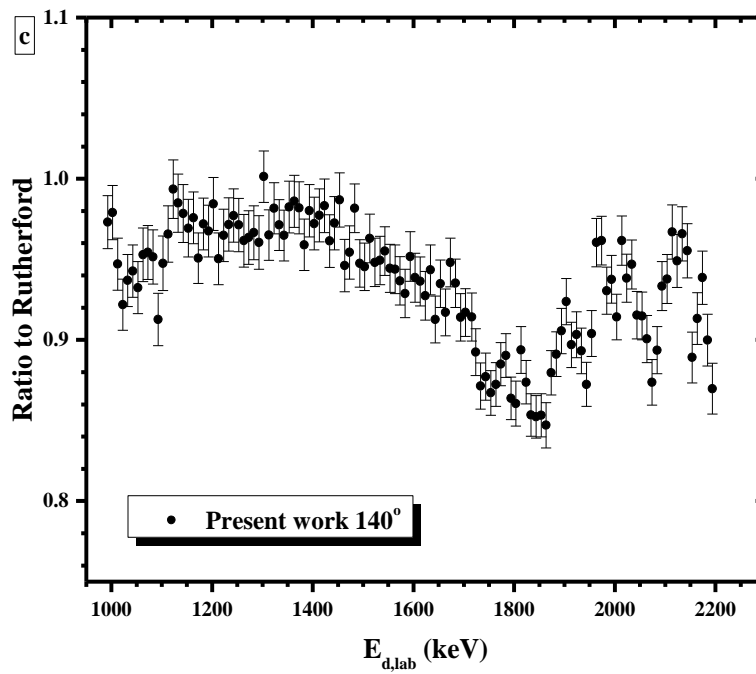
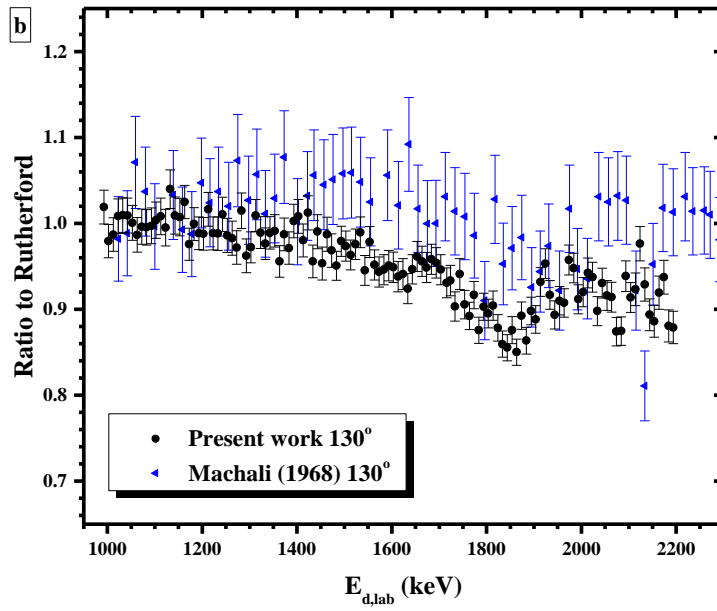
4.8.3 Results and Discussion

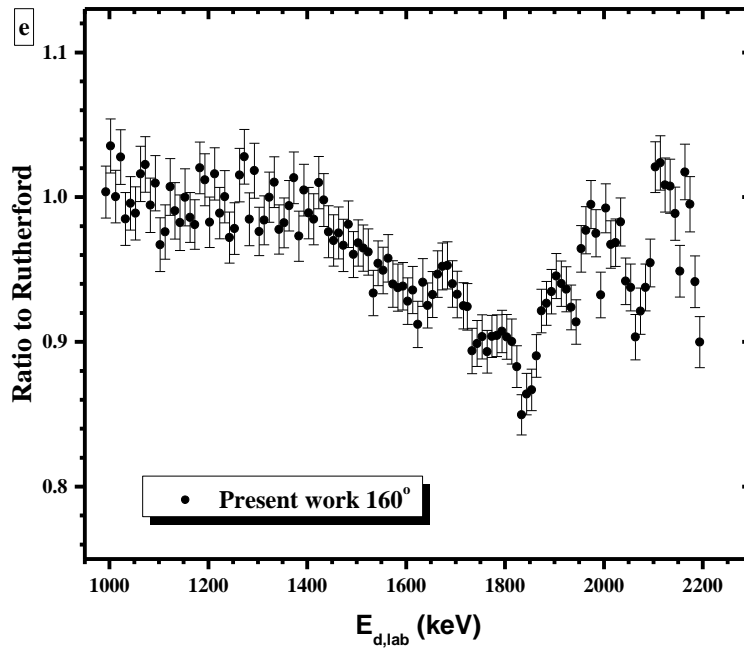
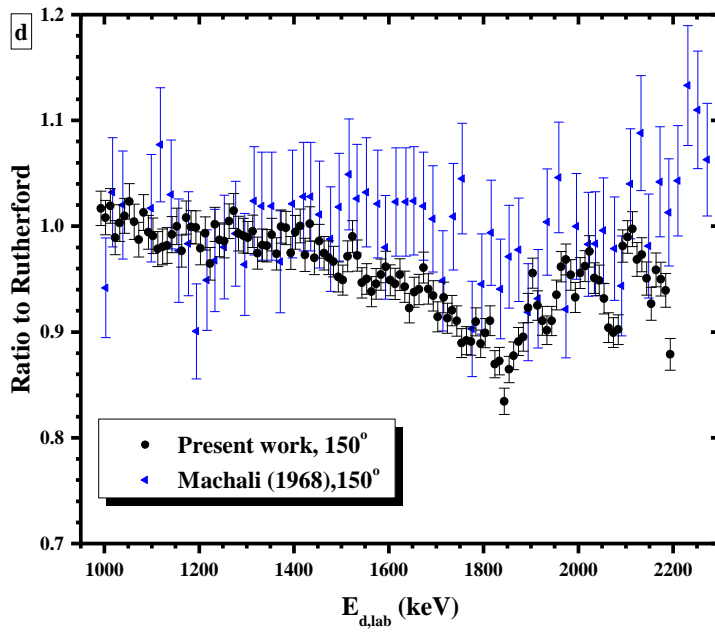
The determined differential cross section values of the deuteron elastic scattering in ^{nat}Si in the energy range of 1000-2200 keV in steps of 10 keV and for the scattering angles of 120°, 130°, 140°, 150°, 160° and 170° are presented in ratio to Rutherford form in Figs. 4.38 a-f and the absolute values are tabulated in Table 4.7. Moreover, in Figs. 4.38 a-f the preexisting data from literature have also been included for comparison purposes. The uncertainties in the beam energy are not visible in the figures due to the selected scale.

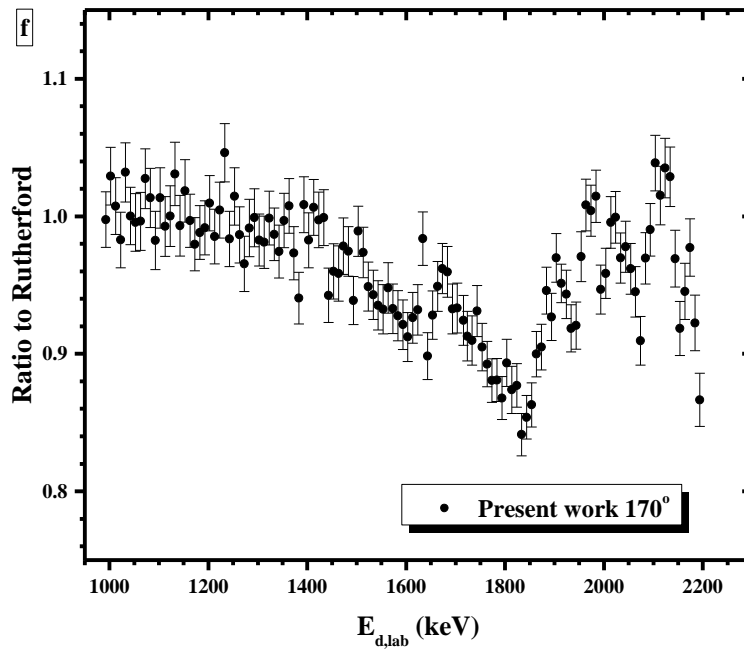
For the common scattering angles (120°, 130°, 150°) with Machali et al. [20] good agreement was observed in the low energies (up to 1400 keV), whereas for higher energies deviations were evident, with the previously measured data being systematically higher. Although the reason for the acquired differences is unknown, target related effects could be involved. The obtained cross section values for all the scattering angles revealed small deviations for the corresponding Rutherford values in the low energy part (up to ~1600 keV), while for higher energies the deviations tend to increase and the obtained structure involves lower values than the Rutherford ones. Due to the lack of information on the energy levels of the formed compound nucleus, the effect of the resonant mechanism cannot be assessed. Moreover, the possible effect of Ericson fluctuations should be examined due to the energies that the formed compound nucleus is excited. Hence, by examining the angular variation (Fig. 4.39 and Fig. 4.40), for energies above ~1800 keV, a clear correlation between the measured angles is observed where 170° displays the highest cross section values, 120° displays the lowest cross section values and in between the cross section values of the intermediate scattering angles are included. By examining different reaction channels in the same energy region, resonant-like behavior is also observed in the $^{28}\text{Si}(d,p_0)^{29}\text{Si}$ reaction channel with a general trend of an increase in the cross section as the deuteron energy increases, although a doubtful angular variation was observed [89]. For the $^{28}\text{Si}(d,p_1)^{29}\text{Si}$ reaction channel

the situation seems similar. However, for both of the aforementioned reaction channels, there are no adequate datasets with a small energy step to proceed to certain conclusions. Concerning the $^{28}\text{Si}(d,\alpha_0)^{26}\text{Al}$ reaction channel, according to [20], similar fluctuations are also displayed in the cross section structure, although such data cannot be found in IBANDL or EXFOR. Therefore, indications exist that the obtained cross section structure is not caused by Erickson fluctuations, although their existence cannot be excluded, due to the lack of known levels of the compound nucleus and due to the lack of coherent datasets on the reaction channels.









Figures 4.38 a-f Ratio to Rutherford of the obtained differential cross section values for the deuteron elastic scattering on ^{nat}Si in the energy range of 1000-2200 keV in steps of 10 keV for the scattering angles of 120° , 130° , 140° , 150° , 160° , 170° along with the preexisting data from literature.

Table 4.7 Tabulated differential cross sections (mb/sr) of the $^{nat}\text{Si}(d,d_0)^{nat}\text{Si}$ elastic scattering in the energy range of 1000-2200 keV in steps of 10 keV and for the backscattering angles of 120° , 130° , 140° , 150° , 160° , 170° . The corresponding combined cross-section statistical uncertainties are also included.

$E_{d,\text{lab}}$ (keV)	$\delta E_{d,\text{lab}}$ (keV)	$d\sigma/d\Omega$ (mb/sr)											
		120°		130°		140°		150°		160°		170°	
992	4	440	7	380	7	314	5	294	5	268	5	254	5
1002	4	436	7	358	7	310	5	285	5	271	5	257	5
1012	4	434	7	354	7	294	5	283	5	257	5	247	5
1022	4	412	6	355	7	280	5	269	4	259	5	236	5
1032	4	396	6	348	7	279	5	268	5	243	4	243	5
1042	4	410	6	342	7	276	5	264	4	241	4	231	5
1052	4	390	6	332	7	268	5	263	4	235	4	226	5
1062	4	396	6	322	7	268	5	253	4	237	4	222	5

1072	4	386	6	319	7	264	5	244	4	234	4	224	5
1083	4	375	6	313	6	258	5	246	4	223	4	217	5
1093	4	370	6	308	6	243	4	237	4	223	4	207	4
1103	4	363	6	304	6	248	4	232	4	210	4	210	5
1113	4	356	6	300	6	248	5	225	4	208	4	202	4
1123	4	352	6	291	6	251	5	222	4	211	4	200	4
1133	4	342	6	299	6	245	4	218	4	204	4	202	5
1143	4	344	6	285	6	239	4	217	4	198	4	191	4
1153	4	332	6	279	6	232	4	215	4	198	4	193	4
1163	4	332	5	280	5	230	4	206	3	192	3	186	4
1173	4	321	5	262	5	220	4	209	3	188	3	179	4
1183	4	325	5	263	5	221	4	204	3	192	3	178	4
1193	4	311	5	256	5	217	4	200	3	188	3	176	3
1203	4	303	5	252	5	217	4	193	3	179	3	176	3
1213	4	298	5	255	5	206	3	193	3	182	3	169	3
1223	4	294	5	244	5	206	3	184	3	175	3	169	3
1233	4	289	4	240	5	204	3	188	3	174	3	173	4
1243	4	283	4	241	5	202	3	182.4	2.9	166	3	160	3
1253	4	287	5	232	5	197	3	179.4	2.9	165	3	163	3
1263	4	274	4	227	5	192	3	179.9	2.9	168	3	156	3
1273	4	273	4	221	4	190	3	178.8	2.9	168	3	150	3
1283	4	264	4	228	5	187	3	172.3	2.8	158	3	152	3
1293	4	260	4	213	4	183	3	169.4	2.8	161	3	151	3
1303	4	253	4	211	4	188	3	166.5	2.6	151.9	2.6	146.0	2.8
1313	4	254	4	216	4	178.7	2.9	165.0	2.5	150.8	2.6	143.6	2.8
1323	4	251	4	209	4	179.1	2.9	159.1	2.5	151.0	2.6	143.9	2.8
1333	4	241	4	203	4	174.6	2.8	158.0	2.5	150.3	2.6	140.1	2.7
1343	4	246	4	203	4	170.8	2.8	155.5	2.4	143.3	2.5	136.3	2.7

1353	4	237	4	200	4	171.4	2.8	154.9	2.4	141.8	2.5	137.4	2.7
1363	4	238	4	190	4	169.5	2.8	149.9	2.4	141.4	2.5	136.9	2.7
1373	4	235	4	194	4	166.4	2.7	151.6	2.4	142.1	2.5	130.3	2.6
1383	4	230	4	188	4	160.2	2.7	149.2	2.4	134.5	2.4	124.1	2.5
1393	4	228	4	191	4	161.4	2.7	143.6	2.3	136.9	2.4	131.2	2.6
1403	4	222	3	189	4	157.8	2.7	144.4	2.3	132.9	2.4	126.0	2.6
1413	4	218	3	182	4	156.4	2.6	143.3	2.3	130.4	2.3	127.3	2.6
1423	4	215	3	185	4	155.2	2.6	137.4	2.2	131.9	2.4	124.4	2.5
1433	4	211	3	172	3	149.6	2.5	139.6	2.3	128.6	2.3	122.9	2.5
1443	4	211	3	176	4	149.3	2.5	133.3	2.2	124.0	2.3	114.3	2.4
1453	4	205	3	167	3	149.4	2.5	133.6	2.2	121.6	2.2	114.8	2.4
1463	4	201	3	171	3	141.3	2.4	130.2	2.1	120.6	2.2	113.1	2.4
1473	4	198	3	165	3	140.6	2.4	127.9	2.1	117.9	2.2	113.9	2.4
1483	4	198.9	2.9	159.9	2.8	142.7	2.2	125.7	1.9	118.1	1.9	111.9	2.1
1493	4	189.3	2.8	162.5	2.9	135.9	2.1	122.2	1.8	114.0	1.9	106.4	2.0
1503	4	189.7	2.8	159.5	2.8	133.8	2.1	120.2	1.8	113.4	1.9	110.6	2.0
1513	4	186.9	2.7	155.7	2.8	134.5	2.1	121.5	1.8	111.5	1.9	107.5	2.0
1523	4	188.8	2.8	155.7	2.8	130.7	2.1	122.2	1.8	109.8	1.8	103.4	1.9
1533	4	185.1	2.7	155.8	2.8	129.2	2.0	118.4	1.8	105.2	1.8	101.4	1.9
1543	4	178.8	2.6	146.9	2.7	128.3	2.0	113.8	1.7	106.1	1.7	99.3	1.9
1553	4	176.9	2.6	150.1	2.8	125.3	2.0	112.8	1.7	104.2	1.8	97.7	1.9
1563	4	173.6	2.6	144.2	2.7	123.6	2.0	109.9	1.7	103.8	1.8	98.1	1.9
1573	4	173.9	2.6	141.1	2.6	121.1	1.9	109.4	1.7	100.6	1.7	95.3	1.8
1583	4	169.7	2.5	139.8	2.6	118.6	1.9	109.0	1.7	99.1	1.7	93.6	1.8
1593	4	169.5	2.5	138.7	2.6	120.0	1.9	108.5	1.7	97.9	1.7	91.8	1.8
1603	4	163.0	2.5	136.7	2.6	116.9	1.9	105.8	1.6	95.7	1.7	89.7	1.8
1613	4	158.3	2.4	133.5	2.5	115.2	1.9	104.1	1.6	95.3	1.7	90.0	1.8
1623	4	159.2	2.4	132.3	2.5	112.7	1.8	103.7	1.6	91.7	1.6	89.5	1.8

1633	4	152.1	2.3	128.3	2.4	113.2	1.9	101.3	1.6	93.5	1.6	93.3	1.8
1643	4	152.9	2.2	129.8	2.3	108.2	1.7	97.9	1.5	90.8	1.5	84.2	1.6
1653	4	150.2	2.2	130.3	2.4	109.5	1.7	98.3	1.5	90.4	1.5	85.9	1.6
1663	4	151.9	2.2	128.0	2.3	106.2	1.7	97.4	1.5	90.7	1.5	86.8	1.7
1673	4	149.6	2.2	125.5	2.3	108.4	1.7	98.3	1.5	90.1	1.5	86.9	1.7
1683	4	152.6	2.3	125.3	2.3	105.7	1.7	95.1	1.5	89.1	1.5	85.7	1.6
1693	4	148.9	2.2	123.3	2.3	102.1	1.6	93.4	1.4	86.9	1.5	82.3	1.6
1703	4	145.1	2.2	120.8	2.2	101.2	1.6	90.3	1.4	85.2	1.5	81.4	1.6
1716	4	142.7	2.1	117.5	2.2	99.8	1.6	91.1	1.4	83.5	1.4	79.7	1.6
1724	4	138.9	2.1	116.5	2.2	96.3	1.6	88.1	1.4	82.5	1.4	77.8	1.5
1734	4	136.9	2.1	111.4	2.1	92.9	1.5	87.8	1.4	78.9	1.4	76.6	1.5
1744	4	132.8	2.0	114.8	2.2	92.5	1.5	85.9	1.3	78.4	1.4	77.5	1.5
1754	4	133.2	2.0	109.2	2.0	90.4	1.4	83.0	1.3	77.9	1.3	74.5	1.4
1764	4	133.6	1.9	106.4	1.9	89.9	1.4	82.2	1.2	76.2	1.3	72.7	1.3
1774	4	130.5	1.8	108.0	1.9	90.2	1.4	81.2	1.2	76.2	1.2	70.9	1.3
1784	4	127.4	1.8	102.1	1.8	89.7	1.4	82.0	1.2	75.4	1.2	70.1	1.3
1794	4	126.4	1.8	104.1	1.8	86.1	1.3	79.3	1.2	74.8	1.2	68.3	1.2
1804	4	123.8	1.9	102.0	1.9	84.8	1.4	79.3	1.2	73.7	1.3	69.6	1.3
1814	4	123.3	1.8	102.0	1.9	87.1	1.4	79.4	1.2	72.6	1.3	67.3	1.3
1824	4	119.1	1.6	98.0	1.7	84.2	1.3	75.0	1.1	70.4	1.1	66.8	1.2
1834	4	116.9	1.7	94.8	1.7	81.4	1.3	74.5	1.1	67.0	1.1	63.4	1.2
1844	4	115.0	1.7	93.4	1.7	80.4	1.2	70.4	1.1	67.4	1.1	63.6	1.2
1854	4	113.3	1.6	94.5	1.7	79.6	1.2	72.2	1.0	67.0	1.1	63.6	1.2
1864	4	112.9	1.6	90.8	1.6	78.2	1.3	72.5	1.1	68.0	1.1	65.6	1.2
1874	4	111.8	1.6	94.3	1.7	80.3	1.3	72.8	1.1	69.7	1.1	65.3	1.2
1884	4	111.6	1.6	90.3	1.6	80.5	1.3	72.4	1.1	69.3	1.1	67.5	1.2
1894	4	108.0	1.6	92.9	1.7	81.0	1.3	73.8	1.1	69.2	1.1	65.5	1.2
1904	4	108.7	1.6	91.0	1.6	81.7	1.3	75.7	1.1	69.3	1.1	67.8	1.2

1914	4	111.0	1.6	94.4	1.7	78.6	1.2	72.5	1.1	68.1	1.1	65.8	1.0
1924	4	107.5	1.6	95.6	1.7	78.3	1.2	70.6	1.1	67.2	1.1	64.6	1.2
1934	4	107.1	1.6	91.0	1.7	76.6	1.2	69.2	1.0	65.6	1.1	62.3	1.2
1944	4	106.1	1.6	87.8	1.6	74.1	1.2	69.2	1.0	64.2	1.1	61.7	1.1
1954	4	106.7	1.6	88.5	1.6	76.0	1.2	70.3	1.1	67.1	1.1	64.4	1.2
1964	4	104.0	1.5	87.3	1.6	79.9	1.3	71.6	1.1	67.3	1.1	66.3	1.2
1974	4	105.5	1.6	91.2	1.7	79.2	1.2	71.4	1.1	67.8	1.1	65.3	1.2
1984	4	104.2	1.6	89.4	1.6	75.9	1.2	69.6	1.1	65.8	1.1	65.3	1.2
1994	4	101.2	1.5	85.1	1.6	75.7	1.2	67.4	1.0	62.3	1.1	60.4	1.1
2004	4	100.2	1.5	85.1	1.6	73.1	1.1	68.3	1.0	65.6	1.1	60.5	1.1
2014	4	100.2	1.5	86.3	1.6	76.1	1.2	68.1	1.0	63.3	1.1	62.2	1.2
2024	4	99.2	1.5	85.0	1.6	73.5	1.2	68.4	1.0	62.8	1.1	61.9	1.2
2034	4	97.8	1.5	80.6	1.5	73.5	1.2	66.0	1.0	63.1	1.1	59.4	1.1
2044	4	95.9	1.4	82.7	1.5	70.3	1.1	65.2	1.0	59.9	1.0	59.4	1.1
2054	4	94.9	1.4	80.6	1.5	69.6	1.1	63.4	1.0	59.0	1.0	57.8	1.1
2064	4	91.8	1.4	79.7	1.5	67.9	1.1	61.0	0.9	56.3	1.0	56.3	1.1
2074	4	89.0	1.4	75.5	1.4	65.2	1.1	60.1	0.9	56.9	1.0	53.6	1.0
2084	4	88.6	1.4	74.8	1.4	66.0	1.1	59.7	0.9	57.4	1.0	56.6	1.1
2094	4	90.0	1.4	79.5	1.5	68.3	1.1	64.3	1.0	57.8	1.0	57.3	1.1
2104	4	94.0	1.4	76.7	1.5	68.0	1.1	64.2	1.0	61.3	1.1	59.5	1.2
2114	4	93.1	1.5	76.7	1.6	69.5	1.2	64.1	1.1	60.9	1.1	57.6	1.2
2124	4	90.5	1.5	80.4	1.7	67.5	1.2	61.7	1.0	59.4	1.1	58.2	1.2
2134	4	92.4	1.5	75.8	1.6	68.1	1.2	61.4	1.0	58.8	1.1	57.3	1.2
2144	4	87.5	1.4	72.2	1.5	66.7	1.2	59.4	1.0	57.1	1.1	53.5	1.1
2154	4	86.6	1.4	70.9	1.5	61.5	1.1	57.4	1.0	54.3	1.0	50.2	1.1
2164	4	87.2	1.4	72.9	1.5	62.6	1.1	58.8	1.0	57.7	1.1	51.2	1.1
2174	4	85.9	1.4	73.7	1.5	63.8	1.1	57.8	1.0	56.0	1.1	52.5	1.1
2184	4	81.1	1.3	68.6	1.5	60.6	1.1	56.6	1.0	52.5	1.0	49.1	1.1

2194	4	82.4	1.4	67.8	1.5	58.0	1.1	52.5	0.9	49.7	1.0	45.7	1.0
------	---	------	-----	------	-----	------	-----	------	-----	------	-----	------	-----

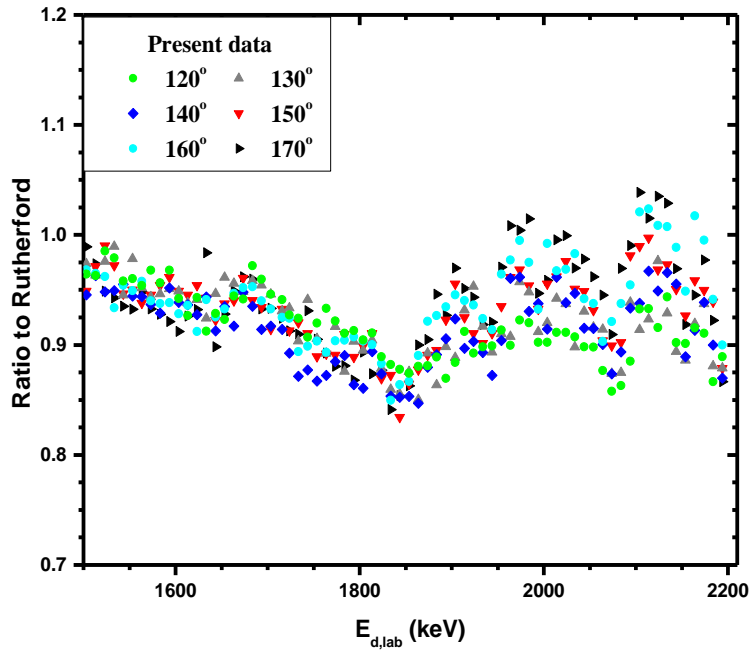


Figure 4.39 Ratio to Rutherford of the differential cross section values of the deuteron elastic scattering on ^{nat}Si for the high energies (1500 – 2200 keV) for all the measured angles.

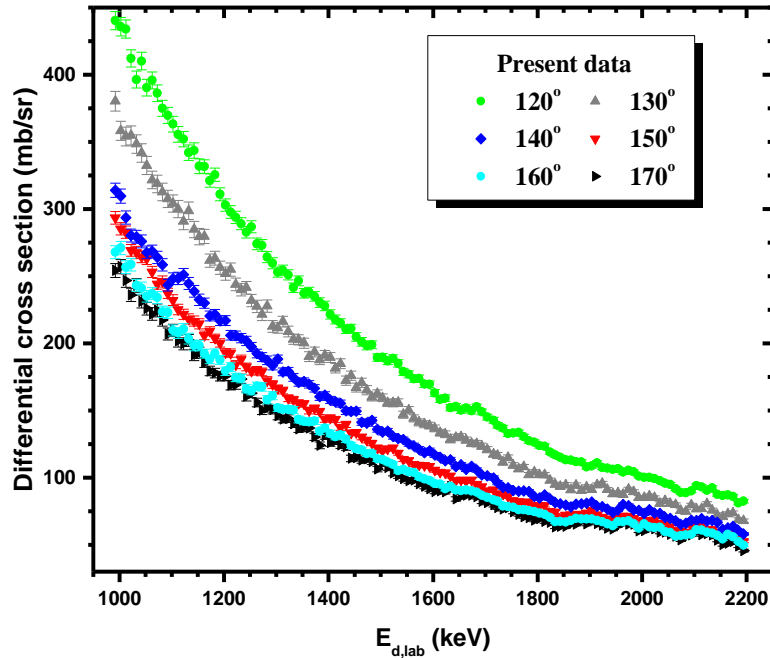
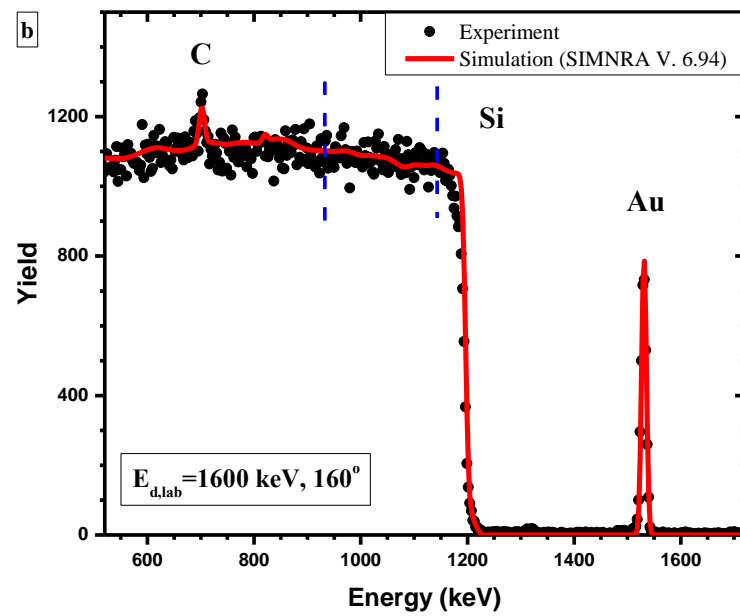
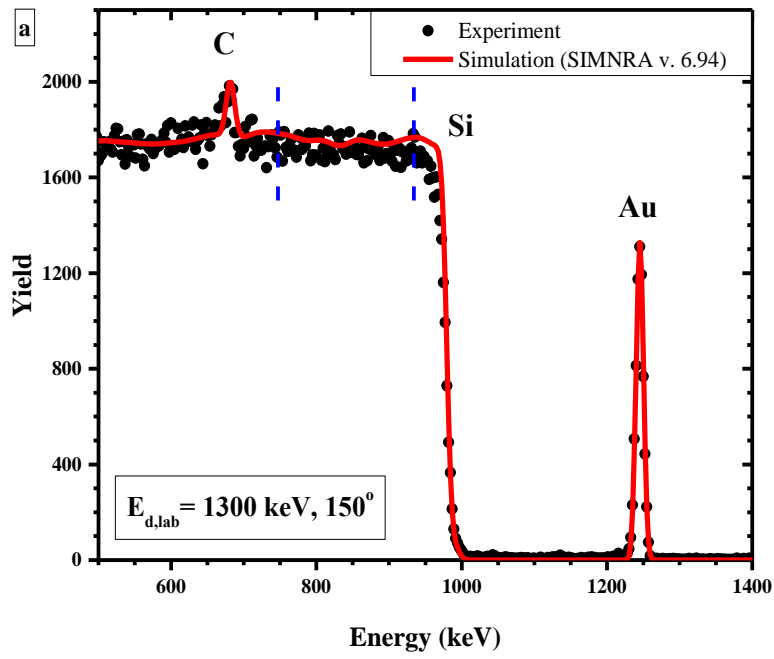


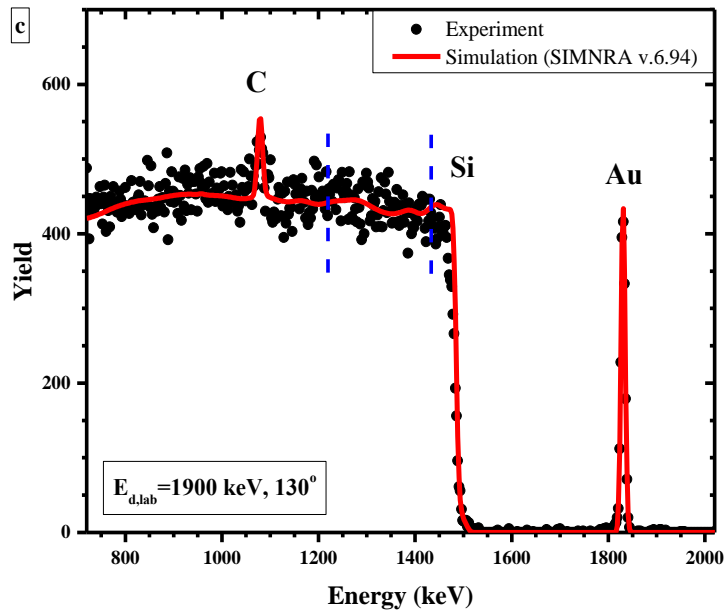
Figure 4.40 Differential cross section values (mb/sr) of the $^{nat}\text{Si}(d,d_0)^{nat}\text{Si}$ elastic scattering in the energy range 1060-2200 keV for all the measured angles.

4.8.4 Benchmarking of the obtained $^{nat}\text{Si}(d,d_0)^{nat}\text{Si}$ differential cross section values

For the validation of the determined cross section values for the deuteron elastic scattering on ^{nat}Si , deuteron spectra were acquired by irradiating a thick Si [111] polished crystalline wafer with a Au layer on top at four energies (1300, 1600, 1900, 2200 keV) and for four scattering angles (130°, 140°, 150° and 160°). The first step of the benchmarking procedure included the accurate description of the target using the $E_{d,\text{lab}}=1300$ keV spectrum at 130° with the implementation of Rutherford cross section values for both Au and ^{nat}Si since in this case the deuteron elastic scattering on silicon follows the Rutherford formula (within ~4%). Thus, by performing a fit in the $Q \times \Omega$ product in the Si edge, the thickness of gold was determined. Subsequently, the experimental spectra at 1300 keV (for the rest of the angles), 1600 keV and 1900 keV were simulated with the $Q \times \Omega$ product being fitted to the integral of the Au peak (differences between simulated and experimental counts in the Au peak were always below 1%) at every deuteron energy/scattering angle combination. The results of such a procedure are visible in Figs. 4.41 a-c along with the corresponding peak/edge identification. As it is shown in the graphs no background subtraction due to the d-NRA levels was needed. However, the situation for higher energies deteriorated, as visible in Fig. 4.42, for the deuteron energy of 2200 keV and 160°, since new levels were excited

under the silicon elastic scattering edge and thus no benchmarking results were acquired for deuteron energies higher than 1900 keV. Even so, as can be seen in Figs. 4.41 a-c, for deuteron energies up to 1900 keV, the reproduction of the experimental spectra using the obtained cross section values was very good, within ~4-5% over an integrated window of ~200 keV (~90 channels) below the surface of silicon. The results of the benchmarking procedure are shown in Table 4.8. As reported in the table, the maximum difference between the simulated and the experimental counts within the integrated window was found for the deuteron energy of 1600 keV at 140°. However, these numbers do not indicate the necessity of renormalizing the obtained cross section values since no coherent behavior was revealed. Moreover, it should be pointed out that even though the narrowest channel ([111]), regarding the geometry of the crystal, was carefully selected in order to lead to a rapid de-channeling of the beam with a minor misalignment, small channeling perturbations were still visible near the silicon surface. In order to avoid any significant channeling contribution, the integrated window was selected well below the narrow, distorted area. However, the appearance of channeling perturbations does not constitute the choice of the certain target inadequate, because the implementation of a silicon compound containing a lower than silicon Z element (e.g. SiO₂, SiB₃) would have created a background under the silicon edge due to the d-NRA induced channels, whereas if a compound containing a heavier Z element than silicon (e.g. Si₂Br₆, SiCl₄) was implemented, then a background would exist below the silicon edge due to the deuteron elastic scattering on the heavier Z element. Alternatively, an unpolished silicon wafer could have also been employed for the benchmarking measurements.





Figures 4.41 a-c Experimental and simulated benchmarking spectra from a polished thick crystalline Si [1 1 1] wafer target with a thin Au layer on top, acquired at (a) 150° and 1300 keV, (b) 160° and 1600 keV and (c) 130° and 1900 keV. The integrated window used in the benchmarking procedure is marked in the graphs and it was ~230 keV (~90 channels).

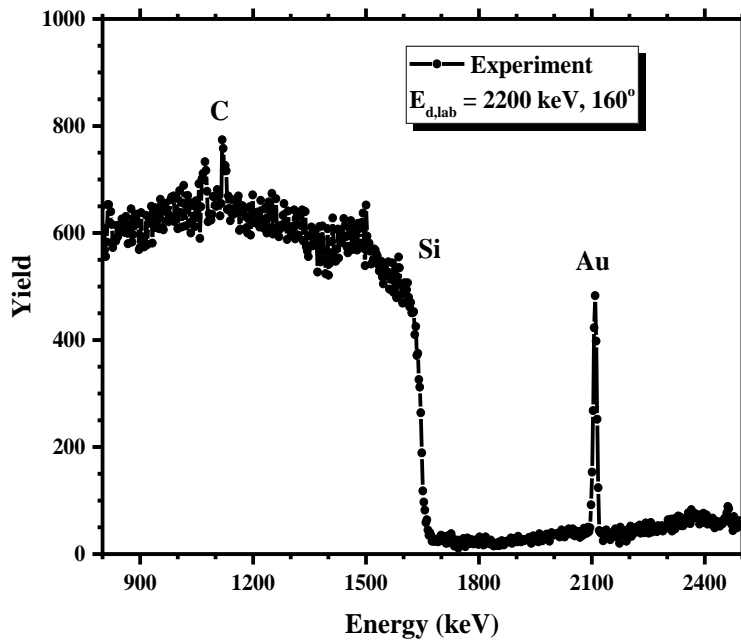


Figure 4.42 Experimental benchmarking spectrum at 2200 keV and 160°. Due to excited d-NRA levels under the Au peak and the Si edge no results could be obtained for energies higher than 1900 keV.

Table 4.8 Differences (in %) between the simulated and the experimental counts within the integrated window for every beam energy/scattering angle combination. The negative numbers correspond to lower value of the integral for the simulated spectrum than the integral of the experimental spectrum whereas the positive ones correspond to higher integral for the simulated spectrum than the integral of the experimental spectrum.

Energy (keV)	130°	140°	150°	160°
1300	1.2	-1.5	2.3	4.1
1600	-1.3	-5.4	1.8	0.2
1900	-0.6	-2.5	1.1	1.9

Chapter 5

The study of the $^{nat}\text{O}(d,d_0)^{nat}\text{O}$ elastic scattering

In the present chapter the deuteron elastic scattering on oxygen is discussed. Firstly, the differential cross section measurements are described, subsequently the benchmarking results along with several complications that occurred are presented, and in the final section, the theoretical investigation through the implementation of the code developed by Dr. A. F. Gurbich, implementing the R-matrix theory along with optical model calculations, is analyzed.

The deuteron elastic scattering on oxygen was accompanied by a theoretical investigation since oxygen is the most important element in applications compared to the studied ones.

5.1 Cross section measurements for the $^{nat}\text{O}(d,d_0)^{nat}\text{O}$ elastic scattering

The $^{nat}\text{O}(d,d_0)^{nat}\text{O}$ was studied in the energy range of 1500 – 2500 keV with steps of 10-20 keV and for the scattering angles of 130°, 140°, 150°, 160° and 170°. The level scheme of the formed compound nucleus $^{18}\text{F}^*$ for the most abundant isotope of natural oxygen, that is ^{16}O , is illustrated in Fig 5.1. These levels were retrieved from [90] and [91] and de-excite via the emission, of not only deuterons, but a variety of particles in the exit channel, such as protons (e.g. at the ground and at the first excited state of the residual nucleus), neutrons and alpha particles. Since such levels, with unknown widths and tentative J^π assignments exist in the studied energy region, the energy steps in the measurements were variable and depended on the existence of levels in the compound nucleus near the impinging energy in order to accurately describe possible resonances in the structure of the obtained cross section values.

The implemented target was a Na_2HPO_4 layer on top of a carbon foil, along with a gold layer on top. This specific powder was selected due to the high amount of oxygen within it. A typical spectrum is shown in Fig. 5.2 for the deuteron energy of 2500 keV and for 150°. The parasitic contribution of nitrogen, caused by the mixture of soap used in the manufacturing of self-supporting carbon foils, was evident in the experimental spectra via the elastic scattering, as well as the reaction channels, shown in Fig. 5.2. However, the multiple peaks caused by nitrogen did not impede the peak integration/fitting procedure. Moreover, a small peak was visible in the left side of the main Au peak and was attributed to the existence of Au in the back side of the target, since the energy difference was only ~40 keV, equal to the total target thickness. The possibility

of such a peak being a reaction channel of a different isotope/element was excluded, since it presented the same kinematic behavior with the main peak of gold as the beam energy was changing; and since the elastic scattering of another isotope/element present in the target was not anticipated at this energy, the peak was solely attributed to gold being situated in the back side of the target. This was probably caused by a micro fracturing of the underlying thin carbon foil prior to the gold evaporation. Thus, the integration and fitting (when necessary) of both peaks was performed in order to acquire the total counts attributed to the deuteron elastic scattering on gold.

In the present work, due to the fact that the theoretical evaluation for $^{16}\text{O}(d,d_0)^{16}\text{O}$ reached up to 1980 keV, it was used for the calculation of the final differential cross section values via the following equation:

$$\left(\frac{d\sigma}{d\Omega}\right)_{\theta,E}^{nat_O} = \left(\frac{d\sigma}{d\Omega}\right)_{\theta,E'}^{Au} \times \frac{Y_{nat_O}}{Y_{Au}} \times F_{\theta} \quad (5.1)$$

The factor F_{θ} was a scaling factor determined from the SigmaCalc evaluation (2012) at each angle for beam energies between 1500 keV and 1980 keV, replacing the target thickness ratio calculation in the determination of the final cross section values. More specifically, the analytical procedure was initiated with the determination of the excitation function for each scattering angle, that is the first two terms in Eq. 5.1. Subsequently, each of the 27 experimental yield ratios that were measured in the energy range 1500-1980 keV, were used for the calculation of a scaling factor, in order for the agreement between the evaluated differential cross section value and the excitation function value to be equal at each beam energy. The mean value of these 27 scaling factors was calculated at each scattering angle. These mean values are in principle expected to be identical for all scattering angles, since they mainly correspond to the target thickness ratio. These values are tabulated in Table 5.1 along with the corresponding uncertainties, as determined by the statistical analysis. As displayed in Table 5.1, they are all in excellent agreement within $\pm 1\sigma$, except for the scaling factor attributed to the scattering angle of 130° , which agrees within $\pm 2\sigma$ with the one for 140° . This specific scaling factor value is excluded from the comparison, since the mathematical procedure for determining the differential cross section values at 130° was slightly different, for reasons explained below. Even though the agreement for the rest of the values is within $\pm 1\sigma$, slight differences are observed in the mean values (a slowly decreasing trend towards steeper backscattering angles is evident) and hence, it was deemed more appropriate to implement a different scaling factor for each angle (namely the values reported in Table 5.1), rather than to adopt a mean value of the scaling factor for all scattering angles. These slight differences may also be attributed to the inherent behavior of the evaluated differential cross section datasets. It should also be noted here that they also include the uncertainties in the integration procedure for each scattering angle (namely the background selection and the limits of the peak during the integration procedure).

At the scattering angle of 130° and for lower energies, the peak of the $^{197}\text{Au}(d,d_0)^{197}\text{Au}$ elastic scattering had a rather extended tail towards the left side. Thus, in order to avoid integrating such a peak, as this integration is highly user-dependent and it would have inserted a higher uncertainty

in the final values, the integration of the elastic gold peak at 160° was used instead. Therefore, a term needed to be inserted in Eq. 5.1 for the scattering angle of 130° in order to account for the different solid angle subtended by the two detectors set at 130° and 160°. This process was allowed only because the deuteron elastic scattering on gold follows the Rutherford formula and thus no anomalies are expected in the theta angular dependence. Thus, the differential cross section values for the scattering angle of 130° were calculated using the following equation:

$$\left(\frac{d\sigma}{d\Omega}\right)_{130^\circ,E}^{natO} = \left(\frac{d\sigma}{d\Omega}\right)_{160^\circ,E'}^{Au} \times \frac{Y_{oxyg,130^\circ}}{Y_{Au,160^\circ}} \times F_\theta \times \frac{\Omega_{160^\circ}}{\Omega_{130^\circ}} \quad (5.2)$$

Where the ratio of the solid angles was calculated using the following formula:

$$\frac{\Omega_{160^\circ}}{\Omega_{130^\circ}} = \frac{\left(\frac{d\sigma}{d\Omega}\right)_{130^\circ,E}^{Au}}{\left(\frac{d\sigma}{d\Omega}\right)_{160^\circ,E}^{Au}} \times \frac{Y_{Au,160^\circ}}{Y_{Au,130^\circ}} \quad (5.3)$$

In order to calculate the solid angle ratio, eight energy values were used, namely the higher ones in order for the peak separation to be enhanced. The obtained value was $\Omega_{160^\circ}/\Omega_{130^\circ} = 1.248 \pm 0.023$, yielding a relative uncertainty of 1.8%, originating from the integration of the corresponding Au peaks. This uncertainty was also included in the total uncertainty budget for the scattering angle of 130°. Such a different mathematical approach for the determination of the differential cross section values at 130° might have affected the determination of the scaling factor value at this angle and thus the comparison of this specific value with the ones for the rest of the scattering angles is not necessarily correct, even though the solid angle ratio determination procedure was performed prior to the scaling factor determination. One possible reason for the discrepancy at 130° could also be, as mentioned above, the inherent nature of the existing evaluation, meaning the different weights used for each scattering angle and the scattering angles of the experimental datasets that were taken into account during the evaluation procedure.

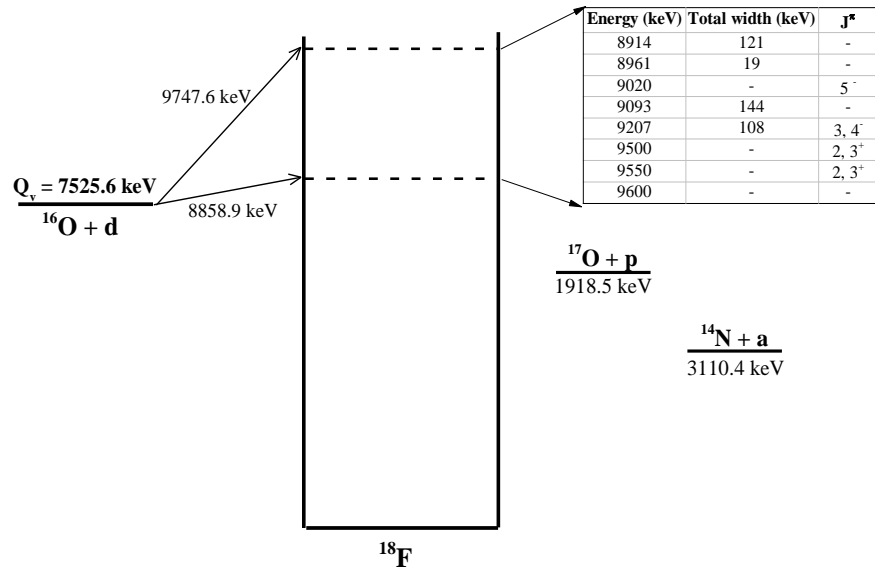


Figure 5.1 Level scheme of the $^{16}\text{O}+d$ system in the CM reference frame.

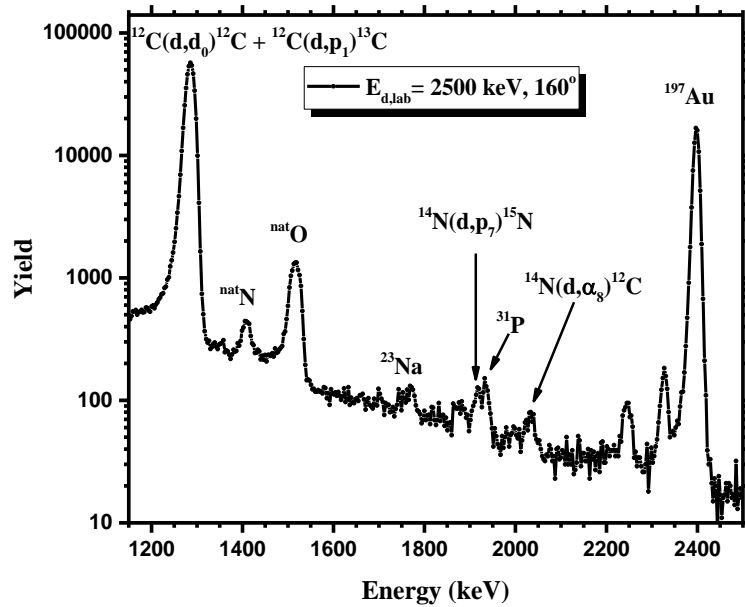


Figure 5.2 Typical experimental spectrum of the used target consisting of a Na_2HPO_4 layer on top of a carbon foil along with a gold layer on top acquired at 2500 keV and for 160° .

Table 5.1 Values of the scaling factor for each scattering angle. The uncertainties for each measured angle, as resulted from the statistical analysis, are also reported.

Scattering angle	Scaling factor	Relative uncertainty (%)
130°	0.275 ± 0.009	3.3
140°	0.248 ± 0.014	5.7
150°	0.237 ± 0.009	3.8
160°	0.231 ± 0.008	3.5
170°	0.227 ± 0.011	4.9

5.1.1 Target characterization

The target thickness ratio calculation was thus not necessary for the determination of the final cross section values, as shown in Eq. 5.1. However, for the calculation of the energy to which the cross-section values were attributed, the determination of the energy loss inside the target was mandatory, as discussed in the previous chapter. Thus, for the target characterization, proton spectra were acquired at the energies of 1050 and 1470 keV and for the scattering angles of 160° and 170°. For the simulation of the obtained spectra Rutherford cross section values were used for the proton elastic scattering on Au and Cl, whereas for proton elastic scattering on ^{nat}C [82], ^{nat}N [26], ^{nat}O [84], ²³Na [85] and ³¹P [85] the evaluated datasets of SigmaCalc 2.0 were implemented via the SIMNRA code. Following this procedure, the target was analyzed and the energy loss and energy straggling values were subsequently calculated at every deuteron beam energy.

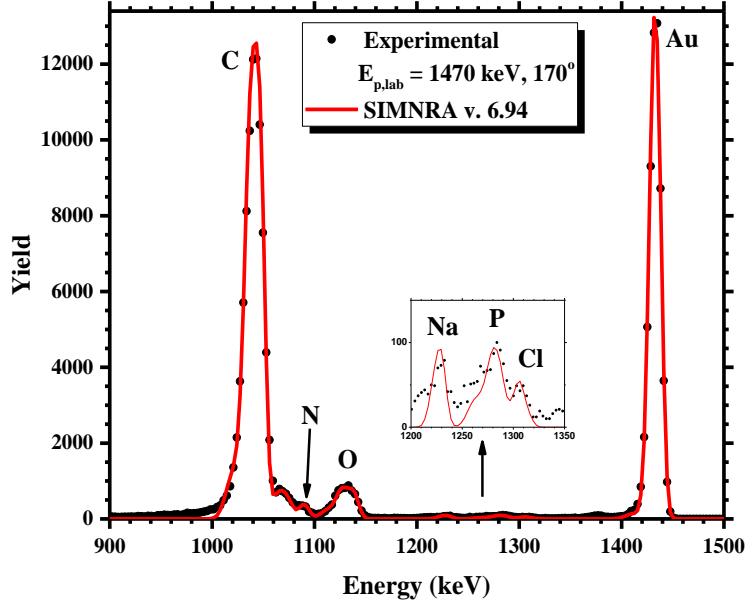


Figure 5.3 Experimental and simulated proton spectra acquired for the target characterization process at the energy of 1470 keV and for 170° along with the peak identification.

5.1.2 Uncertainties

The statistical uncertainty originating from the integration/fitting procedure was below 4%, a value slightly higher than usual, attributed to the proximity of the oxygen and nitrogen peaks in the experimental spectra and due to the double Au peak. The uncertainty of each scaling factor is reported in Table 5.1 and these values were inserted in the final cross section values calculation. Especially for the scattering angle of 130° , the ratio of the solid angle subtended by the 130° and 160° detectors inserted an extra uncertainty of 1.8%. Thus, the combined statistical uncertainty for 130° did not exceed ~6.5%, for 140° ~7%, for 150° and 160° ~5%, and for 170° ~6.5%.

For the systematic uncertainties, their origin was attributed once again to the differences between compiled and experimental stopping power data and their corresponding values were ~2.8% for oxygen and ~3.6% for gold, as obtained from the SRIM website.

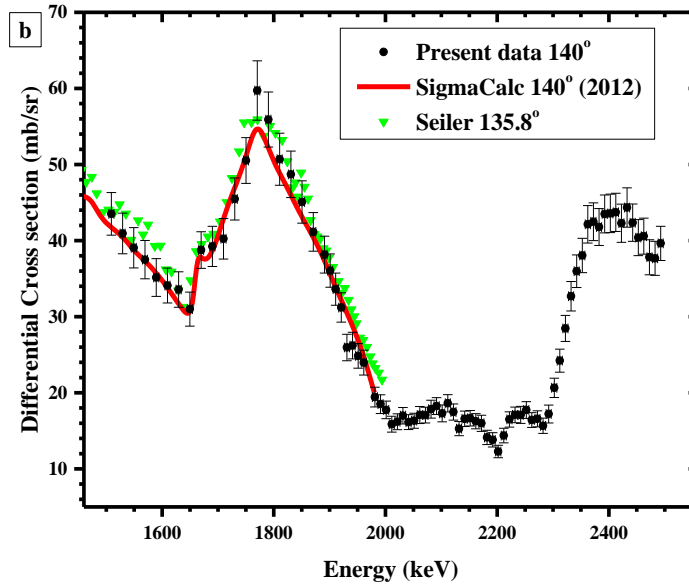
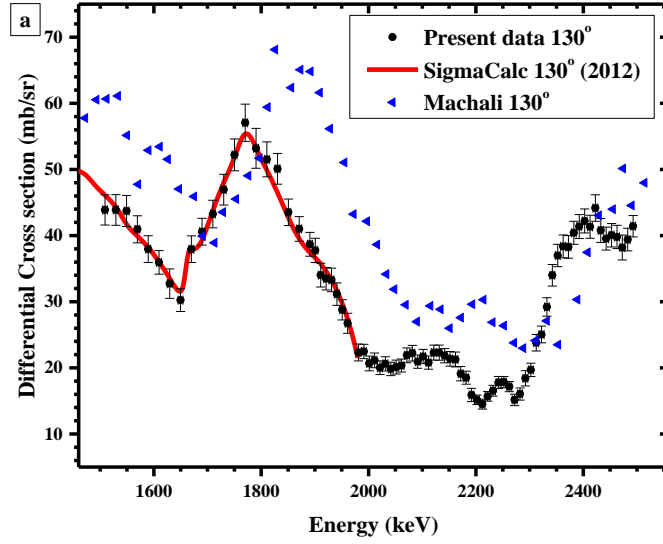
The uncertainties concerning the beam energy calculation included the accelerator ripple (~2 keV) and the energy straggling inside the determined target (4.6 keV for all energies).

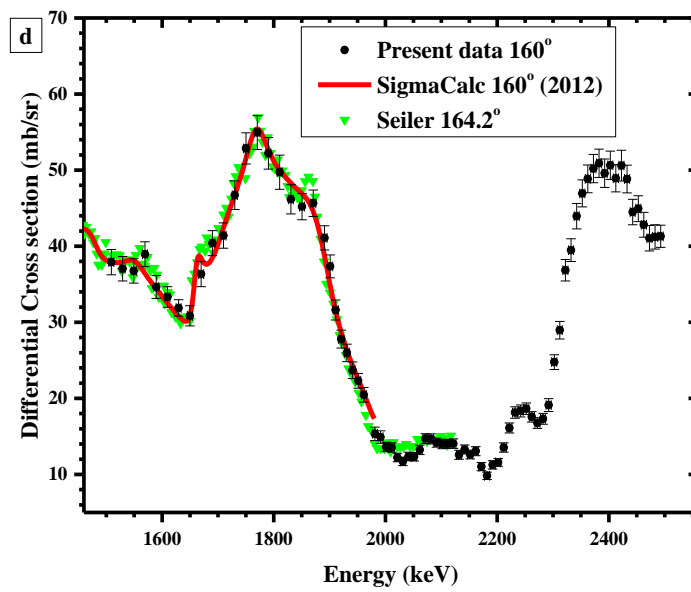
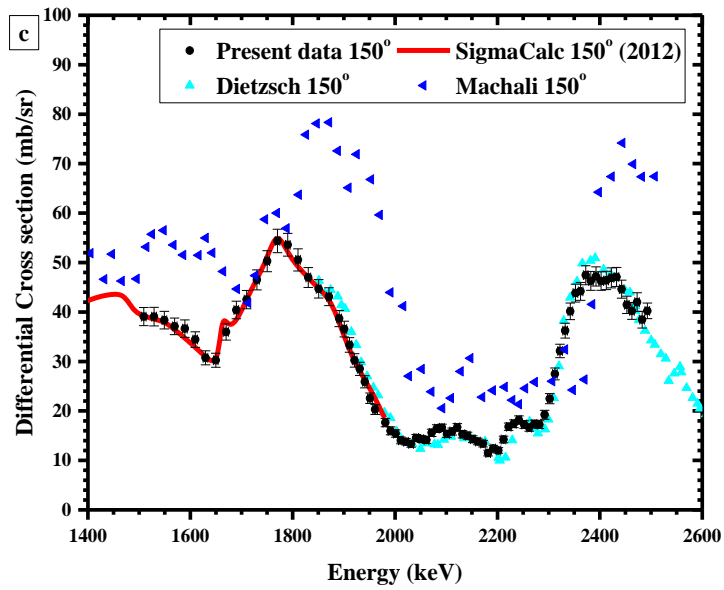
5.1.3 Results and Discussion

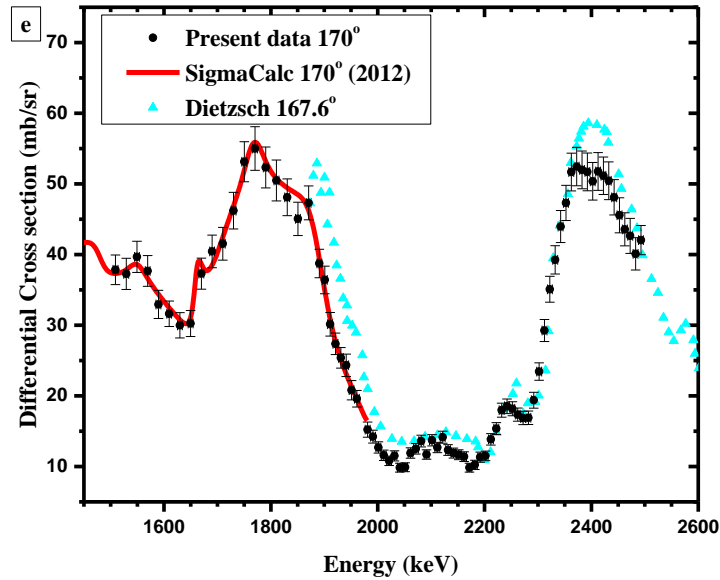
The final cross section values of the deuteron elastic scattering on oxygen for the energy range of 1500-2500 keV and for the scattering angles of 130°, 140°, 150°, 160° and 170° are presented in graphical form in Figs. 5.4a-e and in tabulated form in Table 5.2. In Figs. 5. 4a-e the statistical uncertainties in the differential cross section values are included, as well as the corresponding ones for the energy values, but the latter are not visible due to the adopted scale. The preexisting data from literature were added in every figure for comparison purposes.

As shown in the figures, the obtained cross section is dominated by a wide minimum and a wide maximum in the corresponding structure. The shape of the presented cross sections could be attributed to the superposition of the energy levels of the compound nucleus $^{19}\text{F}^*$, with energies 8.91 MeV, 8.96 MeV, 9.09 MeV and 9.20 MeV, visible in the level scheme (Fig. 5.1). Concerning the comparison with the preexisting data, a similar shape, but shifted up and right was observed in the data by Machali et al. [28]. It should be noted here that these datasets were not available in IBANDL or EXFOR and thus the values were digitized directly from the publication. Since the corresponding figures were rather small in the manuscript, the digitization might have included errors. In any case, the shape seems similar. Concerning the data by Seiler et al. [32] there seems to be an agreement within errors with the present values, which is expected, since the evaluation included the Seiler et al. dataset. However, a clear energy shift is observed between the evaluated data by SigmaCalc (and accordingly the obtained data from the present work) and the data by Dietzsch et al. [29], despite the overall excellent agreement, although the origin of this shift has not become clear from the corresponding publication.

In Figure 5.5, where the ratio to Rutherford of the obtained cross section values for all measured angles is displayed, it is observed that for the two maxima, namely at ~1800 keV and at ~2400 keV, the most backward angles displayed higher cross section values whereas for the minimum, at ~2200 keV, the behavior was the opposite with the most forward angles displaying higher cross sections.







Figures 5.4 a-e Differential cross section values (mb/sr) of the $^{nat}O(d,d_0)^{nat}O$ in the energy range of $E_{d,lab}=1500$ -2500 keV for the scattering angles of 130° , 140° , 150° , 160° and 170° along with data from the literature.

Table 5.2 Differential cross section values of the deuteron elastic scattering on ^{nat}O for the energy range of 1500-2500 keV and for the scattering angles of 130° , 140° , 150° , 160° and 170° . The statistical uncertainties are included for the differential cross section values while for the beam energies the accelerator ripple and the energy straggling in the target have been taken into account.

$E_{d,lab}$ (keV)	$\delta E_{d,lab}$ (keV)	$d\sigma/d\Omega$ (mb/sr)									
		130°		140°		150°		160°		170°	
1509	5	43.9	2.3	43.5	2.8	39.1	1.8	37.9	1.7	37.8	2.1
1529	5	43.9	2.3	40.9	2.7	39.1	1.9	37.0	1.6	37.3	2.2
1549	5	43.7	2.4	39.1	2.6	38.4	1.8	36.8	1.6	39.7	2.2
1569	5	40.9	2.0	37.5	2.5	37.1	1.7	38.9	1.6	37.7	2.2
1589	5	37.9	2.0	35.1	2.5	36.6	1.8	34.6	1.5	32.9	2.0
1610	5	36.0	1.8	34.1	2.3	34.4	1.6	33.3	1.4	31.6	1.8
1630	5	32.7	2.2	33.6	2.3	30.7	1.4	31.9	1.1	30.0	1.8
1650	5	30.2	1.7	31.0	2.2	30.3	1.4	30.9	1.3	30.2	1.8
1670	5	37.9	2.0	38.8	2.4	36.0	1.6	36.3	1.7	37.3	2.2

1690	5	40.6	2.0	39.2	2.6	40.4	1.8	40.4	1.6	40.4	2.3
1710	5	43.3	2.1	40.2	2.7	42.5	1.8	41.4	1.7	41.5	2.3
1730	5	46.9	2.3	45.5	2.8	46.5	2.0	46.7	1.9	46.2	2.6
1750	5	52.2	2.4	51	3	50.3	2.1	52.9	2.0	53.1	2.8
1770	5	57.1	2.8	60	4	54.4	2.4	54.9	2.2	55	3
1790	5	53.2	3.0	56	4	53.6	2.3	52.2	2.1	52.3	2.9
1810	5	51.5	2.6	51	3	50.5	2.3	49.7	2.2	50.5	2.9
1831	5	50.1	2.3	49	3	47.0	2.0	46.2	1.9	48.1	2.6
1851	5	43.5	2.0	45.1	2.8	44.7	1.9	45.2	1.7	45.1	2.4
1871	5	41.0	1.9	41.2	2.5	43.1	1.8	45.7	1.7	47.3	2.4
1891	5	38.7	1.8	38.2	2.4	38.7	1.6	41.1	1.6	38.7	2.0
1901	5	37.8	1.8	36.1	2.2	36.5	1.6	37.3	1.5	36.4	1.9
1911	5	34.0	1.8	33.6	2.1	33.3	1.5	31.6	1.3	30.1	1.7
1921	5	33.5	1.7	31.2	1.9	30.2	1.4	27.8	1.2	27.4	1.5
1931	5	33.3	1.8	26.0	1.7	28.5	1.3	26.0	1.2	25.4	1.5
1941	5	31.1	1.7	26.2	1.8	25.9	1.2	23.7	1.1	24.3	1.6
1951	5	28.8	1.5	24.8	1.6	22.6	1.1	22.3	1.0	20.8	1.4
1961	5	26.7	1.5	24.0	1.6	20.3	1.0	20.5	1.0	19.6	1.2
1981	5	22.3	1.3	19.4	1.3	17.6	0.8	15.3	0.9	15.2	1.1
1991	5	22.5	1.1	18.5	1.2	16.0	0.8	14.9	0.8	14.2	0.9
2001	5	20.7	1.1	17.8	1.2	15.4	0.7	13.6	0.6	12.7	0.8
2011	5	21.1	1.1	15.9	1.0	14.0	0.7	13.5	0.6	11.6	0.7
2021	5	20.0	1.0	16.2	1.0	13.8	0.6	12.2	0.6	10.8	0.7
2031	5	20.6	1.1	17.0	1.1	13.3	0.6	11.7	0.5	11.5	0.7
2041	5	19.8	1.0	16.1	1.0	14.6	0.7	12.4	0.6	9.8	0.6
2051	5	20.1	1.0	16.3	1.0	14.3	0.7	12.3	0.6	9.9	0.6
2061	5	20.4	1.0	17.1	1.1	14.1	0.7	13.2	0.6	11.9	0.7
2071	5	21.9	1.1	17.1	1.0	15.6	0.7	14.7	0.6	12.5	0.8

2081	5	22.2	1.2	17.8	1.2	16.4	0.8	14.7	0.7	13.6	0.8
2091	5	20.9	1.0	18.3	1.1	16.6	0.7	14.2	0.6	11.7	0.7
2102	5	21.7	1.1	17.3	1.1	15.3	0.7	14.0	0.6	13.7	0.8
2112	5	20.8	1.0	18.6	1.1	15.8	0.7	14.0	0.6	12.7	0.7
2122	5	22.3	1.1	17.5	1.1	16.7	0.8	14.0	0.6	14.2	0.8
2132	5	22.3	1.1	15.3	0.9	15.3	0.7	12.6	0.6	12.3	0.8
2142	5	21.8	1.1	16.6	1.0	15.0	0.7	13.3	0.6	11.9	0.7
2152	5	21.4	1.1	16.7	1.0	14.3	0.7	12.6	0.6	11.7	0.7
2162	5	21.3	1.1	16.3	1.0	13.8	0.7	13.1	0.6	11.4	0.7
2172	5	19.1	1.1	16.0	1.1	13.4	0.7	11.0	0.5	9.8	0.6
2182	5	18.5	1.0	14.1	0.9	11.5	0.6	9.8	0.5	10.2	0.7
2192	5	15.9	1.0	13.8	0.9	12.4	0.6	11.3	0.5	11.3	0.7
2202	5	15.2	0.7	12.3	0.8	12.0	0.6	11.6	0.5	11.5	0.7
2212	5	14.5	0.8	14.4	1.0	14.2	0.7	13.5	0.6	13.8	0.8
2222	5	15.7	0.7	16.5	1.0	16.8	0.7	16.1	0.7	15.4	0.8
2232	5	16.5	0.8	17.1	1.0	17.4	0.8	18.1	0.7	18.0	1.0
2242	5	17.8	0.9	17.1	1.1	18.2	0.8	18.3	0.8	18.5	1.0
2252	5	17.8	0.8	17.7	1.1	17.3	0.8	18.6	0.8	18.2	1.0
2262	5	17.2	0.8	16.4	1.0	16.6	0.7	17.6	0.7	17.3	0.9
2272	5	15.2	0.9	16.6	1.0	17.4	0.8	16.8	0.7	16.9	0.9
2282	5	16.0	0.9	15.7	1.0	17.2	0.8	17.3	0.7	16.9	0.9
2292	5	18.4	1.2	17.2	1.2	19.2	0.9	19.1	0.8	19.4	1.1
2302	5	19.7	1.0	20.7	1.3	22.5	1.0	24.8	1.0	23.4	1.2
2312	5	23.8	1.3	24.2	1.5	27.5	1.2	29.0	1.2	29.2	1.6
2322	5	25.0	1.3	28.5	1.7	32.1	1.4	36.8	1.4	35.1	1.8
2332	5	29.2	1.4	32.7	1.9	36.2	1.5	39.5	1.5	39.2	2.0
2342	5	34.0	1.6	36.0	2.1	40.1	1.7	44.0	1.7	44.0	2.3
2352	5	37.0	1.7	38.0	2.3	43.8	1.8	46.9	1.8	47.3	2.5

2362	5	38.4	1.7	42.1	2.5	44.2	1.8	48.9	1.8	51.7	2.7
2372	5	38.3	1.7	42.5	2.5	47.4	1.9	50.2	1.9	52.5	2.7
2382	5	40.4	1.7	41.8	2.4	46.3	1.9	50.9	1.9	52.0	2.7
2392	5	41.4	1.8	43.5	2.5	47.2	1.9	49.6	1.9	51.7	2.7
2402	5	42.2	1.8	43.6	2.5	46.3	1.9	50.6	1.9	50.4	2.7
2412	5	41.3	1.7	43.7	2.5	46.4	1.9	48.9	1.8	51.8	2.7
2422	5	44.2	2.0	42.3	2.5	46.9	2.0	50.6	2.0	51.2	2.7
2433	5	40.8	1.8	44.3	2.6	47.1	1.9	48.8	1.8	50.4	2.7
2443	5	39.5	1.7	42.4	2.5	44.6	1.8	44.5	1.7	48.1	2.5
2453	5	40.1	1.8	40.4	2.4	41.5	1.8	44.9	1.7	45.6	2.5
2463	5	39.8	1.8	40.6	2.4	40.2	1.7	42.8	1.6	43.6	2.3
2473	5	38.2	1.9	37.8	2.3	42.0	1.9	41.0	1.7	42.6	2.5
2483	5	39.4	1.7	37.7	2.2	38.5	1.7	41.2	1.6	40.1	2.3
2493	5	41.4	1.6	39.6	2.2	40.2	1.6	41.3	1.5	42.1	2.1

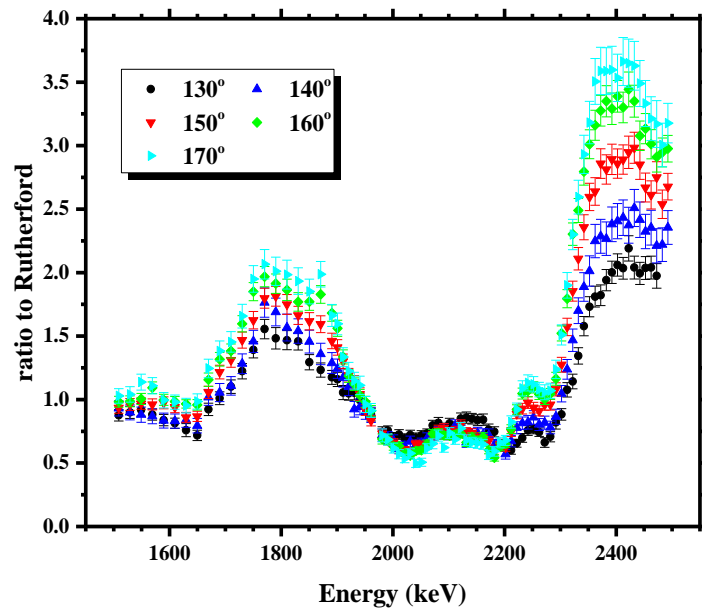


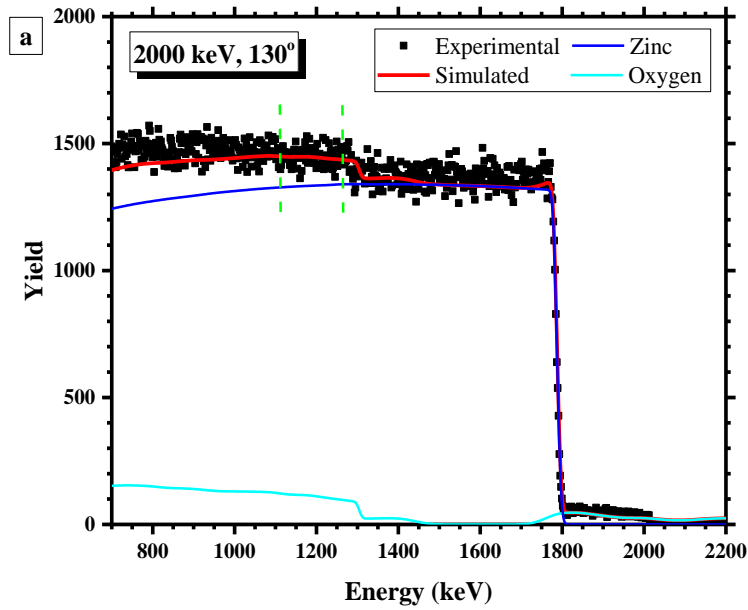
Figure 5.5 Ratio to Rutherford of the obtained differential cross sections of the $^{nat}O(d,d_0)^{nat}O$ for the energy range of 1500-2500 keV and for all the measured scattering angles.

5.2 Benchmarking procedure of the $^{nat}\text{O}(\text{d},\text{d}_0)^{nat}\text{O}$ elastic scattering

For the validation of the obtained cross section values for the deuteron elastic scattering on oxygen, spectra of a ZnO thick target were used that were acquired at the IPPE tandem accelerator and were provided by Dr. A. F. Gurbich. The deuteron energies were 2000 keV and 2250 keV for the scattering angles of 130° and 150° and 2000, 2250 and 2500 keV for the scattering angle of 170° . The experimental spectra were simulated by fitting the $Q \times \Omega$ product in the Zn edge by using Rutherford cross section values at every scattering angle/energy value combination. The integrated window below the oxygen surface, for which the comparison between the experimental and the simulated counts of $^{nat}\text{O}(\text{d},\text{d}_0)^{nat}\text{O}$ peak was performed, was chosen to be ~ 100 keV (~ 65 channels). The results of the validation procedure are shown in Figs. 5.6a-c, along with the integrated window indicated with dashed green lines. The contribution of the $^{16}\text{O}(\text{d},\text{p}_1)^{15}\text{O}$ reaction is quite important under the zinc edge, as well as in the integrated window at higher energies, as displayed in the experimental spectra. This contribution was simulated using the evaluated data from SigmaCalc [14] when available (up to 1650 keV), whereas for higher energies data from literature were used. More specifically, the dataset by Debras et al. [30] was used for the scattering angle of 130° , for 150° the dataset by Cavallaro et al. [31] at 150° was implemented, whereas for 170° the dataset from Seiler et al. [32] at 164.25° was chosen. It should also be mentioned here that the fit of the $Q \times \Omega$ product was carefully performed in the channels where the $^{16}\text{O}(\text{d},\text{p}_1)^{15}\text{O}$ contribution was minimal. However, as noted in Fig. 5.6b, a significant contribution of the $^{16}\text{O}(\text{d},\text{p}_1)^{15}\text{O}$ reaction is observed within the integrated window. In fact, the number of the counts originating from the $^{nat}\text{O}(\text{d},\text{d}_0)^{nat}\text{O}$ elastic scattering was only $\sim 30\%$ higher than the one originating from the $^{16}\text{O}(\text{d},\text{p}_1)^{15}\text{O}$ reaction within the integrated window, thus the results are significantly affected by the used datasets from literature. Hence, the deuteron energy of 2250 keV was rejected, since it cannot lead to accurate results for the benchmarking of $^{nat}\text{O}(\text{d},\text{d}_0)^{nat}\text{O}$ cross section values at any scattering angle. The results of the benchmarking procedure for the energies of 2000 and 2500 keV are shown in Table 5.2. The effect of the dual scattering was also examined due to the existence of zinc in the target. In Table 5.3 the values using the dual scattering in SIMNRA v.7.02 are also included and in Figs. 5.6b and c the simulation with the dual scattering option is also presented. The differences due to the dual scattering are more pronounced in the deuteron elastic scattering on zinc, as expected. The maximum difference between the experimental and the simulated counts was observed for the deuteron energy of 2000 keV and for the scattering angle of 170° (12%). This value, as well as all the values in Table 5.3, reveal a rather fair agreement, since these differences include the uncertainty of the used datasets for the $^{16}\text{O}(\text{d},\text{p}_1)^{17}\text{O}$ reaction contribution ($\sim 5\%$ for the Seiler et al. dataset, $\sim 6\%$ for the Cavallaro et al. dataset) which is unavoidably included in the integrated window. At this point, it is rather important to mention that even though the energies and angles for which the validation was performed did not correspond to the whole energy range and to all the measured scattering angles, the benchmarking results represent the whole cross

section measurement, since the cross section values were calculated in a coherent way for all scattering angles and energy values in the present work.

The complications discussed above regarding the benchmarking procedure are quite severe, hence any kind of renormalization of the obtained cross section values could not emerge from this specific benchmarking procedure. However, the whole scope of the present work, which was the general confirmation of the obtained cross section values, was achieved in the cases where the $^{16}\text{O}(d,p_1)^{15}\text{O}$ contribution was minimal, proving the overall accuracy of all the obtained differential cross section values.



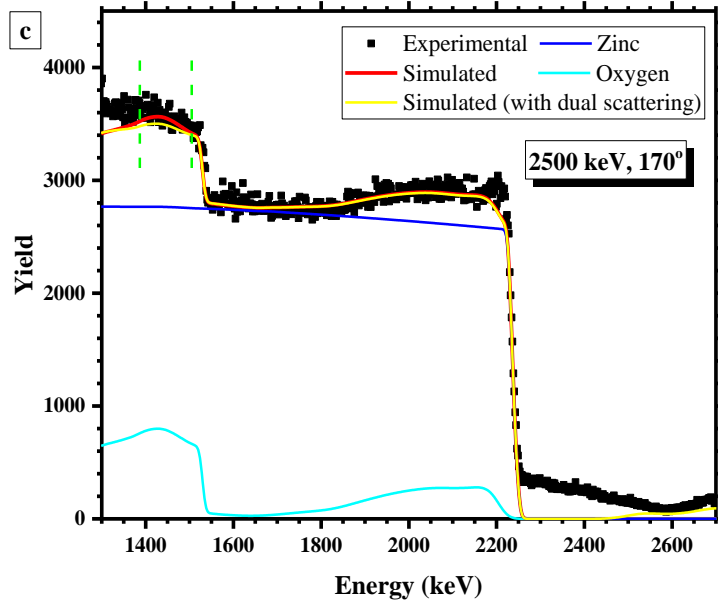
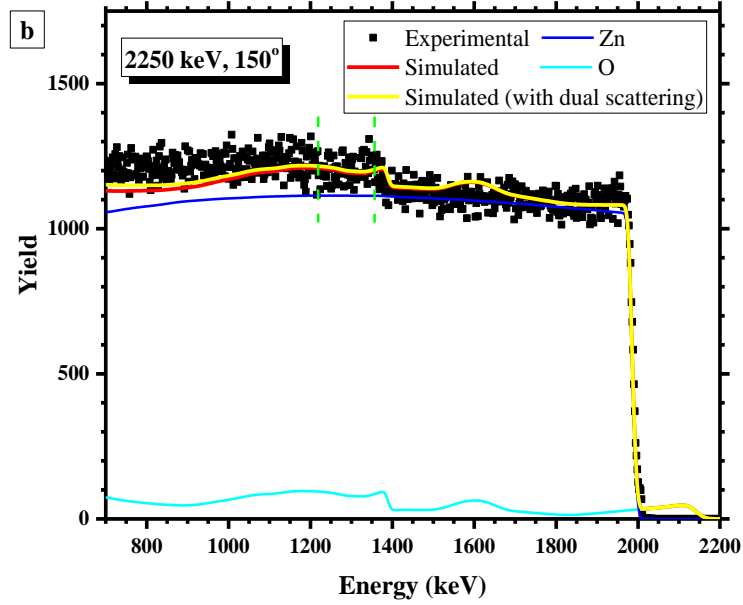


Figure 5.6a-c Experimental and simulated benchmarking spectra from a ZnO thick target at (a) 130° and 2000 keV, (b) 150° and 2250 keV and (c) 170° and 2500 keV. The integrated window used in the benchmarking procedure is marked in the graphs and it was ~100 keV (~65 channels).

Table 5.3 Differences (in %) between the simulated and the experimental counts within the integrated window for every beam energy/scattering angle combination. The numbers correspond to a higher integral of the simulated spectrum with respect to the integral of the experimental one.

Energy (keV)	130°	150°	170°
2000	3.1	4.4	7.9
2000 (dual scattering)	5.8	8.1	12.0
2500	-	-	6.1
2500 (dual scattering)	-	-	9.2

5.3 Theoretical Investigation of the $^{16}\text{O}(\text{d},\text{d}_0)^{16}\text{O}$ elastic scattering

In the studied case the single channel multi-level R-matrix analysis was applied in order to theoretically reproduce the measured cross section values of deuteron elastic scattering on oxygen in the energy range of 1.5-2.5 MeV.

Calculations were performed in the framework of the compound nucleus mechanism, since it is the dominant reaction mechanism at these low deuteron energies and for a light nucleus such as oxygen.

5.3.1 The Code

The code used was developed by Dr. A.F. Gurbich and it can perform multilevel, multiple channel R-matrix analysis. The equations included in the code are the ones from Lane and Thomas [33] that are used in the classic R-matrix theory and are mentioned in Section 1.5. The code could be employed for the calculation of both elastic scattering and reaction cross sections.

The most widely used model for R-matrix calculations is the hard sphere one, which assumes the interaction between a projectile and a nucleus represented by a solid sphere with radius R , where the potential is $U(r)=\infty$ for $r<R$ and $U(r)=0$ for $r>R$, leading to calculable differential cross section values. According to this model the changes in the differential cross-section values, which correspond to eigenstates of the compound nucleus, should be inserted individually in the code. The hard sphere R-matrix is implemented in other widely used codes for calculating scattering cross sections as well, such as AZURE [34], [37] and SAMMY [35]. On the other hand, as suggested by Johnson [36], the off resonant scattering can be attributed to the effect of the optical model potential. In fact, this approach might lead to significant information regarding the potential itself. Thus, some of the especially broad changes may also be reproduced as resonances of the potential, similar to the effect of a standing wave inside the nucleus. Such broad single particle

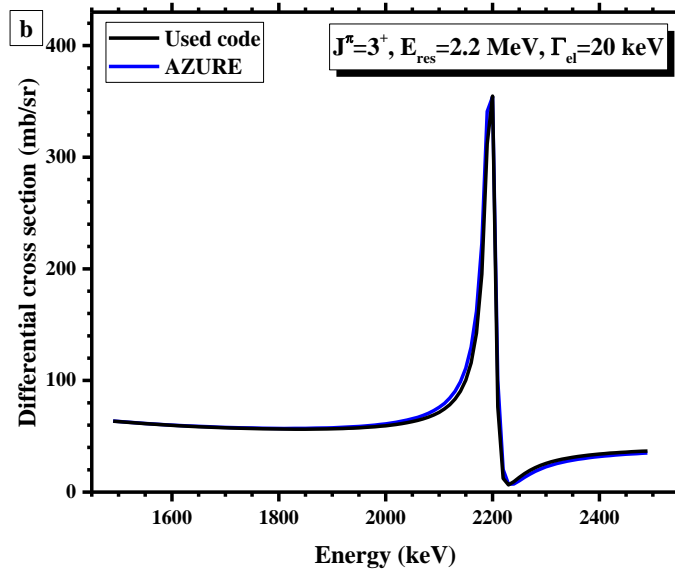
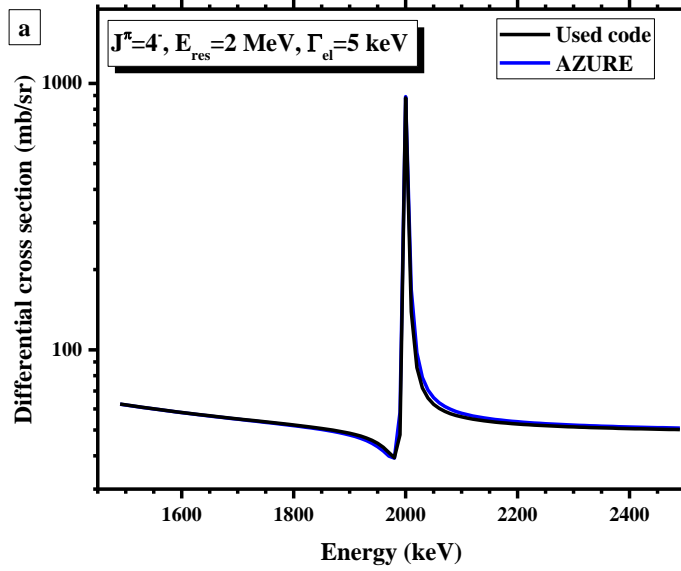
resonances can be calculated in the code by employing optical model phases and currently, only the R-matrix code developed by A. F. Gurbich can implement this alternative approach.

In the studied case, the differential cross section is mainly characterized by wide resonances due to the implementation of deuterons as projectiles and due to the overlapping levels of the compound nucleus. At the same time, using the optical model for the phase shift calculation, wide resonances could in principle naturally occur via the selected parameters of the optical model potential. Besides, the difference between the optical model and the hard sphere model does not lie in the agreement between the theoretical and the experimental datasets, since both options could lead to equally good fitting results, but in the physical interpretation of the obtained results. More specifically, the parameters used in the optical model (soft phases analysis) may lead to conclusions regarding the deuteron potential in the proximity of light elements. Hence, for the aforementioned reasons and the fact that in the studied case the hard sphere scattering phase shift appeared not to give an adequate description of the off-resonance background, the optical model approach was chosen for the phase shift calculation. The potential is implemented in the code via Eq. 1.23 and the parameters of the optical model potential are fitted to the experimental cross section values using χ^2 minimization routines.

The scattering amplitude is calculated in the code using three phase shifts, instead of the two terms included in Eq. 1.32, namely the resonant phase shift, the potential scattering phase shift, calculated via the optical model and the phase shift due to the Coulomb potential. These three terms are added coherently in the code. This unified R-matrix, which corresponds to the resonances of the compound nucleus plus the optical model, in order to account for the potential scattering contribution, was proven to be the most suitable approach for calculating cross section values in the case of low energy charged particle scattering in the past [26].

Since, as mentioned above, the used code is the only one that can calculate the potential scattering via the optical model, a comparison between the used code and another code implementing the optical model is not possible. Thus, the next best thing to do is to compare the code used with the AZURE one, via the hard sphere approach. The AZURE code is the most widely used R-matrix code for differential cross sections and it calculates the potential scattering using the hard sphere approximation by adding a distant resonance for each of the relevant J^π values at a higher energy value than the studied energy range (background poles). Hence, for comparison purposes, the code used was set to calculate the phase shifts through the hard sphere approximation. For each comparison only one resonance was added with three different J^π values (4^+ , 3^+ , 2^- , 2^-), with four different total level widths which were equal to the elastic channel width in each case (5, 20, 100, 200 keV, respectively), at three different energies (2.0, 2.2, and 1.8 MeV, respectively) for the scattering angle of 170° and for the studied energy range (1.5-2.5 MeV). Also, the channel radii were set equal in both codes. The results of the comparison are shown in Figs. 5.7a-d. For Figs. 5.7a and b, the agreement is excellent with minimal differences. For Figs. 5.7c and d, in the resonant region the minima and the maxima are in good agreement whereas in the non-resonant region differences are observed. Hence, as the level width becomes larger, the differences seem to increase far from the maximum and minimum values of the differential cross section and this may

lead to different fitting parameters. Such discrepancies exist due to the different conversions between the observed width gamma (Γ) and the reduced one. The used code uses eq. IV.1.17b (p. 273) of [33] and AZURE makes the conversion according to Eq. 41 of [34].



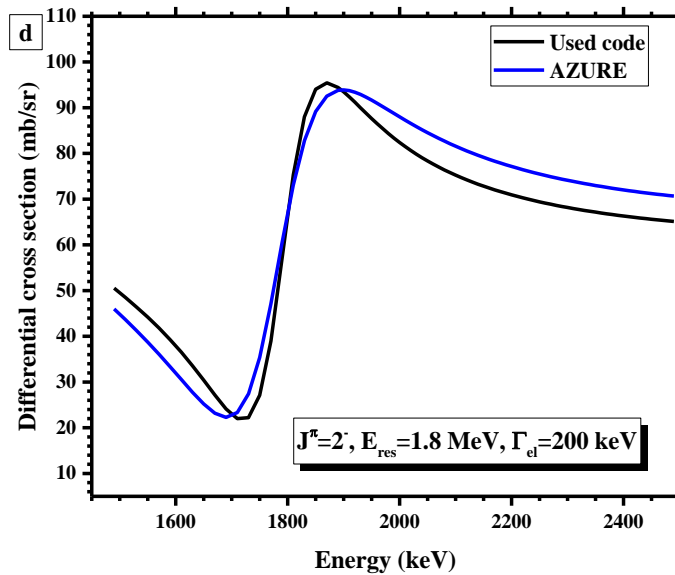
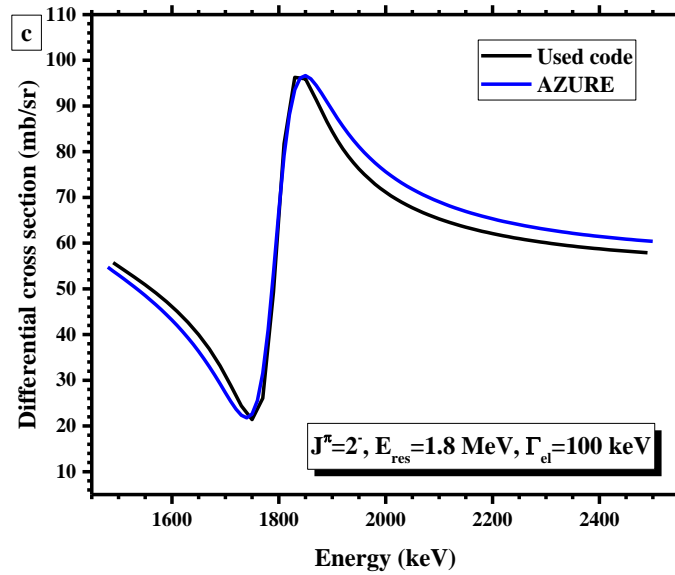


Figure 5.7a-d Comparison between the used code using the hard sphere model and the AZURE code, implementing different J^π values, different resonant energy values and different elastic scattering width amplitudes in each case.

5.3.2 The $^{16}\text{O}+d$ channel

For the studied channel $^{16}\text{O}+\text{d}$, the target spin $I_t = 0^+$ is coupled to the projectile spin $I_p = 1^+$ forming the entrance channel with spin $s=1$ and positive parity. This channel spin was combined with the relative orbital angular momentum ℓ in order to form the spin of the compound nuclear state J . The parity of each compound state is calculated via the $(-1)^{\ell+\ell'}$ rule, where ℓ' is the parity of the channel. In Table 5.3 the possible entrance channels are listed for J values up to 6 and $\ell \leq 6$.

In the studied case, only ℓ mixing is possible. The ℓ mixing ratio is defined as:

$$\varepsilon_1 = \pm [\Gamma_{1,\ell+2}/\Gamma_{1,\ell}]^{1/2} \quad (5.4)$$

The corresponding mixing angles ψ_1 are defined for convenience as $\tan(\psi_1) = \varepsilon_1$ and their range varies between -90° to $+90^\circ$ [92].

The formed compound nucleus is $^{19}\text{F}^*$ and the parameters needed as input in the code for each excited state are the spin, the parity, the resonance energy, the elastic width, the total width, the boundary conditions and the potential parameters. All these parameters can also be fitted in the code. For the studied beam energy range, 1500-2500 keV in the laboratory system, which corresponds to the energy range of 8858-9748 keV in the CM system (that is, relative to the compound nucleus itself, taking into account the Q-value for deuteron capture plus the deuteron beam energy in the CM reference frame), the parameters of the known levels were taken from the Ajzenberg-Selove compilation [90]. In the studied energy range three levels emitting deuterons are included, two of them with unknown J^π values and one with a tentative assignment. More details concerning the parameters of the implemented compound nucleus levels are included in Section 5.3.3.

Table 5.3 Elastic scattering channels for target spin $I_t = 0^+$ and $\ell \leq 6$.

J	ℓ	s
0^-	1	1
1^+	0 2	1
1^-	1	1
2^+	2	1
2^-	1 3	1
3^+	2 4	1

3^-	3	1
4^+	4	1
4^-	3	1
	5	
5^+	4	1
	6	
5^-	5	1
6^+	6	1
6^-	5	1

5.3.3 Parameters and calculations

In this section the parameters of the optical model, as well as the parameters of each level used in the theoretical investigation are discussed, while their values are listed.

5.3.3.1 Optical model calculations

The theoretical reproduction procedure was initiated with the optical model calculations without adding any resonances. The potential parameters are usually adjusted to energy regions that do not display resonances. In the studied energy range, no such region exists, thus the parameters were approximated in lower energy regions where the cross section is smoother and through the course of the cross-section reproduction procedure their values were modified until the optimal agreement was accomplished. Their final values are listed in Table 5.4 and the differential cross sections containing only the potential scattering through the optical model calculations for the scattering angles of 130° , 150° and 170° are presented in Fig. 5.8. As shown in Fig. 5.8, none of the resonances is reproduced from the optical model. However, the interference of the partial waves leads to lower values of the theoretical differential cross sections compared with the ones emerging from the hard sphere model. This is a desired characteristic, since the lower theoretical values are closer to the experimental ones. A separate real potential depth was used for each one of the ℓ quantum numbers since, in some cases (e.g. [93]), a resonance might be reproduced only by fitting a specific wave potential well. However, in the studied case, this did not occur. Moreover, it was proven that the values of the V_{r4} and V_{r5} parameters, which correspond to the potential of the g and h partial waves, do not affect the cross section in the studied energy range, as expected for high ℓ values at such low beam energies.

Although a few global optical model potentials exist for deuterons, namely [94], [95], they are mainly focused on heavier elements ($21 \leq A \leq 238$) and for higher energies (12-120 MeV), hence the comparison with any of these is unsuitable. However, two studies exist that, even though the ranges are still quite wide, they include a set of parameters for a global deuteron potential for lower energies and for lighter target nuclei, namely for energies between 1-200 MeV and nuclei ranging from ^{12}C to ^{238}U ; these include the work by An H. and Cai H. [96] and the work by Han Y. et al [97]. In both of these contributions the optical potential has the same Woods–Saxon form as in Eq. 1.23. The parameters for the global deuteron optical model potential, in the two latter works, were determined by a code which minimizes the χ^2 , which represents the deviation of the calculated results from the experimental values. In [96] certain parameters were determined as: $V_{R0}=91.85$ MeV, $W= 10.83$ MeV, $V_{SO}=3.557$ MeV and $R_C=1.303$ fm, while in [97] certain parameters were $r_0=1.174$ fm, $a_c=0.809$ fm, $V_{R0}=82.18$ MeV, $W=20.968$ MeV, $V_{SO}=3.703$ MeV and $R_C=1.698$ fm (values obtained from RIPL-3 [98] and the notation is the same as the one used in Table 5.4). The agreement between the determined nuclear radius (r_0) and the diffuseness (a_c) in the present work compared with the latter study is decent. It should be pointed out here that the obtained values corresponding to the real part of the potential depth, which are responsible for the description of the elastic scattering, are close to the ones existing in the literature and mentioned above. The differences in the imaginary part of the depth of the potential should be expected, since the accurate determination of the W parameter originates from the reaction channels, since it mainly affects them, and not through the elastic channel. It should also be mentioned here that the revealed differences in all the parameters between the literature values and the ones determined in the present work, are expected, since both of the pre-existing works include higher deuteron energies and thus the sets of parameters might have been calculated giving more weight on higher impinging energies and heavier nuclei.

Table 5.4 Optimal optical model potential parameters implemented in the used code. The optical potential has the form of (Section 1.2, Eq. 1.23):

$$\begin{aligned}
 U(r) = & -V_R \{1 + \exp[(r - R)/a]\}^{-1} + -i W \{1 + \exp[(r - R)/a]\}^{-1} \\
 & + 4i a_I W_D \frac{d}{dr} (\{1 + \exp[(r - R_I)/\alpha_I]\}^{-1}) + s \\
 & \cdot \ell \left(\frac{\hbar}{m_\pi c^2} \right)^2 V_{SO} \frac{1}{r} \frac{d}{dr} (\{1 + \exp[(r - R_S)/\alpha_S]\}^{-1}) + U_C(r)
 \end{aligned}$$

where r_0 corresponds to the parameter used in the nuclear radius equation ($r = r_0 \cdot A^{1/3}$), a_c to the diffuseness, V_{R0} , V_{R1} , V_{R2} , V_{R3} to the depth of the potential of the s , p , d , f partial waves, respectively, W to the depth of the imaginary potential, V_{SO} to the depth of the spin-orbit potential and R_c to the Coulomb radius.

r_0	a_c	V_{R0}	V_{R1}	V_{R2}	V_{R3}	W	V_{SO}	R_C
(fm)	(fm)	(MeV)	(MeV)	(MeV)	(MeV)	(MeV)	(MeV)	(fm)

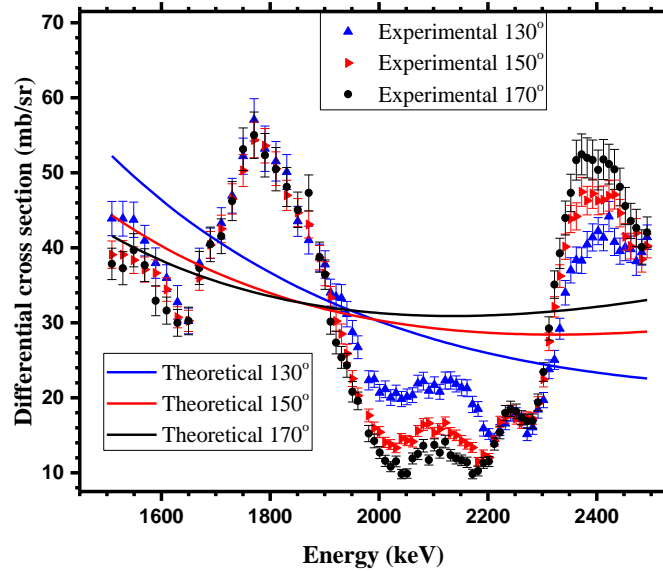


Figure 5.8 Experimental and theoretical (taking into account only the potential scattering via optical model calculations) differential cross section values for three scattering angles in the laboratory reference frame.

5.3.3.2 Resonances

After the potential scattering has been taken into account in the differential cross sections, the resonances need to be reproduced as well. In the studied case, the full spectroscopic information of the excited states is missing. The only available information in the literature regarding the levels of the compound nucleus ^{19}F is summarized in Table 5.5. Among the levels which are included in Table 5.5, four of them (1.616, 2.221, 2.280, 2.340 MeV) have not been reported to de-excite via deuteron emission, according to [90], but since they were visible in the experimental cross section structures, they were taken into account in the calculations, as mentioned below.

The procedure was initiated with the addition of the levels which create wider resonances that dominate the cross-section structure, i.e. the levels at 1.765, 2.221 and 2.340 MeV. The rest of the parameters which characterize each level (J^π , total width, partial width of the elastic channel and mixing angle ψ) along with the exact energy of each level as visible in the experimental excitation functions, were acquired by trial-and-error procedures. The obtained differential cross section which includes only these three resonances is presented in Fig. 5.9 for the scattering angles of 130° , 150° and 170° . Subsequently, additional levels which yield a finer structure of the differential cross section values were added, along with the rest of the parameters of each level, again with

trial-and-error procedures. The values of the parameters of such additional levels were based on the available information in the literature, but they were adjusted to the experimental points. This procedure resulted in a few modifications of the used parameter values compared with the ones in the literature, mainly in the low energy region, along with the addition of a level having an energy of 2.053 MeV which has not been observed in the past in the $d+^{16}\text{O}$ system, but clearly affects the experimental cross section structure. All the parameters regarding the implemented levels within the investigated energy region (1.5-2.5 MeV) are summarized in Table 5.6. As shown from the comparison between Table 5.5 and Table 5.6, the main differences are observed in the low energy region. More specifically, below the level at ~ 1.7 MeV, three levels exist in the literature (1.563, 1.616, 1.681 MeV), whereas in the present study only two (1.650, 1.665 MeV) were used. Furthermore, two levels were added in the calculations which are outside the studied energy region, at energies 1.353 MeV ($J^\pi=3^+$, $\Gamma=900$ keV, $\Gamma_d/\Gamma=0.15$, $\Psi=0$) and 2.55 MeV ($J^\pi=2^+$, $\Gamma=50$ keV, $\Gamma_d/\Gamma=0.25$, $\Psi=0$). In the literature such levels exist in energies 1.325 and 2.55 MeV but with all the other parameters unknown. However, their addition was deemed necessary, since the level at 2.55 MeV contributes in the last maximum of the differential cross section structure, whereas the level at 1.353 MeV creates a smooth background, while it contributes to the creation of the minimum at ~ 1900 keV, following the calculation of the matching radius at this energy. The large width of the latter level should not come as a surprise, since the existence of levels with large widths in the cases of deuteron impinging on light elements is not unique, namely in the e.g. $^{10}\text{B}+d$ system, the formed compound nucleus is ^{12}C and it displays levels having widths of $\Gamma=1700$ keV and $\Gamma=3000$ keV.

It should be pointed out here that in order to determine the final values of Tables 5.4 and 5.6 and complete the theoretical investigation, a re-iterative procedure was carried out, which included the repeated altering of the values of the parameters (including the parameters of the optical model), in order to obtain the best possible combination; meaning the smallest difference between theory and experiment. However, it is important to stress here that the parameters used for the calculation of the differential cross sections were not unambiguously determined and thus they do not constitute a unique source of nuclear spectroscopic information, although they are mandatory for the reproduction of the obtained differential cross sections and thus for the calculation of the cross sections in scattering angles and energies (in between the measured values) where no experimental datasets exist, which was the main goal of the present theoretical investigation. Even though, from the spectroscopic point of view, the final values of the parameters cannot be considered as fixed, a crucial remark can be made; in the levels that have tentative J^π assignments in the literature and the present work uses one of these values, then this is a strong indication regarding the true value of the J^π of such level. In the present study, this situation occurred for the levels at 2.221 and 2.28 MeV (literature values) where both levels exhibit tentative J^π assignments $2,3^+$ and in the present investigation the used value was 2^- .

A key point of the present work is the matching with the pre-existing evaluation. This was performed using the last available point of the previous evaluation, that is, at 1.98 MeV, hereinafter referred to as the matching point. Thus, the values obtained with the present reproduction for the

matching point and the corresponding previous ones are shown in Table 5.7, along with the differences, for several scattering angles. The larger difference is observed -as expected- for the scattering angle of 130° .

Table 5.5 Maxima in the yield of $^{16}\text{O}+d$ retrieved mainly from the Ajzenberg - Selove compilation [90], which was more thorough, and the NNDC library [91]. E_x values correspond to the energy in the CM system (that is, relative to the compound nucleus itself, taking into account the Q -value for deuteron capture plus the beam energy in the CM reference frame).

E_d (MeV)	J^π	Γ (keV)	E_x (MeV)
1.563	-	121 ± 15	8.914
1.616	-	19 ± 15	8.961
1.681	(5 ⁻)	-	9.020
1.765	-	141 ± 10	9.093
1.886	3, 4 ⁻	108 ± 12	9.207
2.221	2, 3 ⁺	-	9.500
2.280	2, 3 ⁺	-	9.550
2.340	-	-	9.600

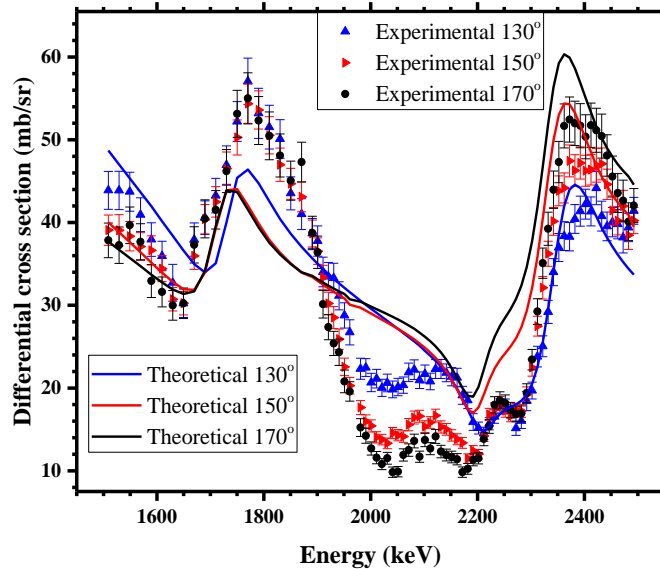


Figure 5.5 Experimental and theoretical (including only three resonances at the energies of 1.765, 2.221, 2.340 MeV) differential cross section values for the scattering angles of 130° , 150° and 170° .

Table 5.6 Optimal level parameters as implemented in the R-matrix code that was used.

E_d (MeV)	J^π	Γ (keV)	Γ_{el}/Γ	ψ
1.650	2^-	50	0.070	0
1.665	1^+	119	0.063	79
1.740	1^+	94	0.162	0
1.854	1^+	7.4	0.146	85
2.053	1^-	115	0.134	0
2.242	2^-	82	0.095	0
2.294	2^-	71.8	0.119	0
2.381	1^+	130	0.36	0

Table 5.7 Differential cross section values (mb/sr) using the pre-existing evaluation and the presented theoretical reproduction at the matching point (1.98 MeV), along with the differences (in %) for several scattering angles.

Scattering angle (degrees)	Differential Cross section values using the pre-existing evaluation (mb/sr)	Differential Cross section values using the presented theoretical reproduction (mb/sr)	Differences (%)
130	21.49	26.43	23.0
140	20.02	21.85	9.1
150	18.58	18.28	1.6
160	17.33	15.68	9.5
170	16.49	14.11	14.4

5.3.4 Results

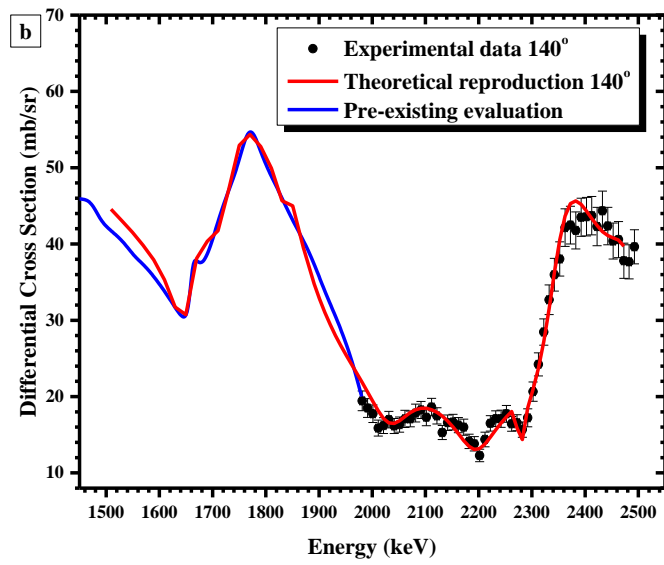
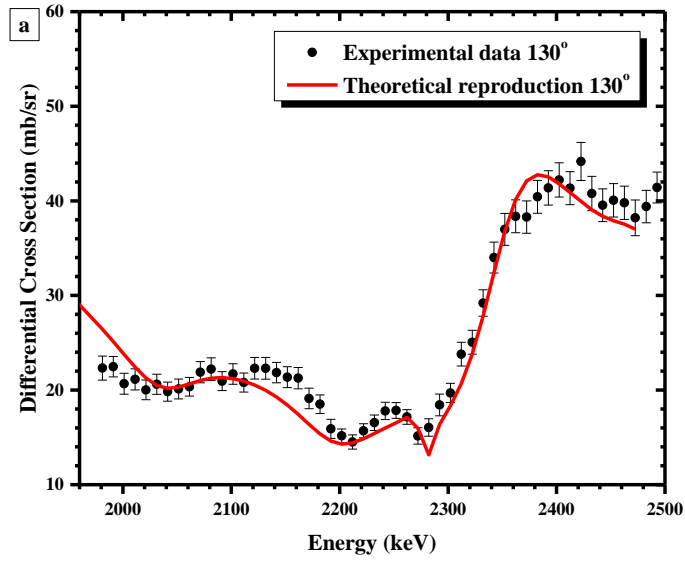
The obtained results are presented in Figs. 5.9a-e along with the experimental values, for the five measured angles and for the energy range of 1.98-2.5 MeV. In Fig. 5.9b, for the scattering angle of 140° , the obtained results are presented for the energy range of 1.5-2.5 MeV along with the pre-existing evaluation (1.5-1.98 MeV) and the experimental values in order to make sure that the differences between the evaluation and the present theoretical study are not significant. The energy

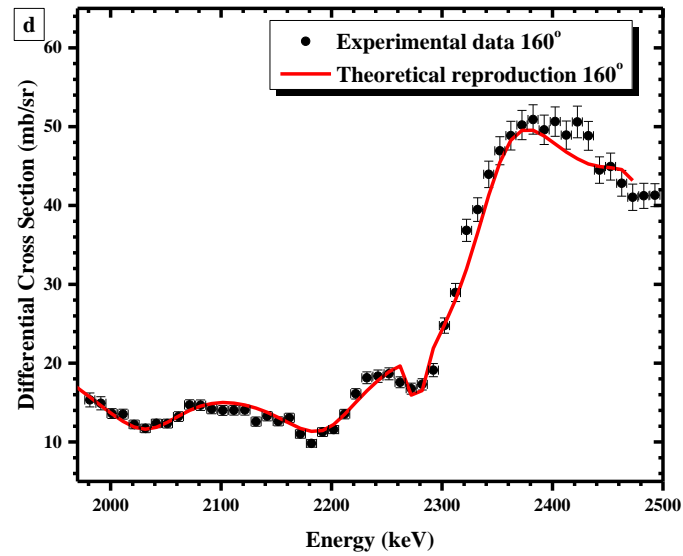
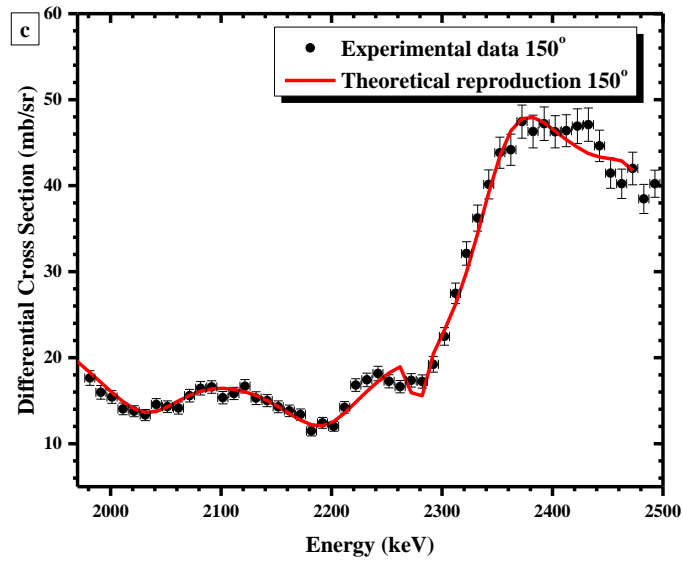
range 1.5-1.98 is not included for the other scattering angles (130° , 150° , 160° and 170°) since the results will be used from the energy of 1.98 MeV and in Fig. 5.9b are only included for indicative reasons. However, it should be noted here that for the other scattering angles the agreement between the theoretical curves was not as satisfying as it is for this specific scattering angle. In Fig. 5.9a, the theoretical curve seems to adequately reproduce the experimental datasets within uncertainties. The most significant differences are observed at ~ 1990 keV and at ~ 2150 keV. The situation in Fig. 5.9b is even better showing a quite satisfactory agreement over the whole energy region although the difference at ~ 1990 keV is also displayed. In Fig. 5.9c-e the agreement with the experimental dataset is excellent within uncertainties, however a small difference is observed at ~ 2420 keV. Overall, the obtained theoretical investigation has led to a quite good agreement with the experimental datasets following the same trend.

Regarding the uniqueness of the obtained solution which includes the values of the optical model and the resonance parameters, the experimental differential cross section values were 390 (78 at each scattering angle), which resulted in an equal number of equations. The unknown parameters of the system that needed to be determined were 66 in total (18 from the optical model and 48 from the 8 resonances). Such a system mathematically leads to a unique solution. However, the possibility of performing the same calculations with different resonant settings and different values in the optical model parameters, or even with the implementation of the hard-sphere model, thus leading to a different set of unknown parameters, and hence obtain an equally good agreement between theory and experiment, cannot be in principle excluded.

Concerning the reliability of the obtained theoretical reproduction, the interpolation between the used angles indeed leads to accurate results, since the second term of Eq. 1.22 becomes more important [99] and resonances dominate the differential cross section. Concerning the extrapolation to more forward scattering angles, it should be noted here that, although in principle it is possible, at very small angles ($\theta \ll 90^\circ$) the Coulomb scattering amplitude is naturally expected to dominate the cross section. Moreover, the accuracy of the present investigation lies in the values of the Legendre polynomial coefficients. Hence, for scattering angles where the Legendre polynomials approach zero values (as e.g. at $\theta=90^\circ$ where $\cos\theta=0$) severe deviations between the theoretical predictions and the experimental results may occur.

Furthermore, accurate spectroscopic information regarding all the implemented parameter values could be used in the future in order to ensure the validity of the obtained results. Moreover, additional channels could also be added in the theoretical calculations, e.g. $^{16}\text{O}(d,p_0)^{15}\text{O}$ and/or $^{16}\text{O}(d,\alpha_0)^{14}\text{N}$ and/or $^{16}\text{O}(d,p_1)^{15}\text{O}$, in order to accurately determine the imaginary part of the potential (W parameter) and, possibly some of the parameters of the used levels. However, the lack of accurate experimental datasets in multiple scattering angles in the studied energy range impede for the moment the completion of such a procedure.





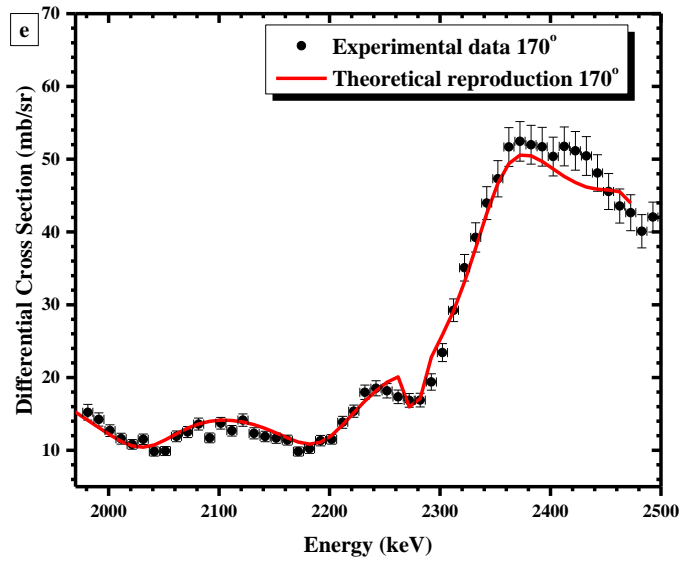


Figure 5.9a-e Results of the theoretical reproduction along with the experimental differential cross section values from 1.98 MeV regarding the $^{16}\text{O}(d,d_0)^{16}\text{O}$ elastic scattering in the scattering angles of 130° , 140° , 150° , 160° , 170° . In (b) the pre-existing evaluation is also included.

Conclusions and future perspectives

In the context of the present thesis, deuteron differential cross section datasets of several light elements ($Z < 15$) were measured and in certain cases the obtained results were also benchmarked. Moreover, a theoretical investigation was performed for the case of deuteron elastic scattering on oxygen aiming at the extension of the evaluation to higher energies.

More specifically, the determined deuteron differential cross sections are:

- ${}^6\text{Li}(d,d_0){}^6\text{Li}$ in the deuteron energy range 940 - 2000 keV, for the scattering angles of 125° , 140° , 150° , 160° and 170°
- ${}^7\text{Li}(d,d_0){}^7\text{Li}$ in the deuteron energy range ~ 1280 - 2000 keV, for the scattering angles of 125° , 140° , 150° , 160° , 170° and the sum ${}^7\text{Li}(d,d_0){}^7\text{Li} + {}^7\text{Li}(d,p_0){}^6\text{Li}$ in the deuteron energy range ~ 1000 - 1280 keV, for the scattering angles of 125° , 140° , 150° , 160° , 170°
- ${}^9\text{Be}(d,d_0){}^9\text{Be}$ in the deuteron energy range 1600 – 2200, for the scattering angles of 120° , 140° , 150° , 160° , 170°
- ${}^{14}\text{N}(d,d_0){}^{14}\text{N}$ in the deuteron energy range 1000 – 2200, for the scattering angles of 120° , 130° , 140° , 150° , 160° , 170°
- ${}^{\text{nat}}\text{O}(d,d_0){}^{\text{nat}}\text{O}$ in the deuteron energy range 1500 – 2500 keV, for the scattering angles of 130° , 140° , 150° , 160° , 170°
- ${}^{23}\text{Na}(d,d_0){}^{23}\text{Na}$ in the deuteron energy range 1060 – 2400 keV, for the scattering angles of 140° , 150° , 160° , 170°
- ${}^{\text{nat}}\text{Si}(d,d_0){}^{\text{nat}}\text{Si}$ in the deuteron energy range 1000 – 2200 keV, for the scattering angles of 120° , 130° , 140° , 150° , 160° , 170°

The differential cross section values of the aforementioned cases have already been uploaded in IBANDL, in order to facilitate future analytical simultaneous d-EBS/d-NRA depth profiling studies of light elements, especially since, for most cases, such coherent datasets for several backscattering angles and for typical IBA energies were measured for the first time.

Furthermore, the results of the three last cases, namely ${}^{\text{nat}}\text{O}(d,d_0){}^{\text{nat}}\text{O}$, ${}^{23}\text{Na}(d,d_0){}^{23}\text{Na}$, ${}^{\text{nat}}\text{Si}(d,d_0){}^{\text{nat}}\text{Si}$, were validated by irradiating thick targets of known stoichiometry. In most cases, despite the complications, mainly regarding the existence of d-NRA reaction channels, the results of the benchmarking procedures revealed that the obtained cross section values could reproduce the thick target spectra in a quite satisfactory manner. Therefore, as indicated by the benchmarking results, the differential cross section datasets were accurately measured and are suitable for performing both evaluation and analytical studies.

Moreover, the deuteron elastic scattering on oxygen was theoretically investigated in the framework of the R-matrix theory, achieving the extension of the pre-existing evaluation up to 2.5 MeV. The investigation resulted in a quite satisfactory reproduction of the determined cross section values over a broad angular range (130°-170°). Hence, the present theoretical investigation enables the calculation of the differential cross section at any scattering angle, where no experimental measurements exist, contributing to the implementation of the IBA techniques and facilitating the study of oxygen profiles at relatively higher depths. Moreover, the determined parameters of the optical model seem to be in good agreement with the corresponding values in the literature, while new information was added regarding the accurate value of the J^π of two levels, where only tentative assignments existed.

Despite the contribution of the present thesis to the deuteron elastic scattering measurements which resulted in the enrichment of IBANDL, there is still a lot to be done in order to further improve the implementation of the corresponding IBA techniques. It would be very useful to extend the deuteron elastic scattering measurements for the remaining light elements (e.g. ^{10}B , ^{11}B , ^{27}Al) in order to complete this systematic study, thus enhancing the implementation of the simultaneous combination of the d-EBS and d-NRA techniques which could lead to more accurate depth profiling results. Such an experimental study has already been scheduled in the forthcoming months. Moreover, benchmarking experiments need to be performed for the remaining cases, so that the differential cross section values be validated, ideally in a different laboratory than the one where the cross sections values have been determined. During such measurements, the emerging complications, described in the present thesis, could be avoided with the implementation of a more sophisticated experimental setup, capable of distinguishing between deuterons, protons and alpha particles.

Although the proton and now the deuteron elastic scattering differential cross sections on the majority of the light elements have been studied, the situation dramatically changes regarding the implementation of a ^3He beam, where only a few and scarce datasets exist in the literature. The study of the ^3He -induced elastic scattering on light elements is desirable for depth profiling studies, due to the improved mass separation and depth resolution obtained with a ^3He beam compared to a deuteron or a proton one. This is important, not only for the study of fusion materials, but also for the ongoing research in nuclear astrophysics, namely the one related to the rp-process [100].

From the theoretical point of view, evaluation studies could be performed for the deuteron elastic scattering on light elements which manifest the highest technological interest and for which spectroscopic information of the compound nucleus exists, namely e.g. ^{14}N , and thus conclusions can be extracted regarding the deuteron potential at low beam energies. Finally, the coherent and accurate measurement of the deuteron induced reactions in ^{16}O would be highly desirable, since the determined in the present thesis resonance parameters could be tested on different reaction channels. Additionally, the evaluation, in the case of d-NRA, displays challenges regarding the combination of two reaction mechanisms, namely the compound nucleus and the direct one. To conclude, despite the outstanding progress accomplished so far, as evidenced in the IBANDL and

SigmaCalc websites, there are still many open questions and interesting problems in the field of nuclear data which need further investigation.

REFERENCES

- [1] A. F. Gurbich, *Handbook of Ion Beam Analysis - Chapter 3*, Second. .
- [2] K. S. Krane, *Introductory Nuclear Physics*. JOHN WILEY & SONS, 1988.
- [3] P. E. Hodgson, E. Gadioli, and E. Gadioli Erba, *Introductory Nuclear Physics*. 1997.
- [4] C. A. Bertulani and P. Danielewicz, *Intoduction to Nuclear Reactions*. .
- [5] E. P. Wigner and L. Eisenbud, “Higher angular momenta and long range interaction in resonance reactions,” *Phys. Rev.*, vol. 72, no. 1, pp. 29–41, 1947.
- [6] E. Ntemou *et al.*, “Differential cross-section measurements for deuteron elastic scattering on natSi for elastic backscattering purposes,” *Nucl. Instruments Methods Phys. Res. Sect. B Beam Interact. with Mater. Atoms*, vol. 450, no. October 2017, pp. 24–30, 2019.
- [7] C. A. Kalfas, M. Axiotis, and C. Tsabaris, “SPECTRW: A software package for nuclear and atomic spectroscopy,” *Nucl. Instruments Methods Phys. Res. Sect. A Accel. Spectrometers, Detect. Assoc. Equip.*, vol. 830, pp. 265–274, 2016.
- [8] J. Theuerkauf *et al.*, “Program Tv.” Institute for Nuclear Physics, Cologne.
- [9] M. Mayer, “Improved physics in SIMNRA 7,” *Nucl. Instruments Methods Phys. Res. Sect. B Beam Interact. with Mater. Atoms*, vol. 332, pp. 176–180, 2014.
- [10] V. Paneta, A. Kafkarkou, M. Kokkoris, and A. Lagoyannis, “Differential cross-section measurements for the ${}^7\text{Li}(p,p\ 0)\ {}^7\text{Li}$, ${}^7\text{Li}(p,p\ 1)\ {}^7\text{Li}$, ${}^7\text{Li}(p,\alpha\ 0)\ {}^4\text{He}$, ${}^{19}\text{F}(p,p\ 0)\ {}^{19}\text{F}$, ${}^{19}\text{F}(p,\alpha\ 0)\ {}^{16}\text{O}$ and ${}^{19}\text{F}(p,\alpha\ 1,2)\ {}^{16}\text{O}$ reactions,” *Nucl. Instruments Methods Phys. Res. Sect. B Beam Interact. with Mater. Atoms*, vol. 288, pp. 53–59, 2012.
- [11] V. Foteinou *et al.*, “Differential cross section measurements of the ${}^{19}\text{F}(d,d0)$ elastic scattering for Ion Beam Analysis purposes,” *Nucl. Instruments Methods Phys. Res. Sect. B Beam Interact. with Mater. Atoms*, vol. 396, pp. 1–4, 2017.
- [12] U. Fasoli, E. A. Silverstein, D. Toniolo, and G. Zago, “The elastic scattering of protons by ${}^6\text{Li}$ in the Energy Range (1.3-5.6) MeV,” *Nuovo Cim.*, vol. 34, no. 6, pp. 1833–1836, 1964.
- [13] M. Kokkoris *et al.*, “Differential cross section measurements of the ${}^{12}\text{C}(d,p1,2,3){}^{13}\text{C}$ reactions in the energy range $E_{d,\text{lab}} = 900\text{--}2000$ keV for nuclear reaction analysis,” *Nucl. Instruments Methods Phys. Res. Sect. B Beam Interact. with Mater. Atoms*, vol. 254, no. 1, pp. 10–16, 2007.
- [14] A. F. Gurbich, “SigmaCalc recent development and present status of the evaluated cross-sections for IBA,” *Nucl. Instruments Methods Phys. Res. Sect. B Beam Interact. with Mater. Atoms*, vol. 371, pp. 27–32, 2016.
- [15] J. L. C. Ford, “Elastic Scattering of Deuterons by Lithium-7*,” *Phys. Rev.*, vol. 136, no. 4B, pp. B953–B960, 1964.
- [16] J. M. Lombaard and E. Friedland, “Optical model and DWBA analysis of the ${}^7\text{Li}(d, d)$ - and ${}^7\text{Li}(d, p0)$ -reactions in the energy region 1.0 to 2.6 MeV,” *Zeitschrift für Phys.*, vol.

- 268, no. 4, pp. 413–417, 1974.
- [17] L. Zhengmin and W. Rong, “Non-Rutherford elastic scattering cross sections for 170° backscattering of 0.15–3.00 MeV protons from beryllium,” *Nucl. Instr. Methods Phys. Res. B*, vol. 93, no. 4, pp. 404–408, 1994.
- [18] S. Krat, M. Mayer, and C. Porosnicu, “The ${}^9\text{Be}(p,p) {}^9\text{Be}$, ${}^9\text{Be}(p,d) {}^8\text{Be}$, and ${}^9\text{Be}(p,\alpha) {}^6\text{Li}$ cross-sections for analytical purposes,” *Nucl. Instruments Methods Phys. Res. Sect. B Beam Interact. with Mater. Atoms*, vol. 358, pp. 72–81, 2015.
- [19] J. M. Lombaard and E. Friedland, “The elastic scattering of deuterons by ${}^9\text{Be}$ from 1.00 to 2.20 MeV,” *Z. Phys.*, vol. 249, pp. 349–355, 1972.
- [20] F. Machali, Z. A. Saleh, A. T. Baranik, F. Asfour, I. Boundouk, and V. E. Storizhko, “Elastic scattering of deuterons by $\text{Be}9$ and $\text{Si}28$,” *ATKE*, vol. 13–7, pp. 29–32, 1968.
- [21] J. H. Renken, “Elastic scattering of Deuterons by Beryllium,” *Phys. Rev.*, vol. 132, no. 6, pp. 2627–2631, 1963.
- [22] V. Paneta, J. L. Colaux, A. F. Gurbich, C. Jeynes, and M. Kokkoris, “Benchmarking experiments for the proton backscattering on ${}^{23}\text{Na}$, ${}^{31}\text{P}$ and nat S up to 3.5 MeV,” *Nucl. Instruments Methods Phys. Res. B*, vol. 328, pp. 1–7, 2014.
- [23] R. F. Seiler, D. F. Herring, and K. W. Jones, “Elastic Scattering of Deuterons by N 14 from 700 to 2100 keV*,” *Phys. Rev.*, vol. 136, no. 4B, pp. 994–1000, 1964.
- [24] V. Gomes Porto *et al.*, “Deuteron Induced Reactions on ${}^{14}\text{N}$,” *Nucl. Phys. A*, vol. 136, pp. 385–413, 1969.
- [25] L. Csedreki, I. Uzonyi, Z. Szikszai, G. Gyürky, G. Á. Szíki, and Á. Z. Kiss, “Measurement of gamma-ray production cross sections for nuclear reactions ${}^{14}\text{N}(d,p\gamma) {}^{15}\text{N}$ and ${}^{28}\text{Si}(d,p\gamma) {}^{29}\text{Si}$,” *Nucl. Instruments Methods Phys. Res. Sect. B Beam Interact. with Mater. Atoms*, vol. 328, pp. 20–26, 2014.
- [26] A. F. Gurbich, “Evaluation of non-Rutherford proton elastic scattering cross section for nitrogen,” *Nucl. Instruments Methods Phys. Res. Sect. B Beam Interact. with Mater. Atoms*, vol. 266, no. 8, pp. 1193–1197, 2008.
- [27] A. F. Gurbich, “Evaluation of non-Rutherford proton elastic scattering cross section for silicon,” *Nucl. Instruments Methods Phys. Res. Sect. B Beam Interact. with Mater. Atoms*, vol. 145, pp. 578–583, 1998.
- [28] F. Machali, Z. A. Saleh, A. T. Baranik, P. Asfour, I. Bondouk, and V. E. Storizhko, “Energy Levels of ${}^{19}\text{F}$ from ${}^{16}\text{O}(d,d) {}^{16}\text{O}$,” *Ann. Phys.*, vol. 7, pp. 1–11, 1968.
- [29] O. Dietzsch *et al.*, “Deuteron-induced Reaction on ${}^{16}\text{O}$,” *Nucl. Phys. A*, vol. 114, pp. 330–352, 1968.
- [30] G. Debras and G. Deconninck, “debras-oxygen dp1,” *Anal. Chem.*, vol. 38, p. 193, 1977.
- [31] S. Cavallaro, A. Cunsolo, R. Potenza, and A. Rubbino, “ ${}^{16}\text{O}+d$ Reactions at $E_d < 2$ MeV,” *Nuovo Cim.*, vol. 14, no. 4, pp. 692–710, 1973.
- [32] R. F. Seiler, C. H. Jones, W. J. Aznick, D. F. Herring, and K. W. Jones, “The Elastic scattering of Deuterons by ${}^{16}\text{O}$ from 0.65 to 2.0 MeV,” *Nucl. Phys.*, vol. 45, pp. 647–656, 1963.

- [33] R. G. Lane, A. M. , Thomas, “R-Matrix Theory of Nuclear Reactions,” *Rev. Mod. Phys.*, vol. 30, pp. 257–353, 1958.
- [34] R. E. Azuma *et al.*, “AZURE: An R-matrix code for nuclear astrophysics,” *Phys. Rev. C - Nucl. Phys.*, vol. 81, no. 4, pp. 1–17, 2010.
- [35] N. M. Larson, *Updated users’ guide for SAMMY: Multi-level R-matrix fits to neutron data using Bayes’ equation*, no. October. 2008.
- [36] C. H. Johnson, “Unified R-Matrix-Plus-Potential Analysis for 16O+n Cross Sections,” *Phys. Rev. C*, vol. 7, no. 2, pp. 561–573, 1973.
- [37] “AZURE - R-matrix program.” [Online]. Available: <http://azure.nd.edu/login.php>.
- [38] “Ion Beam Aanalysis Nuclear Data Library.” [Online]. Available: <https://www-nds.iaea.org/exfor/ibandl.htm>.
- [39] F. A. Deeney and J. P. O. Leary, “An understanding of the properties of the dineutron and the deuteron in terms of quantum wave function interference,” *Phys. Lett. A*, vol. 376, pp. 2533–2537, 2012.
- [40] C. E. Rolfs, W. S. Rodney, and D. D. Clayton, *Cauldrons in the Cosmos*, vol. 57, no. 2. 1989.
- [41] Ericson Torleif, “A Theory of Fluctuations in Nuclear Corss Sections,” *Ann. Phys. (N. Y.)*, vol. 23, pp. 390–414, 1963.
- [42] H. M. Omar, V. Y. Gontchar, M. H. S. Bakr, and M. A. Ali, “The Mechanism of the Reactions Mg²⁴(d,p)Mg²⁵ and Mg²⁶(d,p)Mg²⁷ in the Deuteron Energy Range 1.3-2.5 MeV,” *Ann. Phys.*, vol. 7, no. 26, pp. 8–22, 1971.
- [43] P. Von Bretano, J. Ernst, O. Hausser, T. Mayer-Kuckuk, A. Richter, and W. Von Witsch, “Statistical Fluctuations in the Cross Sectons of the Reactions Cl³⁵(p,a)³²S and Cl³⁷(p,a)³⁴S,” *Phys. Lett.*, vol. 9, no. 1, 1964.
- [44] S. T. Butler, “Angular Distributions from (d ,p) and (d ,n) Nuclear Reactions,” vol. 208, pp. 559–579, 1951.
- [45] E. Vogt, “R-Matrix Theory,” 2004.
- [46] E. Vogt, “Theory of Low Energy Nuclear Reactions,” *Rev. Mod. Phys.*, vol. 34, no. 4, pp. 723–747, 1962.
- [47] J. Nebe and G. J. Kirouac, “Elastic neutron scattering from ⁴⁰Ca for neutron energies to 2 MeV,” *Nucl. Physics, Sect. A*, vol. 185, no. 1, pp. 113–130, 1972.
- [48] S. Cierjacks, G. Schnalz, R. Topke, R. R. Spencer, and F. Voss, “Thick Sample Transmission Measurement and Resonance Analysis of the Total Neutron Cross Section of Iron,” *NBS Spec. Publ.*, vol. 2, pp. 754–757, 1975.
- [49] H. G. Mcwhinney *et al.*, “Diffusion of lithium-6 isotopes in lithium aluminate using neutron depth profiling ceramics,” *J. Nucl. Mater.*, vol. 203, pp. 43–49, 1993.
- [50] A. Schulz, D. Derosa, S. Higashiya, M. Rane-fondacaro, H. Bakhru, and P. Haldar, “Evaluating the effect of solid electrolyte interphase formers on lithium depth pro fi les of the solid electrolyte interphase layer and bulk with lithium nuclear reaction analysis,” *J.*

- Energy Storage*, vol. 14, pp. 106–111, 2017.
- [51] Y. Sunitha and S. Kumar, “Depth profiling Li in electrode materials of lithium ion battery by $7\text{Li}(p,\gamma)8\text{Be}$ and $7\text{Li}(p,\alpha)4\text{He}$ nuclear reactions,” *Nucl. Inst. Methods Phys. Res. B*, vol. 400, pp. 22–30, 2017.
- [52] S. Yamanaka and K. Kurosaki, *Neutron Reflector Materials (Be , Hydrides)*. Elsevier Inc., 2012.
- [53] J. Scherr and P. Tsvetkov, “Annals of Nuclear Energy Reactor design strategy to support spectral variability within a sodium-cooled fast spectrum materials testing reactor,” *Ann. Nucl. Energy*, vol. 113, pp. 15–24, 2018.
- [54] J. L’Ecuyer, J. A. Davies, and N. Matsunami, “How accurate are absolute rutherford backscattering yields,” *Nucl. Instruments Methods*, vol. 160, no. 2, pp. 337–346, 1979.
- [55] W. A. Lanford, “Analysis for hydrogen by nuclear reaction and energy recoil detection,” *Nucl. Inst. Methods Phys. Res. B*, vol. 66, no. 1–2, pp. 65–82, 1992.
- [56] G. E. Coote, “Ion beam analysis of fluorine: Its principles and applications,” *Nucl. Inst. Methods Phys. Res. B*, vol. 66, no. 1–2, pp. 191–204, 1992.
- [57] A. Climent-Font, A. Muñoz-Martin, M. D. Ynsa, and A. Zucchiatti, “Quantification of sodium in ancient Roman glasses with ion beam analysis,” *Nucl. Instruments Methods Phys. Res. Sect. B Beam Interact. with Mater. Atoms*, vol. 266, no. 4, pp. 640–648, 2008.
- [58] N. Carmona, I. Ortega-Feliu, B. Gómez-Tubío, and M. A. Villegas, “Advantages and disadvantages of PIXE/PIGE, XRF and EDX spectrometries applied to archaeometric characterisation of glasses,” *Mater. Charact.*, vol. 61, no. 2, pp. 257–267, 2010.
- [59] A. F. Gurbich, “SigmaCalc.” [Online]. Available: <http://sigmacalc.iate.obninsk.ru/>.
- [60] G. Terwagne, “Cross section measurements of the reactions induced by 3He particles on carbon,” *Nucl. Instruments Methods Phys. Res. Sect. B Beam Interact. with Mater. Atoms*, vol. 122, no. 1, pp. 1–7, 1997.
- [61] J. B. Marion, “Accelerator calibration energies,” *Rev. Mod. Phys.*, vol. 38, no. 4, pp. 660–668, 1966.
- [62] G. E. Knoll and J. Wiley, *Radiation Detectibn and Measurement Third Edition*. .
- [63] J. F. Ziegler, J. P. Biersack, and M. D. Ziegler, *SRIM : the stopping and range of ions in matter*. 2008.
- [64] “Thin Film Evaporation.” [Online]. Available: https://cleanroom.byu.edu/TFE_materials.
- [65] W. Catford, “CATKIN.” [Online]. Available: <http://personal.ph.surrey.ac.uk/~phs1wc/kinematics/>.
- [66] J. Pujol, “The solution of nonlinear inverse problems and the Levenberg-Marquardt method,” *Geophysics*, vol. 72, no. 4, 2007.
- [67] I. B. Radović, Z. Siketić, M. Jakšić, and A. F. Gurbich, “Measurement and parametrization of proton elastic scattering cross sections for nitrogen,” *J. Appl. Phys.*, vol. 104, no. 7, 2008.
- [68] M. Kokkoris *et al.*, “Benchmarking the evaluated proton differential cross sections

- suitable for the EBS analysis of natSi and ^{16}O ,” *Nucl. Instruments Methods Phys. Res. Sect. B Beam Interact. with Mater. Atoms*, vol. 405, pp. 50–60, 2017.
- [69] G. Konac, S. Kalbitzer, C. Klatt, D. Niemann, and R. Stoll, “Energy loss and straggling of H and He ions of keV energies in Si and C,” *Nucl. Instruments Methods Phys. Res. Sect. B Beam Interact. with Mater. Atoms*, vol. 136–138, pp. 159–165, 1998.
- [70] G. Konac, C. Klatt, and S. Kalbitzer, “Universal fit formula for electronic stopping of all ions in carbon and silicon,” *Nucl. Instruments Methods Phys. Res. Sect. B Beam Interact. with Mater. Atoms*, vol. 146, no. 1–4, pp. 106–113, 1998.
- [71] R. O. Bondelid and E. E. Dowling Whiting, “(p,n) Threshold-Curve Shapes and Measurement of Threshold Energy with H^1+ Beams,” *Phys. Rev.*, vol. 134, no. 3B, pp. B591–B594, 1964.
- [72] W. N. Lennard, S. Y. Tong, G. R. Massoumi, and L. Wong, “On the calibration of low-energy ion accelerators,” *Nucl. Inst. Methods Phys. Res. B*, vol. 45, no. 1–4, pp. 281–284, 1990.
- [73] R. O. Bondelid, J. W. Butler, and C. A. Kennedy, “Absolute determination of the $\text{O}^{16}(\text{d}, \text{n})\text{F}^{17}$ threshold energy,” *Phys. Rev.*, vol. 120, no. 3, pp. 889–890, 1960.
- [74] L. Csedreki, G. Szíki, Z. Szikszai, and I. Kocsis, “Resonance parameters of the reaction $^{12}\text{C}(\text{d}, \text{p}\gamma)^{13}\text{C}$ in the vicinity of 1450 keV for accelerator energy calibration,” *Nucl. Instruments Methods Phys. Res. Sect. B Beam Interact. with Mater. Atoms*, vol. 342, pp. 184–187, 2015.
- [75] J. W. Olness, W. Haerberli, and H. W. Lewis, “Levels of C^{133} from $\text{S}^{32}(\text{p}, \text{p})\text{S}^{32}$ and $\text{S}^{32}(\text{p}, \text{p}'\gamma)\text{S}^{32*}$,” vol. 112, no. 5, pp. 1702–1716, 1958.
- [76] J. Räisänen and P. O. Tikkanen, “Calibration of accelerator proton energy by the $^{14}\text{N}(\text{p}, \text{p}'\gamma)^{14}\text{N}$ reaction resonances,” *Nucl. Instruments Methods Phys. Res. Sect. A Accel. Spectrometers, Detect. Assoc. Equip.*, vol. 723, pp. 5–7, 2013.
- [77] W.-T. Chu, J. W. Mayer, and M. Nicolet, “Backscattering Spectrometry,” p. 389, 1978.
- [78] J. P. Biersack and J. F. Ziegler, “Refined Universal Potentials in Atomic Collisions,” *Nucl. Instruments Methods Phys. Res. B*, vol. 194, pp. 93–100, 1982.
- [79] “National Nuclear Data Center - Brookhaven National Laboratory.” [Online]. Available: <https://www.nndc.bnl.gov/>.
- [80] U. Fasoli, D. Toniolo, and G. Zago, “Elastic and inelastic scattering of protons by Li^7 in the Energy Interval (3.0-5.5) MeV,” *Nuovo Cim.*, vol. 34, no. 3, pp. 542–551, 1964.
- [81] S. Bashkin and H. T. Richards, “Proton Bombardment of the Lithium Isotopes,” *Phys. Rev.*, vol. 84, no. 6, pp. 1124–1129, 1951.
- [82] A. F. Gurbich, “Evaluation of non-Rutherford proton elastic scattering cross section for carbon,” *Nucl. Instruments Methods Phys. Res. Sect. B Beam Interact. with Mater. Atoms*, vol. 136–138, pp. 60–65, 1998.
- [83] P. R. Malmberg, “Elastic scattering of protons from Li^7 ,” *Phys. Rev.*, vol. 101, no. 1, pp. 114–118, 1956.
- [84] A. F. Gurbich, “Evaluation of non-Rutherford proton elastic scattering cross section for

- oxygen,” *Nucl. Instruments Methods Phys. Res. Sect. B Beam Interact. with Mater. Atoms*, vol. 129, pp. 311–316, 1997.
- [85] A. F. Gurbich, “Evaluated differential cross-sections for IBA,” *Nucl. Instruments Methods Phys. Res. Sect. B Beam Interact. with Mater. Atoms*, vol. 268, pp. 1703–1710, 2010.
- [86] R. Bass, “Fusion of heavy nuclei in a classical model,” *Nucl. Physics, Sect. A*, vol. 231, pp. 45–63, 1974.
- [87] A. Z. El-Behay, M. A. Farouk, M. L. Jhingan, M. H. Nassef, and I. I. Zaloubovsky, “The (d,p) reaction on ^{23}Na in the deuteron energy range from 1.0 to 2.5 MeV,” *Nucl. Phys.*, vol. 74, no. 1, pp. 225–233, 1965.
- [88] K. V. Karadzhev, “-,” *Yad. Fiz.*, vol. 4, p. 909, 1966.
- [89] M. Kokkoris *et al.*, “Study of selected differential cross-sections of the reactions for NRA purposes,” *Nucl. Inst. Methods Phys. Res. B*, vol. 267, no. 8–9, pp. 1744–1747, 2009.
- [90] F. Ajzenberg-Selove, “Energy levels of light nuclei $A = 18-20$,” *Nucl. Physics, Sect. A*, vol. 475, pp. 1–198, 1987.
- [91] “National Nuclear Data Center - Brookhaven National Laboratory.” .
- [92] R. O. Nelson, E. G. Bilpuch, and G. E. Mitchell, “Analysis of Proton Resonance Scattering from non-zero Spin Targets,” *Nucl. Instruments Methods Phys. Res. A*, vol. 236, pp. 128–141, 1985.
- [93] D. Abriola, A. F. Gurbich, M. Kokkoris, A. Lagoyannis, and V. Paneta, “Proton elastic scattering differential cross-sections for ^{12}C ,” *Nucl. Instruments Methods Phys. Res. Sect. B Beam Interact. with Mater. Atoms*, vol. 269, no. 18, pp. 2011–2016, 2011.
- [94] J. Bojowald, H. Machner, H. Nann, W. Oelert, M. Rogge, and P. Turek, “Elastic deuteron scattering and optical model parameters at energies up to 100 MeV,” *Phys. Rev. C*, vol. 38, no. 3, pp. 1153–1163, 1988.
- [95] W. W. Daehnick, J. D. Childs, and Z. Vrcelj, “Global optical model potential for elastic deuteron scattering from 12 to 90 MeV,” *Phys. Rev. C*, vol. 21, pp. 2253–2274, 1980.
- [96] H. An and C. Cai, “Global deuteron optical model potential for the energy range up to 183 MeV,” *Phys. Rev. C - Nucl. Phys.*, vol. 73, no. 5, 2006.
- [97] Y. Han, Y. Shi, and Q. Shen, “Deuteron global optical model potential for energies up to 200 MeV,” vol. 044615, no. July, pp. 1–11, 2006.
- [98] E. S. S. and P. T. R. Capote, M. Herman, P. Oblozinsky, P.G. Young, S. Goriely, T. Belgya, A.V. Ignatyuk, A.J. Koning, S. Hilaire, V.A. Plujko, M. Avrigeanu, O. Bersillon, M.B. Chadwick, T. Fukahori, Zhigang Ge, Yinlu Han, S. Kailas, J. Kopecky, V.M. Maslov, G. Reffo, M. Si, “Reference Input Parameter Library (RIPL-3).” [Online]. Available: <https://www-nds.iaea.org/RIPL-3/>.
- [99] P. G. Burke, *R-matrix theory of atomic collisions : application to atomic, molecular and optical processes*. 2011.
- [100] S. Kubono, “Study of explosive hydrogen burning in the universe using ^3He beams,” *Nucl. Instruments Methods Phys. Res. Sect. A Accel. Spectrometers, Detect. Assoc. Equip.*, vol. 402, no. 2–3, pp. 412–416, 1998.

